Bose-Einstein condensation of polaritons in a ring microcavity

by

Shouvik Mukherjee

B.Sc. (Hons) and M.Sc. in Physics, Indian Institute of Technology Kharagpur, 2014

M.S. in Physics, University of Pittsburgh, 2016

Submitted to the Graduate Faculty of

the Kenneth P. Dietrich School of Arts and Sciences in partial fulfillment

of the requirements for the degree of

Doctor of Philosophy

University of Pittsburgh

2021

UNIVERSITY OF PITTSBURGH

KENNETH P. DIETRICH SCHOOL OF ARTS AND SCIENCES

This dissertation was presented

by

Shouvik Mukherjee

It was defended on

April 28, 2021

and approved by

David W. Snoke, Professor, Physics and Astronomy

Sergey Frolov, Associate Professor, Physics and Astronomy

David Pekker, Assistant Professor, Physics and Astronomy

Vittorio Paolone, Professor, Physics and Astronomy

David H. Waldeck, Professor, Chemistry

Dissertation Director: David W. Snoke, Professor, Physics and Astronomy

Bose-Einstein condensation of polaritons in a ring microcavity

Shouvik Mukherjee, PhD

University of Pittsburgh, 2021

Excitons are bound states of electrons and holes formed when light is absorbed in a semiconductor with a radiative lifetime typically of the order of a few nanoseconds. Putting these excitons inside a cavity allows them to mix strongly with the cavity photons, which creates a new quasi-particle called an exciton-polariton. These dressed photons have a small effective mass and an effective repulsive interaction, allowing them to thermalize and form a Bose-Einstein condensate within their lifetime.

In this thesis, I will report some recent experiments which I performed in the Snoke group on exciton-polariton condensation in a ring-shaped semiconductor microcavity. In a first set of experiments, the ring geometry along with a unidirectional force acting on the polaritons helped us realize the rigid pendulum potential for the polaritons. Exciton-polaritons are monitored by detecting the photons leaking from the microcavity allowing us to observe real-time dynamics of the polariton condensate in the potential. I observed pendulum-like oscillations of the polariton condensate which were damped about the potential minimum. By measuring the temporal evolution of the density and the spectral energy shift of the polariton emission, I made a direct measurement of the polariton-polariton interaction strength. In the course of these measurements, I found a non-equilibrium population of excitons traveling much further than previously anticipated, which demonstrates the anomalous "polariton effect" on the transport of excitons. The polaritons constitute an example of a pseudospin-1/2 Bose gas which shows distinct properties from electrons in a semiconductor. By quenching a gas of polaritons in the rigid pendulum potential I observed the spinor dynamics, which showed characteristics of the optical spin Hall effect. The role of the free carrier reservoir on the energy dissipation of the condensate is theoretically investigated and applied to the interpretation of the recently observed "polariton drag effect", in our group, where driving an electric current through the neutral polariton condensate produced momentum and energy shift of the condensate. These experimental and theoretical studies on transport

and equilibration of the polariton condensate in narrow waveguide microcavities move towards making coherent polariton circuits for optical information processing.

Table of contents

Preface . . . xiii

1.0 Introduction . . . 1

1.1 Overview . . . 1

1.2 Thesis outline . . . 5

1.3 Introduction to exciton-polaritons . . . 6

1.3.1 Cavity photons . . . 6

1.3.2 Microcavity . . . 7

1.3.3 Excitons in quantum wells . . . 10

1.3.4 Strong coupling . . . 13

1.3.5 Exciton-photon coupling . . . 14

1.3.6 Polariton dispersion . . . 15

1.4 Forces on polaritons . . . 18

1.5 Polariton-polariton interaction . . . 20

1.6 Bose-Einstein condensation of polaritons . . . 23

2.0 Experimental methods . . . 27

2.1 Skeleton of an experiment . . . 27

2.2 Optical pumping . . . 29

2.2.1 Non-resonant pump . . . 30

2.2.2 Resonant pump . . . 33

2.3 Imaging concepts and optical setup . . . 35

2.4 Fabrication of rings . . . 40

2.4.1 Recipe for photolithography . . . 45

3.0 Pendulum oscillations of a polariton condensate . . . 47

3.1 Radially confined states in the ring . . . 48

3.2 Non-equilibrium motion and pendulum oscillations . . . 52

3.3 Open-dissipative condensate dynamics . . . 54

3.4 Density dependence of thermalization . . . 56
3.5 Measurement of the polariton-polariton interaction strength . . . 60
3.6 Conclusion . . . 62
3.7 Supplementary information . . . 63
3.7.1 Photon counting . . . 63
3.7.2 Example of streak images used for measuring interaction strength . . . 63
3.7.3 Finding the interaction strength from a streak image . . . 68
3.7.4 Determining error bounds on g_{fit} . . . 71
3.7.5 Theoretical model . . . 74
3.7.6 Evidence of the exciton reservoir at low density . . . 76
4.0 Spin dynamics of a polariton condensate . . . 80
4.1 Motivation . . . 80
4.2 Experiment . . . 83
4.3 Theoretical model . . . 91
4.4 Conclusion . . . 98
4.5 Supplementary information . . . 99
4.5.1 Derivation of Hamiltonian . . . 99
4.5.2 Stokes vector measurement . . . 104
5.0 Drag and dissipation of a polariton condensate . . . 108
5.1 Motivation . . . 108
5.2 Theory . . . 111
5.3 Polariton drag effect . . . 119
5.4 Conclusion . . . 126
5.5 Supplementary information . . . 126
5.5.1 Quantum master equation . . . 126
5.5.2 Weyl-Wigner transformations . . . 132
5.5.3 Calculation of the scattering amplitude $M(\mathbf{r}-\mathbf{r}')$ . . . 132
5.5.4 Drag potential in one-dimension . . . 133
6.0 Final remarks . . . 135
Appendix A . . . 139

A.1 Radial modes in the ring 139
Bibliography 142

List of tables

1 Time period comparison of oscillations 56
2 Parameter values used in the simulation for Figure 24(b) in the main text. 76
3 Stokes vector measurement scheme 105

List of figures

1 Dispersion of cavity photons 7
2 Light cone of cavity photons 8
3 Basic microcavity design 9
4 Reflection spectrum of empty microcavity 10
5 Exciton dispersion for different hydrogenic levels 11
6 Energy bands in a GaAs quantum well 12
7 Characteristics of strong coupling 14
8 Reflectivity spectra of a polariton microcavity 16
9 Photoluminescence showing lower polariton dispersion 18
10 Polariton dispersion dependence on detuning 19
11 Cross-section of a microcavity wafer 20
12 Edge trapping example 21
13 Evidence of polariton BEC 25
14 Reflectivity spectra of a single DBR 30
15 Non-resonant pump excitation 32
16 Sketch of optical setups 37
17 Working principle of a streak camera 39
18 Pumping geometries 41
19 Fabrication process overview 42
20 SEM image of etched rings 45
21 Confined energy states in a ring 50
22 Spectrally resolved PL from ring 50
23 Ring channel microcavity 51
24 Pendulum-like oscillations in ring 53
25 Streak images from rings with different radii 55
26 Intensity oscillations from rings with different radii and radial widths 57

27 Density dependence on thermalization 58
28 Effect of stimulated scattering on BEC 59
29 Measurement of the exciton-exciton interaction strength 61
30 Interaction strength measurement for different cases 65
31 Example of a fit with no exciton reservoir 66
32 Range of PL emission angles 71
33 Normalized PL intensity plotted on a log-linear scale 72
34 Comparison of fits with and without an energy offset 73
35 Theoretically calculated time evolution of the polariton condensate density . . . 75
36 Exciton transport experiment sketch 77
37 Polariton dispersion as a function of distance from the pump spot 78
38 Relative occupation of the momentum states 79
39 TE-TM splitting the microcavity 82
40 Schematic of the experimental setup 83
41 Condensate energy and linewidth in the ring 85
42 Comparison of the polarization between the top and bottom of the ring 87
43 Temporal PL intensity in the ring 88
44 Linear polarization wrapping in the ring 89
45 Example of time and polarization resolved PL from tilted ring 90
46 Position resolved Stokes vector 92
47 Sketch of energy modes in the ring 93
48 Theoretical spin dynamics in the ring 94
49 Temporal snapshots of the S_1 and S_2 components 106
50 Drag effect on expanding wavepacket 119
51 Sketch of the polariton drag experiment 120
52 Model of the potential profile in the wire 121
53 Momentum shift of the condensate PL 122
54 Theoretical and experimental comparison of the drag effect 123
55 Spectrally resolved PL from the condensate in the wire 124
56 Compare energy shifts in the wire 125

57 Effect of current on the momentum distribution of the condensate 125

Preface

The work in this thesis is a culmination of projects I undertook in Prof. David Snoke's lab. Over the years at Pitt, I had the good fortune to learn from and the pleasure to work with an exceptional group of people. While there is no way to completely express my gratitude towards them in writing, I humbly attempt to acknowledge the support I received from them in these few lines.

I'm indebted to my advisor David Snoke for allowing me to be a part of his research group. I thank him for his guidance and for teaching me the ways of a scientist. The trust he has shown in each of us (members of the Snoke group) made us believe in ourselves and motivated us to reach our goals. He is a great teacher who cares for his students and I have personally benefited from his vast knowledge in theoretical and experimental methods. I value the conversations we had, be it about science, philosophy, or general matters of life. I wish to thank him and his wife Sandy, for having me every year for Thanksgiving and making me feel a part of their big family.

I am extremely fortunate to meet Prof. Daniel Boyanovsky in my first year at Pitt. Besides being an exceptional physicist, he is a wonderful teacher. Over the years I have spent numerous hours in his office discussing various topics in theoretical physics. I thank him for patiently teaching me techniques useful for my research as well as answering all my questions. Dan's lectures on Particle physics and Quantum field theory are some of the best lectures I have attended so far. I am always in awe of the breadth and depth of his knowledge, tying together seemingly unrelated topics in Cosmology, High energy physics, and quantum optics. The bookshelf on the wall of his office is only a testimony to this. I also wish to thank him for the support, encouragement, and advice he has given me over the years.

I thank Prof. David Pekker for advising me in the first two-and-a-half years at Pitt. David is a very talented physicist and he often comes up with unconventional, yet brilliant ideas for solving problems. I have learnt so much from him while working with him. Some of the topics he taught me are still relevant and useful in my present research. He introduced

me to the world of ultracold atoms and my initial interest in Bose-Einstein condensates was ignited by him.

Transitioning from theoretical to experimental research wouldn't have been smooth if not for the support, encouragement, and mentorship from my labmates at that time, David Myers, Jonathan Beaumariage, and Burcu Ozden. David accepted me under his wings and taught me everything I know about the lab today. He seemed to have very practical technical knowledge about everything, right from how oil pumps and turbo pumps work to designing electronic circuits for measurements. He always had advice on any technical difficulty I encountered in the lab. I have had the pleasure of collaborating with him on several projects and engaging in countless stimulating discussions which led to many fruitful projects. Johnny has been instrumental in making our lab run smoothly. His code on automating the instruments has simplified conducting the experiments over time and I'm confident that they will immensely help the future graduate students joining our lab. I'm thankful to him for performing the non-trivial task of designing and characterizing the microcavity samples which we receive from our collaborators Lauren Pfeiffer and Keith Nelson at Princeton. I have enjoyed countless debates and discussions with Johnny and David on a wide range of non-physics topics. I thank Burcu for teaching me and guiding through the fabrication process in the cleanroom and for fabricating the sample I used in my work.

It was a great pleasure to work with Ryan Balili, a past member of our group, during a few of his visits to our lab. The energy and enthusiasm he brings to the lab are highly infectious. He helped me with the laser cavity alignment and he mentored me to learn several skills necessary for independently designing and making optical setups. I had a successful collaboration with him and Peng Ji, then a graduate student with Prof. Gurudev Dutt, investigating nitrogen-vacancy centers in diamond.

I thank Prof. David Jasnow for helping me appreciate the "quantum" aspect of quantum mechanics and Prof. Roger Mong for demystifying the idea of topology in condensed matter physics. Collaborations with Prof. Andrew Daley and Prof. Ashton Bradley helped me understand the nuances of the physics of condensates. I also wish to thank our collaborators Rosaria Lena, Valera Kozin, and Anton Nalitov for helping us interpret our experimental observations. I am grateful to Mark Steger and Yosoeb Yoon for providing their suggestions

on installing the spatial light modulator in our experiments. I thank our office staff and especially Leyla Herschfeld for keeping a record and helping me meet all the academic and administrative deadlines. I am thankful to our machinist staff who are incredibly skilled at making our requested custom design parts. I thank the financial support provided by the National Science Foundation (Grant No. DMR-2004570) and Army Research Office (Grant No. W911NF-15-1-0466) for my work.

I am very pleased to collaborate with Zheng Sun, who joined our lab as a postdoc in 2017. I thank him for his encouragement and advice he had given me over the years as well as for introducing me to the research area of two-dimensional materials. I am happy to see Qi Yao and Hassan Alnatah taking over the reins of GaAs project and wish them success in their endeavors. I am glad to have friends in the department on whom I can depend - Amro, Christian, Sebastian, Brian, Yuhe, and Hao whose company has made my stay in Pittsburgh enjoyable. I am thankful to Meghanath for being an excellent friend, for feeding me, and for all the memorable camping trips to the National Parks we went on together.

I am grateful to my family for always supporting me and praying for my well-being. Living apart 12,883 Km from them has only made our bond grow stronger and not a single day has passed without my mother inquiring whether I'm eating timely and how's my research progressing. I'm thankful to them all; my parents - *Maa*, *Baba*, my maternal uncle, aunt and brother - *Mambhai*, *Mimi*, *Bhodor*, and my maternal grandparents *Didun*, and *Bapi dadu*. *Bapi dadu* would have been very happy today to learn how much I have come along this journey. It has been almost three years since he left us. I hope from wherever he is, he is still showering his blessings on us. To him, I dedicate this thesis.

1.0 Introduction

1.1 Overview

Bosons are integer spin particles which show the fundamental quantum effect of Bose–Einstein condensation (BEC) [1, 2, 3]. At sufficiently low temperatures or high particle densities, when the thermal de-Broglie wavelength is comparable to the average separation between the particles, a macroscopic coherent state is formed in an otherwise incoherent, thermalized many-particle system. The discovery of superconductivity in mercury at low temperatures [4] and superfluidity in liquid ^{4}He below a critical temperature while flowing through a capillary were the first examples of a fluid to show such a coherent behavior [5, 6]. Since the first demonstration of Bose-Einstein condensation in dilute atomic gases in 1995 [7, 8], a number of other platforms have emerged, including molecules [9, 10, 11], photons [12] and exotic quasi-particles [13, 14, 15, 16, 17, 18], which regularly produce this state of matter. Early experiments with ultracold atoms have studied several fundamental properties of these atomic condensates like coherence [19, 20], bosonic stimulation [21], sound propagation [22, 23, 24], collective excitations [25, 26, 27], superflow [28, 29] , critical velocity [30], vortices [31, 32, 33, 34, 35], matter-wave amplification [30, 36] etc. These studies have contributed to our understanding of macroscopic coherent phenomena in nature.

One of the challenges of accessing this state of matter in atomic gases is the requirement of extremely low temperatures ($\sim$ 100 - 200 nK) and elaborate experimental setups for trapping and cooling atoms [37, 38]. Thus miniaturization is a technical challenge at present in cold atom experiments [39]. On the other hand, solid-state based systems are known for compact design. Semiconductors are also known to host quasi-particles which are much lighter than atoms [40]. One such quasi-particle is an exciton [41], a bound state of an electron and a hole. Due to its lighter mass the same density of excitons as atoms may undergo condensation at much higher temperatures ($\sim$ 0.2 mK [42]). Mixing these quasi-particles with photons produces even lighter quasi-particles, known as exciton-polaritons [43] which can undergo condensation from 4 K (in GaAs [18]) to room temperature (in perovskites [44], GaN [45],

ZnO [46] and potentially transition-metal dichalcogenides). Therefore semiconductor based platforms show promise for making practical future devices which harness the properties of Bose-Einstein condensates.

Over a decade has passed since the first demonstration of Bose-Einstein condensation of exciton-polaritons in a semiconductor microcavity [17, 18]. It stands out as a unique platform for exploring physics of out-of-equilibrium systems. Recent reports on the observation of thermal equilibration [47, 48] have triggered interest in studying equilibrium physics in non-hermitian systems [49, 50, 51, 52, 53] and offer promise for making devices based on polariton condensates which operate near equilibrium [48]. Such a feat has been achieved in microcavities with $Q > 10^5$, allowing several collision events between polaritons to distribute energy and thermalize within their lifetime [47, 48, 54, 55]. In cold atom systems, the lifetime of the atoms trapped in magnetic traps or optical dipole traps are typically $\sim 1 - 10$ seconds, while the particle-particle scattering times range from $1 - 100$ ms [7, 8, 56]. Several scattering events are required to achieve thermal equilibrium, leading to thermalization times consistently ~ 10 times longer than the scattering times [57]. Efficient thermalization in a dilute Bose gas is required to achieve quantum degeneracy limit. For dilute atomic gases, the thermalization times range between $0.01 - 1$ seconds. This gives lifetimes about $10 - 1000$ times greater than the thermalization times, leading to equilibrated populations of the atoms in the trap. For polaritons, the scattering time is estimated to be ~ 1 ps [58, 59]. This leads to thermalization times typically about 10 ps, which was found to be consistent with a previous study on thermalization [60]. In the earlier generation of the microcavities, the polariton lifetimes were about $2 - 10$ ps, which prevented the polaritons from reaching equilibrium in a trapping potential. In the latest generation of polariton microcavities the lifetimes have significantly improved making way for equilibrated polariton populations. With an average polariton lifetime of approximately 200 ps [54, 47], nearly $10 - 20$ times longer than the thermalization times the polaritons reach thermal equilibrium.

One of the most debated questions in the polariton community is on the strength of the polariton-polariton interactions. Despite measurements reported from several groups there is a spread of two orders of magnitude in the measured values for the interaction strength in GaAs quantum wells [61], leading to strong disagreement with theory [62]. Interactions be-

tween polaritons are what separates them from photonic platforms, which are non-interacting at low photon fluence and only weakly interacting due to the $\chi^{(3)}$ nonlinearity at high photon fluence [63]. In a typical polariton system, the effective $\chi^{(3)}$ is several orders of magnitude higher than nonlinear crystals due to the Coulomb mediated scattering of the excitons. Interactions also play a key role in the process of thermalization of a polariton gas. In this thesis, I provide strong bounds on the interaction strength in the condensate regime by directly observing the density and the energy shift of the polaritons as a function of time. All the previous measurements were reported in a continuously pumped steady state regime. The ability to monitor continuously the evolution of the polaritons through the leakage light from the microcavity allowed us to study dynamics of the long lifetime polaritons thermalizing in a trap. These studies are complimentary to the studies in cold atom systems, and we observed motion of the polariton condensate in a macroscopic trap. The trap was created in a circular waveguide with an energy gradient along a diameter.

Repulsive interaction between the polaritons and the reservoir excitons is at the heart of creating optical traps for polaritons [64]. The question of the transport of the excitons in polaritonic system is central for precisely controlling trap geometries. Several theoretical proposals explore this mechanism for creating and studying polaritons in trapped optical networks [65]. One of the main assumptions is that the excitons have a small diffusion length ≈ 1 μm. In the old generation of polariton microcavities, this assumption was not carefully tested, as almost all the studies looked at the polaritons at the location where they were created by the pump laser. For the present generation of the polariton microcavities with long lifetime ($\sim 200ps$) this assumption was used to design optical traps and interpret the blueshift of the polariton energy away from the pumping region [66]. This looked reasonable, because in bare GaAs quantum wells excitons do not show anomalous transport characteristics. We found that the scenario is drastically altered when the quantum wells are placed within a microcavity. In both two- dimensional and one-dimensional microcavities we found evidence of an exciton reservoir away from the pump spot [67, 68], challenging the long-held viewpoint of small diffusion lengths of excitons in polariton microcavities.

Polaritons have been studied extensively for spintronic applications due to their pseudospin - 1/2 nature (see chapter 9 in Ref. [69] and references within). In a microcavity, the

longitudinal and transverse splitting of the excitons is enhanced after mixing with the transverse electric (TE) and transverse magnetic (TM) modes of the cavity [69]. This gives rise to an in-plane magnetic field which makes the spin of the polaritons precess as they move. It manifests itself in the formation of complex polarization textures [70, 71, 72]. In the long-lifetime cavity, the polaritons can travel long distances and their motion can be directed by the waveguide. The interplay between the polariton wavevector and the in-plane magnetic field gives rise to non-trivial polarization patterns. I investigated this phenomenon using time-resolved techniques to study the spin dynamics of the polariton condensate as it flowed and relaxed in a circular trap. In this study, I showed the onset of polariton BEC in the trap minimum monitored through the polarization build-up. In this thesis, the connections with the optical spin Hall effect are also illustrated in the dynamics as the polaritons are transported from the region of their creation to the minimum energy region in the trap. This study lays the foundation for future studies investigating topological phases in a network of polariton waveguides.

In all the experiments discussed in this thesis, the polariton condensate is formed spontaneously as a result of bosonic stimulation [21] from a hot bath of polaritons, excitons and free-carriers into the $k = 0$ state. Once the condensate is formed it shows energy dissipation despite showing characteristics of a superfluid. For example, the observation of strong damping of the pendulum motion in the tilted rings [68] was seen in a region spatially separated from the pump spot. This raises the question of how a superfluid dissipates energy and what role the reservoir plays in this mechanism. I develop a theory describing energy and momentum- conserving interactions between polaritons in the condensate and the excitons and free electrons comprising the reservoir without any particle exchanges, along similar lines as previous theories describing the energy dissipation in atomic BEC in a trap. I adopt this theory to explain the observations in a series of experiments driving an electric current through a polariton condensate. The surprising result is that an electric current flowing through a neutral polariton condensate can produce a drag effect, i.e., change the average momentum of the the particles in the condensate while also giving rise to an energy shift, and it can be explained from the perspective of the effect of a moving bath on a BEC.

1.2 Thesis outline

The thesis is organized as follows:

- Chapter 1 provides an introduction to the exciton polaritons which are produced inside a monolithic semiconductor based microcavity. Properties of these quasi-particles are discussed to familiarize the readers with the main concepts and the jargon that are used in the polariton community.
- Chapter 2 provides an overview of the experimental techniques used to study the polariton condensates in this thesis. It describes both the optical methods used to detect the polariton luminescence and the semiconductor fabrication process used to design the quasi-one dimensional ring shaped circular waveguides.
- Chapter 3 details the spectral properties of the fabricated rings and the experiments on measuring the time-period of oscillations of a polariton condensate in a rigid pendulum potential. It discusses the method for measuring the interaction strength of the polaritons in the condensate using dynamics and also provides evidence for the presence of an exciton reservoir away from the pump region.
- Chapter 4 looks at the spin polarization dynamics in a highly non-equilibrium condensate undergoing energy relaxation in a rigid pendulum potential. Spontaneous generation of non-trivial polarization pattern of the condensate in the course of the dynamics was observed. Dynamical signatures of the optical spin Hall effect are shown and a theoretical model is developed to account for the observed effects.
- Chapter 5 develops a theory from an open quantum system perspective to describe the mechanism of dissipation in polariton condensates. The theory is applied to the interpretation of the polariton drag effect observed in recent experiments where the effect of driving an electric current through a polariton condensate was studied.
- Chapter 6 summarizes the main results of the thesis and discusses next directions for future work.

1.3 Introduction to exciton-polaritons

1.3.1 Cavity photons

Light trapped between two perfectly reflecting plane mirrors forms a standing wave just like a plucked guitar string. The dispersion relation of such a light wave in a dielectric medium of refractive index n_{cav} is given by

$$E_{cav} = \frac{\hbar c k}{n_{cav}} = \frac{\hbar c}{n_{cav}} \sqrt{k_{||}^2 + k_{\perp}^2}. \tag{1.1}$$

where $k_{||}$ is the component of the wavevector $\vec{k}$ in the plane of the mirrors while $k_{\perp}$ is the component normal to the mirrors. Due to confinement, $k_{\perp}$ will take discrete values given by $k_{\perp} = m n_{cav} \pi / L$, where m is the order of the confined mode and L is the separation between the mirrors. An example of the dispersion of different modes of the confined light wave is shown in Figure 1. The energy of the modes could be tuned by changing the separation between the mirrors. In the example the cavity length is chosen as 1.2 μm, much smaller than the cavity length of typical Ti:Sapphire lasers, which ranges from a few centimeters to few hundreds of centimeters. A small cavity will have larger energy separation between two consecutive order modes. A larger energy separation is desirable for making the cavity work in single mode regime when a mechanism is introduced to select a desired mode.

When the mirrors of the cavity are not 100% reflecting, a small amount of light could be coupled out of the cavity. Since the cavity is usually made of an optically dense medium ($n_{cav} > 1$), the photons leak from optically denser medium to optically rarer medium (air or vacuum). Energy and momentum conservation implies that the photons can escape into the vacuum only within a range of in-plane momentum ($k_{||}$). In Figure 2, the dispersion of the photons outside the cavity, for critical angle of incidence at the boundary ($E = \hbar c |k_{||}|$), is plotted over the energy dispersion of the m = 1 mode of the cavity. Photons with energy and momentum dispersion lying within the region bounded by the dispersion curves $E = \hbar c |k_{||}|$ are within the lightcone and could couple out of the cavity. Photons with dispersion lying outside the light cone will undergo total internal reflection at the boundary and will remain trapped within the cavity.

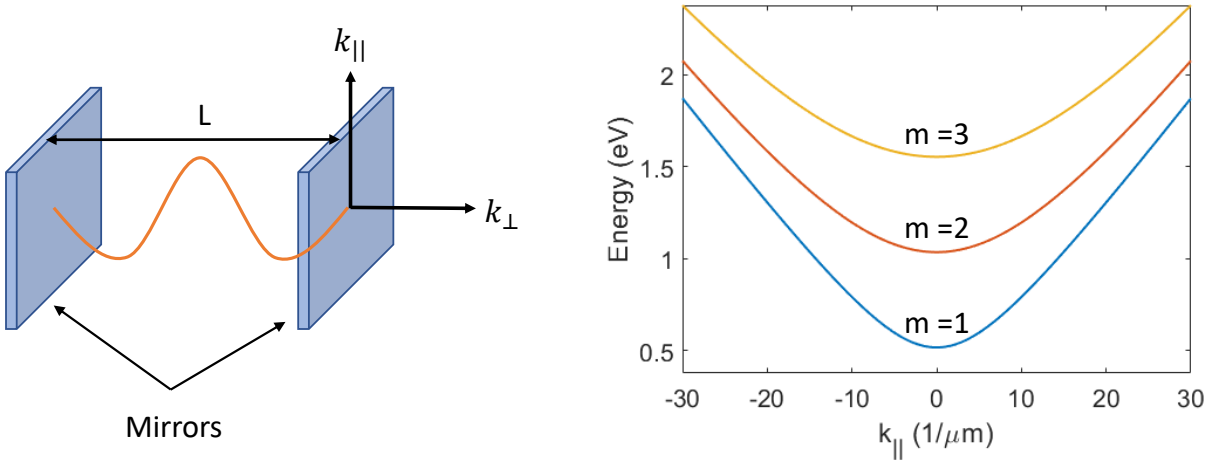

Figure 1: Dispersion of the cavity photons as a function of the in-plane momentum $k_{||}$ for a cavity length of 1.2 μm and $n_{cav} = 3.3$. The energy separation between the modes normal to the mirror ($k_{||} = 0$) is $\hbar c\pi/L$.

1.3.2 Microcavity

A cavity with dimensions in the range of a few hundreds of nanometers to a few micrometers is called a microcavity [73]. Microcavities are fabricated in different shapes and the most common designs are pillar [74], disc [75] and toroid [76] microcavites. The microcavity used in the present work resembles a pillar structure made of III-V group elements. A sketch of an empty microcavity is shown in Figure 3. High quality mirrors of the microcavity are made of alternating layers of high (n_H) and low (n_L) refractive index dielectric materials stacked on top of each other. When the thickness of each layer is made a quarter wavelength of the light wavelength it is designed to trap, the structure is known as a distributed Bragg reflector (DBR). An example of the reflectivity of such a structure is shown in Figure 4. The high reflectivity of such periodic structures emerges due to the constructive interference between reflected beams in each layer and also across different layers producing the unique features in the reflectivity spectra; stop band and Bragg modes. The stop band is the region of the spectrum (wavelengths) for which the reflectivity is nearly 100 %. Bragg modes are

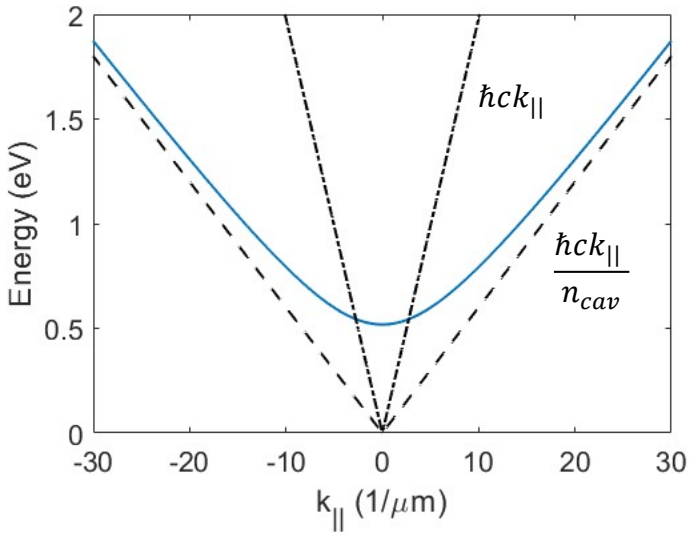

Figure 2: Re-plot of the m = 1 cavity mode showing the region of the dispersion bounded by the light cone boundary $\hbar c|k_{||}|$. Only the photons with energy and momentum falling within the light cone can couple out of the microcavity. At very high in-plane momenta, all the modes m = 1,2,3, etc. approach the linear dispersion $\hbar c|k_{||}|/n_{cav}$.

the dips in the reflectivity beyond the stop band; the DBR is a poor reflector at these wavelengths. The reflectivity spectrum of a DBR is calculated using a transfer matrix formalism [69] which is an efficient way of solving the boundary conditions of Maxwell's equations at each interface considering both the incoming and the outgoing waves at the boundary.

As shown in Figure 3, the microcavity is made by a spacer layer sandwiched between two DBRs. For the optimal case, the thickness of the spacer layer, which forms the cavity, and the thickness of the layers forming the DBR are not independent. If the cavity is designed to operate at a central wavelength λ_0 at order m, then the cavity length L = $m\lambda_0/2n_{cav}$, and the thickness of the layers are $\lambda_0/4n_H$ and $\lambda_0/4n_L$ for high and low refractive index layers, respectively. Figure 4 shows the reflectivity spectra of a microcavity designed at λ_0 = 775 nm. In addition to the features of a single DBR spectrum, there is an additional dip in the reflectivity of the cavity in the middle of the stop band at λ_0. This dip is known as

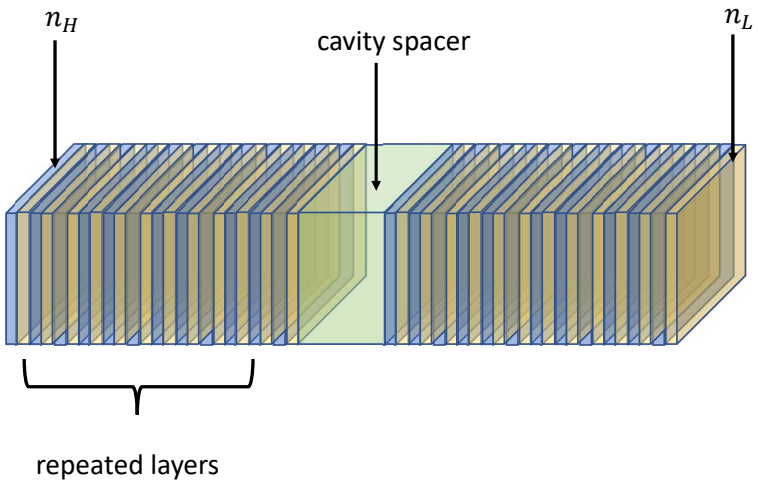

Figure 3: Sketch of a basic microcavity design showing the DBRs formed by alternating layers of high and low refractive index dielectric and the cavity spacer filling the region between the DBRs. The DBRs and the cavity spacer is usually made with a high bandgap dielectric, such that the light at the designed central wavelength of the cavity is not absorbed in the DBRs.

the cavity mode and can be used to couple light directly into the cavity. In this example the free spectral range (wavelength separation between any two successive modes of the cavity) of the cavity is larger than the stop band width, as a result only a single cavity mode is trapped. For large m cavity, many modes can be trapped in this structure. Since the reflectivity is not 100 % at this wavelength, the trapped cavity light has a finite lifetime and eventually leaks from the cavity. The instantaneous electric field of the trapped light is given by $\vec{E}(\mathbf{r},t) = \vec{E_0}(\mathbf{r})e^{i\omega_0 t - \gamma t/2}$, where γ is the rate at which the photons decay. Transforming to the frequency domain, the Fourier transform of an exponential decay function is a Lorentzian function. Thus, the linewidth of the cavity mode is due to the decay rate of the photons; narrower linewidth implies slower decay rate.

How good a microcavity is in trapping the light can be assessed by the quantity Q, known as the quality factor, which is defined as the ratio of the frequency of the cavity mode to the linewidth of the mode, i.e. $Q = \omega_0/\gamma$. The microcavity used in this work is a high Q cavity

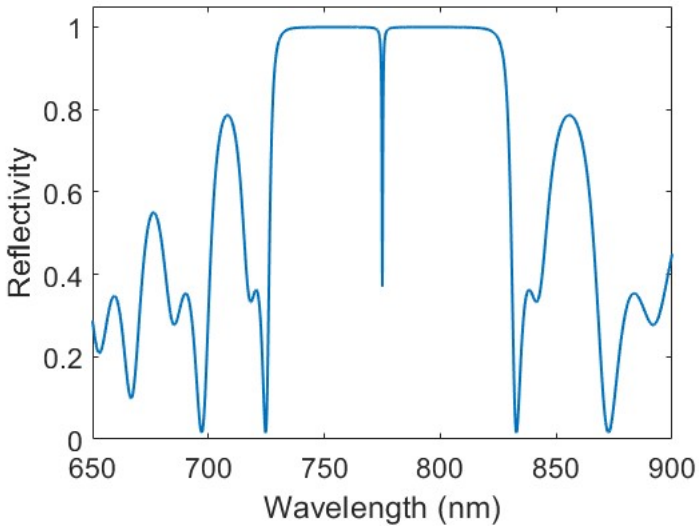

Figure 4: Reflection spectra of an empty microcavity formed by 16 periods DBR calculated using transfer matrix method. The central designed wavelength of the microcavity is 775 nm which is shown as a dip in the reflectivity in the middle of the stop band.

with $Q > 10^5$ corresponding to a cavity photon lifetime of about 100 ps [55, 54]. There are two ways to increase the quality factor of a cavity: (1) increase the number of layers of the DBR, and (2) increase the contrast between the refractive indices of the layers in the DBR. Changing the refractive index of a material means choosing a different material which may not always be an option due to other constraints from the growth and design considerations. Therefore we chose the first method to design a high-Q cavity.

1.3.3 Excitons in quantum wells

Excitons are neutral excitations of a dielectric medium. They can be described as bound states of an electron and a hole, much like a positronium or a hydrogen atom. In our work, excitons are formed in a thin layer of direct-bandgap semiconductor whenever the attractive Coulomb energy between the electrons and holes wins over their kinetic energy. Since the energy cost of forming the bound pair is cheaper than the cost of having free electrons and

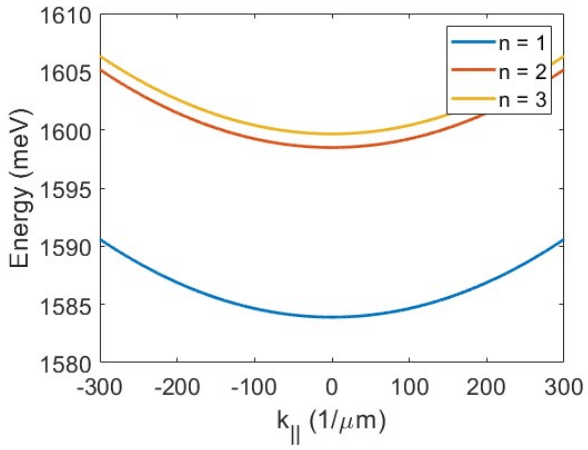

Figure 5: Energy and in-plane momentum dispersion of the heavy-hole exciton in a 7 nm thick quantum well for different hydrogenic levels n = 1s, 2s and 3s.

holes, excitons are naturally formed at low temperatures when the thermal energy is not sufficient to break the pair, i.e., the binding energy (E_B) is greater than the average thermal energy (k_BT). The energy of a free exciton in a GaAs quantum well is given by,

$$E_X = E_g - \frac{Ry}{\left(n - \frac{1}{2}\right)^2} + \frac{\hbar^2 n_q^2 \pi^2}{2m_r l^2} + \frac{\hbar^2 k_{||}^2}{2m_p}, \tag{1.2}$$

where E_g is the bulk band gap of GaAs at the Brillouin zone center, the second term is the two-dimensional binding energy of the exciton, the third term is the confinement energy due to the quantum well of thickness l, assuming an infinite square well potential, and the last term is the in-plane kinetic energy of the exciton. If m_e and m_h are the effective masses of the electron and hole in the conduction and valence bands in GaAs, then the reduced mass $m_r = m_e m_h/(m_e + m_h)$ and the total mass $m_p = m_e + m_h$. Ry is the Rydberg energy in GaAs, which is about 4.1 meV and n_q is the mode order in the confinement direction. The dispersions of the exciton confined to the lowest mode in a quantum well for n = 1s, 2s and 3s states are shown in Figure 5.

In GaAs, the valence shell is formed by mixing of 4s and 4p orbitals. A linear combination of these orbitals give rise to bonding and anti-bonding states each comprised of 8 states.

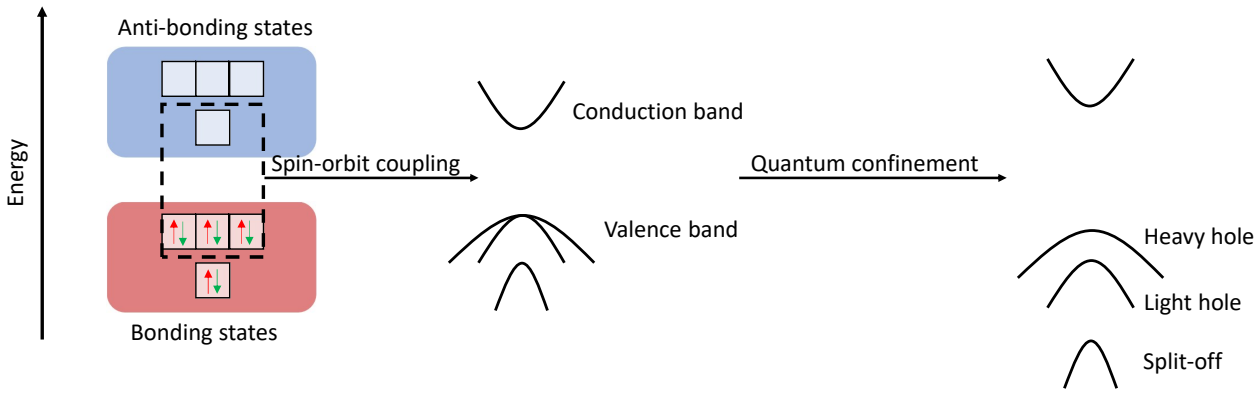

Figure 6: Energy bands in a GaAs quantum well. The spin-orbit coupling splits the p-type valence bands into split off band ($J = 1/2$) and heavy-and light-hole bands ($J = 3/2$). The heavy hole and the light hole bands are degenerate at $k = 0$. Since these two bands have different effective masses, they are split in energy when confined in a quantum well structure.

The bonding states are lower in energy and are therefore completely occupied while the anti-bonding states are empty. The highest energy of the bonding states to be occupied are p-type while the lowest energy of the anti-bonding states are s-type. Together they form the valence and conduction bands respectively. The excitons, which consist of holes from a p-type band and electrons from an s-type band classify into states with total angular momentum $J = \frac{3}{2} \otimes \frac{1}{2} = 2 \oplus 1$. Only the states with $J = 1$ can couple with light and thus these states can be optically controlled. The manifold of valence and conduction band states at the Brillouin zone centre for a GaAs quantum well is shown in Figure 6.

Excitons, which are viewed as excitations in the quantum well, live only for a finite amount of time. The electrons and holes in the exciton can recombine and emit a photon. This process determines the radiative lifetime of the exciton. It depends on the spatial overlap of the electron and hole wavefunctions. A larger overlap indicates greater probability of recombination and thus shorter lifetime. Since in this process a photon is emitted, the lifetime depends on the available photon states. The density of states for the photons can be modified in a cavity, where fewer states are available in a given energy range than in free vacuum. Thus the radiative lifetime of the excitons are increased inside an optical cavity.

Excitons can also be lost due to collisions with impurities, high energy electrons and other excitons by ionizing them. These processes lead to the non-radiative lifetime of the excitons. The linewidth of the excitons is also broadened due to the disorder in the quantum well and due to coupling with the lattice phonons.

1.3.4 Strong coupling

We have introduced the two components, photons and excitons, which can be coupled inside a cavity to generate polariton states. In an ideal scenario, whenever there is finite coupling between the photons and excitons, the "hybridized states" defined in the polariton basis are always present. This picture may not always hold when both photons and excitons have a finite lifetime. Let us illustrate this by writing a Hamiltonian for this system and allowing complex-valued energy for both photons and excitons,

$$\mathcal{H} = (E_c - i\Gamma_c)|C\rangle\langle C| + (E_X - i\Gamma_X)|X\rangle\langle X| + g_0|X\rangle\langle C| + g_0^*|C\rangle\langle X|. \tag{1.3}$$

States $|C\rangle$ and $|X\rangle$ represent cavity photons and excitons, respectively, with real energies E_c and E_X. The term g_0 is the strength of coupling between the photons and excitons, Γ_c and Γ_X are introduced to account for the finite lifetime of the photons and excitons. Figure 7 shows the real and imaginary parts of the eigenenergies of this system at zero in-plane momentum as Γ_c is varied from 0 to $5g_0$ while keeping Γ_X fixed.

From these figures we see that when the photon lifetime is infinite, which corresponds to $\Gamma_c = 0$, the energy gap between the two eigenenergies, "upper polaritons " and "lower polaritons", is maximal and is equal to $2g_0$. As the photon lifetime is decreased, the gap also decreases and eventually closes when $\Gamma_c = 2g_0$. The decrease in the energy splitting between the two states could be viewed as an effective decrease in the coupling between the two states, i.e., g_0 decreases with increasing loss. Therefore, the regime where the splitting between the states can be observed is known as the strong coupling regime. When the loss in the system dominates the coupling energy scale, the splitting vanishes and the system is said to be in the weak coupling regime. The condition for strong coupling could be expressed as $\Gamma_c, \Gamma_X \ll 2g_0$ and also $|\Gamma_c - \Gamma_X| \ll 2g_0$. Note that when the system is in strong coupling

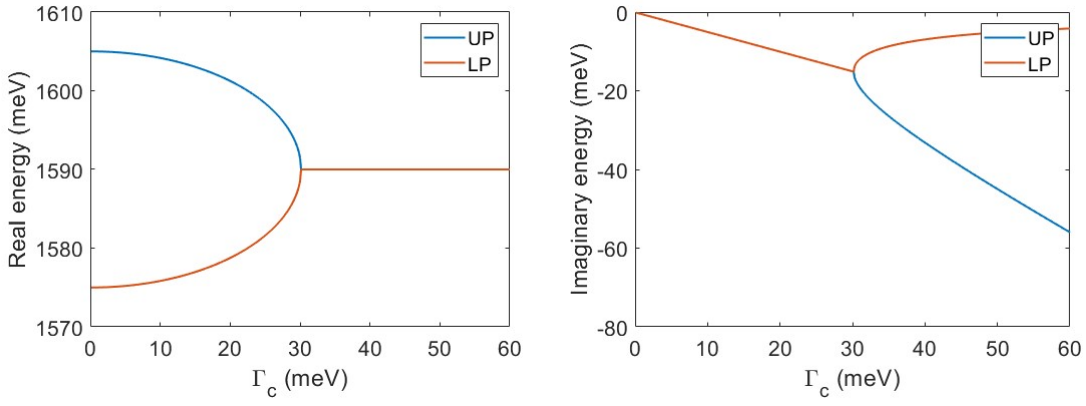

Figure 7: Plot of the real and imaginary parts of the upper and lower polariton energies as a function of photon lifetime $\Gamma_c = \hbar/\gamma$. In the example, Γ_X is chosen as $g_0/100$, with $g_0 = 15$ meV. In the microcavity used in the thesis, the excitons in the GaAs quantum wells show a linewidth of about 4 meV (due to inhomogeneous broadening) and the cavity linewidth is much narrower than the resolution of our spectrometer (< 50 μeV). The Rabi splitting in our samples are typically around 15 meV, which puts our system in the strong coupling regime.

regime, the imaginary parts of the energies of upper and lower polaritons are same.

When strong coupling is present, the system rapidly switches between photons and excitons in a reversible cycle and therefore it is appropriate to perform a basis change from excitons and photons to upper and lower polariton states, which are indeed the eigenstates of the system. The crossover from strong to weak coupling in this system leads to lasing at the energy of the cavity photons.

1.3.5 Exciton-photon coupling

The strength of coupling between excitons and photons is derived by considering the interaction between electrons (in conduction band $|c\rangle$, electron creation operator $b^\dagger_{c,k}$) and holes (in valence band $|v\rangle$, electron annihilation operator $b_{v,k}$) with the photons (creation

operator $a_k^\dagger$). The interaction Hamiltonian is given by [77],

$$\mathcal{H}_{int} = -\frac{e}{m}\sum_{k,k'}\sqrt{\frac{\hbar}{2\epsilon V\omega_k}}\Big[\langle c|\vec{p}|v\rangle\Big(a_k b^\dagger_{c,k'+k}b_{v,k'} + a_k^\dagger b^\dagger_{c,k'-k}b_{v,k'}\Big) + \langle c|\vec{p}|v\rangle^*\Big(a_k b^\dagger_{v,k'+k}b_{c,k'} + a_k^\dagger b^\dagger_{v,k'-k}b_{c,k'}\Big)\Big]. \tag{1.4}$$

Introducing the exciton creation operator in the 1s state, $X_k^\dagger = \sum_{k'}\varphi(k/2-k')b^\dagger_{c,k'-k}b_{v,-k'}$, where $\varphi(k)$ is the Fourier transform of the 1s exciton wavefunction with Bohr radius a_B

$$\varphi(k) = \frac{1}{\sqrt{V}}\frac{8\sqrt{\pi a_B^3}}{(1+a_B^2k^2)^2}, \tag{1.5}$$

we calculate the matrix element $\langle X|\mathcal{H}_{int}|C\rangle$ which gives the strength of the exciton-photon coupling g_k,

$$\langle X|\mathcal{H}_{int}|C\rangle = -\frac{e}{m}\sum_{k'}\varphi(k/2-k')\sqrt{\frac{\hbar}{2\epsilon V\omega_k}}\langle c|\vec{p}|v\rangle. \tag{1.6}$$

Summation over k' gives a factor of $\sqrt{V/\pi a_B^3}$. Putting this back in the above expression we obtain,

$$\langle X|\mathcal{H}_{int}|C\rangle = g_k = -\sqrt{\frac{\hbar e^2}{2m^2\epsilon\omega_k\pi a_B^3}}\langle c|\vec{p}|v\rangle. \tag{1.7}$$

Although this calculation is done in three dimensions, it shows an important consequence of the formation of excitons which enhances the coupling strength by a factor of $V/\pi a_B^3$. In the two-dimensional limit, the coupling strength will be further enhanced as the Bohr radius decreases due to an increase in the binding energy of the excitons.

1.3.6 Polariton dispersion

Figure 8 shows the upper (UP) and lower (LP) polariton states in a strongly coupled microcavity. The eigenstates of the microcavity are split due to the exciton-photon coupling and their energies are given by,

$$E_{UP,LP} = \frac{E_{cav}+E_X}{2} \pm \frac{\sqrt{(E_{cav}-E_X)^2+4|g_k|^2}}{2}. \tag{1.8}$$

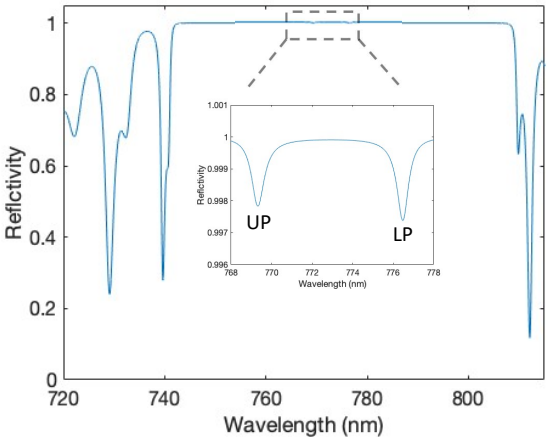

Figure 8: Typical reflectivity spectra of a microcavity with quantum wells obtained under a broadband (white light) low power light source. This is a transfer matrix simulation of the reflectivity of the microcavity at normal incidence. Due to the strong coupling between the excitons in the quantum wells and the cavity photons, two new dips in the spectra are seen. These correspond to the upper and lower polaritons. The splitting between these dips is given by the exciton-photon coupling strength. [Figure is produced using the code written by Mark Steger and Jonnathan Beaumariage.]

We are primarily interested in a narrow range of in-plane momentum for which we can ignore the momentum dependence of the exciton-photon coupling. Further, we can approximate the dispersion of the cavity photons with a parabolic dispersion near $k_{||} = 0$ with an effective mass $m_{cav} = (n_{cav}/c)^2 E_{cav}(k_{||} = 0)$. Since the cavity photons are much lighter than the excitons ($m_{cav} \ll m_p$), the dispersion of the excitons is flat for small $k_{||}$. With these approximations the lower polariton dispersion is given by,

$$E_{LP}(k_{||}) = \frac{E_{cav}(0) + \hbar^2 k_{||}^2/2m_{cav} + E_X(0)}{2} - \frac{\sqrt{(E_{cav}(0) - E_X(0) + \hbar^2 k_{||}^2/2m_{cav})^2 + 4g_0^2}}{2}. \tag{1.9}$$

We define the energy mismatch between the excitons and the photons at zero in-plane momentum as detuning, which is given by $\delta = E_{cav}(0) - E_X(0)$. The LP and UP eigenstates are given by [43],

$$\begin{aligned} |LP\rangle &= \alpha_{k_{||}}|C\rangle + \beta_{k_{||}}|X\rangle, \\ |LP\rangle &= \alpha_{k_{||}}|C\rangle - \beta_{k_{||}}|X\rangle. \end{aligned} \tag{1.10}$$

$\alpha_{k_{||}}$ and $\beta_{k_{||}}$ are complex valued numbers satisfying,

$$\begin{aligned} |\alpha_{k_{||}}|^2 &= \frac{1}{2}\left(1 - \frac{\delta + \hbar^2 k_{||}^2/2m_{cav}}{\sqrt{(\delta + \hbar^2 k_{||}^2/2m_{cav})^2 + 4g_0^2}}\right), \\ |\beta_{k_{||}}|^2 &= \frac{1}{2}\left(1 + \frac{\delta + \hbar^2 k_{||}^2/2m_{cav}}{\sqrt{(\delta + \hbar^2 k_{||}^2/2m_{cav})^2 + 4g_0^2}}\right). \end{aligned} \tag{1.11}$$

$|\alpha_{k_{||}}|^2$ and $|\beta_{k_{||}}|^2$ represent the photonic and excitonic fractions of the polariton state. A larger photonic fraction implies that the polariton is more "photon-like". Figure 9 shows a comparison between the dispersion of lower polaritons as the photonic fraction varies in the microcavity sample. From this figure we see that the curvature of the dispersion becomes flatter as the photonic fraction is decreased. Since the curvature determines the effective polariton mass, the mass becomes heavier with decreasing photonic fraction. For comparison, I plot the UP and LP dispersion with corresponding photon fraction at positive, negative and resonant detunings in Figure 10.

The reason why there is a spatial variation of detuning in the microcavity sample can be traced back to the inhomogenenous growth rate of the microcavity during the molecular beam epitaxy (MBE) process. A typical cross-section of the microcavity is plotted in Figure 11 where a thickness variation of the wafer from the centre to the circumference is shown. The variation in thickness leads to a smaller cavity photon energy near the center of the wafer, where it is thicker than the edge. The spatial dependence of the exciton energy is much weaker; as a result the polaritons have a smaller photonic fraction near the edge of the wafer because the photon energy is higher than the exciton energy.

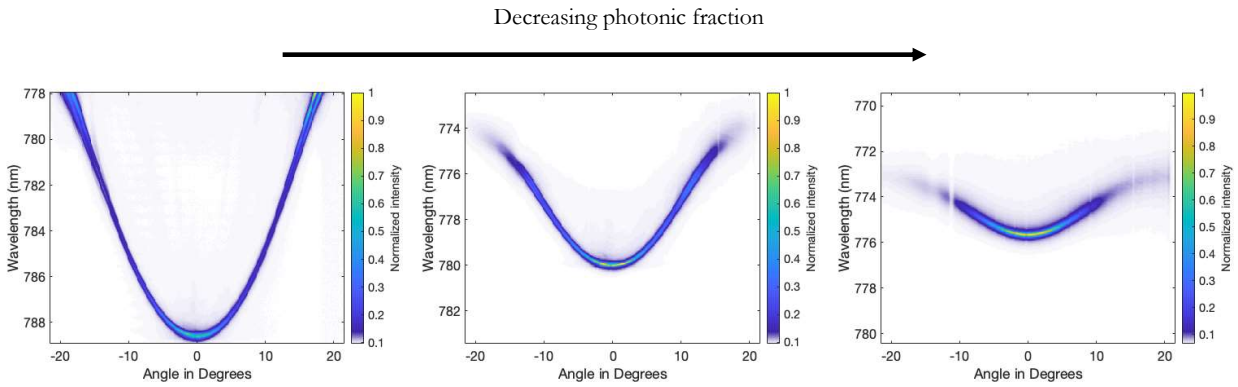

Figure 9: Energy and momentum resolved photoluminescence images from different locations on the microcavity sample. It shows how the lower polariton dispersion changes when the photonic fraction changes from one location in the sample to the other. This data is taken from a $3\lambda/2$ GaAs microcavity at 5 K.

1.4 Forces on polaritons

Polaritons, being neutral particles, do not respond to the electric and magnetic fields as electrons respond in semiconductors. Therefore applying a force to manipulate the polaritons is not so straightforward. We know that a particle in an inhomogeneous potential (U) experiences a force ($\vec{F}$) given by the negative gradient of the potential, i.e. $\vec{F} = -\nabla U$. Therefore any spatial variation of the exciton energy or the cavity photon energy will lead to a force on the polaritons. The tilt in the microcavity wafer applies a net force on the polaritons, pushing them radially inwards towards the center of the wafer (since the photon energy decreases towards the center). The exciton energy can be spatially varied by applying strain on the quantum wells. The strain redshifts the exciton energy; this can be used to create a local trap for the polaritons [79]. Further, the cavity can be etched to create a strain mismatch near the free boundary, which again causes redshift of the exciton energy near the boundary. Figure 12 shows the energy profile in an etched square microcavity where an energy minima is found near the edge of the square pillar. This effect of edge trapping is utilized in the present work to create narrow channels for polaritons by bringing

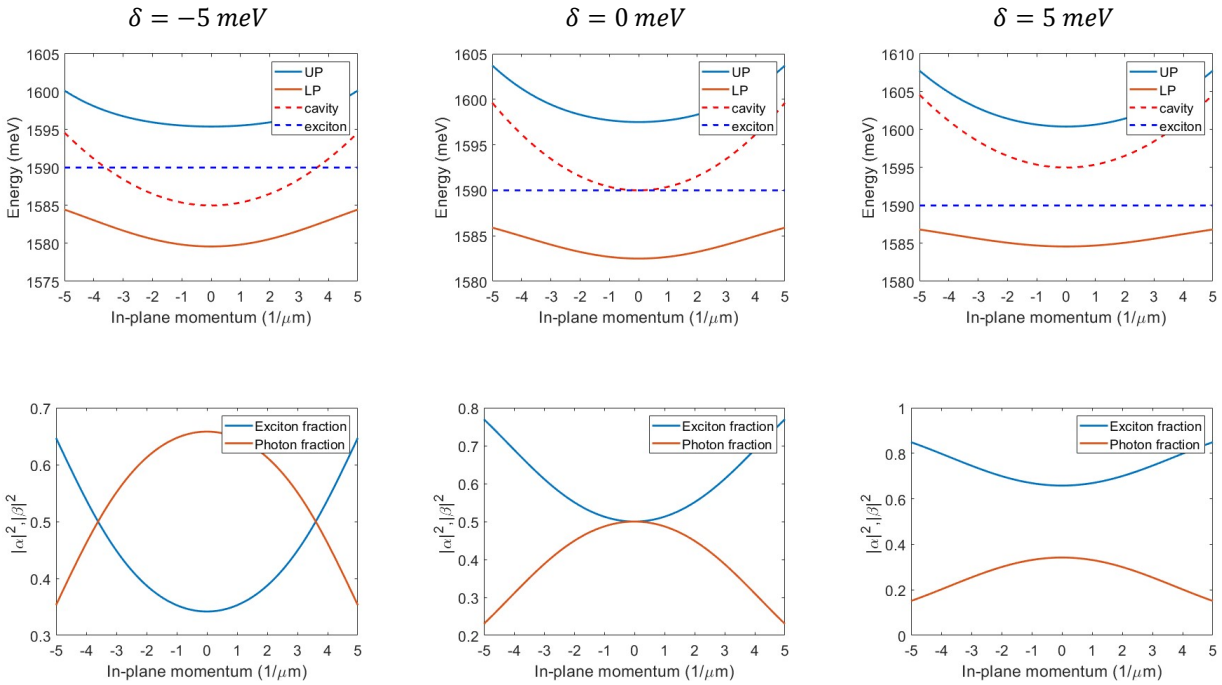

Figure 10: The top row shows the dispersion of the upper and lower polaritons at three different detunings. The bottom row shows the corresponding photonic fraction and the excitonic fraction at those detunings. Note that the photonic fraction varies with the in-plane momentum. This produces a momentum dependent lifetime for the polaritons in the microcavity.

the two opposite edges closer, about twice the healing length of the strain from each edge, thus producing a flat bottom potential for the polaritons in the channel. The minimum of the strain potential is about 7 μm [79] from an edge. A local blueshift in the energy of the polaritons due to interactions with the exciton reservoir pushes the polaritons away from this region. In this work we will use these concepts to engineer a trapping potential for the polaritons.

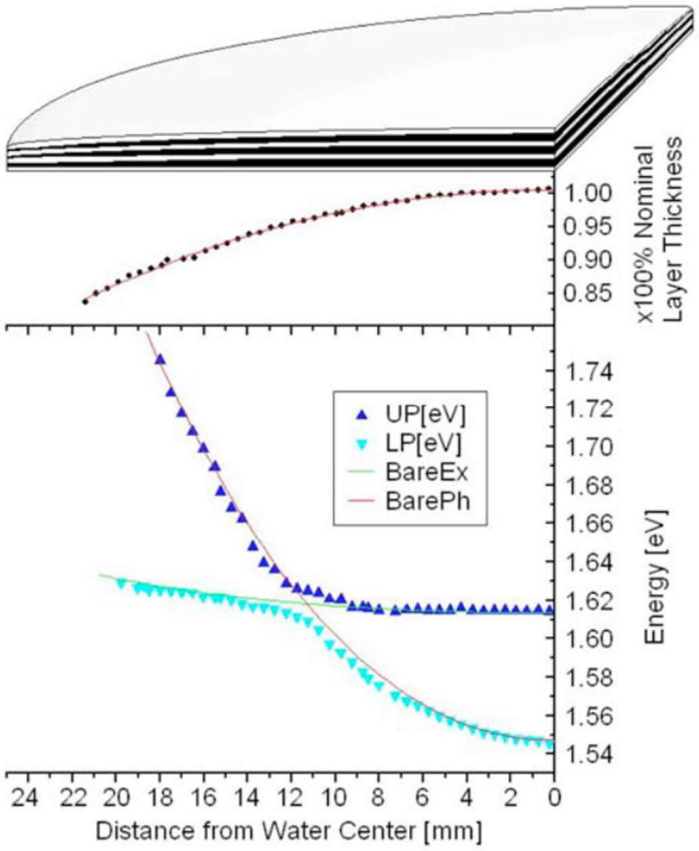

Figure 11: Shows a cut through the microcavity wafer. Due to the growth rate anisotropy the wafer is about 15% thinner at the edges than in the center. This gives rise to large variation in the cavity photon energy and relatively smaller variation in the exciton energy in the wafer. Reprinted with permission from Ref. [78].

1.5 Polariton-polariton interaction

Photons by themselves are only very weakly interacting due to $\chi^{(2)}$ nonlinearity; on the other hand excitons can interact. The interaction between excitons emerges from the Coulomb interactions between the electrons and holes which comprise them. For a dilute gas of excitons ($n_{ex}a_B^2 \ll 1$, a_B is the Bohr radius of the exciton and n_{ex} is the density

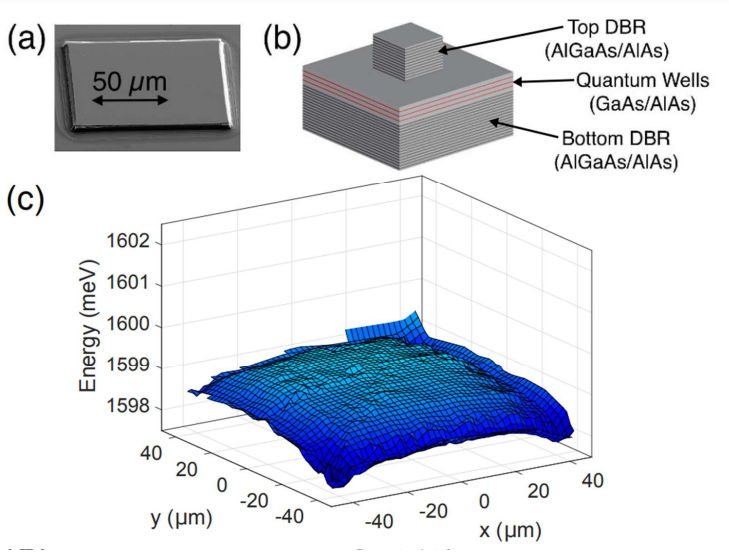

Figure 12: (a) SEM image of an etched pillar. (b) The etched pillar structure, with the top DBR removed except in a square area. The bottom DBR and QW layers are un-etched, leaving an open cavity except at the location of the pillar. (c) Linearly interpolated data showing the resulting low density potential landscape. Since the pillar was a square with $\approx 100\ \mu m$ long sides, these data come from entirely within the pillar and out to about 5 μm from the edges. A mostly flat region in the middle gives way to low energy regions at the edges, with minima at the corners. The overall tilt of the landscape is due to the sample gradient. Figure reprinted with permission from Ref. [79].

of the excitons in the quantum well) the interactions are mostly dominated by elastic two-body scattering. The scattering amplitude between an initial state $|i\rangle$ and a final state $|f\rangle$ due to the hamiltonian H_{int} is given by $\langle f|H_{int}|i\rangle$. $|i\rangle$ and $|f\rangle$ are two particle states with momentum $|k_1; k_2\rangle$ and $|k_1 - q; k_2 + q\rangle$ respectively. Energy conservation implies,

$$\begin{aligned} &\frac{\hbar^2 \mathbf{k_1}^2}{2\mu} + \frac{\hbar^2 \mathbf{k_2}^2}{2\mu} = \frac{\hbar^2(\mathbf{k_1} - \mathbf{q})^2}{2\mu} + \frac{\hbar^2(\mathbf{k_2} + \mathbf{q})^2}{2\mu}, \\ &\Rightarrow \mathbf{q} \cdot \big(\mathbf{q} + 2(\mathbf{k}_2 - \mathbf{k}_1)\big) = 0. \end{aligned} \tag{1.12}$$

H_{int} is the pairwise inter-exciton Coulomb interaction given by

$$H_{int} = \frac{1}{2} \int d^2 r_1 d^2 r_2 V_{int}(r_1, r_2) \Psi^\dagger(\mathbf{r}_1) \Psi^\dagger(\mathbf{r}_2) \Psi(\mathbf{r}_2) \Psi(\mathbf{r}_1) \tag{1.13}$$

with $V_{int}(\mathbf{r}_1^e, \mathbf{r}_1^h, \mathbf{r}_2^e, \mathbf{r}_2^h)$ given by,

$$V_{int}(\mathbf{r}_1^e, \mathbf{r}_1^h, \mathbf{r}_2^e, \mathbf{r}_2^h) = \frac{e^2}{4\pi\epsilon}\left(\frac{1}{|\mathbf{r}_1^e - \mathbf{r}_2^e|} + \frac{1}{|\mathbf{r}_1^h - \mathbf{r}_2^h|} - \frac{1}{|\mathbf{r}_1^e - \mathbf{r}_2^h|} - \frac{1}{|\mathbf{r}_1^h - \mathbf{r}_2^e|}\right). \tag{1.14}$$

Superscripts e and h represent electrons and holes, respectively, and the subscripts 1 and 2 label the two excitons. In the limit of cold collisions ($k_1, k_2, q \ll a_B^{-1}$) for excitons in $1s$ states, and equally averaged over all spin states H_{int} reduces to [58, 80],

$$\begin{aligned} H_{int} &= \frac{1}{2}\int d^2r_1 d^2r_2 V_0 \delta(\mathbf{r}_1 - \mathbf{r}_2)\Psi^\dagger(\mathbf{r}_1)\Psi^\dagger(\mathbf{r}_2)\Psi(\mathbf{r}_2)\Psi(\mathbf{r}_1) \\ &= V_0 \int d^2r \Psi^\dagger(\mathbf{r})\Psi^\dagger(\mathbf{r})\Psi(\mathbf{r})\Psi(\mathbf{r}). \end{aligned} \tag{1.15}$$

Therefore the effective interactions between the excitons with same spin is repulsive and is short-ranged. For GaAs quantum wells V_0 was approximated as $6E_B a_B^2$, where E_B is the binding energy of the exciton. The above result is obtained at the Hartree-Fock level and is entirely due to the exchange terms [58, 80]. Recent experiments [66] have shown that this value may be higher than the theoretical estimate and in general not very well known from the experiments. Another point to be highlighted in the above calculation is the use of 3D Coulomb interaction ($\approx 1/r$) rather than the 2D Coulomb interaction ($\approx ln(r/r_0)$). In Ref. [58] a 2D Fourier transform of the 3D Coulomb interaction was used to calculate the matrix element of the elastic exciton-exciton scattering using $V_k \approx 1/k$. In Ref. [81] it was pointed that the excitons in the quantum wells may not be completely confined and have some 3D character for which $V_k \approx 1/k^2$ was used to calculate the exciton-exciton interaction strength. In this calculation the interaction strength was found to be higher than that reported earlier in Ref. [58].

Polaritons inherit the repulsive interactions from the excitons, and there role is very important for the formation of stable polariton condensates. The repulsive interactions energetically favour the condensate against fragmentation [40]. Polariton-polariton interactions also play a major role in thermalization of the polariton gas, which eventually led to the realization of a fully thermalized polariton gas following Bose-Einstein distribution [47]. In recent years the question of interactions have come up in two-dimensional materials (transition metal dichalcogenides such as WS_2, WSe_2, MoS_2, $MoSe_2$, $MoTe_2$ etc.) where

Rydberg excitons have been reported [82, 83, 84, 85]. In GaAs quantum well microcavities the repulsive interactions have been used to engineer trapping potentials for polaritons by non-resonantly pumping the microcavities [86, 87]. The interaction between the exciton cloud which is formed due to the non-resonant pump and the polaritons reshapes the potential felt by the polaritons. In several studies an optical gate was realized in a microcavity [88, 89, 90, 91] where switching on a non-resonant laser produced an exciton barrier which stopped the flow of polaritons across the laser barrier.

1.6 Bose-Einstein condensation of polaritons

There are two types of particles in the Universe: Bosons and fermions. When two particles are exchanged, the overall wavefunction $\Psi(\mathbf{r}_1, \mathbf{r}_2)$ picks up a phase. If the particles are Bosons, 2π phase is picked such that $\Psi(\mathbf{r}_1, \mathbf{r}_2) = \Psi(\mathbf{r}_2, \mathbf{r}_1)$. On the other hand, fermions pick up a π phase such that $\Psi(\mathbf{r}_1, \mathbf{r}_2) = -\Psi(\mathbf{r}_2, \mathbf{r}_1)$. This property has important consequences when considering a large collection of particles and give rise to very different behaviour. We are interested in the state of matter which is formed when a collection of Bosons is cooled to a very low temperature. In thermodynamic equilibrium, Bosons occupy the available energy states in the system according to Bose-Einstein distribution:

$$n_{BE}(E) = \frac{1}{e^{(E-\mu)/k_B T} - 1} \tag{1.16}$$

where μ is the chemical potential, k_B is the Boltzmann constant and T is the temperature of the system. One consequence of this distribution is that when the chemical potential equals the lowest energy of the system $\mu = E_0$, then the occupation of this state blows up $n_{BE}(E_0) \to \infty$. In experiments we always have a finite number of particles so the ground state occupation never blows up, but instead it is peaked. When the occupation of the ground state becomes much larger than 1, a new state of matter is formed known as Bose-Einstein condensate. Bose-Einstein condensation can occur in a system when number of available excited states are finite. When the number of particles is greater than the number of available excited states, the extra particles are forced to occupy the ground state. So there

is a critical number of particles that are required to form a Bose-Einstein condensate (BEC). The number of particles occupying all the excited state will be smaller at low temperatures, thus the system can undergo Bose-Einstein condensation with a smaller critical number of particles [92].

In two dimensions, due to the constant density of states, the occupation of the excited states cannot be saturated, thus preventing the formation of a BEC. The scenario is changed when a trapping potential is added which modifies the density of states in the trap, saturating the number of particles occupying all the excited states. Therefore polaritons form a BEC whenever they are trapped in a potential. Figure 13 shows the BEC phase transition of polaritons as the density of polaritons is increased in a harmonic trap.

The commutator of the ground state modes a_0, $a_0^\dagger$ asymptotically goes to zero, which makes the ground state mode special than the other modes occupying the excited states; a_0 becomes a complex valued number given by $\sqrt{N}e^{-i\theta}$. All the particles in a BEC act in unison and behave as a single giant wave which can be described classically. The phase of the BEC is not known beforehand and is chosen spontaneously during the phase transition. This freedom of choosing the phase is due to $U(1)$ symmetry (particle number conservation) of the Hamiltonian and is preserved when particles interact by short range collisions.

Polaritons can be regarded as Bosons as long as the commutation relation for the exciton operators hold. As before, exciton operator ($X_{\nu,k}$) can be expressed as a product of electron ($\hat{e}_k$) and hole ($\hat{h}_k$) operators; exciton annihilation operator $X_{\nu,k} = \sum_p \varphi_\nu(p)\hat{h}_{k/2-p}\hat{e}_{k/2+p}$, where $\varphi_\nu(p)$ is the envelope function of the exciton. The commutator $[X_{\nu,k}, X_{\nu,k}^\dagger]$ calculated up to second order in the Fermionic operators give,

$$[X_{\nu,k}, X_{\nu,k}^\dagger] \simeq 1 - \sum_p |\varphi_\nu(p)|^2 \left(\hat{n}_e\Big(\frac{k}{2}+p\Big) - \hat{n}_h\Big(\frac{k}{2}-p\Big) \right). \tag{1.17}$$

As long as the carrier density is small, the second term can be neglected and the excitons can be treated as Bosons. Polariton condensates are described by an order parameter ($\Psi = \langle BEC|a_0|BEC\rangle$) which is non-zero in the condensed phase and zero in the normal phase. Since the condensate is formed in a trapping potential the dynamics of the condensate can

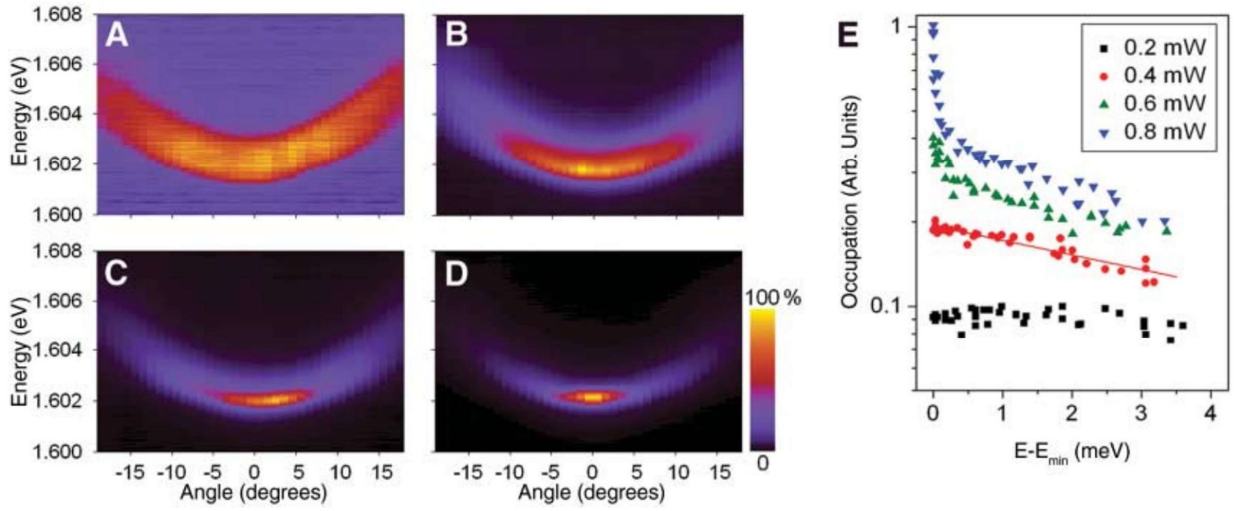

Figure 13: (A-D) Angle and energy resolved PL with increasing pump power. The polaritons were trapped in a harmonic potential created by applying strain to the microcavity wafer. As the polariton density increases in the trap, the spectral linewidth of the PL emission narrows as well as the emission intensity increases around $k_{||} = 0$. (E) Higher pump power shows a peak in the occupation number at the ground state energy. Figure reprinted with permission from Ref. [18].

be described at the mean-field level by Gross-Pitaevskii equation:

$$i\hbar\frac{\partial\Psi(\mathbf{x},t)}{\partial t} = -\frac{\hbar^2}{2m}\nabla^2\Psi(\mathbf{x},t) + V(x)\Psi(\mathbf{x},t) + g|\Psi(\mathbf{x},t)|^2\Psi(\mathbf{x},t), \tag{1.18}$$

where g is the repulsive interaction strength and $V(\mathbf{x})$ is the trapping potential. For polaritons the trapping potential may arise due to both the photonic and excitonic contributions.

To summarize, the polaritons embody the best of features from both the photons and the excitons. From photons they inherit the extremely light mass, approximately 10,000 times lighter than the mass of an electron in vacuum, and size of the order of few hundreds of nanometers. Having a size much larger than the exciton, which is about the size of Bohr radius (a_B, $\approx$ 10 nm in GaAs quantum well), the polaritons can average over the disorder at the scale of tens of nanometers in the quantum wells, which otherwise for excitons would

be trapped in local disorder potential. From excitons they inherit interactions which allow them to rapidly exchange energy and thermalize into a BEC, once the necessary conditions are met. By producing an out-of-equilibrium condensate in a trap, in this thesis we study how the condensate evolves in time, and whether it can cool to the bottom of the trap. This has implications for performing neuromorphic computing which depends on the ability of the polariton condensate to find global minimum in a complex potential landscape.

2.0 Experimental methods

This chapter summarizes the experimental techniques used to study the phenomenon of Bose-Einstein condensation of polaritons. Polaritons as mentioned previously can be considered as renormalized photons trapped inside a microcavity. The photons leaking from this cavity carry spectral information about the polaritons which can be used to study them. We employ optical methods to detect and image various information associated with these photons, namely, their frequency, angular distribution, temporal and spatial location of emission, polarization and phase coherence. Thus these methods not only allow us to make qualitative observations but also quantitative measurements of various features of polariton condensates. I will describe a flexible optical setup which I built to perform the experiments I present in this thesis and discuss the optical lithography technique which was used to produce the ring shaped microcavities used in the study.

2.1 Skeleton of an experiment

We can think of our polariton microcavity as a "light in, light out" system. In a typical experiment we pump the microcavity with a coherent light and make observations of the light coming out of the sample. We can choose either a continuous wave (CW) light source or a pulsed light source depending on the type of experiment we are interested in. The CW light source is used to produce a nonequilibrium steady state which is created by compensating the loss of the polaritons from the microcavity by the leakage through the cavity mirrors. The pulsed light source on the other hand creates an instantaneous population of polaritons which eventually decays away. By monitoring continuously the light leaking from the microcavity we can watch the dynamics of this decaying population of polaritons. It is to be noted that for our experiments both the CW and the pulsed laser have a linewidth smaller than 0.1 nm and are considered as monochromatic. We can not only make a spatially localized pump spot but also have a choice of shaping the phase of the pump beam to create a spatially extended

pump profile which can be used to generate complex optical traps and lattices [93, 94]. We can also control the frequency, angle of incidence and the polarization of the pump light to make polaritons either resonantly (energy and in plane momentum matched with the pump) or non resonantly (energy of the pump is higher than the energy of the polaritons in the microcavity). Another way of creating polaritons is by electrical injection, [95, 96, 97] not discussed in this thesis.

The light coming out of the microcavity is collected by a lens system and subsequently imaged onto a charged coupled device (CCD). It must be noted that the power of the light we collect from the polaritons range from a few nW to μW for which nitrogen cooled, intensified CCDs are sufficiently capable for detection. If the power of the signal is low, in the range of a few pW, then we must consider single photon avalanche photo-diodes (SPAD) or low noise photo-detectors to detect the low signal light. The two-dimensional array of the pixels of the CCD offers spatial resolution of the magnified image of the focal plane of the collection optics from which the light is being emitted. This is highly desirable since we are often interested in knowing the spatial distribution of the light emitted from the microcavity. We can also learn about the spectral distribution of the emitted signal by taking a vertical slice of this image and passing it through a monochromator, which creates a two-dimensional image on the plane of the CCD, where the vertical direction of the image is a slice of the real space image and the horizontal direction corresponds to the wavelength. Thus we have traded the spatial resolution along the horizontal direction to gain spectral resolution for a given vertical slice of the image. We can perform a full tomographic scan of the image along the horizontal direction to construct a three-dimensional image to learn the full spectral composition of the image. We can apply the same principle to a two-dimensional Fourier transform of the real space image and produce a three-dimensional image with spectral and angular resolution. The Fourier transform of the image is produced using a lens. See Ref. [98] for more discussion of Fourier imaging.

A streak camera is used to take a horizontal slice of the image and resolve it in time. The net result is again a two-dimensional image with the vertical direction now representing time axis. Light arriving relatively late appears in the bottom region of such an image. Again performing a tomographic scan across the vertical direction of the image we can learn

about the spatio-temporal features in the signal. A four-dimensional image can also be constructed by adding the spectral resolution to the spatio-temporal signal. If we perform a Fourier transform on the image then we obtain momentum- and temporal- resolved images. In addition we can perform polarimetry on the signal and learn about the spatio-temporal polarization resolution of the signal. By adding holographic interferometry to this technique we can infer the phase of the signal. In the following sections I have outlined some of the commonly used optical image/signal processing tools in our toolbox which are used to retrieve information about the polaritons in the microcavity. Our main focus in this thesis will be on studying dynamics, so temporal measurements will be the workhorse of most of the experiments detailed in this thesis.

2.2 Optical pumping

The efficiency of the photons injected into the microcavity depends on their energy ($\hbar\omega$) and the wavevector ($\vec{k}_{||}$) in the plane of the quantum wells. This is because the mirror of the microcavity is highly reflective (more than 99.5%) only over certain bands of wavelengths and the reflectivity drops below 50% at certain wavelengths which can be used to couple light into the microcavity. The highly reflective band is known as the stop band and is a feature of distributed Bragg reflectors (DBR). It arises due to the interference between light reflected from different interfaces of the DBR. A typical reflectivity spectrum of a DBR structure is shown in Fig.14. Whenever the pump wavelength is tuned to match one of the Bragg dips of the microcavity lying at higher energy (shorter wavelength) with respect to the stop band, the injected photons have higher energy than the resonant modes of the cavity. Such a pumping scheme is called non-resonant pumping. On the other hand when the wavelength of the pump laser is tuned to match with one of the resonant modes of the cavity it is called resonant pumping. Below we discuss how the two schemes differ in the process by which the polaritons are produced inside the microcavity.

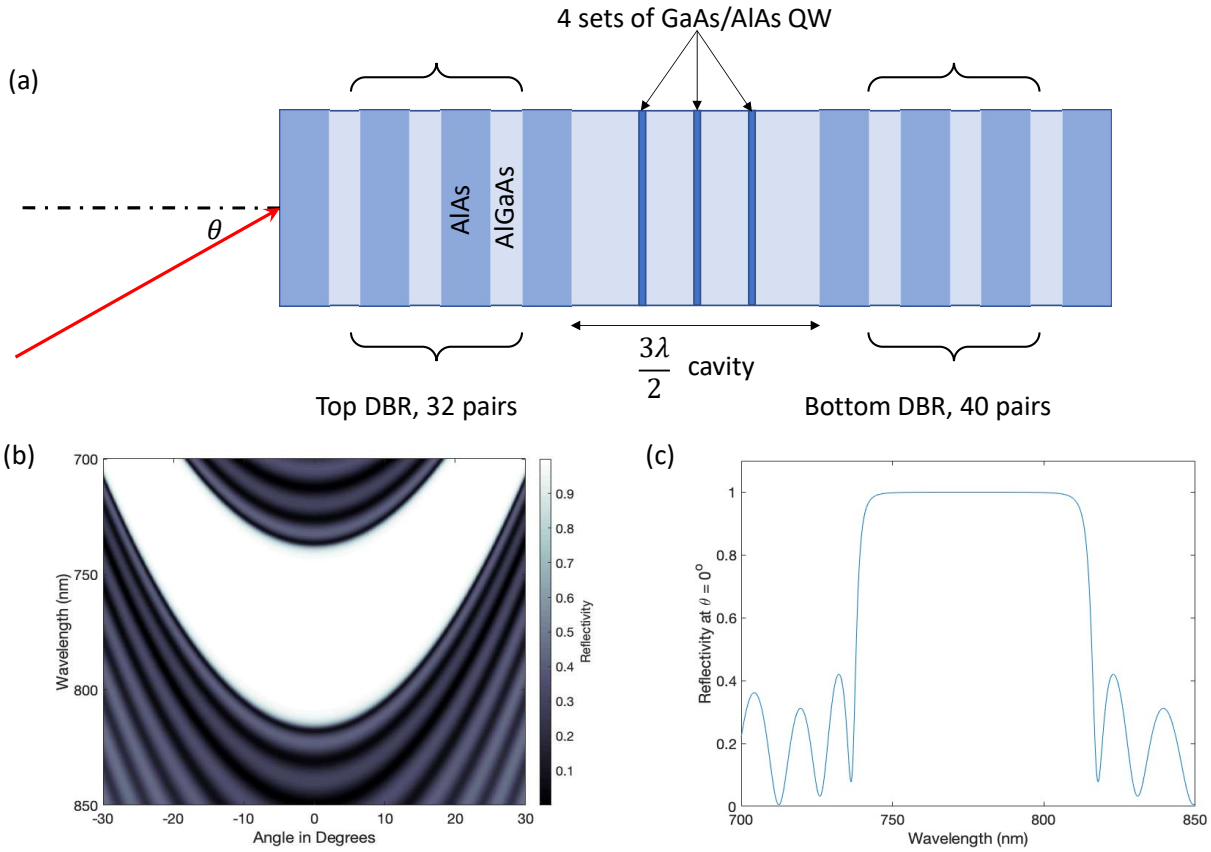

Figure 14: (a) Shows a simplified sketch of the microcavity sample comprising of top and bottom DBR mirrors and embedded quantum wells inside the cavity. (b) A typical reflectivity spectra as a function of the angle of incidence θ labeled in the sketch and calculated for a top DBR using the transfer matrix method. [99] (c) A cross section of the reflectivity spectrum for normal incidence ($\theta = 0$) showing the stop band and the Bragg modes.

2.2.1 Non-resonant pump

When the energy of the incident photons injected into the microcavity is higher than the energy of the resonant modes of the cavity (upper and lower polaritons), the pump is said to be non-resonant. Since the energy of the non-resonant pump is higher than the bandgap of the quantum well semiconductor, a hot distribution of free electrons and holes is generated. Due to the free carrier scattering and coupling with phonons this hot distribution

rapidly cools and produces a distribution of excitons and excitonic polaritons at cold lattice temperatures. Further cooling occurs due to the polariton-polariton interactions, and the lower polariton branch near $k_{||} \sim 0$ is occupied. This occupation can be further stimulated due to the bosonic nature of the polaritons, and a macroscopic occupation of the $k_{||} = 0$ state is possible if the pump has enough photon flux. During the entire thermalization process, the phase information about the pump is completely lost. It is believed that the polarization information may not be completely lost due to the much slower relaxation of the spin degree of freedom of the polaritons. Figure 15 pictorially summarizes the relaxation process which produces polaritons with non-resonant pump.

If the lifetime of the polaritons is longer than the time of collisions, it is expected that the gas of polaritons will reach thermal equilibrium. In recent experiments, the polaritons have been shown in thermal equilibrium in high Q microcavities [47]. Therefore the polaritons created non-resonantly in a high Q microcavity are useful for studying thermalization and dynamics in a potential trap. Associated with the polaritons created by non-resonant pump is a reservoir of heavy mass excitonic polaritons and excitons. Due to the polariton-exciton interactions, this reservoir acts as an additional potential for the polaritons. Since the lifetime of the particles forming the reservoir is much longer than the lifetime of the polaritons, the reservoir can also act as a source of polaritons, which can be depleted by stimulated scattering into the polariton states. A non-resonant pump was used to show spontaneous coherence in the polariton microcavities [18, 17, 86].

The dynamics of a polariton condensate under non-resonant pumping by the modified Gross-Pitaevskii equation,

$$i\hbar\frac{\partial\psi}{\partial t} = \mathcal{H}\psi + \frac{i\hbar}{2}\Big(Rn_r - \gamma\Big)\psi, \tag{2.1}$$

where ψ is the condensate order parameter and n_r is the density of the reservoir. $\mathcal{H}$ is the mean field Hamiltonian of the system given by the sum of kinetic, potential and interaction terms. The explicit imaginary term in the equations of motion of the order parameter accounts for the gain and loss of the density of the condensate. Parameters γ and R account for the process of polariton decay due to the finite lifetime of the cavity and the process of stimulated scattering of particles from the reservoir to the condensate respectively. Assuming

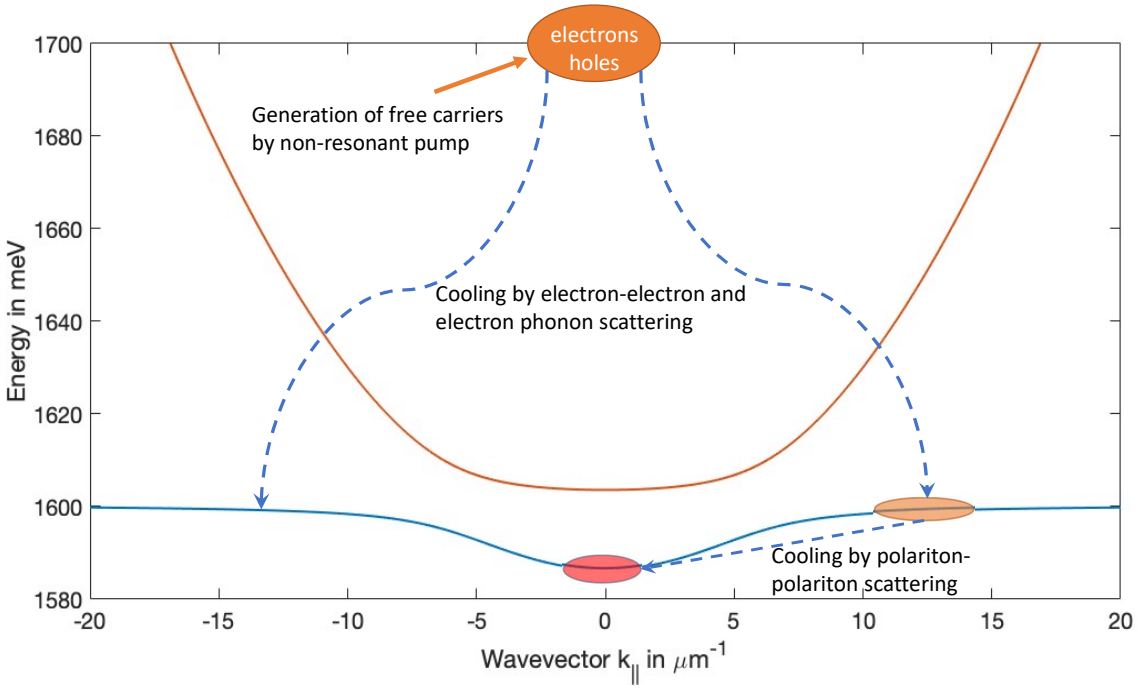

Figure 15: Describes the excitation mechanism of polaritons due to a non-resonant pump. Energy relaxation pathways are necessary for cooling down the hot electron-hole free carriers created by the pump laser. We only highlight the most important channels for energy relaxation, namely free carrier relaxation and charge-phonon scattering to occupy high momentum polariton states. In the next stage, polariton-polariton collisions and multiple polariton-phonon emissions further cool down the hot polariton gas.

that the pump replenishes the reservoir, the dynamics of the reservoir is modelled classically by a rate equation

$$\frac{\partial n_r}{\partial t} = D \bigtriangledown^2 n_r - R|\psi|^2 n_r - \gamma_r n_r + P \tag{2.2}$$

where D is the diffusion coefficient of the reservoir and it is often neglected because the mass of the reservoir particles is three orders of magnitude heavier than the mass of the polaritons. Therefore the timescale of the dynamics is much slower than the timescale of reservoir dynamics of the polaritons. Parameter γ_r accounts for the loss of reservoir particles

due to both radiative and non-radiative processes. P is the spatio-temporal pump feeding the reservoir. Some theoretical models make an explicit distinction between the reservoir states into active, inactive and dark states [100]. The active reservoir is the one which couples directly to the condensate as shown in the above equation. The inactive reservoir is the one which does not have the correct energy and momentum to couple with the condensate and are comprised of hot excitons which must undergo further cooling to become part of active reservoir. The dark reservoir comprises of optically inactive exciton states which can't couple to light because they have total angular momentum $J = 2$.

The reservoir can be used to produce a complex-valued potential for the polaritons. Under a CW pump, a steady state can be reached where the stationary reservoir density is given by,

$$n_r = \frac{P}{\gamma_r + R|\psi|^2}. \tag{2.3}$$

Substituting for the stationary reservoir density in Equation 2.1, we find

$$i\hbar\frac{\partial\psi}{\partial t} = \mathcal{H}\psi + \frac{i\hbar}{2}\Big(\frac{RP}{\gamma_r + R|\psi|^2} - \gamma\Big)\psi. \tag{2.4}$$

Also, due to the interactions between the polaritons and the reservoir, the polaritons experience a blueshift in energy proportional to the density of the reservoir ($= 2gn_r$). We see that the non-resonant pump creates a complex potential which depends on both the pump shape and the intensity. By reshaping the pump interesting gain and loss scenarios can be created to study non-Hermitian physics.

2.2.2 Resonant pump

When the energy and the incident in-plane wavevector ($\vec{k}_{||}$) of the pump matches with a certain region of the dispersion of one of the eigenmodes (upper and lower polariton branches) of the cavity then the pump is said to be resonant with that eigenmode. In most experiments resonant pumping implies pumping the lower polariton branch. The energy, propagation wavevector, pseudospin and phase of the coherent polaritons generated is determined by the wavelength, incident in-plane wavevector ($\vec{k}_{||}$), polarization and the phase of the pump laser.

The polaritons created in this way are similar to an oscillator driven, by an external force. The resonant pump is therefore useful to generate a coherently driven out-of-equilibrium polariton fluid.

Such coherently driven polaritons usually show no sign of thermalization since all the polaritons flow in the same direction with the same velocity and the probability of them cooling by collisions is low. It was shown that polaritons generated resonantly showed signatures of superflow while flowing past a stationary defect [101, 102]. However, the interpretation of these experiments was later challenged, and it was argued that for coherently driven polaritons the superfluid response, which is the difference between responses to longitudinal and transverse forces, is zero [103]. Thus the signature of dissipationless flow is a sign of a new rigid state and not a superfluid. In further applications of resonant pumping, the polarization of the pump laser (right or left circularly polarization) can be used to create polaritons with a particular pseudo-spin [104, 105]. Solitons can be generated by pumping the negative curvature part of the polariton dispersion [106, 107]. Since the pump beam directly creates the polaritons it is expected that the reservoir comprising of excitons or mostly excitonic polaritons are absent. In a recent experiment this notion was challenged by directly measuring the dispersion of the collective excitations in a resonantly driven polariton fluid [108].

The dynamics of the coherent polaritons (ψ) can be described by a different modification of the Gross-Pitaevskii equation,

$$i\hbar\frac{\partial\psi}{\partial t} = \mathcal{H}\psi - \frac{i\hbar}{2}\gamma\psi + P. \tag{2.5}$$

In contrast to non-resonant pumping the spatio-temporal pump P directly pumps the polaritons in this case.

One of the main challenges for resonantly pumping our microcavity sample is the separation of the incident pump from the polariton photoluminescence (PL). Since the bottom DBR has 8 additional pairs compared to the top DBR, the photons leaking from the bottom DBR are exponentially suppressed. Therefore the photons primarily escape the microcavity through the top DBR. Due to momentum conservation of the in-plane pump wavevector and the polariton wavevector, it is difficult to distinguish the polariton PL from the reflected pump. Since the polariton emission is coming with the same $\vec{k}_{||}$ as the reflected pump, any

Fourier filtering is not helpful. Real space filtering may be attempted only for the emission away from the pump region. However, such images have a high background noise due to scattered pump from the roughness of the top DBR. Adding a Fourier filter to such an image may cut down the noise signal from the scattered pump in the region of interest. It is possible to reject maximally the reflected pump by coming with the pump at an angle greater than the numerical aperture of the imaging setup. This criterion usually inhibits us from using a high numerical aperture microscope objective with a short working distance. Such techniques were employed to observe ballistic polariton propagation [54]. Another difficulty with resonant pumping of high Q microcavities is that the linewidth of the lower polariton mode is narrow. This makes coupling light into the microcavity inefficient if the laser linewidth is broader than the linewidth of the dip in the stopband.

Most of these problems are alleviated while considering non-resonant pumping. Firstly, since the pump wavelength is different than the emission wavelength of the polaritons, using a wavelength filter we can filter out the reflected pump from the emission. Secondly, the non-resonant coupling efficiency of light into the microcavity is higher than the resonant coupling efficiency. This helps us to reach much higher polariton densities using the same pump power.

2.3 Imaging concepts and optical setup

The designed optical microscope serves to accomplish two objectives: (1) to perform differential reflectivity measurements to characterize the microcavity, and (2) to image the emission from the microcavity with a high spatial resolution. For both types of measurements we require a well-calibrated imaging setup. The most important consideration in designing the setup is the available working distance between the objective lens and the sample placed at the imaging plane. Since we perform all our measurements below 10 K, the choice of the cryostat is the limiting factor in deciding the objective lens because of the dead space between the sample and the outer window of the cryostat. For my experiments discussed in this thesis, I worked with a continuous flow liquid Helium transfer cryostat from Oxford

with a short working distance. It provided ample space to use a 0.4 NA (numerical aperture) microscope objective with a 2 cm working distance from Mitutoyo. The microscope objective consists of infinity-corrected optics and can be thought of as a lens with a focal length of 10 mm. It produces collimated light for any source placed at its focal plane. This light can be directly sent to a CCD for imaging. However, for spectroscopy it is desirable to spatially select light from a region of interest. This is done by reconstructing a secondary real space image plane and carefully placing an aperture in that plane. The secondary image plane is formed at the focal plane of another lens (f_1) which is inserted after the objective. By using another pair of plano-convex lenses (f_2, and f_3) we image the secondary plane to the entrance slit of the spectrometer. A schematic of this setup is shown in part (a) of Figure 16. The overall magnification of this setup is given by the ratio (f_1 (in mm)/10 mm)·(f_3 (in mm)/f_2 (in mm)).

To obtain angular resolution of the light emitted from the cavity we perform Fourier imaging. A Fourier plane of a lens is where rays coming from different parts of the object but travelling with the same angular direction meet. For a microscope objective this plane is formed inside its body (approximately 1 cm from its rear end). The same lens (f_1) forms an image of this plane with 1:1 magnification at a distance of twice the focal length of this lens, as shown in part (b) of Figure 16. This is the secondary Fourier plane formed in free space, and we can place an aperture in this plane to select emission within a narrow range of angles. We use another pair of lenses (f_4, and f_5) to form a real space image of the secondary Fourier plane at the entrance slit of the spectrometer. The choice of the focal lengths of these lenses (f_4, and f_5) is such that a demagnified image is formed which fits within the width of the CCD array. This is done to avoid clipping of the Fourier image. It is to be noted that the region between the lenses f_2, and f_3 in part (a) and (f_4, and f_5) in part (b) of Figure 16 has collimated light. This is particularly useful for introducing various optical elements such as a dove prism in this space without causing noticeable distortion of the images. The design took a careful consideration of the size of the real space and Fourier space (k-space) planes along the image path to avoid unwanted clipping while introducing optical elements such as neutral density filters, wavelength filters, polarizers, waveplates etc.

For performing energy spectroscopy of the image, a spectrometer is placed before the

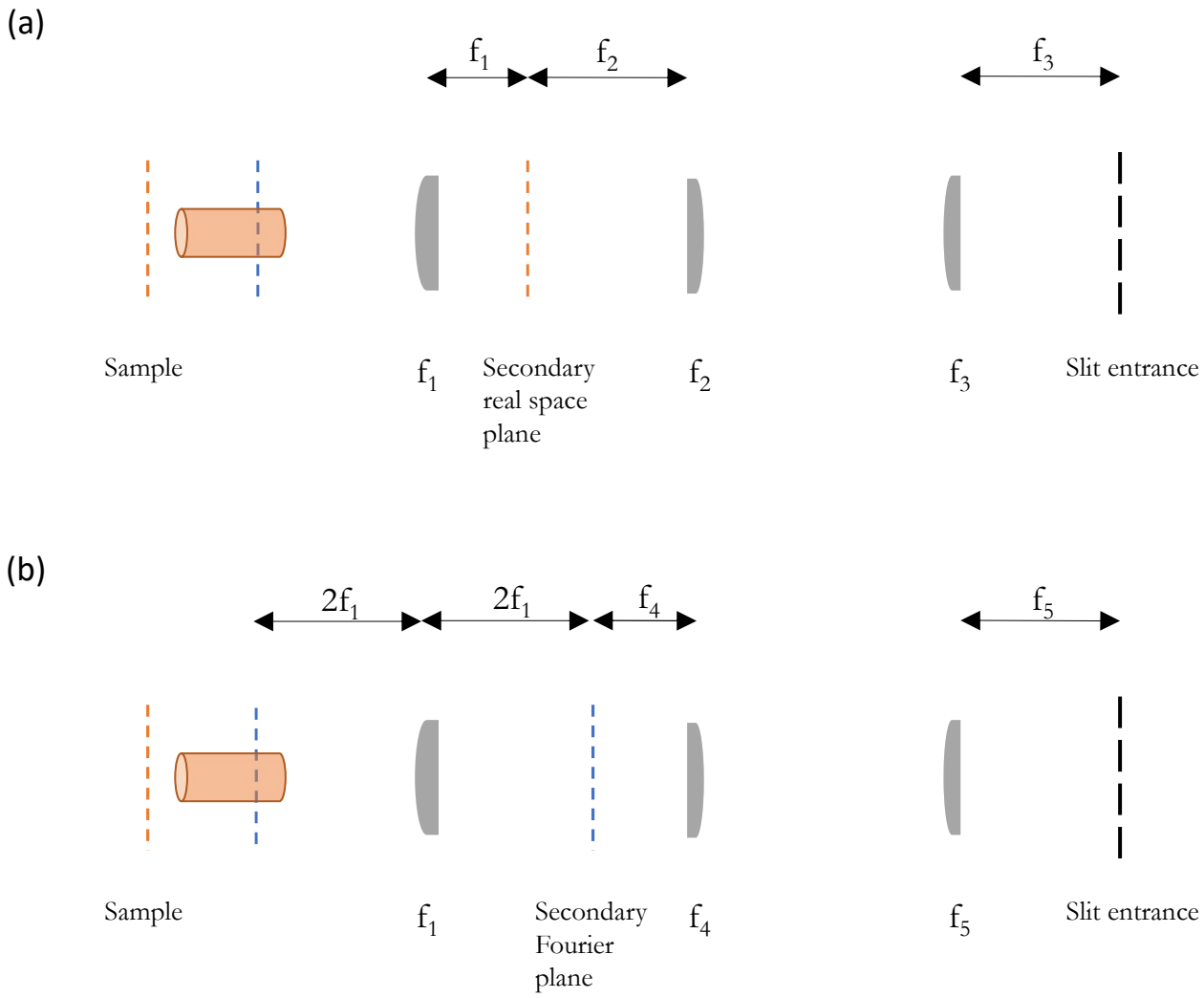

Figure 16: Basic outline of the optical setup for performing (a) real space imaging and (b) Fourier (k-space) imaging. The Fourier plane is indicated inside the microscope objective with a dashed line.

CCD. The spectrometer is made of four components: an entrance slit, a concave mirror placed at a focal length away from the slit, a reflective blazed diffraction grating mounted on a rotating turret, and a focusing concave mirror placed at a focal length away from the CCD chip. The image formed at the entrance slit is collimated by the first concave mirror and is sent to the grating. The zero-order mode of the grating acts as a plane mirror (with

polarization and wavelength dependent reflectivity). The entire zero-order reflected image from the grating is focused by the last concave mirror on the CCD mounted at the exit port. To get energy resolution, the spectrometer slit is closed to select a narrow slice of the image (parallel to the grating lines), and the turret of the grating is rotated to send the first diffracted order to the CCD. The angular rotation of the turret is calibrated with a light source of known wavelength to map the horizontal pixel row of the CCD to the angular spread of the diffracted image. Thus this setup preserves the real space or k-space information along the narrow image slice and the corresponding energy information is added to the perpendicular direction to produce a real space or k-space energy spectra which can be recorded by the CCD.

There is a second exit port of the spectrometer where we attached a streak camera from Hamamatsu. A streak unit is a device which can temporally resolve any optical signal with a resolution of 2 ps. The time scale of dynamics of the polariton condensate ranges between 10 ps - 1 ns, which makes the streak camera an appropriate tool to perform time resolved studies in this system. The main components of the streak camera are shown in Figure 17. The light enters the streak unit through a horizontal slit and illuminates a photocathode which is biased with a high voltage. Here the photons are absorbed and electrons are emitted with a quantum efficiency of about 60%. These emitted electrons are accelerated and passed through a pair of sweep electrodes. A 2 kV sinusoidal voltage is applied to these electrodes which causes a time-dependent deflection of the passing electron beam. This voltage is generated by a synchroscan and delay unit which is triggered by the optical pulses from a stable modelocked laser operating at 76 MHz. It is important to adjust the delay between the signal from the emission and the trigger from the laser such that the electrons are always deflected while passing through the sweep electrodes by the linear part of the sinusoidal signal, to maintain linearity of the temporal axis. The deflected electron beams strike a micro-channel plate (MCP) which amplifies the electron beam without losing spatial resolution. The MCP consists of hundreds of small channels with high bias voltages to guide and amplify the electron signal as they cascade to the other side. Emerging from the MCP, these amplified electron beams strike a phosphor screen causing it to luminescence; the final image is recorded by a CCD. The vertical axis of the image represents events in time, while

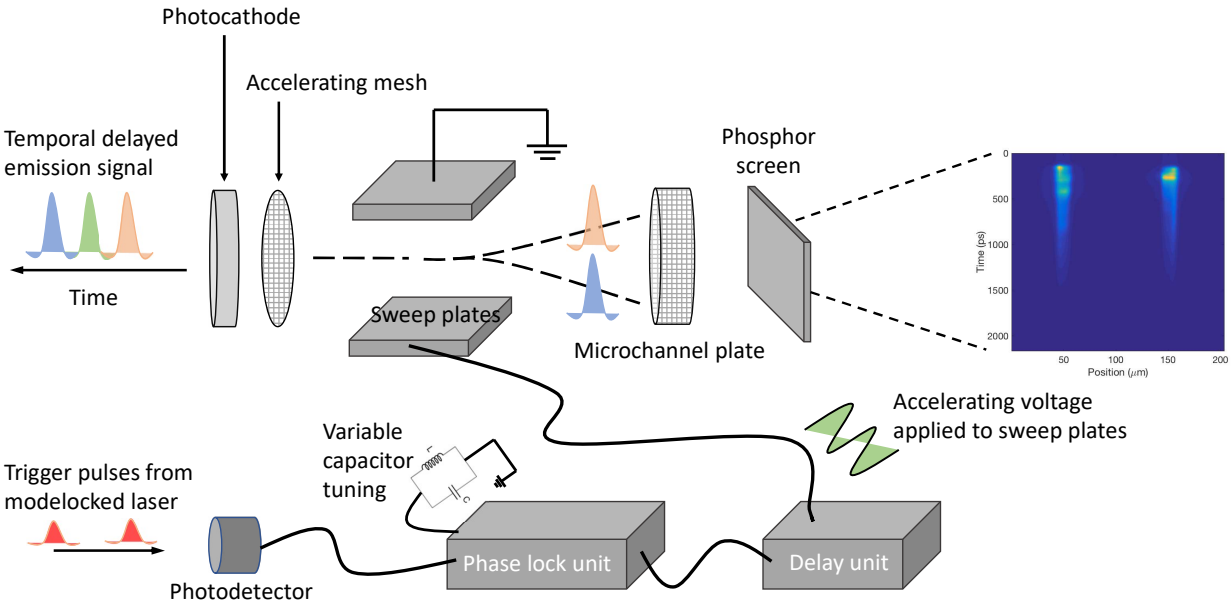

Figure 17: Working principle of a streak camera. The detection starts with the arrival of the laser pulse at the photodiode/photodetector. We used a laser with a repetition rate of 76 MHz which corresponds to 13.1 ns time delay between two consecutive pulses. This trigger signal is phase locked to an internal oscillator signal which is used to apply sinusoidally varying voltage with appropriate electronic delay on the sweep electrodes. The delay is used to compensate the time difference between the laser pulse reaching the photodiode and the emission signal from the microcavity arriving at the streak camera port. The emission signal arriving at the photocathode of the streak camera is shown in color; red - arriving earlier and blue - arriving later in time. The photons hitting the photocathode generate electrons with spatial resolution which are accelerated by the accelerating mesh. The electron beam on passing through the sweep electrodes deflect vertically, such that the earlier signal is deflected upwards with respect to the later signal. These electrons pass through MCP and hit a phosphor screen, and the phosphorescence is captured by the CCD as shown.

the horizontal axis either contains spatial, spectral or momentum information about the polaritons.

Figure 18 shows the two configurations for the incident pump laser. In most experiments

when a high NA microscope objective (for example 0.7 NA objective) is used normal pumping is the only option. In normal pumping the imaging region and the pumping region are the same because the objective which is used to bring the pump laser and collect the emission from the microcavity is the same. This may be a disadvantage if the region of interest to be imaged lies much further away from the pump location. The remedy would be to use a different lens to focus the pump which could be done by bringing in the pump laser at an oblique angle. To accommodate the necessary space a lower-NA objective with larger working distance must be used. If the angle of incidence is greater than the angular field of view of the microscope objective, the reflected laser doesn't enter the imaging setup and can be blocked by a beam dumper. In contrast to a normal-incidence, non-resonant pump either wavelength filters or dichroic beam splitters must be used to separate the pump from the emission. Due to its oblique angle of incidence, the pump spot is asymmetric at the sample plane which could be not favoured in some experiments. If the sample plane is fixed with no freedom for translation then the only way to scan the sample surface is to put the microscope objective on a three-axis translation stage. However it must be pointed out that when the objective is moved, the principal axis for all the downstream optics are offset, which may cause additional spherical aberrations. Therefore, in our setup we leave the microscope objective fixed and mount the cryostat on a three-axis movable stage. The setup also accommodates a Michelson interferometer for measuring phase coherence and an additional pump path for reshaping beam with a spatial light modulator, which will be useful for future experiments.

2.4 Fabrication of rings

In this section I will describe the fabrication process which was used to etch the top DBR of the microcavity in the shape of a ring. For a more detailed overview of fabrication of III-V semiconductors see Ref. [109]. The MBE grown microcavity sample by our collaborators is a wafer of 2 inch diameter which is cleaved into small 5 mm square chips for fabrication. From the characterization process of the wafer, the region of resonance (where the cavity photon

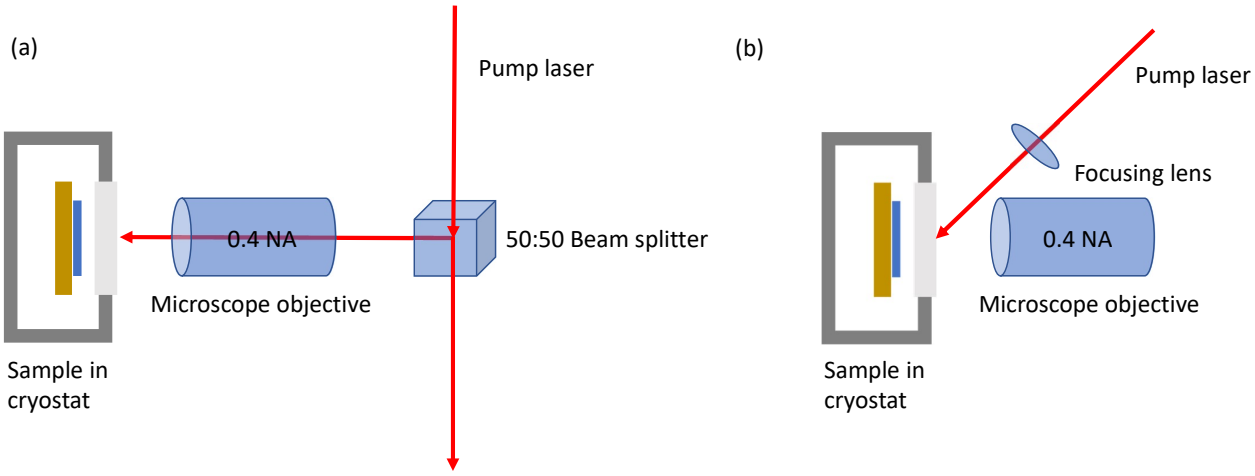

Figure 18: Pump configurations used in the experiments to produce polaritons. (a) Pump at normal incidence, (b) pump at oblique incidence.

energy equals the exciton energy of the quantum wells) is determined. The chip containing this resonance region is used to fabricate the rings.

Before beginning the process it is important to clean the chip surface of any contaminants which may produce undesired results. In standard semiconductor processing a combination of acetone, methanol and isopropanol is used to clean wafers/chips. Acetone is a polar, aprotic solvent. It will dissolve commonly occurring organic contaminants from the wafer surface. However, due to its high evaporation rate it will leave behind the dissolved residues. To maximize the effectiveness of acetone as a solvent one can use a bath of acetone in a sonication chamber. This will remove the organic contaminants from the wafer surface and mix it with a large volume of acetone bath. Having an acetone bath reduces the contaminant concentration when the acetone vaporizes after the wafer/chip is taken out of the bath. Methanol is polar, protic solvent which has lower evaporation rate than acetone and can be used after the acetone bath to clean the wafer. Isopropanol is used for dissolving non-polar contaminants and is suitable as a secondary chemical for removing impurities left by acetone and methanol. Solvents act better when stirred and in high volume; therefore a sonication bath is the most commonly used method for cleaning wafers using solvents. Finally, deionized

water is used to rinse the wafer after it has been cleaned using the organic solvents. The wafer is dried by blowing dry nitrogen over the wafer surface, and sometimes, even heated to vaporize the solvents before being secured safely for future processing.

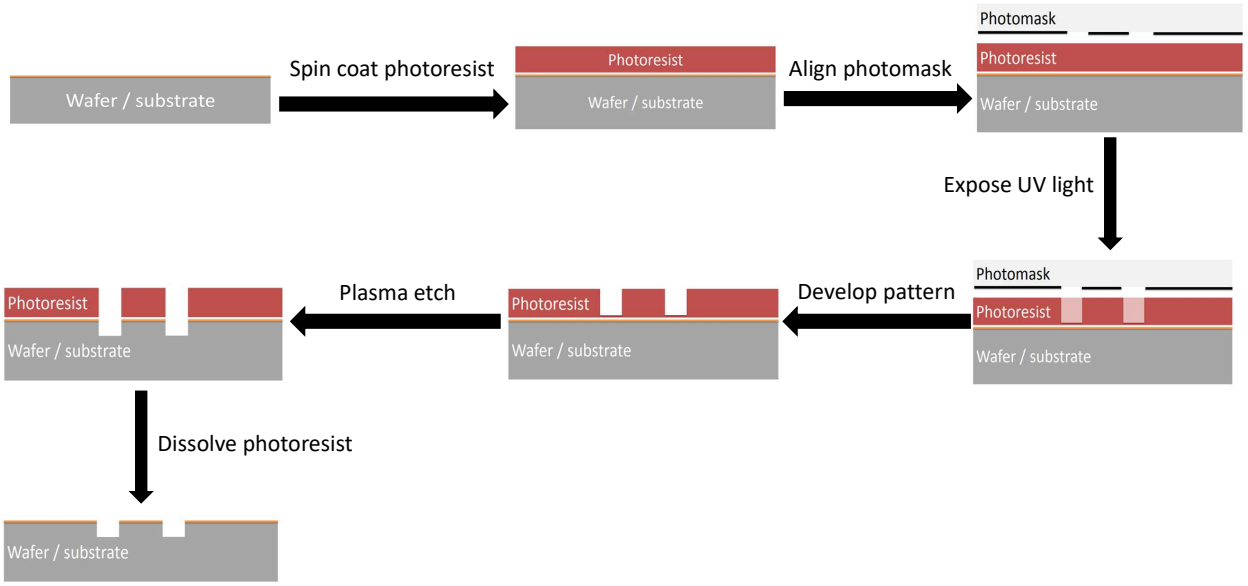

Figure 19: Process flow of the fabrication process depicting the main steps in photolithography for patterning the wafer/substrate. Details for each step and GaAs specific recipe is given in the main text. The above processes were carried out in a clean room environment.

The rings are designed to have a diameter between 60 μm and 120 μm, and the radial width between 10 μm and 20 μm. Since the nominal dimensions of the rings are much larger than the wavelength of ultraviolet (UV) light, we can transfer sharp patterns using UV photolithography. The main steps of the process are shown in Figure 19.

Ultraviolet photolithography is usually considered as the first step in transferring a desired pattern from a mask to a photoresist. In this step, a layer of photoresist is spin coated on the surface of the wafer. The thickness of the photoresist is chosen depending on the depth that needs to be etched underneath. In the recipe, thickness is controlled by the speed at which the wafer is rotated inside the spin-coating chamber and the photoresist viscosity. The thickness is generally proportional to (spin speed in rpm)$^{-1/2}$. A photoresist is typically an organic compound which undergoes a chemical reaction when exposed to light; exposure

to light modifies the solubility of the photoresist in a basic solution, commonly known as developer. Photoresists are classified into two categories: i) positive tone, and ii) negative tone. A positive tone photoresist becomes more soluble in the developer after exposure to light while a negative tone photoresist becomes less soluble after exposure to light. A mercury lamp is the most commonly used light source for exposing the photoresist. Typical available wavelengths from this source are 436 nm (G-line), 405 nm (H-line) and 365 nm (I-line). It is desirable to have a uniform absorption and chemical reaction throughout the entire thickness of the photoresist. This will produce straight-walled profile. However, to ensure such a profile, a dose test is usually preceded to fix an optimum intensity and exposure time. Nitrogen gas is the by-product of the chemical reaction that occurs when the photoresist is exposed to radiation. A correct dose ensures gas escape at an acceptable rate without causing any deformities in the photoresist profile, which can cause unwanted etch patterns. To ensure uniformity in photoresist behavior the wafer is pre-baked on a semiconductor hotplate before exposure to radiation. This step helps to remove excess moisture and thicken the photoresist. The development time is selected to provide adequate time for the exposed areas to dissolve without degradation of the unexposed resist. Gentle agitation during this process helps with uniformity. Post-development baking of the patterned wafer helps to toughen the photoresist and improve its resistance to the subsequent etch process. One must be cautious to not overheat the wafer as it may cause re-flow of the photoresist to minimize the surface area (it starts bulging at the center and becomes dome shaped) when temperatures exceed the glass transition temperature of the resist. Details of the recipe are provided at the end of the chapter.

In the next step we etch the exposed areas of the chip which are not covered by the photoresist. We chose a dry etch process over wet etch due to the higher degree of anisotropy between the etching rates in the vertical and horizontal directions. Processes with isotropic etch rates will produce curved sidewalls with significant undercut below the photoresist which is undesirable. The etching is performed in an inductively coupled plasma (ICP) chamber. The plasma consists of electrons, positively charged ions, neutral molecules and neutral radicals. Typically the degree of ionization of the plasma is less than 1%. The neutral radicals chemically react with the exposed wafer surface forming volatile compounds

which are released as gases due to the bombarding of the heavier ions. Since the ions are accelerated along the vertical direction, the etch rate is significantly higher in this direction. The chemical reactivity and selectivity are determined by the gases which are used to make the plasma while the feature profile and the etch rate depends on the kinetic energy of the ions. Too energetic ions may cause surface damage. The etching process was carried out in a Plasma Therm Versaline ICP RIE system with a chamber pressure of 3 mTorr, 600 W ICP power, 75 W RF bias power, and 20:7 BCl_3/Cl_2 gas mixture ratio [110]. The ICP power is used to produce a high density plasma at the center of the chamber in a toroid geometry. The inhomogeneous plasma diffuses out from this region and forms a uniform plasma at the wafer location. The wafer is placed on an electrode to which the RF bias power is applied. This controls the directionality and the kinetic energy of the ions hitting the wafer. A low chamber pressure implies less collisions with gas molecules and hence higher kinetic energy for the ions reaching the wafer. The gas composition is chosen to provide equal etch rates for AlAs and AlGaAs alloy and provides an etch selectivity of 3:1 over the photoresist while also giving smooth etched profiles. The top DBR is about 3.2 μm thick and it takes approximately 340 s to etch it completely.

Some feedback about the number of layers etched can be obtained in real time by monitoring the reflectivity of the wafer which changes periodically as each layer is etched (DBR is a periodic structure). This can be used to set the endpoint for the process. The chip is placed on a silicon wafer whose back surface remains in contact with a closed Helium line to extract the heat that is generated due to the sputtering effect of ions. After etching, the photoresist mask is removed by sonicating in Microposit Remover 1165 for 1 minute, followed by soaking in a different container of the same solution for 4 minutes. The sample is then immediately rinsed in acetone then methanol (or isopropanol) then DI water to avoid having any residue settle on the surface, and then dried by blowing with compressed Nitrogen. A scanning electron microscope image of sample with etched rings is shown in Figure 20.

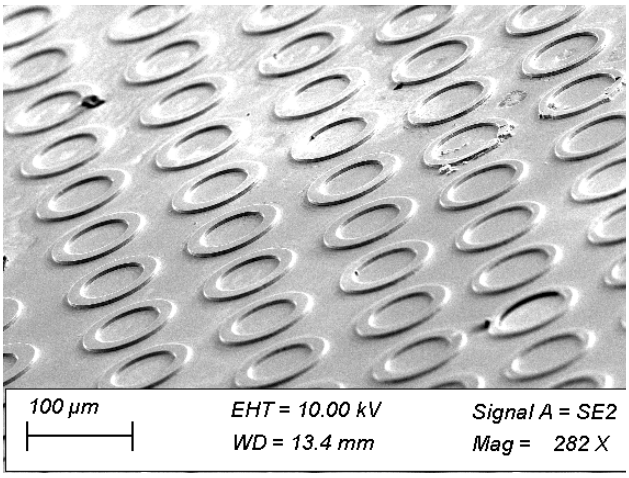

Figure 20: An example of scanning electron microscope image of the surface of the etched microcavity sample.

2.4.1 Recipe for photolithography

Spin coat. AZ P4210 photoresist is spin coated on a clean chip at spin speed of 4000 rpm for 60 seconds in Laurell WS-400B Spin Processor. This gives a photoresist thickness of about 2700 nm. The high rotation speed keeps the photoresist edge bead width to a minimum. After spinning, the chip is soft-baked at 95 °C for 2 minutes.

UV expose. A lithography mask containing the pattern to be printed is first aligned on top of the chip in a Suss MJB-3 mask aligner. The mask is made from chromium on a quartz glass. Once the alignment is made, the mask is brought in close contact with the chip for exposure, which was done using 405 nm radiation at 25 mW/cm2 for 6 seconds, giving a total exposure energy density of 150 mJ/cm2.

Develop pattern. Following exposure, the pattern is developed in a solution of AZ400K and DI water with a developer:water ratio of 1:3 by volume. A development time of 45 seconds usually gives desired results. Following development the chip is baked at 115 °C for 30 minutes to harden the photoresist. Higher temperatures will cause difficulty in removing the photoresist after etching.

Descum unmasked surface. To remove any residue left after the development on the

exposed chip surface a short O_2 plasma is used. This is done in a Trion Phantom III LT RIE, set to 500 mTorr chamber pressure and 50 mW RF power for 10 seconds. Next we proceed for etching.

3.0 Pendulum oscillations of a polariton condensate

Exciton-polaritons in microcavities are now ubiquitous for studying fundamental properties of Bose-Einstein condensation [111, 92]. In many ways, polariton condensate studies are complementary to cold atom condensate studies [112, 113, 114, 115, 116], with continuous decay due to leakage through the confining mirrors of the microcavity allowing direct, time-resolved, non-destructive monitoring of the polariton condensate by external optics. Although this decay tends to also deter equilibration, in recent years it has been possible to make this term small enough that equilibrium condensation can be reached [47, 48]. Studies of polariton condensates near equilibrium, however, have so far been restricted to steady-state conditions [48, 117, 118]. In this work, we present results for microcavity polaritons with long lifetimes ($\approx$ 200 ps as compared to 20 ps in the older generation microcavity samples) and transport distances up to hundreds of microns, which allow us to see macroscopic dynamics of a condensate all the way from a quench event (i.e. generation of a highly non-equilibrium gas of polaritons by a short pulse) to equilibrium; in particular, as the condensate nears equilibrium, we observe damped oscillations of a polariton condensate corresponding to pendulum motion modified by interaction effects in the condensate. These observations show that the kinetic and interaction energies play a significant role in the temporal dynamics, which we observe directly in real-time movies of the condensate. These studies also allow us to extract quantitative information about the polariton-polariton interaction constant, and lay the foundation for future studies of one-dimensional motion, including networks of paths with nodes and thermalization of strongly interacting gases.

The top mirror of the microcavity structure used in this experiment consists of 32 alternating layers of $Al_{0.2}Ga_{0.8}As$ and AlAs, while the bottom mirror consists of 40 alternating layers of the same materials. The entire structure was grown on a GaAs substrate by molecular beam epitaxy (MBE) with three sets of four 7 nm thick GaAs quantum wells with AlAs barriers embedded at the three antinodes of the cavity photon mode as shown in the sketch in Figure 14. The large Q-factor ($\sim 10^6$) of this microcavity results in long-lived polaritons with the lifetime of the order of 200 ps. Due to the spatial gradient in the rate of deposition

of the layers during the MBE process, there is a thickness variation of the cavity. This leads to a strong variation of the cavity photon energy ($\approx 6-9$ meV/mm) across the microcavity wafer.

The gradient of the cavity also leads to a variation of the detuning, defined as the mismatch $\delta = E_C - E_X$ between the cavity photon energy E_C and the quantum well exciton energy E_X. Since the detuning regulates the relative photonic and excitonic properties of the polaritons, we can have control of the lower polariton (LP) mass and the strength of the polariton-polariton interactions simply by examining rings at different places on the wafer. Typically the detuning is nearly constant over a single ring, while varying more significantly from ring to ring.

This chapter is an adaption of the work published in papers [68, 67]. The polariton rings were fabricated by Burcu Ozden. Jonathan Beaumariage, Mark Steger and David Myers performed characterization of the microcavity grown by Loren Pfeiffer and Ken West. David Myers and I designed the experiment. Rosaria Lena, Andrew Daley, David Snoke and I developed the theoretical model. I performed the measurements and carried out numerical simulations with Rosaria Lena. The project was supervised by David Snoke.

3.1 Radially confined states in the ring

Etching away the top DBR in the shape of a thin ring, as shown in Figure 20, produces a trapping potential for the polaritons in the radial direction. The strain mismatch in the quantum well at the outer and inner edges of the ring produce an energy minimum within the ring width. The polaritons are pushed away from the edges into the minimum which acts as a channel for the polaritons to flow around the ring. This restricts the polariton condensate to one-dimensional motion, while not decreasing their lifetime too much; as shown in previous work,[79] strain effects push the polaritons away from the free, etched surfaces, so that surface recombination does not play a significant role. The trapping in the radial direction gives rise to a ladder of states in the channel as shown in Figure 21. These states are arranged from lower to higher energy with increasing number of nodes,

just like states in a harmonic potential. Earlier work with confined states of polaritons in a harmonic potential were reported in Refs. [119, 120]. The spacing between these states is approximately 220 μeV for a 15 μm channel. Figure 21 is an energy resolved image of the PL from a small region (radial slice) of the ring. To produce polaritons, the whole ring is uniformly illuminated by a defocussed, low power pulsed laser with wavelength tuned to one of the Bragg modes of the cavity. A mode-locked Ti:sapphire pump laser with a pulse repetition of 76 MHz, a pulse width of ≈ 2 ps, and incident at an angle of $\approx 45^\circ$ was used for non-resonant excitation ($E_{\text{pump}} \approx 1750$ meV) of the rings at their highest energy region. A 0.5 m spectrometer was used to spectrally resolve the photoluminescence (PL) with a 1200 grooves/mm reflective grating. PL from the rings was collected using a microscope objective with a numerical aperture (NA) of 0.40. All measurements were performed by cooling the microcavity to low temperature (below 10 K) in a continuous-flow cold-finger cryostat. Non-resonantly excited polaritons undergo significant energy relaxation to occupy the low lying radial states in the ring. Another example of the radial states in a ring of diameter 100 μm and a channel width of 20 μm is shown in Figure 22. The PL is collected from a diametric slice of the ring and it also shows the energy difference between these opposite regions in the ring. In this case, the energy separation between the two lowest radially confined states in the channel is approximately 150 μeV. In the azimuthal direction, each of these confined states allows continuous one-dimensional motion.

The polaritons also experience an overall gradient of their potential energy due to a wedge in the optical cavity; as discussed in earlier work, [54] this gradient leads to an effective "gravity" for the polaritons, demonstrated in macroscopic ballistic parabolic motion of the polaritons. Because of this analogy to gravitational force, in this work we will refer to the point of highest potential energy on the ring as the "top" of the ring, and the point of lowest potential energy as the "bottom" of the ring. The combination of the restriction to one-dimensional circular motion and the overall potential-energy gradient gives rise to dynamics similar to rigid pendulum, up to modifications from interactions between condensate polaritons. In this work we directly image the real-time motion of the condensate in the azimuthal trap to show damped pendulum-like oscillations in the ring. The oscillation period depends on the mass in the present case, unlike the case of a gravitational pendu-

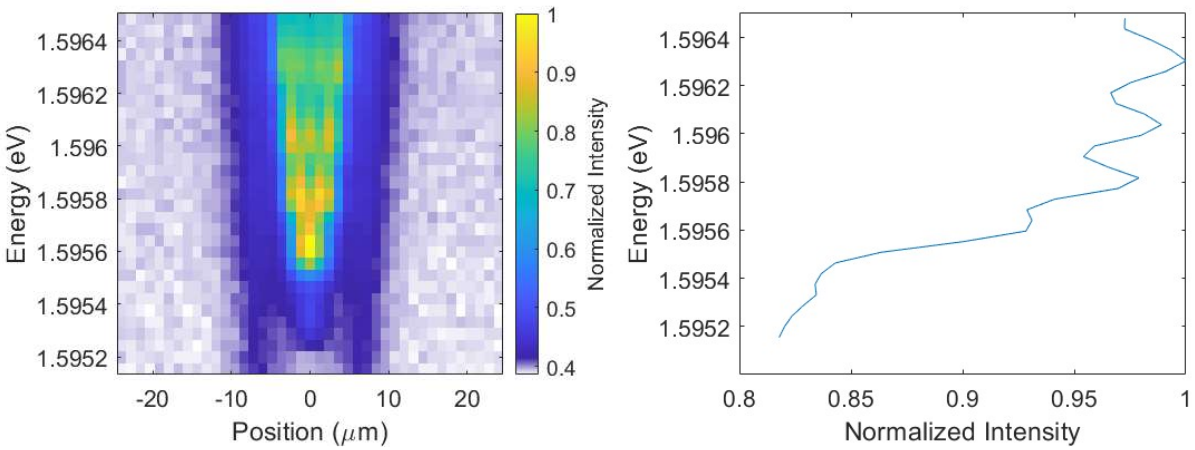

Figure 21: Confined radial states in a ring with radial width 15 μm at quantized energies. Separation between these states is approximately 220 μeV.

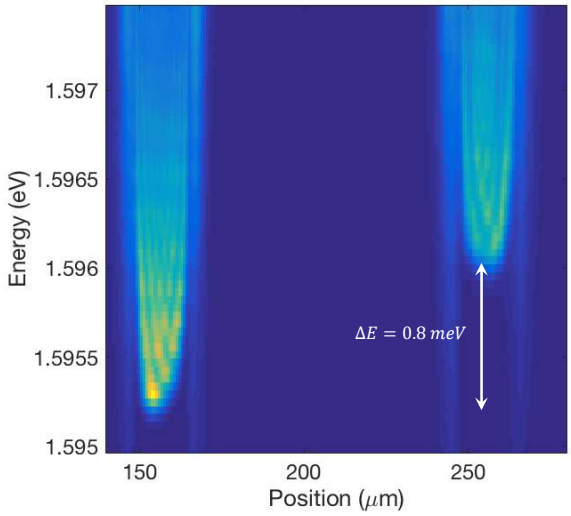

Figure 22: A normalized intensity image of the energy resolved polariton PL from the top and bottom of a ring with radius 50 μm and radial width 20 μm. The ring is uniformly illuminated with a low power, non-resonant laser. It shows the trapped polariton states in the channel as well as the overall energy difference between the top and bottom of the ring.

lum, because the force on the polaritons due to the cavity gradient is independent of their mass. Thus, although the dynamics of this system are those of a rigid pendulum, there is no equivalent of the gravitational mass.

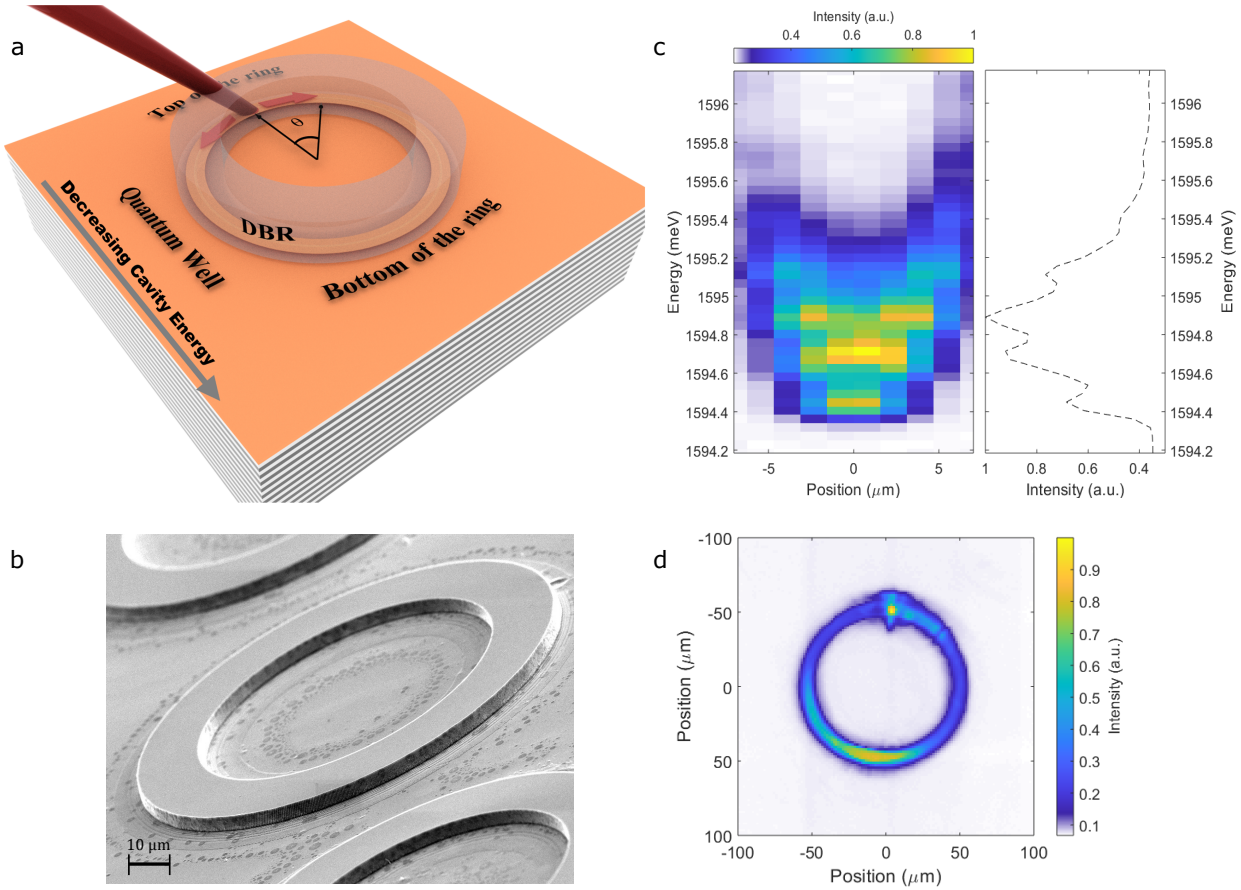

Figure 23: Ring channel microcavity. a) A sketch of the ring structure showing the oblique incidence of the pump laser and introducing 'top' and 'bottom' nomenclature in the ring, and the definition of the angle (θ) which is used to refer to different regions in the ring. b) Scanning electron microscope image of an etched ring used in the experiment. c) Radial mode separation in the ring channel with a width of 15 μm. d) Time-integrated and normalized photoluminescence from a typical ring structure for pulsed, non-resonant laser excitation at the top ($\theta = 0$) of the ring.

3.2 Non-equilibrium motion and pendulum oscillations

In these experiments, the polariton condensate was created by a short (2 picosecond) laser pulse, localized to a spot a few microns in size (≈ 20 μm), at the top of the ring ($\theta = 0$ as defined in Figure 23). As discussed in numerous previous papers (e.g., Refs. [121, 79, 122]) the non-resonant laser light creates a cloud of excitons at the laser excitation spot, which then convert down into polaritons; although there is a continuous transition between polariton and exciton states, it is useful to treat these as two distinct populations, with the exciton population at higher energy known as the "exciton reservoir"[67]. Above a critical threshold of pump power, the polaritons at the creation spot undergo Bose-Einstein condensation in a highly non-equilibrium state, which then ballistically stream out of the exciton spot. As seen in Figure 24, the polaritons then rapidly fill the entire ring in a macroscopic condensate state far from equilibrium. A movie of the motion of the polaritons in the ring is presented in the Supplementary Material of the paper [68]; Figure 24 gives single snapshots from this movie; Figure 23 shows time-integrated photoluminiscence from the ring.

As seen in Figure 24, and also in the movie, after the initial explosive, ballistic motion to fill the ring in the first 100 ps, the condensate then undergoes a much slower equilibration both spectrally and spatially into the bottom of the ring. Although the lifetime of the polaritons is around 200 ps, the time scale for this equilibration is much longer, because there is an interplay between the polariton population and the exciton reservoir with much longer lifetime. A previous study [67] has shown that excitons created by the pump laser diffuse about 30 μm away from the creation spot, but here we see evidence of reservoir excitons all the way around the ring, 150 μm from the creation spot. This indicates that polaritons may convert back into excitons via polariton-polariton collisions. Evidence for the build up of the exciton reservoir under resonant pump was given in Ref. [123]. There are two effects of this background population of excitons. One is to extend the lifetime of the polaritons, as they can convert into excitons, with a lifetime of nanoseconds or greater, and then back into polaritons. The other effect of the exciton population is to give a smooth renormalization of the potential energy profile of the ring trap, due to the repulsion of polaritons from the excitons. This latter effect is seen in the shift to lower energy of the polariton emission

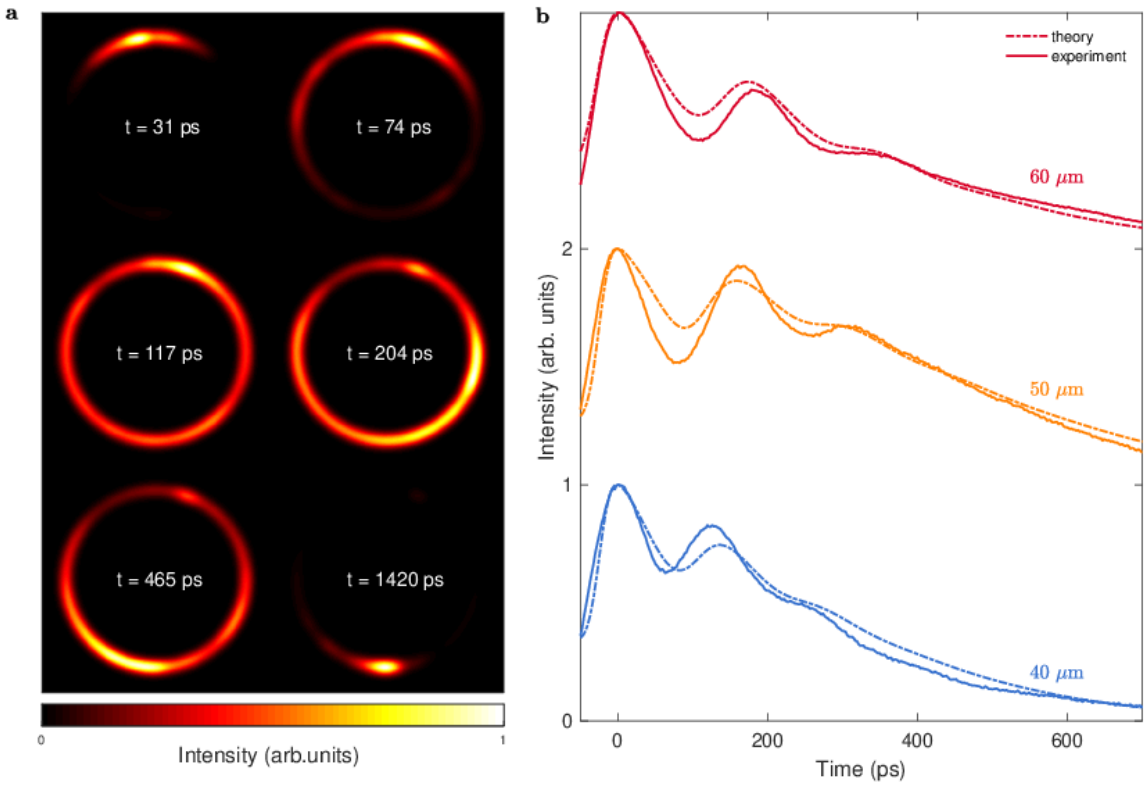

Figure 24: Polariton propagation in the rings and time period of oscillations. a) Time snapshots of the PL from the ring with width 20 μm and radius 50 μm recreated by combining temporal intensity data from various locations on the ring with an angular resolution of 10°. Each time frame has been normalized with respect to the maximum intensity from the ring in that frame. For a movie of the evolution, see the online Supplementary Material [68]. b) **Solid lines**: Intensity oscillations at the bottom of the rings as a function of time, for three different ring radii and with width 15 μm. **Broken lines**: Numerical simulation of the density evolution at the bottom of the ring due to the rigid pendulum potential.

spectrum at late times in Figure 29, as the background exciton population decays.

As seen in Figure 24, and also in Figure 29 when the polaritons are near equilibrium in the trap, pendulum-like oscillations arise. These oscillations are damped over a period of several hundreds of picoseconds and are seen in rings of different radii and widths. The

period of these oscillations at low density is in good agreement with the natural frequency predicted for the classical low-amplitude oscillation frequency of a rigid pendulum, namely $\omega = \sqrt{g/R}$, where R is the radius of the ring and g is the effective gravity constant, given by $mgh = \Delta U$, where m is the effective mass of the polaritons, and ΔU is the potential energy difference for a distance h. The mass of the polaritons was inferred from the curvature of the polariton dispersion as a function of the azimuthal wavevector in the ring. The measurements were done by exciting the entire ring with a low power, non-resonant laser. The pump power used to observe pendulum oscillations in PL intensity as in Figure 24 was approximately 6 times the threshold power for condensation at the source, as seen in the transport to the bottom in these rings, which is not sufficient to drive the polaritons at the bottom into a single transverse mode condensate. Therefore the dominant contribution to the PL intensity comes from higher order transverse and non-zero in-plane momentum $k_{\|}$ states as shown in Figure 25. A comparison of the time-resolved PL intensity for three different ring radii is shown in Figure 24 and the measurement of the ring parameters are given in Table T1. Additional data showing oscillations in rings of different radii and widths are shown in Figure 26.

3.3 Open-dissipative condensate dynamics

Numerical simulations of the temporal and spatial dynamics for a polariton wave packet at late times are plotted with broken lines on top of the respective experimental data in Figure 24, for typical ring parameters given in the end of the chapter. The numerical model consists of a 1D Gross Pitaevskii equation (GPE) with time dependent generation $G(t)$ and loss $\Gamma(t)$ terms,

$$i\hbar\frac{\partial\psi(\theta,t)}{\partial t} = \left[-(1-i\alpha)\frac{\hbar^2\bigtriangledown^2}{2m} + V(\theta) + g_{1D}|\psi(\theta,t)|^2 + iG(t) - i\Gamma(t)\right]\psi(\theta,t), \qquad (3.1)$$

where $\psi(\theta,t)$ is the wavefunction for the condensate, $V(\theta)$ is the potential-energy profile of the ring and $g_{1\mathrm{D}}$ is the effective one dimensional polariton-polariton interaction strength. This model included some simplifications: we start with a wavefunction at the bottom of

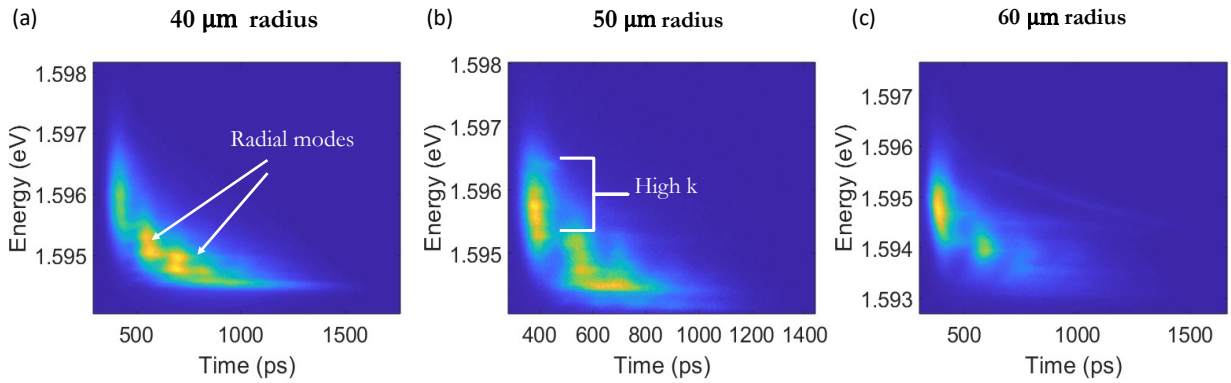

Figure 25: Time- and energy- resolved images of the PL emission from the bottom of the rings of radii 40 μm, 50 μm and 60 μm. The rings were excited non-resonantly with approximately same power. Each of these images is normalized with respect to the maximum pixel value in each image, such that the colorscale ranges between 0 and 1 in each image. Time t = 0 in each image is different and comparison between the arrival time of the signal from the top of the ring cannot be made.

the ring, using the generation term $G(t)$ to account for the fast dynamics of polaritons moving from the top and considered a single radial mode decoupled from higher energy ones. Although we found compelling evidence for the presence of exciton reservoir at the bottom of the trap, we do not attempt to describe its exact dynamics because the mechanism by which they reach there is only speculative at present. Therefore in the model we only describe the condensate dynamics with effective time dependent terms $G(t)$ and $\Gamma(t)$ which empirically account for particle exchange with the reservoir. For the numerical simulation, the above GPE was efficiently solved by using the split step Fourier technique [124, 125].

Although this model has a few simplifications, we can draw two strong conclusions. One is that the oscillations are indeed driven by the interplay between the potential-energy profile and the kinetic energy term of Equation 3.1, which is sensitive to the long-range, spatial curvature of the condensate wave function. The second is that a kinetic-energy damping term, given by $i\alpha$ here in Equation 3.1, is crucial to account for the damping of the oscillations as observed in the experiment. Such a term has been used in previous studies of

R (μm)	ΔU (meV)	m	$2\pi\sqrt{\frac{R}{g}}$ (ps)	T_{meas} (ps)
60	0.88	$6.0 \times 10^{-5}\text{m}_0$	331	343 $\pm$ 5
50	0.83	$6.4 \times 10^{-5}\text{m}_0$	302	306 $\pm$ 5
40	0.66	$6.7 \times 10^{-5}\text{m}_0$	270	272 $\pm$ 5

Table 1: Comparison of time periods for different rings studied in Figure 24. ΔU is found by taking a slice of the PL across a diameter of the ring under a broad, low power pump spot. The uncertainty in this measurement is approximately 10%. Mass of the LP is found by fitting a parabola to the LP dispersion for $k_{\|}$ close to zero. m_0 is the free electron mass in vacuum ($5.1\times10^5\text{eV/c}^2$). T_{meas} is the time period of the oscillations measured between the first and the third peak from the experimental data.

polariton condensates [69, 126, 127, 128], and has been justified in the cold-atom literature by ZNG theory [129] as due to the interplay between the condensate and thermal background particles. In the present experiments, this term may arise due to the interplay between the polariton condensate and the exciton reservoir. There may also be an interaction of the condensate with free carriers, as suggested by prior work [59] on the thermalization processes of polaritons.

3.4 Density dependence of thermalization

These experiments also show the importance of particle-particle scattering in the onset of coherence in the condensate. As seen in Figure 27, at late times the condensate settles down into the global ground state of the ring, renormalized by the polariton interactions. At this point, only the lowest transverse state is occupied, and the emission becomes spectrally very narrow, which is an indication of coherence (see, e.g., Ref.[40], Chapter 9). Figure 27 shows the time-resolved spectra and the spectral width of the ground state emission as a function of time, for two excitation densities. At low density, the thermalization is slow (emission

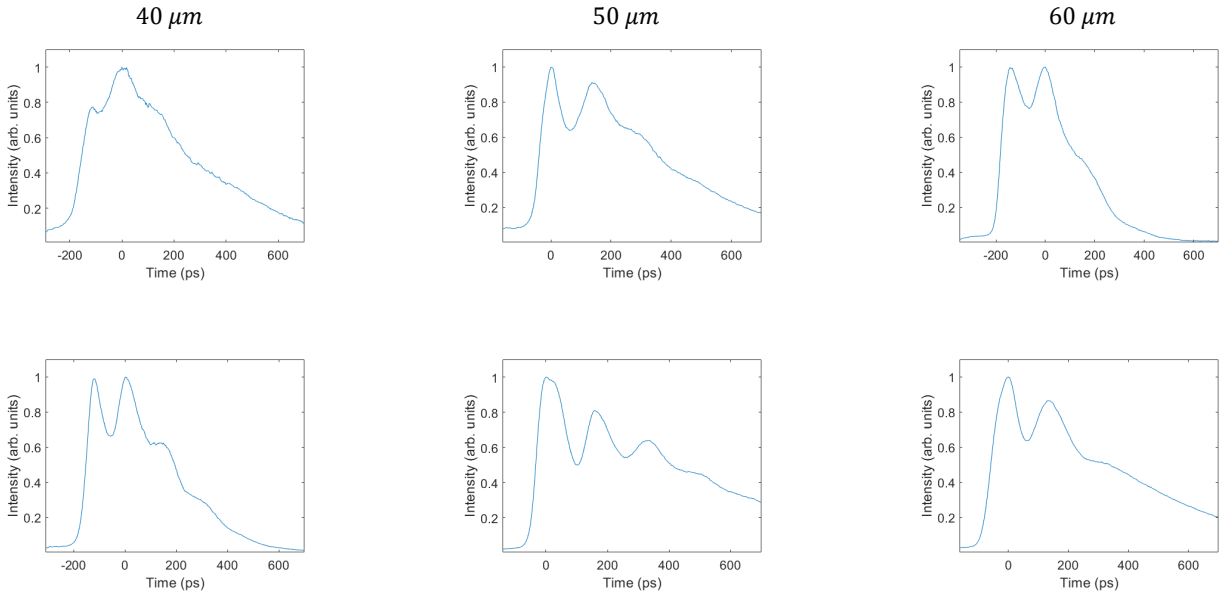

Figure 26: Temporal oscillations in the PL intensity from the bottom of the rings of radii 40 μm, 50 μm and 60 μm. The top row is from rings with width 20 μm and the bottom row is from rings with width 15 μm. Temperature in the cryostat was approximately 7 K. Each of these images is normalized with respect to the maximum intensity. Time t = 0 in each image is different and comparison between the arrival time of the signal from the top of the ring cannot be made.

from the second transverse state persists for over 100 ps), and the narrowing of the spectral width continues over hundreds of picoseconds as the condensate cools. At high density, the thermalization into a coherent condensate occurs much faster, as expected for a collision-dependent process of condensation. Prior theoretical work [130] has shown that both the thermalization rate and the rate of onset of coherence depend on the particle-particle collision rate, which is linear with particle density.

Non-resonant pumping of these rings with pulsed laser shows threshold behaviour, see Figure 28, which is seen commonly in several experiments with a CW pump. Such a behaviour for a non-resonant CW pump is because the pump does not directly feed the condensate, instead it pumps a reservoir state which in turn populates the condensate via

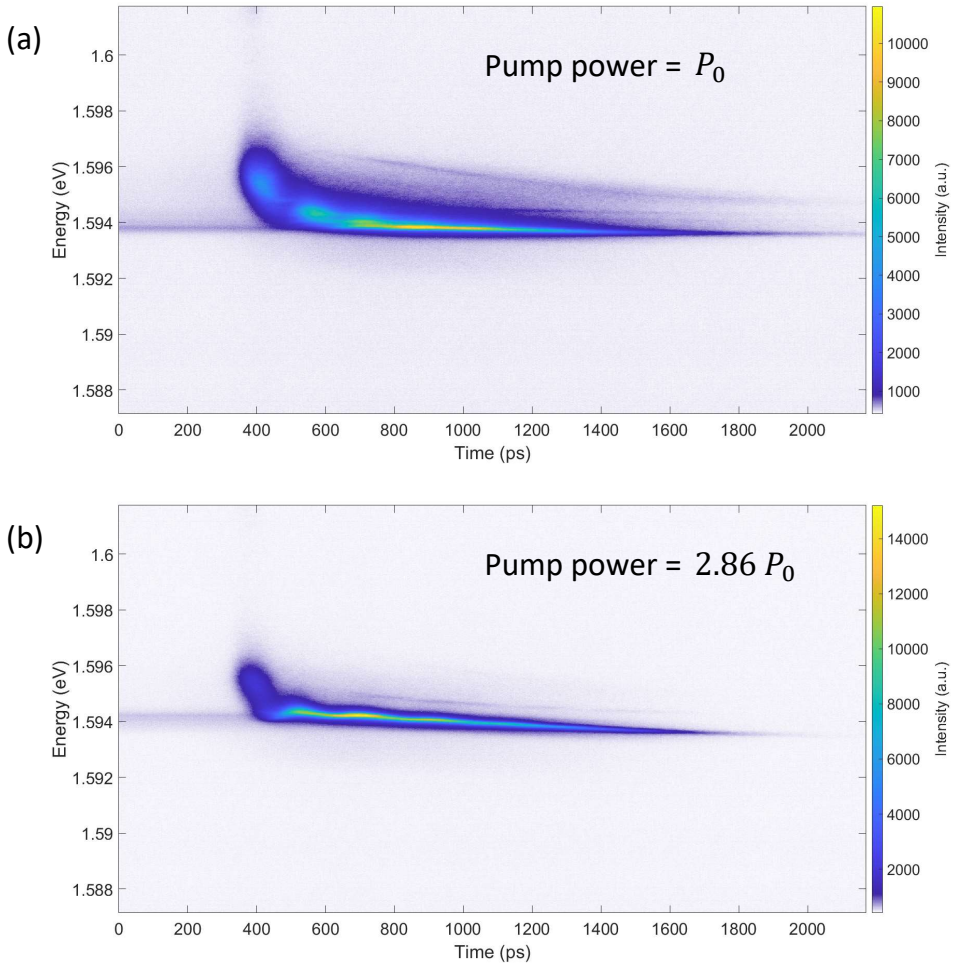

Figure 27: A comparison of energy- and time-resolved images of the PL emission from the bottom of a ring with a 50 μm radius and 15 μm radial width under different excitation power. Note the greater effect of linewidth narrowing at higher excitation density. Also, the signal from the top enters our imaging region relatively earlier at high pump power. This is because the polaritons are launched from a higher potential energy hill when the power is higher.

stimulated scattering. Thus, there is a threshold pumping rate above which the condensate can be formed. It is interesting to note that such a behaviour is also observed when collecting PL emission from the bottom of the ring, where the common assumption is that the reservoir

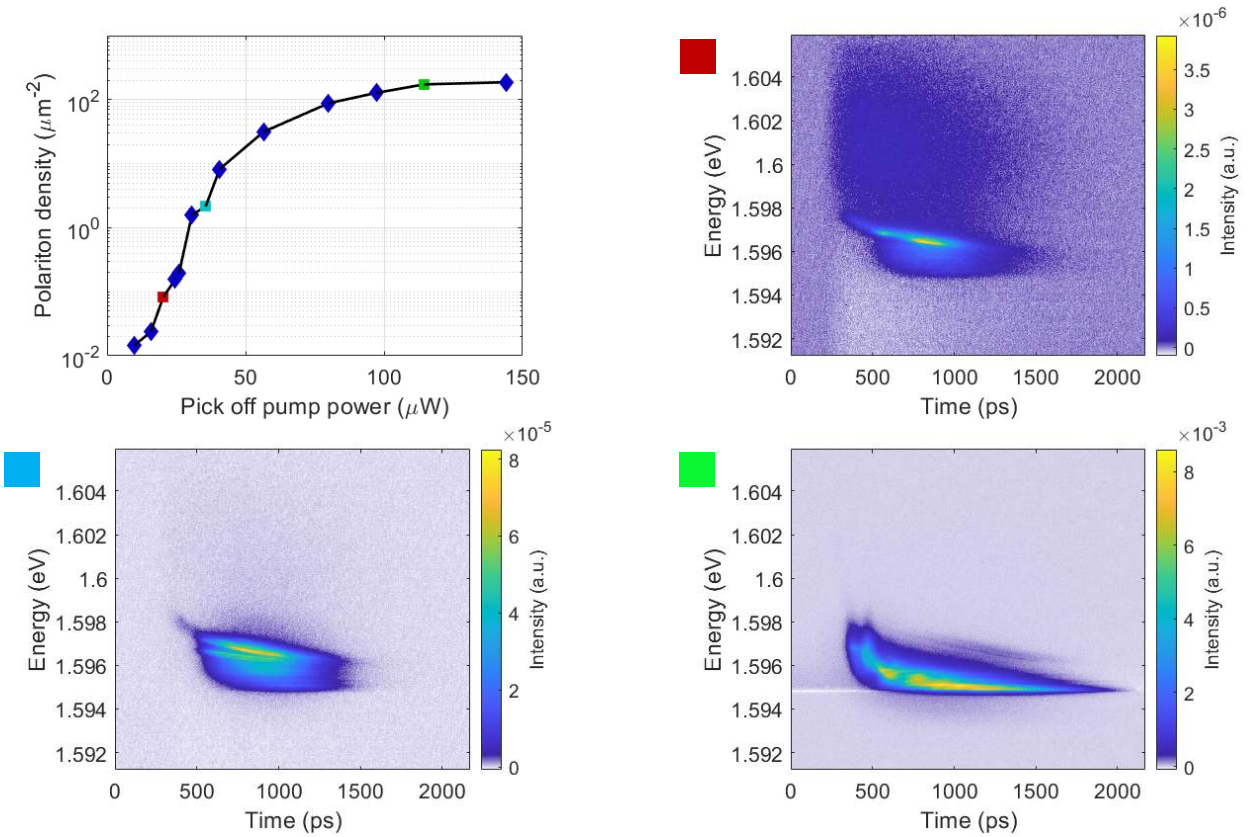

Figure 28: A comparison of the energy- and time- resolved PL from the bottom of a ring of radius 50 μm and radial width 15 μm at different excitation powers. All the three streak images correspond to different polariton peak densities in the bottom of the ring. The peak densities show over three orders of magnitude difference, with low energy radial modes occupied at higher polariton densities. The pick-off pump power was 10% of the power hitting the microcavity sample.

is absent. This behaviour may be interpreted as the formation of a non-equilibrium condensate with the reservoir at the pump location which travels all the way to the bottom of the ring. Depending on the density of the particles (including the polaritons and the reservoir), either a macroscopic occupation of a single mode or several modes form in the bottom region of the ring. Since a two population dynamics occurs at the bottom of the ring, hence the threshold curve is seen while plotting the pump power with peak polariton density in Figure

28. Energy resolved streak images are also shown from three different points on this curve.

3.5 Measurement of the polariton-polariton interaction strength

We can use these data to extract quantitative information about the polariton-polariton interaction strength g_{1D}. As discussed above, the period of the pendulum oscillations depends on the mass of the particles, unlike the case of a real gravitational pendulum, because the potential-energy gradient that gives the restoring force does not depend on the mass in this case, while the kinetic energy does. Therefore we can immediately conclude that the background excitons, which have mass very different from the polaritons, do not contribute to the oscillations, and only contribute a slowly varying, overall potential energy shift of the polaritons.

We can then compare the oscillations seen in two types of data to extract the polariton-polariton interaction parameter. The first is the oscillation of the polariton population at the bottom of the ring, which is observed in the emission intensity of the polaritons. Using the known calibration of photon emission rate to population density, presented in the Supplementary information, we can measure the density $|\psi(\pi, t)|^2$ to within 40% of its absolute value. In addition, we have direct observation of the energy shift due to the renormalization of the polariton ground state energy, seen in the oscillation of the spectral energy position of the polariton photoluminescence, as shown in Figure 29. Assuming that the energy renormalization is linear with the polariton density, as expected for a mean-field energy shift, the comparison of these two oscillation magnitudes therefore allows a direct measurement of the constant g_{1D}, as shown in Figure 29. This number can then be converted to a value for the pure exciton-exciton interaction. The details of this analysis are presented in the Supplementary information of this chapter, and give a value of the pure exciton-exciton interaction in a single quantum well of the order of 10 μeV-μm^2 (12 ± 6 μeV-μm^2). This is in agreement with theoretical calculations [58], and also in the same range as previous experimental measurements using the same sample [81, 47] when the polaritons are at high density, that is, at or above the condensation threshold, as is the case here. It is much

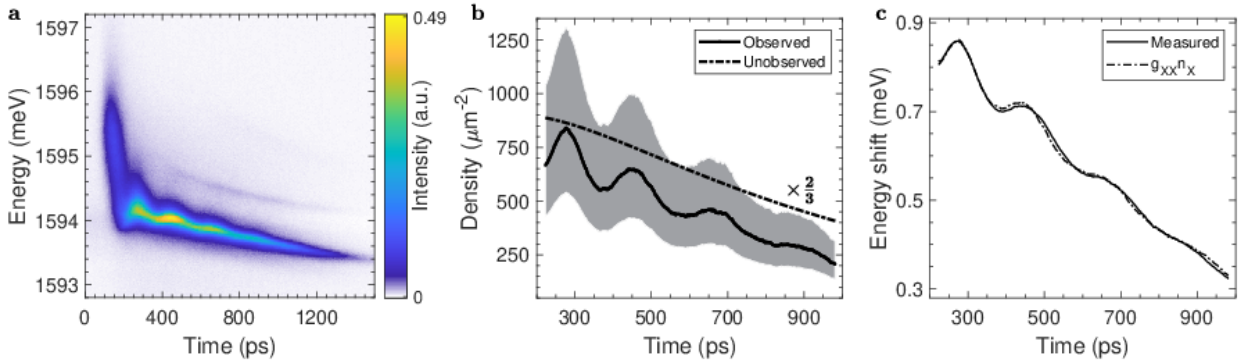

Figure 29: Measurement of the exciton-exciton interaction strength. a) Energy-resolved photoluminescence intensity from the bottom of the ring ($\theta = 180°$) as a function of time following a short (2 ps) laser pulse at the top of the ring ($\theta = 0$), integrated over a wide angle of emission, corresponding to in plane k-vectors of the polaritons $-15° < k_{\|} < +15°$. The approximate level of the pump power used to excite the ring is 19 times the threshold power for condensation at the source, as seen in the transport to the bottom in this ring. b) **Solid lines:** Oscillations in the density of observed polaritons multiplied with the appropriate exciton fraction yielding an effective density of the excitons. The shaded area is the uncertainty in the density originating from the error bounds in the measurement. (Details in the Supplementary information). **Broken line:** Estimate of the exciton density invoked to obtain good fits to the energy shift using the mean field approach. c) **Solid line:** Oscillations in the energy shift of the ground state measured from respective streak images. **Broken line:** Energy shift deduced from the local density of the polaritons and excitons shown in (b), for the best fit case.

lower [1] than prior values reported for polaritons at low density [66, 131, 132], indicating the possibility that the polariton-polariton interaction strength may depend on their density. In

[1] In Ref. [131], the authors were not careful to account that the PL intensity that was measured had contribution from all the quantum wells whereas the observed blue shift was due to repulsion between particles in a single quantum well. Therefore, accounting for the 12 quantum wells give an order of magnitude higher value for g in [131].

contrast, resonant injection experiments [133, 134, 135] estimated a much lower value of the interaction strength.

3.6 Conclusion

The results presented here, which are the only experiment with polaritons to reproduce the damped population oscillations seen in cold atoms, have been made possible by three experimental steps forward: first, the very high Q-factor of the microcavities used, which gives very long lifetime to the polaritons, allowing them to evolve in time all the way from a highly non-equilibrium, quenched initial state to spatial and spectral equilibrium at late times; second, the low disorder in these structures which allows long-range motion of the polariton condensate; and the development of etching processes which allows us to constrain the polariton motion to one dimension. The pendulum-like oscillations are not strongly affected by the interaction between the condensate polaritons in the regime observed here and at late times damped out to produce a fully thermalized, single-mode polariton condensate.

These dynamics are reproduced by a numerical solution of a Gross-Pitaevskii equation which includes generation and continuous decay, as well as energy renormalization due to the polariton-polariton interaction and kinetic energy loss due to interplay with the background population of thermal excitons. Future work will examine the coupling of different radial modes, which can be important at early times after the creation of the polaritons when the density of the polaritons is not too high; at high density, the condensate quickly thermalizes into just the lowest radial state.

By measuring the absolute density of the polaritons and their energy shift, we have extracted the polariton-polariton interaction strength, which is in agreement with other measurements at high particle density; all of the measurements in which there is a condensate give similar values for this parameter, while the outliers that give much higher interaction strength are from experiments with much lower polariton density.

Now that we can create 1D wires for polaritons with macroscopic transport, a natural extension is to create networks of one-dimensional wires for transport of coherent polaritons

over macroscopic distances, i.e., polariton circuits. Because polaritons can be deflected by excitons and/or other polaritons, such circuits could allow all-optical switching networks of coherent light.

3.7 Supplementary information

3.7.1 Photon counting

To count all the photons entering our collection optics and reaching the CCD of the streak camera, we used a half wave plate and a polarizer before the entrance slit of the spectrometer. For all the measurements the orientation of the transmission axis of the polarizer was kept fixed, which removed the polarization sensitivity of all the optics inside the spectrometer as the light that entered the spectrometer was always at a fixed linear polarization. Two images were taken for each individual measurement, one with the half-wave plate fast axis (placed just before the final polarizer) at 0° and one with it at 45°. By adding these two images together, the total contribution of both polarizations (both parallel and orthogonal to the final polarizer) were taken into account. The setup was calibrated to convert the intensity counts on the CCD to the photon counts emitted from the ring. The photon counts were subsequently converted into an absolute polariton number per state after accounting for the lifetime of the LP state. Details about this calibration can be found in the next sections. This method has been shown previously to agree accurately with density measured independently from chemical potential of the polariton gas at the Bose-Einstein condensation threshold [47].

3.7.2 Example of streak images used for measuring interaction strength

Energy resolved streak images of the PL from the bottom of the ring are shown in the first column of Figure 30. The detuning at the bottom of the ring in Figure 30(d-f) which is a re-plot of Figure 29 of main paper is -4.7 meV, while for Figures 30(a) and 30(g) it is -4.1 meV, which leads to a slight variation in the LP mass between these two rings. The

pump power used to capture these streak images is much higher (by approximately a factor of two or more) than the previous condition discussed above. In this high density regime, we measured the time period of the oscillations to be longer than what is predicted from the energy gradient in the rings. This is due to the reshaping of the potential at the bottom of the ring, which makes the effective gravity weaker in the rings. The effect of the nonlinearity arising due to the interactions between the polaritons on the dynamics can be understood as a renormalization of the mass of the lower polaritons. In all of these figures, we see clear oscillations in the intensity as well as in energy with time. At early times we see a significant population in non-zero in-plane momentum states ($k_{\parallel} < 2\ \mu\text{m}^{-1}$), which corresponds to the arrival of the spatially inhomogeneous precondensate from the top of the ring. As the population at the bottom builds up, the occupation in the finite $k_{||}$ states is depleted while the emission from the $k_{\parallel} = 0$ state increases. This is also reflected in the spectral narrowing of the emission with time. The oscillations in the intensity of the emission are related to the dynamics of the condensate in a rigid pendulum potential. As the energy of the emission also tracks the rise and fall of the intensity, which is expected from a mean field approximation, we apply this theory to directly measure the exciton-exciton interaction strength g_{xx} as outlined below. A natural advantage of measuring the repulsive interaction strength in this experiment over other steady-state experiments using the non-resonant pump is that there are constraints on the measured density and energy which come from the dynamics of the system, resulting in tighter bounds on the measured value of the interaction strength.

Mean field theory predicts that the local blue shift in the energy in a condensate having repulsive particle-particle interactions is proportional to the local density of the particles. It therefore seems quite straightforward to directly fit the observed evolution of the ground state at the bottom of the ring to the density evolution of the observed polaritons at the same point in the ring. However, we find poor fits for all the data that we have analyzed if we use this method alone. An example is shown in Figure 31(b), for a 50 μm ring radius with 15 μm etch width. The oscillations in both the density and the energy are correlated in phase and period, but the amplitude of the oscillations is relatively less in the blue shift than in the density. This indicates that something else is giving rise to an additional blue shift besides the polariton-polariton interaction.

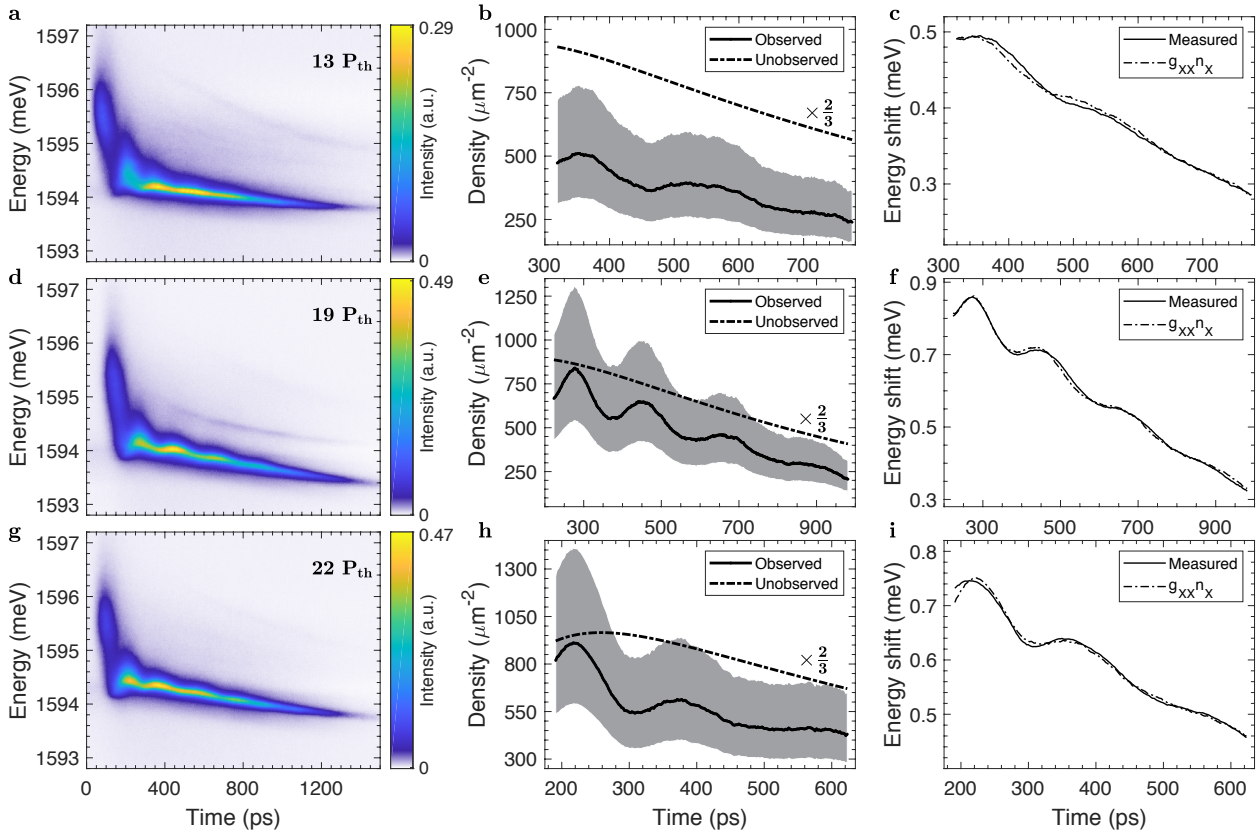

Figure 30: a, d, g) Energy-resolved PL intensity from the bottom of the ring as a function of time following a short (2 ps) laser pulse at the top of the ring. The value reported in the top right corner in each of these plots indicate approximate level of the pump power used to excite the rings. b, e, h) **Solid lines:** Oscillations in the density of observed polaritons multiplied with the appropriate exciton fraction yielding an effective density of the excitons. The shaded area is the uncertainty in the density originating from the error bounds in the measurement. **Broken lines:** Estimate of the exciton density invoked to obtain good fits to the energy shift using the mean field approach. c, f, i) **Solid lines:** Oscillations in the energy shift of the ground state measured from respective streak images. **Broken lines:** Best fit to the observed energy shift using the mean field formula by using the total density of the excitons.

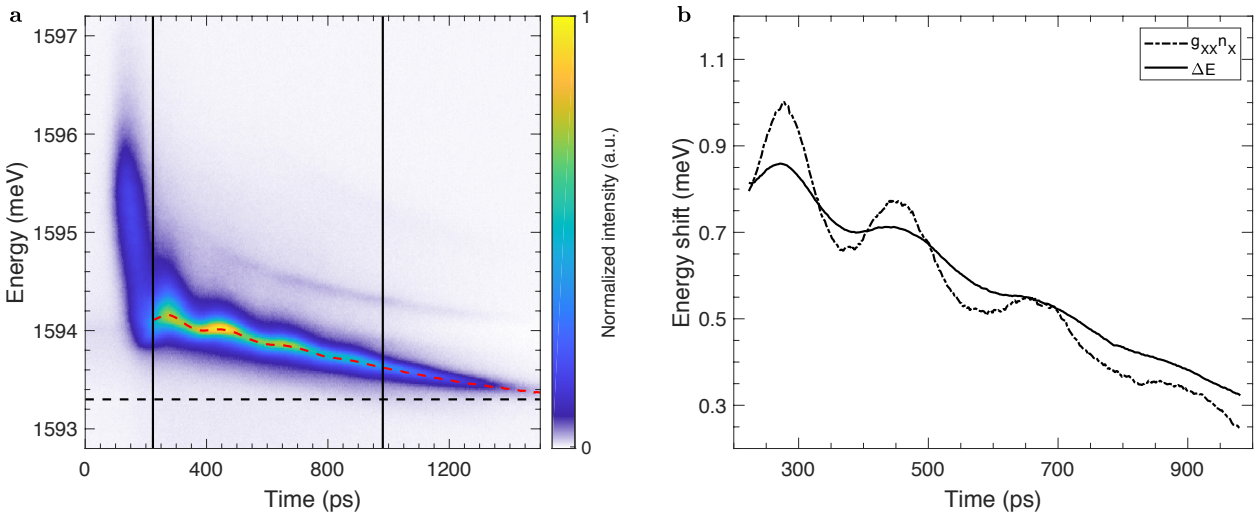

Figure 31: Example of a fit with no exciton reservoir. a) Re-plot of Figure 30(d) with red dashed lines showing the extracted energy oscillations using a Lorentzian linewidth. Black dashed lines show the reference ground state energy measured at 1593.3 meV at the bottom of this ring. Energy shift at early times is measured with respect to this value. Black solid lines show the temporal window used for fitting the density and energy oscillations. b) Black solid curve is the measured energy shift of the ground state from Figure 31(a). Broken lines is the best fit of the energy shift obtained from the observed polariton density and assuming no contribution from the exciton reservoir. The fit returns a value for $g_{XX} = 39.9$ μeVμm^2 which lies within the 95% confidence interval of (39.5, 40.3) μeVμm^2 .

As we have seen above, the oscillation frequency is dependent on the lower polariton mass near the bottom of the ring consistent with the rigid pendulum model. Therefore the cause of the oscillations in both the density and the energy data can be attributed entirely to the local changes in the lower polariton density. A reasonable conclusion is therefore that the remaining, non-oscillating energy shift arises from the polaritons interacting with a background exciton population, which must also have moved around the ring from the laser excitation spot. The presence of the exciton population will not affect the time period of the oscillations because their mass is much greater than that of the polaritons. Motion

of excitons away from the laser spot for distances of 20-30 μm has been directly verified by recent experiments [67]. Here, at least some of the excitons must have traveled 150 μm around the ring from the pump spot, which is quite surprising, because excitons in GaAs quantum wells were previously observed to migrate only a few microns away from the laser excitation region. This indicates that the placement of the quantum wells in the optical cavity to give the strongly coupled polariton effect strongly affects the effective diffusion of the excitons in the quantum wells.

The second column of Figure 30 shows the effective exciton density due to polaritons alone, found by multiplying the measured polariton density by the respective exciton fraction. As discussed above, this density is not sufficient to explain the blue shift of the ground state energy of the polaritons by a linear proportionality. Therefore, we guessed a population evolution of the (unseen) excitons at the same location as the polaritons. The simplest choice for the time dependence of this exciton population is to have a rise time and a fall time as given by

$$n_r = \tilde{n}_r\Big(1 - e^{-(t-t_1)/\tau_1}\Big)e^{-(t-t_2)/\tau_2}. \tag{3.2}$$

The parameters of this function were varied to give the best fits to the measured energy shifts, as shown in the third column of Figure 30, where the fit also gives the exciton-exciton interaction strength g_{xx}. The quality of these fits assessed from the R-squared estimator is above 99% for all the three fits. Knowing the absolute density of the polaritons from photon counting as discussed above, and the number of quantum wells (12) over which the excitons are distributed, we obtain the following values for the pure exciton-exciton interaction g_{xx}: 8.4 μeV-μm^2 with an uncertainty interval of (4.9, 14.2) for Figure 30(c), 13.5 μeV-μm^2 with an uncertainty interval of (8.4, 23.5) for Figure 30(f), and 10.2 μeV-μm^2 with an uncertainty interval of (6.1, 17.8) for Figure 30(i). The uncertainty interval is determined by adding the exciton reservoir density to the upper and lower boundaries of the observed polariton density uncertainty (shown with shaded region in the second column of Figure 30) and fitting the total density to the observed energy shift. We determined the sensitivity of g_{xx} on the reservoir density by varying the density of the reservoir used in each of these fits by changing $\tilde{n}_r$ within a reasonable range while keeping the R-squared estimator of the fits above 99%. We found a drop in the value of the estimator with an increasing spread of the fit residues,

indicating worse fits. Thus we conclude that the dynamics severely constraints our estimate of the reservoir density as well.

3.7.3 Finding the interaction strength from a streak image

The energy and time-resolved image of the PL taken by the streak camera shows how the energy distribution of the polariton states at a given location in the ring evolve with time. To make a direct measurement of the interaction strength we determine the polariton density as a function of time from the image pixel counts. This process involves two steps. The first step is to relate the counts recorded at the pixel to the number of photons leaking from the cavity. This requires a careful calibration of our optical setup at the central wavelength of PL emission. The second step involves converting the photon counts to the number of polaritons inside the microcavity using the lifetime of the polaritons. From the streak image, we find that the polaritons have a spread in their in-plane momentum. Therefore to correctly convert, we must consider the in-plane momentum dependence of the lifetime of the polaritons, which makes this conversion slightly non-trivial. In this regard, the first step is to find a mapping between the energy of the polariton and its in-plane momentum, which is usually provided by the dispersion relation of the polaritons in the microcavity. We consider the effect of the interactions between the polaritons, which renormalises their dispersion relation adding an energy correction proportional to the density at the mean field approximation level. Since the density of the polaritons changes with time, so does the energy-momentum dispersion of the polaritons.

The interactions between the polaritons originate from the exciton part and so for weak interactions, we expect the energy of the excitons to be blue shifted by $g_{\mathrm{xx}} n_{\mathrm{x}}$, where g_{xx} is the exciton-exciton interaction strength and n_{x} is the exciton density. In the absence of any reservoir of excitons (n_{res}) this will be given by $f_{\mathrm{x}} n_{\mathrm{pol}}$, where f_{x} is the exciton fraction of the polaritons, defined as $f_{\mathrm{x}}(k_{\parallel}) = \left(1 + \delta(k_{\parallel})/\sqrt{\delta(k_{\parallel})^2 + \Omega^2}\right)/2$ and n_{pol} is the density of the polaritons. Therefore the blue shift in the exciton energy (ΔE_{x}) can be expressed as

$$\Delta E_{\mathrm{x}} \sim g_{\mathrm{xx}}\Big(f_{\mathrm{x}} n_{\mathrm{pol}} + n_{\mathrm{res}}\Big). \tag{3.3}$$

$\Delta E_{\rm x}$ can be determined by diagonalizing the standard coupled Hamiltonian for the photon and exciton modes both with and without the interaction shift. Given the LP energy defined by $E_{LP} = \left[(E_C + E_X) - \sqrt{(E_C - E_X)^2 + \Omega^2}\right]/2$, the overall shift due to the change in the exciton energy is

$$E'_{\rm LP}(0) - E_{\rm LP}(0) = \frac{\Delta E_{\rm x}}{2} + \frac{1}{2}\left(\sqrt{\delta^2 + \Omega^2} - \sqrt{(\delta - \Delta E_{\rm x})^2 + \Omega^2}\right), \tag{3.4}$$

where $E'_{\rm LP}(0)$ is the interaction-shifted LP energy, and $E_{\rm LP}(0)$ is the low density LP energy, both at $k_\parallel = 0$. The Rabi splitting energy (Ω) and the detuning (δ) are determined from the sample characterization procedure. The detuning (δ) used in the above equation is the strain-adjusted detuning in the ring channel. $E'_{\rm LP}(0)$ is directly measured at each time step from the streak image by fitting the $k_\parallel = 0$ emission with a Lorentzian lineshape. $E_{\rm LP}(0)$ is found from the measurement of the LP energy under a broad and low power pump spot at the region of our interest. The above equation is numerically inverted to find $\Delta E_{\rm x}$ at each time step. It is straightforward to see that the new energy dispersion for the polaritons will have smaller radius of curvature near zone center and thus will have lighter mass.

Polariton lifetime ($\tau_{\rm pol}$) is usually given by the cavity photon lifetime ($\tau_{\rm cav}$) from the relation

$$\tau_{\rm pol} \approx \frac{\tau_{\rm cav}}{f_{\rm cav}}, \tag{3.5}$$

where $f_{\rm cav}$ is the cavity fraction of the polaritons with $k_\parallel$ dependence given by

$$f_{\rm cav}(k_\parallel) = \frac{1}{2}\left(1 - \frac{\Delta E(k_\parallel)}{\sqrt{\Delta E(k_\parallel)^2 + \Omega^2}}\right). \tag{3.6}$$

$\Delta E(k_\parallel)$ is defined as the energy difference between the cavity photon ($E_{\rm cav}$) and the exciton ($E_{\rm exc}$). For the range of $k_\parallel$ considered in our measurements, $E_{\rm exc}$ is essentially constant for varying $k_\parallel$ whereas $E_{\rm cav} \propto \sqrt{k_\parallel^2 + k_\perp^2}$. The dependence of $E_{\rm cav}$ on $k_\parallel$ leads to the dependence of $f_{\rm cav}$ on $k_\parallel$. With $\Delta E_{\rm x}$ known as a function of time, we map the LP energy for each pixel of the image to corresponding $|k_\parallel|$ value using the renormalized dispersion relation. This will help to determine the number of polaritons ($N_{\rm pol}$) in the time interval (t, t + Δt) and energy interval (E, E + ΔE),

$$N_{\rm pol} \approx \Delta N_{\rm phot} \frac{\tau_{\rm cav}}{f_{\rm cav} \Delta t}, \tag{3.7}$$

where $\Delta N_{\rm phot}$ is the number of photons counted by the camera pixel with energy between E and E + ΔE in the time interval (t, t + Δt). Putting everything together the observed polariton density ($n_{\rm pol} = N_{\rm pol}/A$) is

$$n_{\rm pol}(t) = \sum_i \frac{\Delta N_{\rm phot}(E_i,t)\tau_{\rm cav}}{A f_{\rm rep}\Delta T f_{\rm cav}(E_i,t)\Delta t}, \tag{3.8}$$

where index i runs over the energy bins, $f_{\rm rep}$ is the repetition rate of the laser and ΔT is the integration time of the image. As mentioned in the main text, the fits to the energy oscillations are poor when using only the observed polariton density. Therefore, we consider blueshift of the ground state ($k_\parallel = 0$) per particle due to polaritons and reservoir interactions which leads to

$$\begin{aligned}
\Delta E_{LP}(t) &= g_{\rm pol-pol} n_{\rm pol}(t) + g_{\rm pol-ex} n_{\rm res}(t) \\
&= \tilde{g}_{\rm xx} f_{\rm x}^0 \Big(f_{\rm x}^0 n_{\rm pol}(t) + n_{\rm res}(t) \Big) \\
&\simeq \tilde{g}_{\rm xx} f_{\rm x}^0 \Big(\sum_i \frac{f_{\rm x}(E_i,t)\Delta N_{\rm phot}(E_i,t)\tau_{\rm cav}}{A f_{\rm rep}\Delta T f_{\rm cav}(E_i,t)\Delta t} + n_{\rm res}(t) \Big) \\
&= g_{\rm fit} \Big(\sum_i \frac{f_{\rm x}(E_i,t)\Delta N_{\rm phot}(E_i,t)\tau_{\rm cav}}{A f_{\rm rep}\Delta T f_{\rm cav}(E_i,t)\Delta t} + n_{\rm res}(t) \Big),
\end{aligned} \tag{3.9}$$

where $f_{\rm x}^0$ is the low density, $k_\parallel = 0$ exciton fraction given by $(1 + \delta/\sqrt{\delta^2 + \Omega^2})/2$ and $g_{\rm fit} = \tilde{g}_{\rm xx} f_{\rm x}^0$. The term in parenthesis is the total effective density of excitons which is used to fit the energy shift in Figure 3 of main text and Figure 30 above. We considered the $k_\parallel$ dependence of the exciton fraction while calculating the effective density of the excitons from the observed polariton density. It is also noted that the above relation could be derived from Equation 3.3 and Equation 3.4 within the mean field approximation. It is quite straightforward to show $\Delta E_{LP}(t) = f_{\rm x}^0 \Delta E_{\rm x}(t) + O(\Delta E_{\rm x}^2)$ from Equation 3.4. And using Equation 3.3, we find $\Delta E_{LP}(t) = f_{\rm x}^0 \tilde{g}_{\rm xx} \Big(f_{\rm x} n_{\rm pol}(t) + n_{\rm res}(t) \Big)$ after neglecting higher order terms in density. The value of $\tilde{g}_{\rm xx}$ obtained from Equation 3.9 is related to the total density observed for all the quantum wells in the microcavity. In order to make direct comparison with the theoretical prediction of $g_{\rm xx}$ in a single quantum well, we multiply the fit value of $g_{\rm fit}$ by the number of quantum wells N_{QW} and divide by the appropriate exciton fraction.

Additionally, one may consider a contribution to the blueshift from the saturation of the exciton oscillator strength at high exciton density in the quantum wells which result in the decrease of Rabi splitting energy [136]. Since both the contributions are proportional to the exciton density, we cannot distinguish them using the measurement of g_{fit} using Equation 3.9 and g_{fit} will now be given by

$$g_{\text{fit}} = g_{\text{xx}} f_{\text{x}}^0 + g_{\text{sat}} \sqrt{f_{\text{x}}^0 (1 - f_{\text{x}}^0)}. \tag{3.10}$$

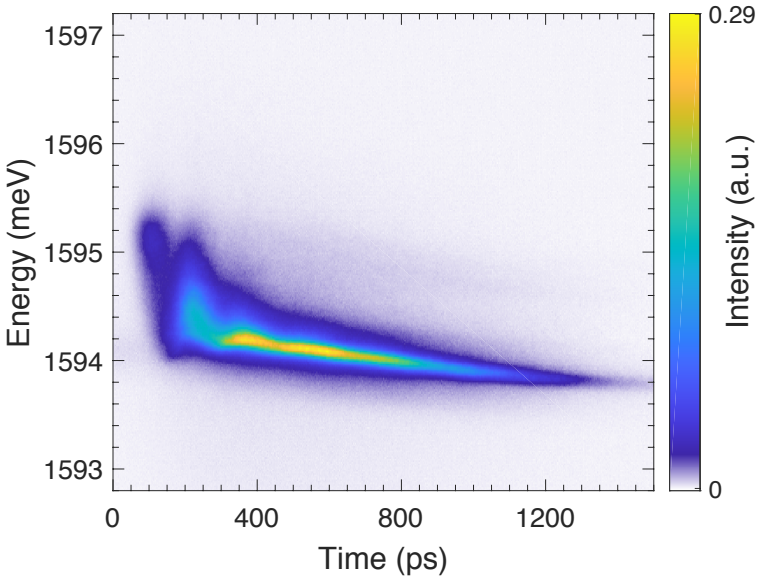

Figure 32: Photoluminescence intensity for the same conditions as that of Figure 30(a), but with the range of in-plane $k_{\|}$ collected in the experiment cut down to $-2° < k_{\|} < +2°$, using an aperture in the collection optics, corresponding to the emission from just the ground state of the ring.

3.7.4 Determining error bounds on g_{fit}

The uncertainty in the fit parameter g_{fit} arises from the measurement of the polariton density. Explicitly this depends on the intensity counts at each pixel in the CCD camera, the

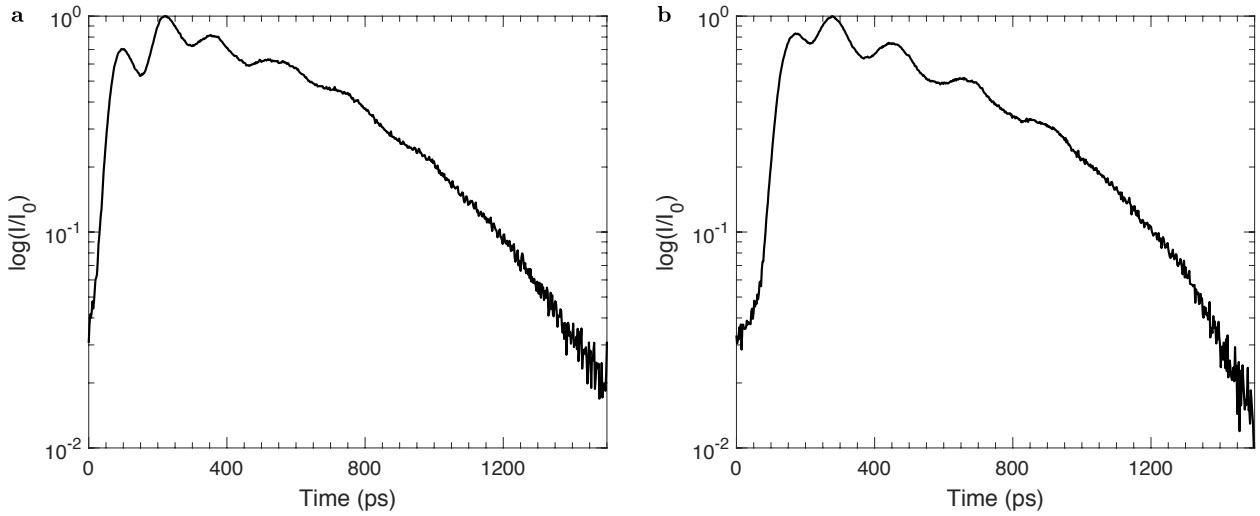

Figure 33: Normalized PL intensity plotted on a log-linear scale. (a) corresponds to the streak image shown in Figure 30(g) while (b) corresponds to the streak image shown in Figure 30(d). We do not observe any single exponential decay of the signal for regions with signal-to-noise ratio > 0.1.

conversion factor (η) to convert intensity counts to photon counts, the cavity lifetime, the absolute cavity fraction and the area of the region from where the PL has been measured. Uncertainty in the intensity recorded by the pixels of the CCD are related to the random noise which follows a normal distribution with full width half maximum of 22 counts. η is the photon collection efficiency of our setup, which was determined by sending a known power of light at the same wavelength as the polariton PL through the setup from the location of the sample, and then imaging it in the same way that the data is collected during an actual experiment. For our setup and typical image parameters, this was 151 ± 11 photons/count. The cavity lifetime (135 ± 10 ps) used in this study was previously estimated for a similar microcavity structure [54]. We could not establish a good estimate for the polariton lifetime from the streak images because it did not show a single exponential decay, even for very late times (see Figure 33), which is an indication for the presence of an exciton reservoir.

Together the spectrometer slit and the time slit of the streak camera selected a rectangu-

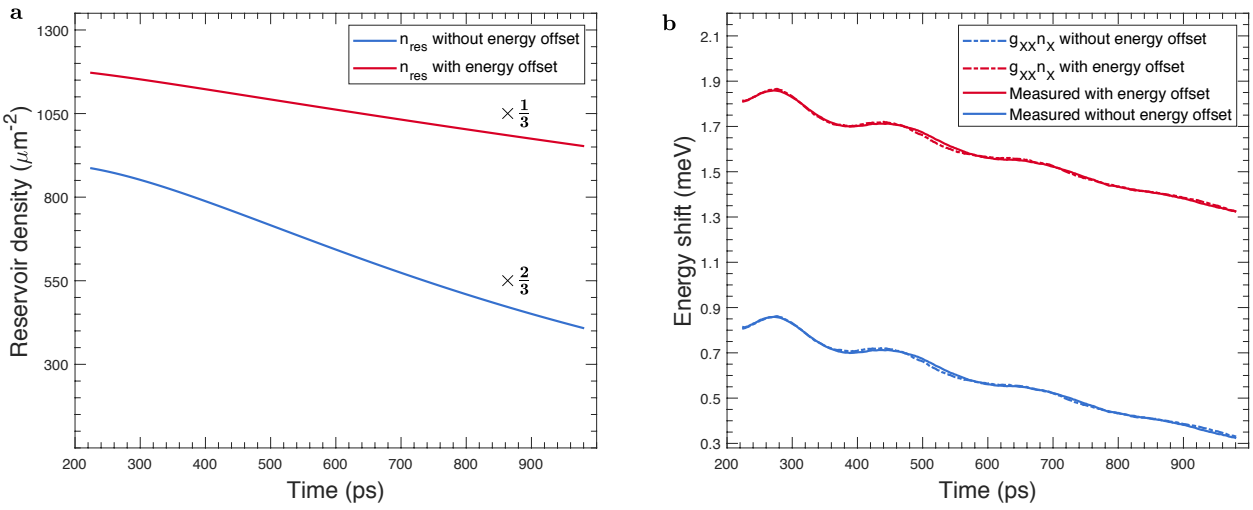

Figure 34: Comparison of fits with and without an energy offset to $E_{LP}(0)$. (a) The red curve shows the new density of the reservoir used to obtain a good fit as shown in (b). The blue curve is the re-plot of the reservoir density from Figure 30(e) in main text. (b) Fit to the measured energy shift with (red solid lines) and without (blue solid lines) an energy offset of 1 meV using the observed polariton density (as plotted in Figure 30(e)) and the reservoir density in (a). The value of g_{XX} obtained from the new fit is 14.5 μeVμm^2 which is within the error bounds $(8.4, 23.5)\mu$eVμm^2 as reported in the main text. This shows that any constant energy shift due to the presence of reservoir does not affect our measurement of g_{XX} due to the constraints from the dynamical feature in the data.

lar region from the image of the PL which corresponded to a collection area of 53.94 $\pm$ 3.72 μm^2 on the sample. The uncertainty in determining the absolute cavity fraction is related to the uncertainty in the sample characterization as discussed in the Appendix of Ref. [67]. These uncertainties are used to find an upper and lower bound on the observed polariton density as shown by the shaded area in Figure 30. Another source of uncertainty arises from the choice of the unobserved exciton reservoir density. We extensively varied the density of the reservoir to determine the best fits to the energy shift. The density of the exciton reservoir shown in Figure 30 corresponds to these best fit cases. It must be noted that any error in part of finding the energy shift due to the uncertainty in finding the ground state energy

of the polaritons is compensated by the assumption of invoking a reservoir density and the value of $E_{LP}(0)$ only determines an offset of the energy, without affecting the oscillations. As a demonstration of this notion we compare the fit obtained in Figure 30(f) with the fit where the measured energy shift is offset by 1 meV. By choosing an appropriate reservoir density we obtained best fit with nearly identical value of the fit parameter (see Figure 34). The uncertainty in measuring $E'_{LP}(0)$ at a given time slice obtained from the 95% confidence interval of the Lorentzian fits are small (< 50 μeV) and is therefore neglected.

3.7.5 Theoretical model

To model the oscillations in the PL from the condensate at the bottom of the ring as shown in Figure 24(b) in main text, we employ the open-dissipative Gross-Pitaevskii (ODGPE) model [137] with a phenomenological kinetic damping term α, a spatially homogeneous generation term with temporal rise and fall behavior G(t) and an effective loss term Γ(t) to account for the overall decay of the total population:

$$i\hbar\frac{\partial\psi(\theta,t)}{\partial t} = \left[-(1-i\alpha)\frac{\hbar^2\bigtriangledown^2}{2m} + \frac{V_0}{2}(1-\cos(\theta)) + g_{1D}|\psi(\theta,t)|^2 + iG(t) - i\Gamma(t)\right]\psi(\theta,t), \tag{3.11}$$

where $\theta \in [-\pi,\pi]$ and $\theta = 0$ is the lowest energy point in the ring. We choose $G(t)$ of the form $G_0(1-exp(-t/\tau_1))exp(-t\tau_2)$ to approximately match the rise time of the PL intensity and $\Gamma(t)$ of the form $\Gamma_0(1-exp(-t/\tau_3))$ to match the particle loss rate at later times. We note that the inclusion of the kinetic damping term not only damps the motion of the condensate about the bottom of the trap, but also results in additional particle loss. We correct for this by appropriately renormalizing the wavefunction in our calculation to obtain only the overall loss implied by the terms in $G(t)$ and $\Gamma(t)$. It is useful to transform the above equation into its dimensionless form by introducing $x_d = x/a_0$, $t_d = \omega t/2\pi$ and $\psi_d = \sqrt{a_0/N}\psi$, where $a_0 = \sqrt{\hbar/m\omega}$ and $\omega = \sqrt{V_0/2mR^2}$ are the natural length scale and the natural angular frequency of the harmonic oscillator potential associated with the bottom of the ring potential respectively. We also choose to work on a linear geometry by unwrapping the co-ordinates on the ring using the relation $x = R\theta$. The dimensionless

equation then takes the form

$$i\frac{\partial\psi_d}{\partial t_d} = \left[-(1-i\alpha)\pi\frac{\partial^2}{\partial x_d^2} + \frac{\pi V_0}{\hbar\omega}(1-\cos(a_0 x_d/R)) + \frac{2\pi g_{1D}N}{\hbar\omega a_0}|\psi_d|^2 + iG_d(t_d) - i\Gamma_d(t_d)\right]\psi_d, \tag{3.12}$$

where $x_d \in [-\pi R/a_0, \pi R/a_0]$, G_d and Γ_d are the appropriate dimensionless gain and loss functions. We choose a dimensionless gaussian wavefunction with a variance of σ centered at $\theta = 0$ with unity norm defined on the domain of x_d as the initial condition

$$\psi_d(x_d, 0) = \frac{1}{\sqrt{\sigma\sqrt{\pi}\,\mathrm{erf}(\pi R/\sigma a_0)}} e^{-x_d^2/2\sigma^2}. \tag{3.13}$$

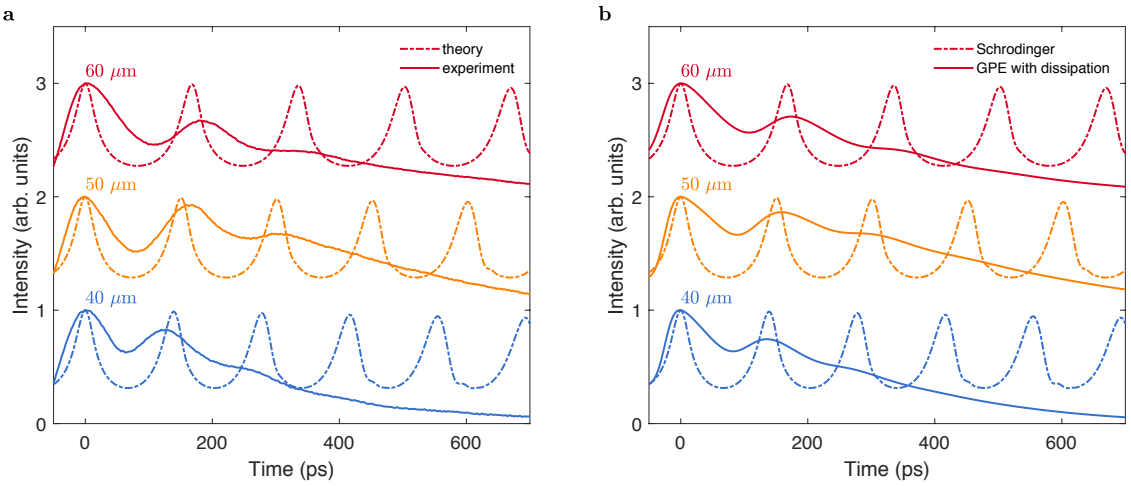

Figure 35: Time evolution of the polariton condensate density at the bottom of the ring. (a) Broken lines show the evolution under the Schrodinger operator and the solid line compares the observed PL intensity. (b) We make a direct comparison between the two theoretical models and show that the simpler model can capture the oscillation time period as long as the potential trap is not reshaped at higher polariton density. We also notice that, while when neglecting the interaction term the density peaks are narrower than the experimental ones, when turning the repulsive interaction on they become broader and their width increases with increasing interaction strengths.

R (μm)	$\omega\tau_1/2\pi$	$\omega\tau_2/2\pi$	$\omega\tau_3/2\pi$	$2\pi G_0/\hbar\omega$	$2\pi\Gamma_0/\hbar\omega$	α	σ
60	0.20	0.6	0.5	1.0	1.0	0.8	5
50	0.20	0.6	1.5	1.0	1.0	1.1	6
40	0.15	0.6	0.5	1.0	0.9	1.1	5

Table 2: Parameter values used in the simulation for Figure 24(b) in the main text.

This initial condition is propagated forward in time according to the dimensionless ODGPE defined above with $g_{1D}N = 0.25$ μeV-mm and the parameters for the generation and loss functions with the damping coefficient as listed in Table 2.

The results from this simulation (in Figure 24(b)) match reasonably well with the oscillation amplitudes with the typical ring parameters given in Table T1. We also compare these results with the linear case when the time evolution is only under the ring potential term and find that the time periods are in good agreement with each other as shown in Figure 35. This underlines the dominant role played by the ring trap potential in determining the oscillations period we observed here.

3.7.6 Evidence of the exciton reservoir at low density

To further investigate the hypothesis of a reservoir population away from the pump spot we performed an experiment where we excited a piece of the planar microcavity sample with a low power, non-resonant CW laser and tightly focused at the plane of the sample. The pump power was below the threshold power (P_{th}) needed to observe polariton condensation. This sample was part of the same wafer which was used to fabricate the rings. In these experiments we searched for PL emission from lower polariton states at high in-plane momentum. We typically don't see this emission because it is outside the NA of our microscope.

We placed the cryostat on a rotation stage as shown in Figure 36 and measured one-sided energy- and momentum-resolved PL emission. We pumped through the microscope objective as shown in Figure 18. By comparing the relative polariton population below and

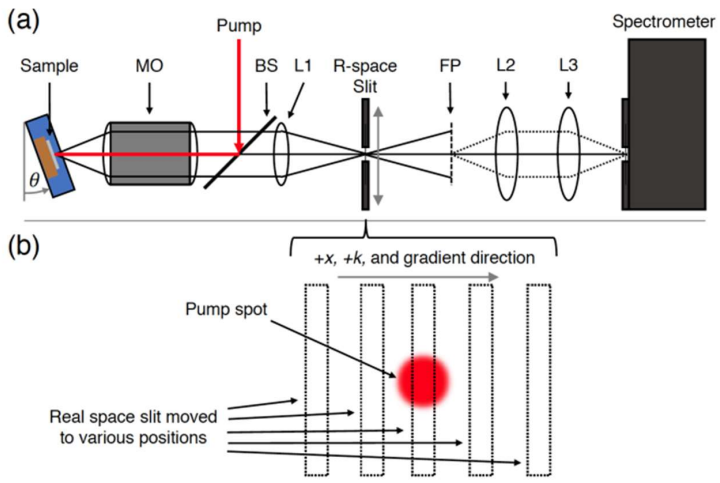

Figure 36: (a) A diagram showing the basics of the optical setup, viewed from above. The sample was mounted in a cold-finger cryostat, which could be rotated by angle θ. The pump laser was reflected off a beam splitter (BS) through the imaging microscope objective (MO). The photoluminescence was collected by the objective and then imaged by lens L1 onto a secondary real-space plane. At this plane, a movable slit (R-space Slit) was placed to select regions of the sample from which to resolve photoluminescence. The Fourier plane of the objective was also imaged by lens L1 at location FP. Lenses L2 and L3 then imaged this secondary Fourier plane onto the slit of the spectrometer. (b) A diagram of the real-space plane at the location of the slit (R-space Slit in (a)) as viewed along the imaging axis. The slit could be moved horizontally to select different regions of the image without changing the pump location. The +x; +k, and cavity gradient ("uphill") directions are all the same.

above the inflection point at $k_{\|} = 2.6\mu m^{-1}$, we determined the population of the bottleneck polaritons ($5.5\mu m^{-1} > k_{\|} > 2.6\mu m^{-1}$). The bottleneck polaritons have significantly different mass than the polaritons near $k_{\|} = 0$ and are therefore assumed to have a different diffusion length. The discovery of these states away from the location of creation of the polaritons by the laser, provides an evidence of the transport of polariton states with high in-plane momentum. The dispersion of the polaritons are shown in Figure 37. It should be noted

that these states are occupied all the way to the maximum limit of the NA of our setup. It is reasonable to assume that these states are also occupied beyond this cut-off $k_{\|}$.

The relative number of polaritons occupying the high $k_{\|}$ branch of the dispersion as a function of distance from the pump spot are also shown in Figure 38. This real space distribution is fit with a Voigt distribution [67] and a diffusion length of 20 μm is deduced.

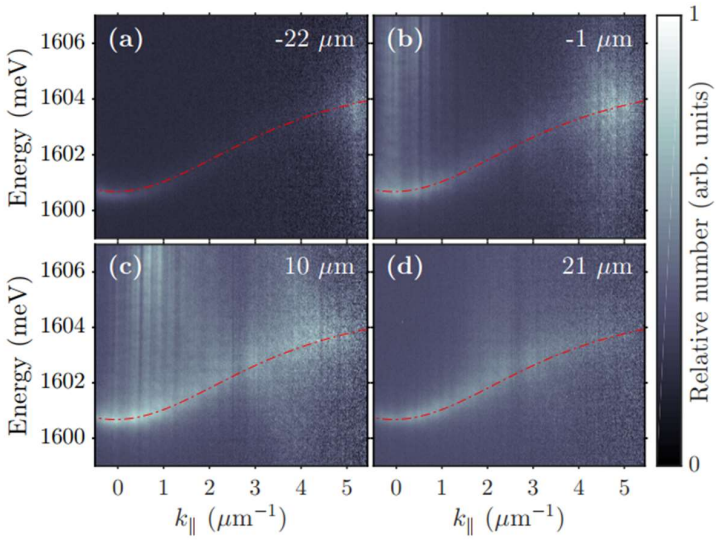

Figure 37: Normalized lower polariton population as a function of energy and momentum, taken from angle-resolved images and adjusted for the momentum-dependent photon fraction to show the relative particle populations. The pump power was about $P_{th}/2$, where P_{th} is the threshold pump power for forming BEC, and the detuning was about 8 meV. The positions of the real-space filter with respect to the pump spot are given in the upper right corners of each plot. The red lines show the theoretical lower polariton dispersion. The counts for each image were normalized separately, so the counts of separate images are not comparable.

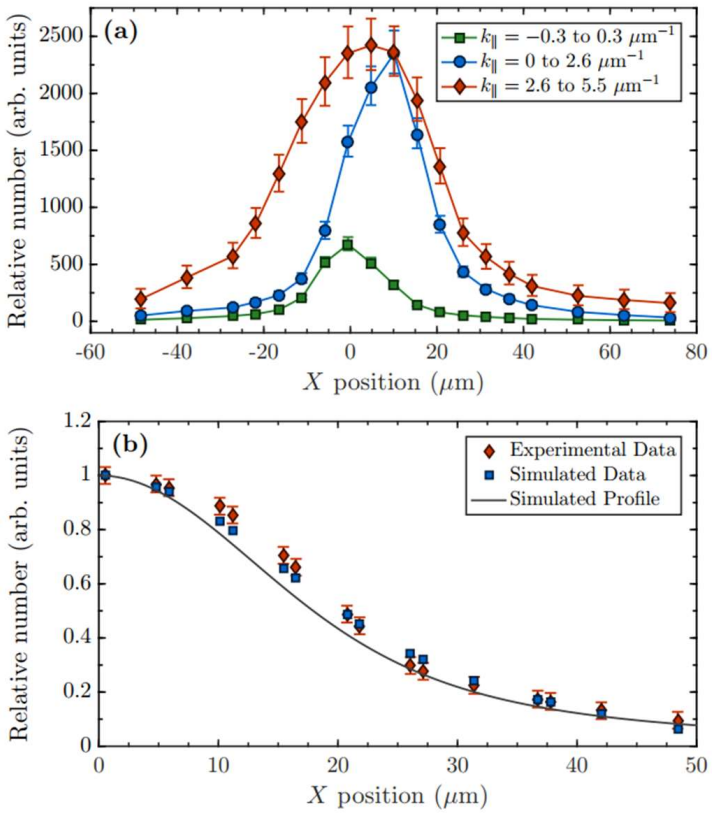

Figure 38: (a) The relative number of particles within the lower polariton band as a function of the real-space filter position for various ranges of $k_\parallel$ for a pump power of about $P_{th}/2$ and detuning of about 8 meV. The zero point in position was set by looking only at the symmetric range of visible $k_\parallel$ near $k_\parallel = 0$ (green squares). (b) The experimental data (red diamonds) are the sum of the relative numbers at opposite sides of the pump spot (opposite x positions) for the $k_\parallel$ range of 2.6 to 5.5 μm^{-1}, shown as red diamonds in (a). The simulated profile (solid black line) is the Voigt profile representing the real-space distribution of the bottleneck excitons, which was normalized to show its shape compared to the data. The simulated data (blue squares) came from integrating the Voigt profile over small bounds in X, simulating the effect of the real-space slit in acquiring the experimental data. For details about the error bounds, see Appendix of Ref. [67].

4.0 Spin dynamics of a polariton condensate

4.1 Motivation

In this chapter we will consider another aspect of a dilute polariton gas which make them behave as a spin-1/2 Bose gas. This behaviour is at the heart of several experimental studies on optical spin Hall effect. First proposed by Kavokin, Malpuech and Glazov [138] in 2005, the optical spin Hall effect originates due to the spin dependent elastic scattering of exciton-polaritons. Two years later after the proposal, this effect was observed in a short lifetime planar microcavity with embedded GaAs quantum wells [71]. As the polaritons are detected from the light leaking from the microcavity, information regarding the spin state of the polaritons is made from the polarization of the emitted light. Thus, the manifestation of the optical spin Hall effect lies in the observation of angle dependent polarized emission from the microcavity.

Exciton-polariton systems naturally offer a way for describing a pseudo-spin 1/2 Bose gas [99]. The order parameter of a polariton condensate is described by a two-component complex valued spinor, which is connected to the electric polarization of the polaritons in the microcavity [40]. The pseudo-spinor describes polarization states of the polaritons in the microcavity. The lowest energy exciton in a GaAs quantum well has total angular momentum $J = 1$ which couples with photons. The projection $\pm\hbar$ along the crystal growth axis forms the two components of the polariton spinor (chapter 9 of Ref. [99]). In the presence of a non-aligned magnetic field the spin of the polaritons precesses similar to the spin of an electron in a magnetic field. It results in polarization patterns of an expanding polariton gas and this phenomenon is known as the optical spin Hall effect [71, 139]. It turns out that for a quantum well embedded inside a semiconductor microcavity, a small but non-negligible momentum dependent effective magnetic field is present which lies in the plane of the quantum well. This effective field is excitonic in origin and is different than the Rashba and Dresselhaus field and arises due to the long range electron-hole exchange interaction of the exciton [140]. This has been used to realize a polaritonic analog of extrinsic [71] as

well as intrinsic [139] spin Hall effect. In contrast to the electronic systems where the spin Hall effect gives rise to a spin current and no mass transport, the optical spin Hall effect is realized by actual transport of polaritons while the spin of the polaritons precess as they move.

Figure 39 shows an example of the dispersion of the polaritons with a large photonic fraction. The dispersion shows an energy splitting of about 1 meV at high $k_{\|} \approx 5.5\mu m^{-1}$. Clearly this energy splitting depends on $k_{\|}$ and is absent (or negligible) for $k_{\|} \approx 0$. These branches of the dispersion can be interpreted as the TE (transverse electric) and TM (transverse magnetic) modes inside the microcavity having slightly different effective masses. These branches are a combined result of the effective field acting on the excitonic part of the polariton in the quantum well and the difference in the reflectivity of the TE and TM polarizations of the photonic component of the polaritons at oblique angle of incidence [141]. In analogy to a spin-1/2 electron in a magnetic field, the degenerate spin states are split, where the splitting energy is proportional to the magnitude of the magnetic field. Similarly, we can think of the splitting of the polariton states as due to an effective magnetic field which depends on the in-plane momentum and is proportional to $k_{\|}^2$.

In this chapter we address how the two spinor components of a gas of highly excited trapped polaritons evolve following a quench in a long lifetime ($\approx$ 200 ps) microcavity. The trapping potential is created by patterning the top mirror of the GaAs microcavity in the shape of a ring. The polaritons in the ring maintain the same long lifetime ($\approx$ 200 ps), high quality ($Q > 10^5$) and low disorder as in the two-dimensional planar microcavity used previously [86, 54, 142, 47, 79]. With the presence of a unidirectional gradient in the energy of the polaritons, the circular symmetry of the ring is broken, giving rise to a rigid pendulum potential. Combined with a momentum dependent effective magnetic field in the trap, this results in intrinsic optical spin Hall effect as the polaritons are transported to the region with the lowest energy in the trap. We map the spin of the condensed polaritons in the ring using space- and time- resolved polarization spectroscopy.

The rings used in this study were fabricated by etching the top distributed Bragg reflector (DBR) of the microcavity as described in previous chapters. Further details may be found in the papers [79, 67, 68]. The rings of width (the difference of the outer and the inner

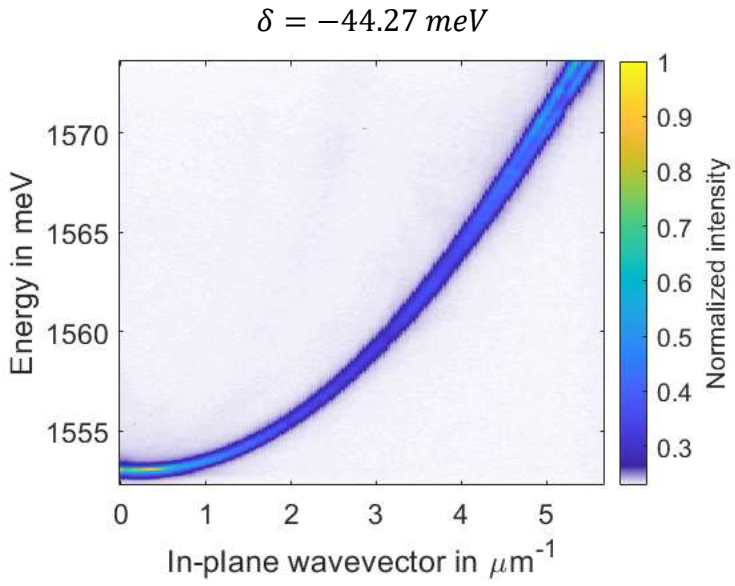

Figure 39: Lower polariton dispersion in a planar microcavity showing the TE-TM branches. The PL is collected from a portion of the microcavity wafer with detuning $\delta = -44.27$ meV.

radii) 15 μm and radius (average of outer and inner radii) 50 μm was chosen for the study. Across the typical dimensions of the ring, the thickness of the microcavity varies which leads to a cavity energy gradient ($\approx 7-9$ meV/mm). The cavity gradient effect is similar to an artificial gravity for the polaritons making the rings look tilted on the potential energy plane. Due to the analogy to gravity, here we will refer to the point of highest potential energy as the "top" of the ring, and the point of lower potential energy, on the opposite side of the ring, as the "bottom". The effect of the artificial gravity on the spin-polarized polaritons have been theoretically studied in Ref. [143].

This chapter is an adaption of the work in Ref. [144]. The polariton rings were fabricated by Burcu Ozden. Jonathan Beaumariage, Mark Steger and David Myers performed characterization of the microcavity grown by Loren Pfeiffer and Ken West. Valerii Kozin and Anton Nalitov developed the theoretical model. I designed the experiment, performed the measurements and carried out numerical simulations. The project was supervised by David Snoke.

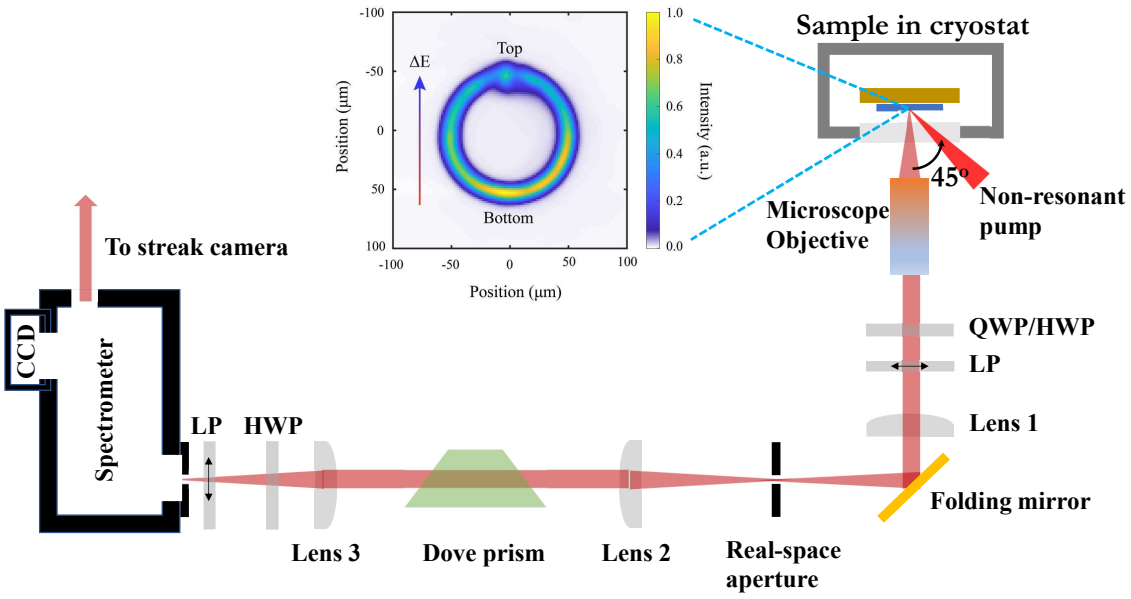

Figure 40: Schematic of the experimental setup. Inset shows a time integrated image of the photoluminiscence from the ring microcavity also showing the direction of the cavity gradient ΔE. QWP: quarter waveplate, HWP: half waveplate, LP: linear polarizer.

4.2 Experiment

The top of the rings are non-resonantly pumped ($E_{\text{pump}} \approx 1710$ meV which is at least 100 meV higher than the energy of the lower branch polaritons at the point of excitation) with a mode-locked Ti:sapphire laser with a pulse repetition rate of 76 MHz, a pulse width of ≈ 2 ps, a spot size of ≈ 15 μm on the sample and incident at an angle of $\approx 45°$ from the plane of the sample with more than 90% linear polarization. Due to the high angle injection, the pump spot is not circular on the plane of the sample and creates asymmetry in the direction of the polaritons streaming from the pump spot. Photoluminescence (PL) from the rings was collected using a microscope objective with a numerical aperture (NA) of 0.40 and imaged onto the entrance slit of a spectrometer. The image was then sent through the spectrometer either to a standard charged coupled device (CCD) chip located at one of the exit ports of the spectrometer for time integrated imaging, or onto a Hamamatsu streak

camera located at the other exit port for time-resolved imaging. All measurements were performed by cooling the microcavity to low temperature (below 10 K) in a continuous-flow cold-finger cryostat. A sketch of the experimental setup is shown in Fig. 40.

The non-resonant optical pulse excites a population of free electrons and holes at the top of the ring which undergo rapid thermalization, turning into excitons. Excitons further relax down in energy and reach the anti-crossing spectral region of the photonic and excitonic dispersion branches, forming a dense polariton gas (see, for example, Tassone et al. [62]), which above a critical density undergoes non-equilibrium Bose-Einstein condensation. This non-equilibrium condensate streams out ballistically from the excitation spot and fills the entire ring, while also dropping in energy as it moves in the ring. Energy resolved streak images from the top and bottom of the ring are combined together in Fig. 41 (c) for direct comparison. As shown in Fig. 41 (c) the polaritons are initially formed with a large blue-shifted energy at the pump spot which rapidly red shifts with time. This is followed by a spectrally narrow emission which slowly drops in energy, asymptotically approaching the $k_{||} = 0$ lower polariton energy at this location. The initial blue shift seen at the pump spot is due to the interaction of polaritons with the exciton cloud. The rate of energy drop of the polaritons measures the rate at which the exciton cloud decays. By the time the polaritons arrive at the bottom of the ring trap it has already undergone considerable energy relaxation (≈ 2 meV). The energy- and time- resolved image from the bottom in Fig. 41 (c) shows that as the occupation density of the polaritons increases, the spectral linewidth of the emission narrows indicating build up of coherence in the bottom of the trap. In Fig. 41 (a) and (b) we show spatially and temporally resolved energy and linewidth of the emission from the bottom of the trap. From these plots we infer that the spatial coherence extends at most to one-third of the ring circumference at any given point in time, which is signaled by the energy locking of the emission. At late times the energy of the emission approaches the local, low density $k_{||} = 0$ lower polariton energy.

We resolved the polarization of the PL from the ring by performing a full Stokes vector measurement (S_0, S_1, S_2, S_3) using combinations of half or quarter waveplate and a linear polarizer. The measurement was done on the collimated signal just after the microscope objective. The transmission axis of the polarizer was chosen to be vertical in the lab frame

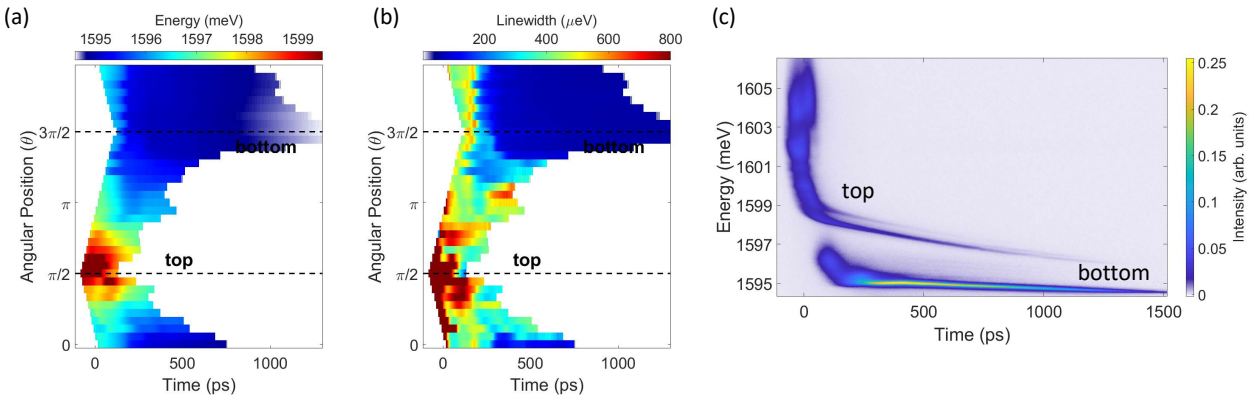

Figure 41: Example of condensate energy (a) and linewidth (b) as a function of time from different locations on the ring. $3\pi/2$ corresponds to the bottom of the ring. The zero of the time axis corresponds to the time of excitation at the top of the ring. The condensate energy is obtained at each spatial location by fitting a lorentzian function to the energy- and time-resolved image captured by the streak camera. (c) shows a spectral comparison between the PL emission from the top and bottom of the ring as a function of time.

and was kept fixed throughout the experiment. This was done to remove the polarization sensitivity of the optics downstream in the setup. We used another half waveplate and a polarizer before the entrance slit of the spectrometer to collect all the signal which didn't get reflected, scattered or absorbed after passing through the optics. For all the measurements the orientation of the transmission axis of the final polarizer was also kept fixed, which removed the polarization sensitivity of all the optics inside the spectrometer as the light that entered the spectrometer was always at a fixed linear polarization. Two images were taken for each individual measurement, one with the half waveplate fast axis (placed just before the final polarizer) at 0° and one with it at 45°. By adding these two images together, the total contribution of both polarizations (both parallel and orthogonal to the final polarizer) were taken into account. Additional details on the full Stokes vector measurement are given in Supplementary information 4.5.2.

Time-resolved Stokes vector measurements were done using the streak camera. Mapping of the observed intensity to the Stokes vector is given in Supplementary information 4.5.2.

A diametric slice of the image of the ring was aligned with the horizontal time slit of the streak camera. To collect the PL from a different location on the ring, the image was rotated using a dove prism. The dove prism was placed in a nearly collimated region of the optical path, as shown in Fig. 40. Before the experiment, the dove prism was carefully aligned to minimize the image walk-off when the prism was rotated by adjusting the tilt screws on the mount. Small adjustments were made during data collection by moving the final imaging lens, Lens 3, in the transverse plane to ensure consistent overlap of the diametric slice of the ring with the time slit.

We note that the intensity collected by the streak camera after a pulsed excitation of the ring is the sum of the intensity of millions of such realizations. The density of polaritons created by each pulse was above the critical density of polaritons required for undergoing Bose-Einstein condensation (BEC) at the given temperature. If the realization of each instance of the BEC picks up a random polarization state in the ring (due to spontaneous symmetry breaking), then by averaging we should obtain a strong component of unpolarized light in the emission. However, from previous time resolved studies on spontaneously formed polariton BEC it is known that the polarization of the BEC is not random and is sensitive to underlying crystal symmetries and other symmetries or imperfections of the microcavity. Due to the sensitivity of the polarization of the polariton BEC we can use the degree of polarization of the PL to distinguish between emission from condensed and uncondensed or excited polaritons.

We compare the time resolved polarization of the PL emission from the point of excitation (top) and the diametrically opposite point (bottom) on the ring in Fig. 42. We find a rapid build up of the degree of polarization (DOP $= \sqrt{S_1^2 + S_2^2 + S_3^2}$) of the emission at the pump spot following the arrival of the pump pulse. This is correlated with a decrease in the PL emission intensity at the pump spot. This signal is post hot thermalization and indicates appearance of a local non-equilibrium condensate which undergoes further energy relaxation. As the condensate streams and fills the ring, the DOP plateaus. At the same time, there is a slow build up of the polarized emission from the bottom of the ring which persists as long as the polaritons leak from the microcavity. In contrast, the DOP drops at the pump location after plateauing because the condensate drifts away from this location

towards the bottom of the ring. The oscillations in the intensity of the PL emission from the bottom of the ring is due to the pendulum like oscillations about the ring trap minimum [68].

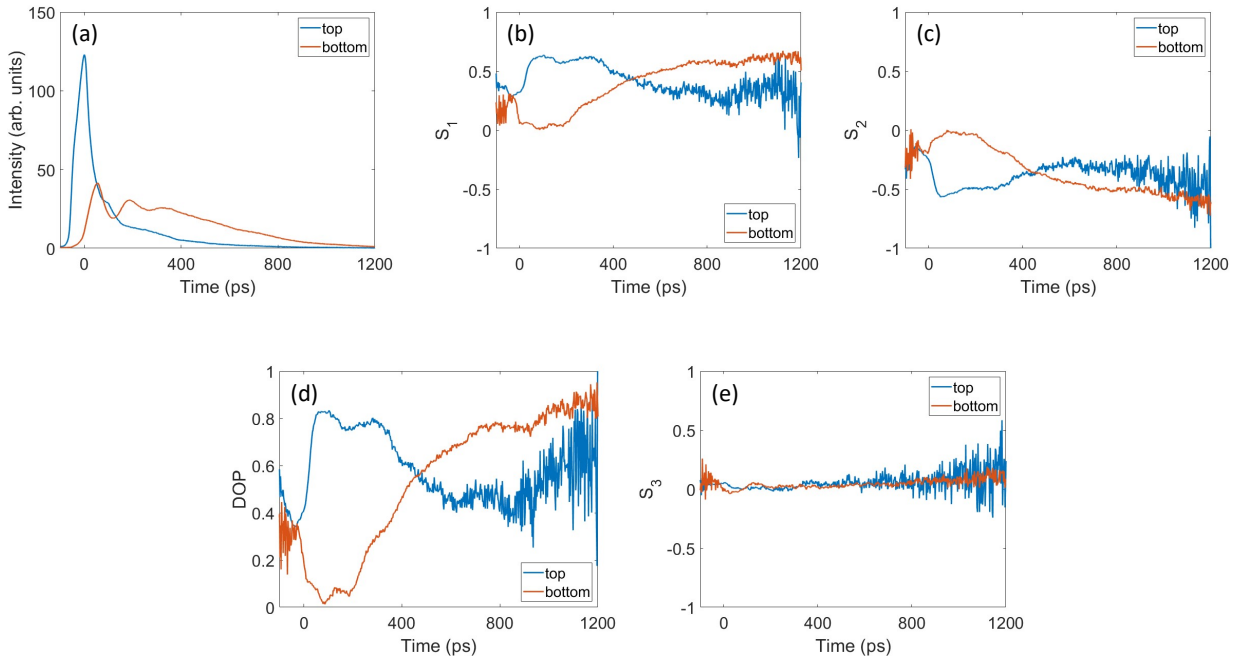

Figure 42: Comparison of the polarization between the top and bottom of the ring as a function of time. Degree of polarization (DOP) is given by $\sqrt{S_1^2 + S_2^2 + S_3^2}$.

Measurement of the time-resolved components of the Stokes vector from different angular positions on the ring are shown in Fig. 45 and a Bloch vector visualization at different time instances are shown in Fig. 46. The circular polarization component S_3 in these measurements reveal that before the appearance of condensate in the ring, highly excited non-thermal polaritons moving out from the pump spot show spin imbalance polarity depending on whether they are moving in the clockwise or anti-clockwise direction. This is due to the polariton pseudo-spins experiencing the effect of the in-plane magnetic field arising due to the splitting of the transverse electric (TE) and transverse magnetic (TM) mode in the cavity and depending on the polariton wave-vector. It is easily verified in a simulation showing the time evolution of a linearly polarized wavepacket under the TE-TM splitting Hamiltonian and is shown in Figure 48.

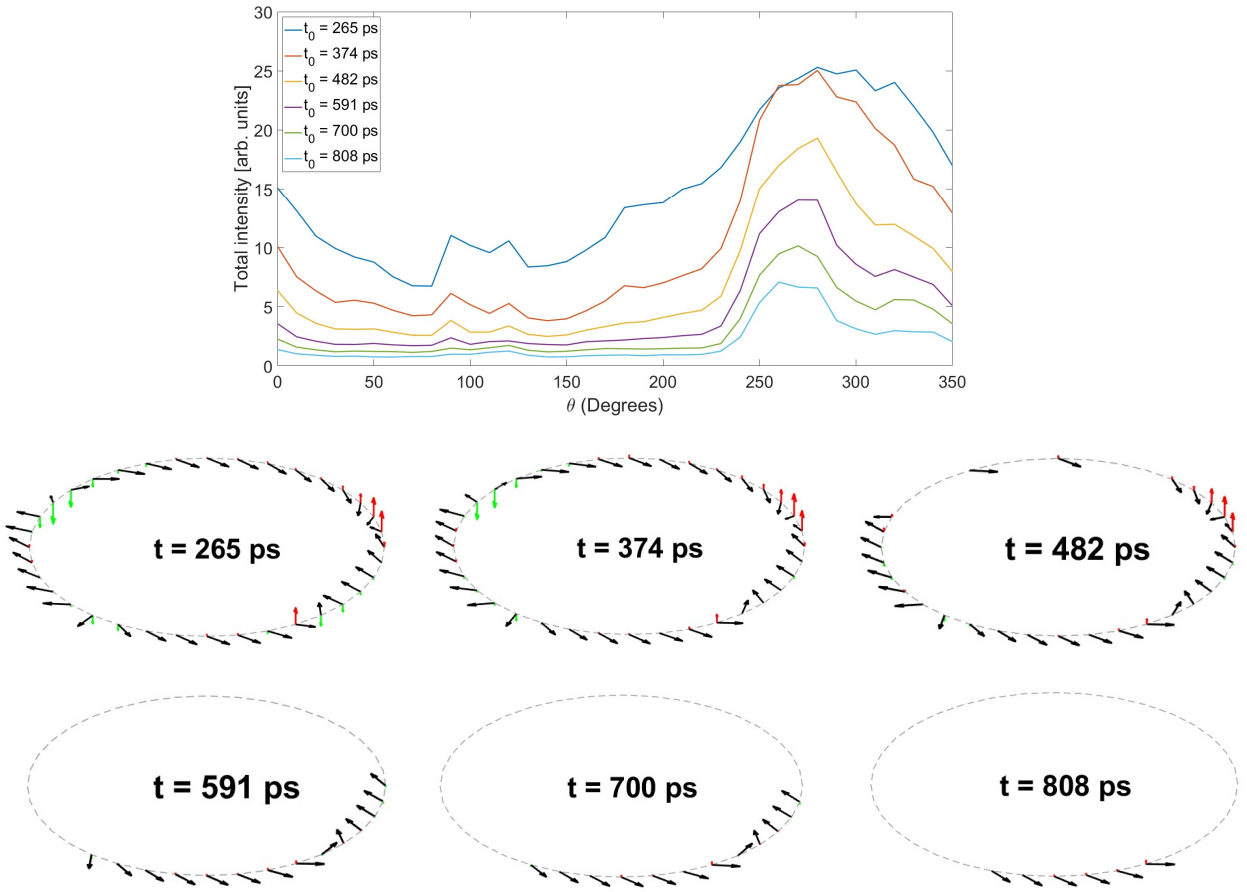

Figure 43: PL intensity from the ring at different time instances t_0 and the corresponding polarized emission shown with the Bloch sphere representation of the Stokes vectors at different angular positions on the ring. Black arrows depict the projection of the Stokes vector on the equatorial plane of the Bloch sphere. The length of the arrow is a measure of the degree of linear polarization within the polarized sector of emission and half of the angle w.r.t. the positive x-axis measures the direction of the linear polarized light. The red and green arrows depict the spin up and spin down projection of the polariton spinor respectively. The length of these arrows indicate the degree of circular polarization (or spin polarization) of the polaritons. Stokes vectors for intensity below a cut-off level ($I_{cut} = 3$) is not plotted due to poor signal to noise ratio.

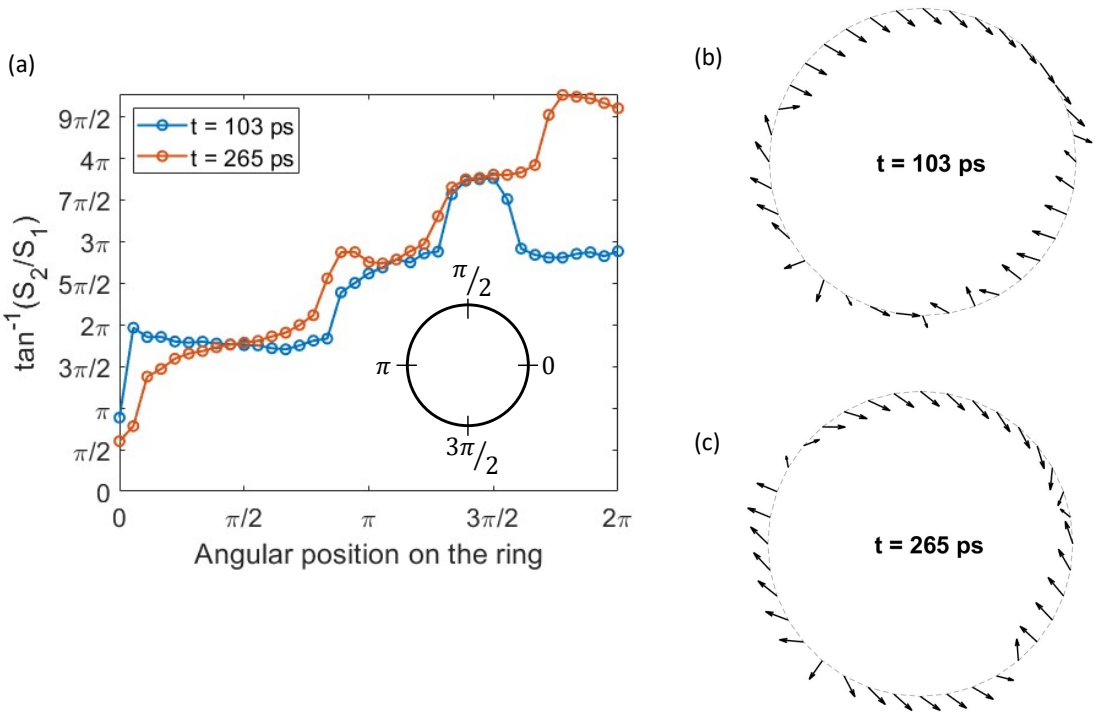

Figure 44: (a) The direction pointed by the linearly polarized Stokes vector $S_1\hat{x}+S_2\hat{y}$ around the ring at two time instances. The angle $\tan^{-1}(S_2/S_1)$ has been unwrapped in the range $[0, 6\pi]$. (b) and (c) show the linearly polarized Stokes vector in the ring at t = 103 ps and t = 265 ps respectively.

The linear polarization components S_1 and S_2 show a spontaneous emergence of four-leaf angular pattern as shown in Fig. 45 (b) and (c). This pattern persists in the ring until the polaritons fully leak from the microcavity. Manifestation of this pattern could be visualized by representing the Stokes vector on the Bloch sphere and tracing it around the ring. The projection of the Stokes vector on the equatorial plane of the Bloch sphere gives the component of linear polarization of the emission. This is shown in black arrows in Fig. 43 at different time instances. We see in these figures and in Fig. 44 that after t = 265 ps, the linear polarization component appears to wrap around the ring by 4π radians, which corresponds to a rotation by 2π radians for the major axis of the elliptically polarized

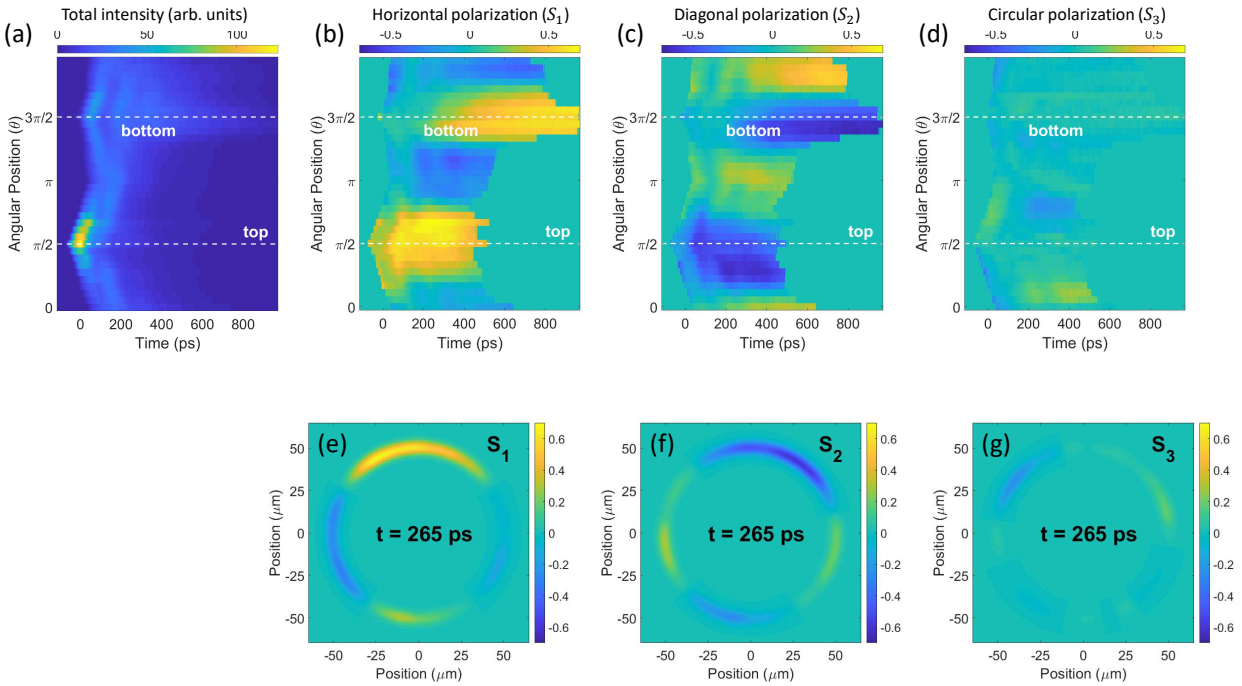

Figure 45: Example of time and polarization resolved PL from tilted ring. Components of the Stokes vector S_0, S_1, S_2 and S_3 measured at an angular resolution of 10° as a function of time. We integrated the polarization resolved PL over the radial width of the ring to process the Stokes components at any given angular position on the ring. The intensity collected by the streak camera after a pulsed excitation of the ring is the sum of the intensity of millions of such realizations. Bottom row shows the four-leaf pattern in the components S_1 and S_2 at t = 265 ps.

emission from the ring. In Fig. 44 we compare the direction of the linear polarization of the Stokes vector from different angular positions in the ring at two different time instances. The wrapping of the linear polarization component by 4π radians is found at t = 265 ps, while it only wraps by 2π radians at t = 103 ps. The linear polarization component forms domains in the ring where the direction changes slowly within a domain while across a domain there is a change in the direction by $\pm\pi/2$ or more. The direction of the linear polarization component from the lower half of the ring remains nearly stationary in time after t = 265 ps. This is despite the fact that there is noticeable angular variation of the intensity of emission from

this region with time as shown in S_0 component in Fig. 45 (a) as well as in Figure 43. Both spatial and temporal dependence of the PL intensity from the ring indicates variation of the density of the polaritons in the ring. The overall polarization component of the emission does not show a strong dependence on the polariton density which could be deduced from plots of the plots of the Stokes vector around the ring in Fig. 43. We can thus conclude that the interactions between the polaritons do not play a dominant role in determining the polarization direction of the emission. At late times, the non-equilibrium state shows very little spin imbalance as shown in Fig. 45 (d) which is due to good spatial overlap of nearly identical density profiles of the two spin components.

In the following section we develop a minimal model capturing the qualitative features discussed above highlighting the essential physics needed to interpret our observations. We derive an effective one-dimensional Hamiltonian by projecting the two-dimensional Hamiltonian onto the ground state of the radially confining potential due to the finite width of the ring channel. The periodicity of the wavefunction in the azimuthal direction results in discrete orbital angular momentum states in the ring. We assume that the polaritons occupy only a small part of the lower polariton dispersion near $k_{||} = 0$, allowing us to make an effective mass approximation for the polaritons. The cavity gradient in the ring reduces the circular symmetry to a left-right mirror symmetry in the ring. It also creates a small spatial anisotropy in the TE-TM splitting energy which is ignored in the present model. A schematic of the quantum states in the ring in absence of a cavity gradient is shown in Fig. 47 (a). We also neglect the spin-dependent interactions for reasons discussed previously.

4.3 Theoretical model

Here we present the theoretical model of a single polariton ring of radius R and width a with a cavity gradient along the vertical axis (see the inset in Fig. 40), where only the lowest radial mode is occupied. In the absence of the polariton-polariton and polariton-reservoir interaction, the ring is described by the following matrix Hamiltonian $\widehat{H}$, whose elements are given by (see the derivation in Supplementary information 4.5.1)

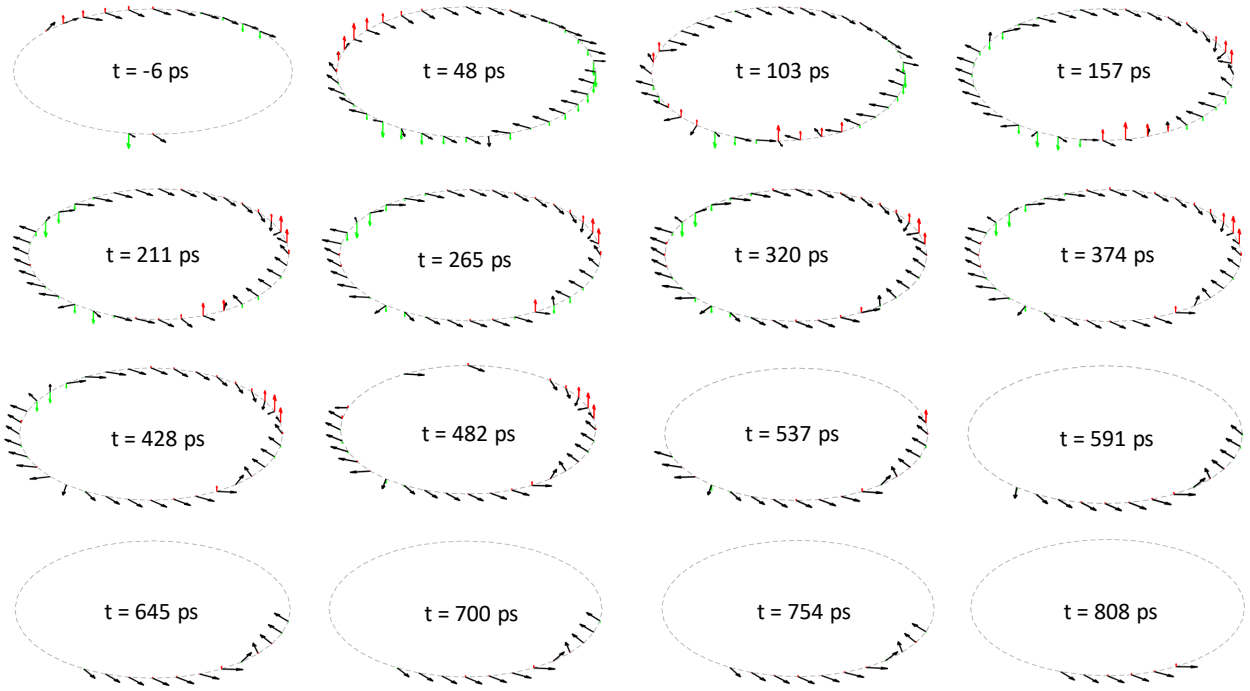

Figure 46: Visualization of the components of the Stokes vector at different angular positions on the ring at different time instances. Black arrows depict the projection of the Stokes vector on the equatorial plane of the Bloch sphere. The length of the arrow is a measure of the degree of linear polarization and half of the angle w.r.t. the positive x-axis measures the direction of the linear polarized light. The red and green arrows depict the spin up and spin down projection of the polariton spinor respectively. The length of these arrows indicate the degree of circular polarization (or spin polarization) of the polaritons. Stokes vectors for intensity below a cut-off level ($I_{cut} = 3$) is not plotted due to poor signal to noise ratio.

$$\widehat{H}_{11} = \widehat{H}_{22} = \frac{\hbar^2}{2m_{\text{eff}}R^2}(\hat{\tilde{k}}^2 + V_0 \sin\varphi), \tag{4.1}$$
$$\widehat{H}_{12} = \widehat{H}_{21}^{\dagger} = \frac{\hbar^2}{2m_{\text{eff}}R^2}\cdot$$
$$\left((B + V_1 \sin\varphi)e^{-2i\varphi}(-\hat{\tilde{k}}^2 + 2\hat{\tilde{k}} + \Delta) + \alpha e^{-i\varphi_0}\right),$$

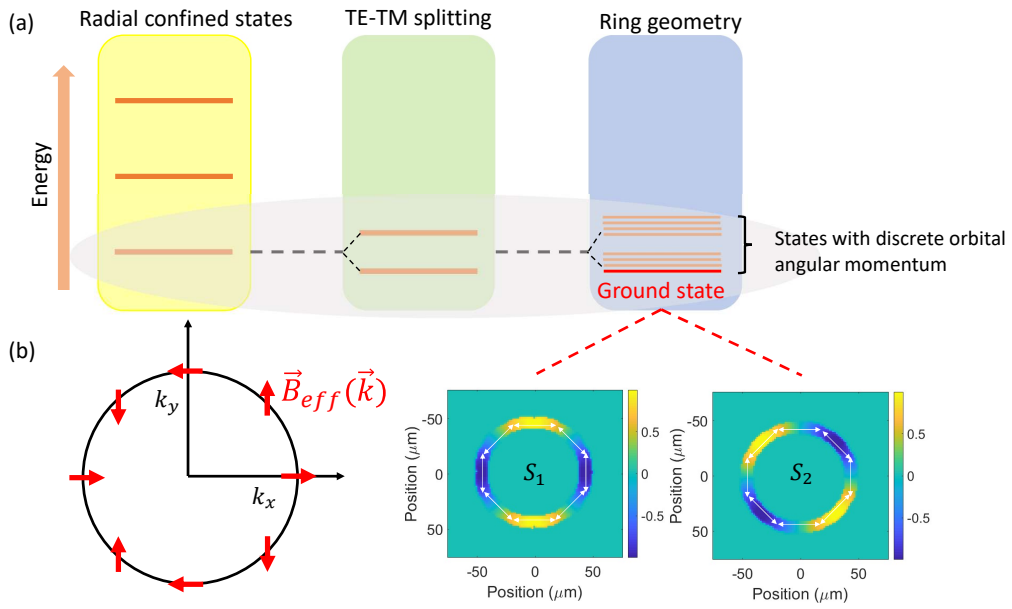

Figure 47: (a) A schematic showing the effect of the radial confinement, TE-TM splitting and the ring geometry on the quantum states in the ring. Visualization of the expectation value of the Stokes components in the ground state of the ring without the tilt is also shown. In the ground state $S_z = 0$ while S_1 and S_2 components are phase shifted by $\pi/4$ w.r.t. each other. The white arrows depict the polarization plane direction, corresponding to the local Stokes parameters. In the ground state the polarization wraps in the azimuthal direction in the ring. (b) Direction of the effective magnetic field due to TE-TM splitting shown with red arrows in the momentum space.

where $\hat{\tilde{k}} = -i(d/d\varphi)$. φ is measured from the positive direction of the x-axis in anticlockwise sense. For the sake of simplicity we introduced the dimensionless quantity $B + V_1 \sin\varphi$ which corresponds to the TE-TM splitting, inherited from the plane microcavity, here $B = 2\beta m_{\text{eff}}/\hbar^2$ (β defines the TE-TM splitting of the plane microcavity without tilt) and V_1 accounts for the dependence of the TE-TM splitting on the changing width of the quantum well. V_0 describes the position-dependent shift of the energy levels due to the cavity gradient. The dimensionless parameter $\Delta = (\pi R/a)^2$ corresponds to the LT-splitting, stemming from the confinement in the radial direction. We also consider an additional splitting between

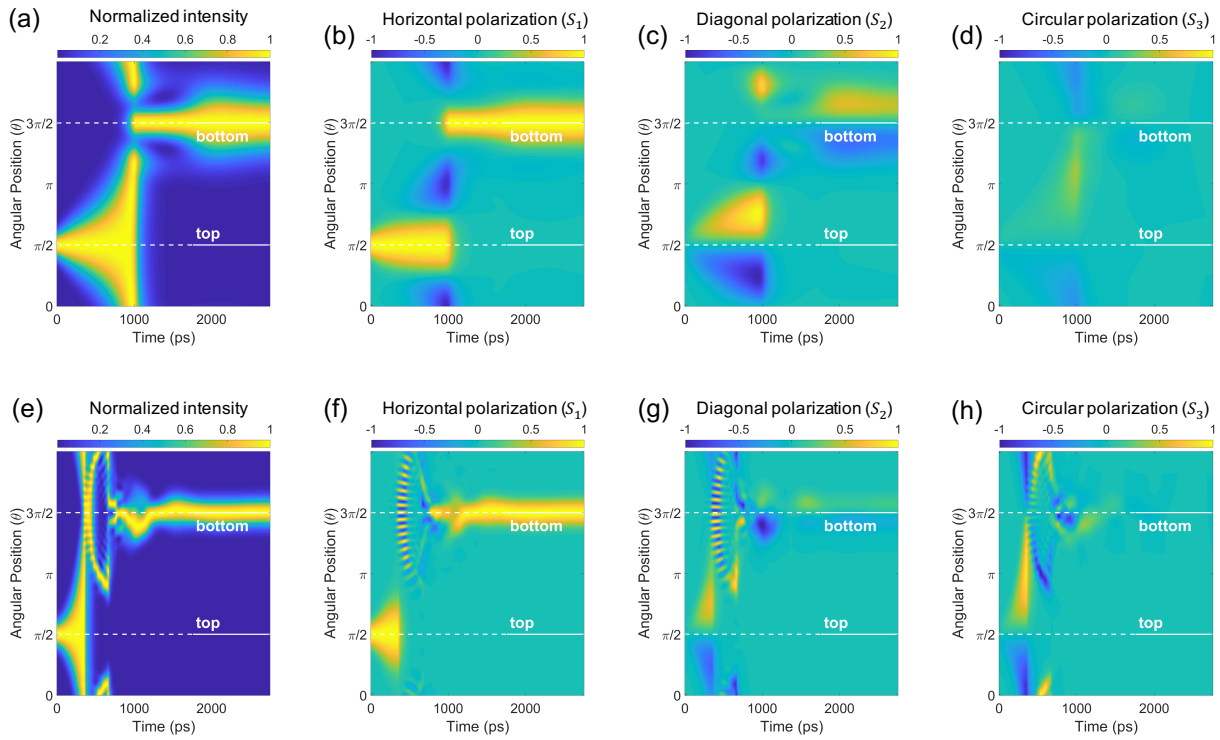

Figure 48: Time evolution of the horizontally polarized condensate spinor. Parameters for both rows are $m_{eff} = 6.14 \times 10^{-5} m_0$, $B = 0.05$ and $\Delta = 250$, where m_0 is the rest mass of an electron in vacuum. Top row (a-d): $V_0 = 16$, $\Lambda = 1$; Bottom row (e-h): $V_0 = 335$, $\Lambda = 0.3$; A larger energy damping rate is chosen for smaller tilt case (top row) because the initial state has a lower potential energy than the larger tilt case (bottom row), so energy relaxation is slower for the same value of Λ in the smaller tilt case.

linear polarizations which acts as a static in-plane field, and described by α and φ_0. This field is usually linked with the crystallographic axes and appears because of the anisotropy of the quantum well.

One can relate the parameters $B = \beta m_{\text{eff}}/\hbar^2$ and V_1 introduced in Eq. (4.1) to the parameters of the DBRs as (see details in Supplementary information 4.5.1)

$$\beta = \frac{2\hbar L_{c,0} L_{\text{DBR}} (\omega_{c,0} - \bar{\omega}) c^2 n_0}{(L_{c,0} + L_{\text{DBR}})^2 n_c^2 \omega_{c,0}^2}, \tag{4.2}$$

and

$$\beta + \frac{\hbar^2 V_1}{m_{\text{eff}}} = \frac{2\hbar L_{c,\pi/2} L_{\text{DBR}} (\omega_{c,0} - \bar{\omega}) c^2 n_0}{(L_{c,\pi/2} + L_{\text{DBR}})^2 n_c^2 \omega_c^2}, \tag{4.3}$$

where n_0 and n_c are the refractive indexes of the surrounding media and the cavity respectively $L_{c,0}$, $L_{c,\pi/2}$ are the widths of the cavity at the points of the ring defined by $\varphi = 0, \pi$, respectively and $\omega_{c,0}$ is the real part of the cavity eigenfrequency at zero in-plane momentum. $L_{\text{DBR}} = n_a n_b \bar{\lambda}/(2(n_b - n_a))$, which is frequently called the effective length of a Bragg mirror, $n_{a,b}$ are the refractive indices of the layers comprising the DBRs and $\bar{\lambda}$ is the wavelength, corresponding to central frequency of the stop-band $\bar{\lambda} = 2\pi c/\bar{\omega}$. In the following discussion, we drop V_1 and α. The time evolution of the polariton condensate spinor Ψ in presence of energy relaxation and finite lifetime τ reads:

$$i\hbar \frac{\partial \Psi}{\partial t} = (1 - i\Lambda)\, \hat{H}\Psi - \frac{i\hbar}{2\tau}\Psi \tag{4.4}$$

Energy relaxation is phenomenologically included in the model by multiplying the Hamiltonian (4.1) by the complex coefficient $1 - i\Lambda$, where Λ is the dimensionless energy relaxation parameter. This is an energy diminishing scheme, where the higher energy eigenstates relax more quickly than the lower energy eigenstates. For longer temporal evolution only the ground state survives. This form of energy relaxation was first suggested by Pitaevskii [145] and applied in context of damped atomic condensates [146, 147]. Since the rate of energy dissipation and the rate of particle loss is not equal, we accounted for the leakage rate with the parameter τ. While numerically integrating the term proportional to Λ we preserve the norm of the wavefunction by adding back the particles that are lost during the energy relaxation step. To account for the finite lifetime of the polaritons we added another imaginary term proportional to Ψ, which describes the loss of particles from the microcavity with time. Thus, the number of polaritons in the simulation exponentially decays with time at a rate $1/\tau$.

We evolve an initial state which is close to the state observed in the experiment after hot thermalization at the pump spot. As shown in Figs. 42 and 45, the Stokes parameters are $S_1 \sim 0.5$ and $S_2 \sim -0.5$ when the degree of polarization is maximum at the top of the ring. This implies that the linear polarization makes an angle of about -22.5° with

the horizontal axis. Any spatially extended state with this uniform polarization is not a polarization eigenstate of the ring because it lacks the left-right mirror symmetry of the ring. In the simulations, we preferred to use an initial state which respects the mirror symmetry of the ring to show that the observed experimental signatures like the four-leaf pattern (in S_1 and S_2) and the spin flips (in S_3) arise in the course of dynamics and do not sensitively depend on the choice of the initial conditions. Since the initial condensate is over 80% horizontally polarized, the initial condensate order parameter in the simulations was chosen to be completely horizontally polarized and localized at the top of the ring,

$$\Psi(\varphi, t=0) = \exp\left[-\frac{(\varphi - \pi/2)^2}{2d^2}\right][1,1]^{\mathrm{T}}. \tag{4.5}$$

This initial polarized state has a left-right mirror symmetry with $S_2(\varphi, t=0) = 0$ as well as spin balanced $S_3(\varphi, t=0) = 0$. The angular width ($d = \pi/10$) of the gaussian wavepacket in the simulations was chosen comparable to the spot size of the pump $\approx 15\mu m$. Numerical solution of Equation (4.4) is shown in Fig. 48 for two different choices of cavity tilt and different energy relaxation rates to elucidate the role of the cavity gradient and the energy damping in the polarization pattern formation in the ring. The simulation captures the coherent evolution of the polariton spinor after excitation by a single pulse.

As the initial spin balanced state diffuses from the top, the two components of the spinor are pushed in opposite directions creating a spin imbalanced state. This is shown at early times in the circular polarization components S_3 in Fig. 48 (d) and (h). In the first 100 ps we observed similar spin imbalance near the top of the ring in the S_3 component as shown in Fig. 45. This imbalance is manifested by the appearance of opposite polarity of the S_3 component for clockwise and counter-clockwise flow of the polariton condensate. From Fig. 45 (c) we also see that after 200 ps, the top half of the ring shows a spin flip, i.e. the region where $S_3 > 0$ in the first 100 ps becomes $S_3 < 0$ and vice-versa. From our simulations we see this when the condensate motion is not strongly damped in Fig. 48 (h). The opposite spin components do not immediately come to rest on reaching the bottom from the top, and continues onward motion converting back the gained kinetic energy into potential energy. It is during this course of motion that we observe spin flip in the ring. In Fig. 48 (d) we do not see this feature because the condensate motion is overdamped, dissipating the

kinetic energy very quickly and bringing the condensate to rest in the bottom of the ring. In the linear polarization sector, which is a measure of the relative phase between the two spinor components, we find rotation of the polarization as the condensate flows out from the point of generation. This is shown by appearance of non-zero S_2 component shortly after evolution of the initial state in Fig. 48 (b) and (f). As the condensate fills the entire ring, we see emergence of the four-leaf pattern in S_1 and S_2. This is clearly seen in Fig. 48 (b) and (c) while obfuscated in Fig. 48 (f) and (g) due to interference between clockwise and anti-clockwise moving waves. Similar observation made in Fig. 45 (b-c) and the four-leaf pattern is shown in Fig. 45 (e-f). As the condensate settles to the minimum of the trap potential, this pattern is seen at the bottom of the ring in Fig. 48 (b), (c), (f) and (g). In this state the circular polarization is nearly absent as the ground state of the ring is not circularly polarized as shown in Supplementary information 4.5.1. The S_3 component at late times in Fig. 45 (d) is also absent in the bottom half of the ring. It should be noted that the model neglects the evolution of the excitonic reservoir in the ring, which dynamically reshapes the effective potential for polaritons. Evidence of long transport of the reservoir was shown in these rings in Ref. [68]. Also the contribution of the higher radial modes are not included which are found to be occupied only at early times after the quench since we address a much slower spin precession dynamics. We found that these are not crucial for understanding the generic polarization patterns in the ring but will be important when addressing details regarding the transport and energy relaxation of the nonequilibrium polariton condensate in the ring. The model introduced in this section captures all the qualitative aspects of the linear and circular polarization precession following a quench, which emphasizes the role of the TE-TM splitting on the condensate dynamics. Finally, we note that the polarization of the condensate observed in the experiment at late times doesn't correspond to any eigenstate of the tilted ring and requires further theoretical investigation into the details of energy relaxation and thermalization processes which could lead to such a pre-thermal state.

4.4 Conclusion

Ring shaped polariton waveguides is attracting a great deal of attention for exploring various topological effects [148, 149, 150, 151] due to the TE-TM splitting in these structures. We present in this direction the first experiments on etched polariton rings. We studied the polarization dynamics of a non-equilibrium polariton condensate formed after a pulsed excitation. Through time resolved measurements we were able to observe the temporal signature of intrinsic optical Hall effect shortly after quench. We provide a qualitative estimate of the length scale over which the spatial coherence builds up in the ring by observing spatial energy locking and linewidth narrowing of the emission. We also present a theoretical model which captures qualitatively the formation of a four-leaf pattern in the S_1 and S_2 components of the Stokes vector, the relative angular phase offset between S_1 and S_2 and finally the contrasting ratio between the degree of linear and circular polarization in the ring thus elucidating the role of the anisotropic pseudo magnetic field originating from the TE-TM splitting and the tilt in the microcavity structure.

Future work will explore making the rings radially thinner pushing further apart the radially confined states in energy while also diminishing the cavity tilt. In the present rings with radial width 15 μm, the separation between the radial modes is about 250 μeV [68]. Rings with negligible cavity gradient would restore the full rotational symmetry and would bring the orbital momentum states into play when the diameter of the rings are also reduced. Another aspect of making thinner rings would be to increase the effective interactions between the polaritons which could be a route to studying the intermediate regime between weakly and strongly interacting Bose gases. These rings could then serve as an ideal platform for studying one-dimensional macroscopic quantum phenomena similar to superconducting rings. Already with these long lifetime samples we could address interesting questions in nonequilibrium physics, such as generation of long lived non thermal states, which could be observed and studied in this system.

4.5 Supplementary information

4.5.1 Derivation of Hamiltonian

In this section we derive the effective Hamiltonian describing a single polariton ring of radius R and width a, accounting for the effect of the TE-TM splitting and the tilt of the well, where only the lowest radial subband is occupied.

We start with the Hamiltonian of 2D polaritons inside a planar microcavity neglecting the cavity width gradient [152]

$$\widehat{H}_{2D} = \begin{pmatrix} \widehat{H}_0(\hat{\mathbf{k}}) & \widehat{H}_{\text{TE-TM}}(\hat{\mathbf{k}}) \\ \widehat{H}^{\dagger}_{\text{TE-TM}}(\hat{\mathbf{k}}) & \widehat{H}_0(\hat{\mathbf{k}}) \end{pmatrix}, \tag{4.6}$$

where the diagonal terms $\hat{H}_0$ describe the kinetic energy of lower cavity polaritons, and the off-diagonal terms $\widehat{H}_{\text{TE-TM}}$ correspond to the TE-TM splitting. We further employ the effective mass approximation

$$\widehat{H}_0(\hat{\mathbf{k}}) = \frac{\hbar^2 \hat{\mathbf{k}}^2}{2m_{\text{eff}}}. \tag{4.7}$$

The TE-TM part is given by

$$\widehat{H}_{\text{TE-TM}}(\hat{\mathbf{k}}) = \beta \left(\frac{\partial}{\partial y} + i \frac{\partial}{\partial x} \right)^2, \tag{4.8}$$

where β governs the strength of the TE-TM splitting and may be expressed in the longitudinal and transverse polariton effective masses m_l and m_t as $\beta = (\hbar^2/4)(m_l^{-1} - m_t^{-1})$. In order to proceed with the derivation of the correct 1D Hamiltonian let us pass to the polar coordinates and add the confining potential $V(r)$ confining the polariton wave functions on the ring in the radial direction to the planar cavity Hamiltonian $\widehat{H}_{2D}$. The confining potential is taken as an infinite square well in the radial direction. The terms associated with the TE-TM splitting in polar coordinates read

$$\begin{aligned} &\left(\frac{\partial}{\partial y} \pm i \frac{\partial}{\partial x} \right)^2 = e^{\mp 2i\varphi} \times \\ &\left(-\frac{\partial^2}{\partial r^2} \pm \frac{2i}{r} \frac{\partial^2}{\partial r \partial \varphi} \mp \frac{2i}{r^2} \frac{\partial}{\partial \varphi} + \frac{1}{r} \frac{\partial}{\partial r} + \frac{1}{r^2} \frac{\partial^2}{\partial \varphi^2} \right). \end{aligned} \tag{4.9}$$

We decompose the Hamiltonian Eq. (4.6) into two parts $\widehat{H}_{2D} = \widehat{H}_0(r) + \widehat{H}_1(r,\varphi)$, where

$$\widehat{H}_0(r) = -\frac{\hbar^2}{2m_{\text{eff}}}\left(\frac{\partial^2}{\partial r^2} + \frac{1}{r}\frac{\partial}{\partial r}\right) + V(r). \tag{4.10}$$

Since we can now separate the variables assuming only the lowest radial mode occupation $\widetilde{\Psi}(r,\varphi) = R_0(r)\Psi(\varphi)$, the effective Hamiltonian [153] for $\Psi(\varphi)$ reads

$$\widehat{H} = \langle R_0(r)|\widehat{H}_1(r,\varphi)|R_0(r)\rangle, \tag{4.11}$$

where $R_0(r)$ is the lowest radial mode of the Hamiltonian (4.10). For an infinite square well potential of width a centered at R in the radial direction, the radial modes, which are non-zero only in $[R-a/2, R+a/2]$, are given by

$$\begin{aligned} &R_n(r) = \\ &A_n\left(Y_0(\frac{\epsilon_n r}{R}) - \frac{Y_0(\epsilon_n(1-\frac{a}{2R})))_0F_1(1;-(\frac{\epsilon_n r}{2R})^2)}{{}_0F_1(1;-(\epsilon_n(1-\frac{a}{2R}))^2/4)}\right), \end{aligned} \tag{4.12}$$

where we introduced the dimensionless energy eigenvalues $\epsilon_n = \frac{\sqrt{2mE_n}R}{\hbar}$ and ${}_0F_1(a;z)$ is the confluent hypergeometric function and A_n is the normalization constant. The eigenvalues ϵ_n satisfy the following equation

$$\frac{Y_0(\epsilon_n(1+\frac{a}{2R}))_0F_1(1;-(\epsilon_n(1-\frac{a}{2R}))^2/4)}{Y_0(\epsilon_n(1-\frac{a}{2R}))_0F_1(1;-(\epsilon_n(1+\frac{a}{2R}))^2/4)} = 1. \tag{4.13}$$

Now we perform the averaging over the lowest radial mode $R_0(r)$ corresponding to the lowest eigenvalue ϵ_0. First we observe $\langle R_0(r)|\frac{1}{r}\frac{\partial}{\partial r}|R_0(r)\rangle = \int_0^\infty R_0(r)R'(r)dr = R_0^2(r)/2|_0^\infty = 0$ for any $R_0(r)$ such that $R_0(0) = R_0(+\infty) = 0$. Then, we calculate $\langle R_0(r)|\frac{\partial^2}{\partial r^2}|R_0(r)\rangle = -C_0/a^2$, where we used that $R_0'' + r^{-1}R_0' = -(2m_{\text{eff}}/\hbar^2)E_0R_0$ and the fact that from dimensional analysis it follows that $E_0 = \hbar^2 C_0/(2ma^2)$, where C_0 is dimensionless. Finally, we have

$$\begin{aligned} &\langle R_0(r)|\frac{\partial^2}{\partial r^2}|R_0(r)\rangle = -C_0/a^2, \\ &\langle R_0(r)|\frac{1}{r}\frac{\partial}{\partial r}|R_0(r)\rangle = 0, \\ &\langle R_0(r)|\frac{1}{r^2}|R_0(r)\rangle = \mathcal{F}(a/R)/R^2, \end{aligned} \tag{4.14}$$

where the equation in the last line is obtained from dimensional analysis and $\mathcal{F}(x)$ is a dimensionless function. We approximate $R_0(r)$ by its first Fourier harmonic, which is reasonable as long as only the lowest radial mode is occupied $R_0(r) \approx \sqrt{\frac{2}{aR}}\sin(\frac{\pi(r-(R-a/2)}{a})$. This function is properly normalized $\int_0^\infty R_0^2(r)rdr = 1$ and satisfy the boundary conditions $R_0(R-a/2) = R_0(R+a/2) = 0$. Then, we have $C_0 = \pi^2$ and for $0 < x < 1$ it follows $\mathcal{F}(x) \approx 1$ to two decimal places. Thus, we finally arrive at the following hamiltonian

$$\widehat{H} = \frac{\hbar^2}{2m_{\text{eff}}R^2}\cdot \begin{pmatrix} \hat{\tilde{k}}^2 & Be^{-2i\varphi}(-\hat{\tilde{k}}^2 + 2\hat{\tilde{k}} + \Delta) \\ Be^{2i\varphi}(-\hat{\tilde{k}}^2 - 2\hat{\tilde{k}} + \Delta) & \hat{\tilde{k}}^2 \end{pmatrix} \tag{4.15}$$

where $\hat{\tilde{k}} = -i(d/d\varphi)$ and the energy levels are now shifted by a constant as compared to the Hamiltonian (4.6). For the sake of simplicity we introduced a dimensionless parameter B corresponding to the TE-TM splitting as $B = 2\beta m_{\text{eff}}/\hbar^2$ and a dimensionless parameter $\Delta = (\pi R/a)^2$ corresponding to the LT-splitting, stemming from the confinement in the radial direction. In the case where the ring is infinitely thin, the model reduces to the one described in [149].

In general, solutions of the stationary Schrodinger equation with the Hamiltonian (4.15) can be represented in the following form

$$\Psi_{k,\alpha}(\varphi) = \widetilde{\chi}_\alpha(\varphi, k)e^{ikR\varphi}, \tag{4.16}$$

where $\widetilde{\chi}_\alpha(\varphi, k)$ is the corresponding spinor

$$\widetilde{\chi}_\alpha(\varphi, k) = \frac{1}{\sqrt{\xi_\alpha(k)^2 + 1}} \begin{pmatrix} e^{-i\varphi} \\ \xi_\alpha(k)e^{i\varphi} \end{pmatrix}, \tag{4.17}$$

and

$$\xi_\alpha(k) = -\frac{a^2B(kR-1)(kR-3) + 8\pi^2R^2}{a^2((kR+1)^2 - E_k^\alpha)}. \tag{4.18}$$

The energy spectrum of the Hamiltonian can be found analytically, the energy levels are given by

$$E_k^{L,U} = 1 + k^2R^2 \mp \frac{\sqrt{B^2\pi^4 + 2a^2B^2\pi^2(3+k^2R^2)R^{-2} + a^4(4k^2R^2 + B^2(9-10k^2R^2+k^4R^4))R^{-4}}}{(a/R)^2} \tag{4.19}$$

in $\hbar^2/(2m_{\text{eff}}R^2)$ units. As we consider polaritons with spin ± 1 as a two-level system, the z-projection of the operator of total angular momentum is $\hat{J}_z = \hbar\hat{\tilde{k}} + \hbar\sigma_z$. One can check that $\hat{J}_z\Psi(\varphi) = \hbar\tilde{k}\Psi(\varphi)$ which clarifies the physical meaning of $\tilde{k} = kR$. The periodic boundary condition imposes the condition $\Psi(\varphi) = \Psi(\varphi + 2\pi)$, which yields integer $\tilde{k}$ corresponding to the quantized orbital angular momentum. According to Eq. (4.19) the energy becomes quantized as well.

To account for the tilt of the well one needs to replace B in the Hamiltonian (4.15) by $B + V_1 \sin\varphi$ and add $V_0 \sin\varphi$ to the diagonal elements, where we assume that the value of the TE-TM splitting as well as the shift of the energy levels linearly depends on the width of the well. Having done that, we arrive at the Hamiltonian (4.1), where an additional splitting between linear polarizations is added (see the text) below Eqs. (4.1).

The dependence of the TE-TM splitting on the local width of the ring can be calculated as follows. Introducing the coefficient

$$L_{\text{DBR}} = \frac{n_a n_b \bar{\lambda}}{2(n_b - n_a)}, \tag{4.20}$$

which is frequently called the effective length of a Bragg mirror, where $n_{a,b}$ are the refractive indexes of the layers comprising the DBRs and $\bar{\lambda}$ is the wavelength, corresponding to the central frequency of the stop-band $\bar{\lambda} = 2\pi c/\bar{\omega}$. Next, introducing

$$\delta = \omega_c - \bar{\omega} \tag{4.21}$$

where ω_c is the real part of the cavity complex eigenfrequency, the TE-TM splitting thus reads [99]

$$\omega^{\text{TE}}(L_c, \omega_c, \phi_0) - \omega^{\text{TM}}(L_c, \omega_c, \phi_0) \approx \frac{L_c L_{\text{DBR}}}{(L_c + L_{\text{DBR}})^2} \frac{2\cos\phi_{\text{eff}} \sin^2\phi_{\text{eff}}}{1 - 2\sin^2\phi_{\text{eff}}} \delta, \tag{4.22}$$

where $\phi_{\text{eff}} \approx \arcsin\left((n_0/n_c)\sin\phi_0\right)$, the coefficients and L_c is the width of the cavity, n_0 and n_c are the refractive indexes of the surrounding media and the cavity respectively. Now, one can relate the parameters $B = \beta m_{\text{eff}}/\hbar^2$ and V_1 introduced in Eq. (4.1) as

$$\begin{aligned}\beta = \\ \lim_{k_{||}\to 0} \frac{\hbar(\omega^{\text{TE}}(L_{c,0},\omega_c,\phi_0) - \omega^{\text{TM}}(L_{c,0},\omega_c,\phi_0))}{k_{||}^2} = \\ = \frac{2\hbar L_{c,0} L_{\text{DBR}}(\omega_{c,0}-\bar{\omega})c^2 n_0}{(L_{c,0}+L_{\text{DBR}})^2 n_c^2 \omega_{c,0}^2},\end{aligned} \tag{4.23}$$

and

$$\begin{aligned}\beta + \frac{\hbar^2 V_1}{m_{\text{eff}}} = \\ \lim_{k_{||}\to 0} \frac{\hbar(\omega^{\text{TE}}(L_{c,\pi/2},\omega_c,\phi_0) - \omega^{\text{TM}}(L_{c,\pi/2},\omega_c,\phi_0))}{k_{||}^2} = \\ = \frac{2\hbar L_{c,\pi/2} L_{\text{DBR}}(\omega_{c,0}-\bar{\omega})c^2 n_0}{(L_{c,\pi/2}+L_{\text{DBR}})^2 n_c^2 \omega_{c,0}^2},\end{aligned} \tag{4.24}$$

where $k_{||} = (\omega_c/c)\sin\phi_0$ and $L_{c,0}$, $L_{c,\pi/2}$ are the widths of the cavity at the points of the ring defined by $\varphi = 0, \pi$, respectively and $\omega_{c,0}$ is a cavity eigenfrequency at $k_{||} = 0$, which also depends on the local width of the cavity.

Let us investigate the ground state of a flat ring (no tilt) and in the absence of birefringence. For the experimentally relevant values $B = 0.052$ and $\Delta = 61.36$, the ground state $\Psi_{0,L}$ is non-degenerate and corresponds to $\tilde{k} = 0$ of the lower branch (minus sign in Eq. (4.19)), the expression for it reads

$$\psi_{0,L} = \frac{1}{\sqrt{2}} \begin{pmatrix} e^{-i\varphi} \\ e^{i\varphi} \end{pmatrix}. \tag{4.25}$$

The Stokes vector for this state is given by

$$\vec{S} = \Psi_{0,L}^{\dagger} \vec{\sigma} \Psi_{0,L} = \begin{pmatrix} -\cos 2\varphi \\ -\sin 2\varphi \\ 0 \end{pmatrix}, \tag{4.26}$$

thus, the ground state of a flat ring with no birefringence is completely linearly polarized with the polarization direction remaining tangential to the ring. It should be noted, that the

Stokes vector in the ground state (4.25) repeats the pattern of the effective magnetic field produced by the TE-TM splitting (shown in Fig. 47 (b)), but in the XY-plane. We observed a large degree of linear polarization and a small degree of circular polarization in the ring as seen in Fig. 45 and Fig. 48; the TE-TM splitting term in the Hamiltonian mixes the left and right circular components of the pseudo spinor creating a large component of linear polarized state with a small circular component. Although, the four-leaf angular pattern in S_1 and S_2 are not phase shifted by $\pi/2$ as predicted from the theory but the 2φ angular dependence of both the patterns point towards the 2φ angular dependence of the pseudo magnetic field originating from the TE-TM splitting in the ring microcavity.

4.5.2 Stokes vector measurement

Jones matrix formalism is a simple method for keeping track of the polarization of light as it interacts with various optical elements. Commonly it is used to characterize only completely polarized light while Mueller matrix formalism can describe a partial polarized state of light. The full polarization state of light is then characterized by a set of four real numbers known as the Stokes vector. In this Supplementary information we discuss our measurement scheme with the help of Jones matrix to characterize any arbitrary state of partially polarized light, so that the connection between our measurements and the state of the polariton spinor remains transparent.

Our goal is to measure any arbitrary input state $|\psi\rangle = (E_x, E_y)^T$, where $E_x(= |E_x|e^{i\theta_x})$ and $E_y(= |E_y|e^{i\theta_y})$ are complex numbers. Such a state can faithfully represent the state of a completely polarized light. To include partially polarized light we can add to the above state random noise $\epsilon(W_x, W_y)^T$, such that $\langle W_x\rangle = \langle W_y\rangle = 0$ and $\langle W_x^2\rangle = \langle W_y^2\rangle = 1/2$. Therefore, we see that in order to characterize the input state, we need to find just four real numbers $\{|E_x|, |E_y|, \theta_{yx}(= \theta_y - \theta_x), \epsilon\}$ requiring only four measurements summarized in Table 3.

The action of $\lambda/2$- and $\lambda/4$-waveplates with fast axis rotated by θ from the vertical on

$|\psi\rangle$ are given by

$$H(\theta) = R(-\theta) \begin{pmatrix} 1 & 0 \\ 0 & e^{i\pi} \end{pmatrix} R(\theta)$$
$$Q(\theta) = R(-\theta) \begin{pmatrix} 1 & 0 \\ 0 & e^{i\pi/2} \end{pmatrix} R(\theta), \tag{4.27}$$

where $R(\theta)$ is the 2D rotation matrix given by,

$$R(\theta) = \begin{pmatrix} \cos\theta & \sin\theta \\ -\sin\theta & \cos\theta \end{pmatrix} \tag{4.28}$$

$\theta_{\lambda/2}$	$\theta_{\lambda/4}$	Polarizer orientation	Measured intensity	Observed intensity
0	–	vertical	$\|E_y\|^2 + \epsilon^2/2$	I_1
$\pi/8$	–	vertical	$\frac{1}{2}\left(\|E_x\|^2 + \|E_y\|^2 + (E_x^* E_y + E_y^* E_x) + \epsilon^2\right)$	I_2
$\pi/4$	–	vertical	$\|E_x\|^2 + \epsilon^2/2$	I_3
–	$\pi/4$	vertical	$\frac{1}{2}\left(\|E_x\|^2 + \|E_y\|^2 + i(E_y^* E_x - E_x^* E_y) + \epsilon^2\right)$	I_4
–	$7\pi/4$	vertical	$\frac{1}{2}\left(\|E_x\|^2 + \|E_y\|^2 - i(E_y^* E_x - E_x^* E_y) + \epsilon^2\right)$	I_5

Table 3: Stokes vector measurement scheme showing the relationship between the observed intensity measured in the experiment and the corresponding expression of the intensity written in terms of the electric field components of the light.

Since $\lambda/2$- and $\lambda/4$-waveplates have different thicknesses, so we expect them to have slightly different transmission efficiency. To compensate for this we found that it is usually more accurate to take two measurements with $\lambda/4$-waveplate which could be added to give the total intensity of light I_{tot} $(= S_0)$. From our measurements we can calculate the

components of the Stokes vector by taking linear combinations as shown below.

$$
\begin{aligned}
I_{tot} &= I_1 + I_3 = I_4 + I_5 = |E_x|^2 + |E_y|^2 + \epsilon^2 \\
S_1 &= \frac{I_3 - I_1}{I_1 + I_3} = \frac{|E_x|^2 - |E_y|^2}{|E_x|^2 + |E_y|^2 + \epsilon^2} \\
S_2 &= \frac{2I_2 - I_1 - I_3}{I_1 + I_3} = \frac{E_x^* E_y + E_y^* E_x}{|E_x|^2 + |E_y|^2 + \epsilon^2} \\
S_3 &= \frac{I_5 - I_4}{I_4 + I_5} = \frac{i(E_x^* E_y - E_y^* E_x)}{|E_x|^2 + |E_y|^2 + \epsilon^2}
\end{aligned}
\tag{4.29}
$$

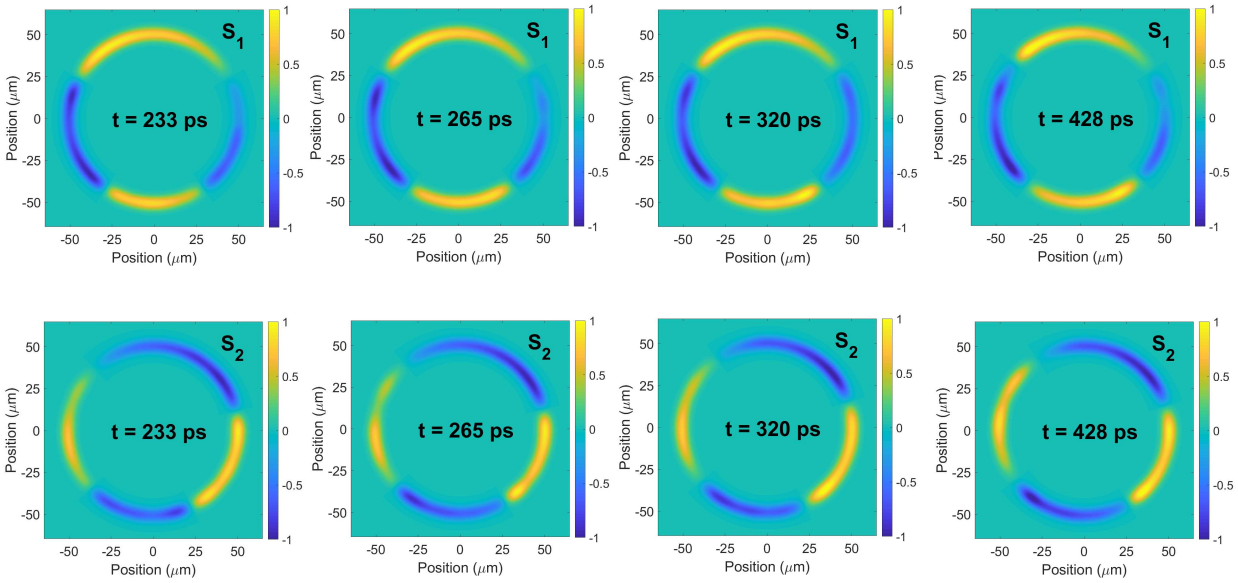

Figure 49: Temporal snapshots of the S_1 and S_2 components from the ring which show nearly stationary dynamics.

It is also straightforward to see that the intensity of the polarized and unpolarized light are given by

$$
\begin{aligned}
I_{pol} &= |E_x|^2 + |E_y|^2 = I_{tot}\sqrt{S_1^2 + S_2^2 + S_3^2} \\
\epsilon^2 &= I_{tot}(1 - \sqrt{S_1^2 + S_2^2 + S_3^2}).
\end{aligned}
\tag{4.30}
$$

The relative phase difference between the spinor component is

$$
\tan\theta_{yx} = \frac{S_3}{S_2} \tag{4.31}
$$

and the amplitudes are given by,

$$\begin{aligned} |E_x|^2 &= \frac{I_{tot}}{2}\Big(\sqrt{S_1^2+S_2^2+S_3^2}+S_1\Big) \\ |E_y|^2 &= \frac{I_{tot}}{2}\Big(\sqrt{S_1^2+S_2^2+S_3^2}-S_1\Big). \end{aligned} \tag{4.32}$$

The direction of the polarization plane φ is given by,

$$\varphi = \frac{1}{2}\tan^{-1}\frac{S_2}{S_1}. \tag{4.33}$$

Four-leaf pattern in the linear polarization sector is shown at different time instances in Fig. 49 supplementing Fig. 42 (e-g). In these plots the Stokes vectors S_1 and S_2 are normalized w.r.t. I_{pol} instead of I_{tot}. Bloch vector representation showing the circular and linear polarization components of the Stokes vectors are shown in Fig. 46, which supplements Fig. 43.

5.0 Drag and dissipation of a polariton condensate

5.1 Motivation

In this chapter we will consider the question of energy dissipation in the polariton condensates. We have already seen in the experiments reported in the previous two chapters how the energy dissipation in propagating polariton condensates is essential to understanding the dynamics of this system. In these experiments, the condensate is created non-resonantly along with a reservoir. The reservoir is primarily made of the excitons, "bottleneck polaritons" and free carriers. Energy, momentum and number-conserving interactions between the coherent polaritons and the reservoir can lead to effective damping of the motion of the polaritons. Such an effect provides a microscopic basis for understanding the simplified models of energy dissipation used in the previous chapters. In particular we will look at the interactions between the polaritons and the free electrons in the quantum wells which act as the reservoir for exchanging energy and momentum with the polaritons. I apply this theory to analyze the experiments in straight wire microcavities which study the effect of an electric current driven through a one-dimensional polariton condensate in a steady state [154], where a second reservoir consisting of excitons is also considered. This chapter is adapted from [154]. The experiments reported in this chapter were performed by David Myers and Qi Yao and I developed the theory to explain the observations. The project was supervised by David Snoke.

It is often stated in simplified terms that a superfluid does not experience drag. More accurately, a superfluid does not react to transverse forces, such as the sliding friction of a wall in a rotating ring condensate [155, 156, 157], and has quantized vorticity, so that a superfluid has no turbulence in the limit of low excitations. A superfluid will still react to longitudinal forces and body forces, such as the force of gravity. It is also well established from experiments and theory of cold atom condensates [147, 158, 159, 160, 161, 162, 163, 164, 165, 166, 167] that a condensate out of equilibrium experiences damping and dissipation due to scattering of condensate particles with non-condensate particles.

It is a natural consequence of this damping force due to non-condensate particles that a steady-state flow of non-condensate particles in one direction will lead to a net drag force on the condensate. Such a situation has already been demonstrated by our experimental work [154] for a polariton condensate in a wire with a net flow of free electrons moving through the condensate in one direction. In those experiments, two effects were observed: first, the average momentum of the condensate was shifted up and down due to the collisions with the electrons, and second, under the same conditions, a shift of the chemical potential of the condensate was seen. One of the advantages of polariton condensate experiments is that both the momentum and energy of the condensate can be easily observed *in situ*, non-destructively, by spectroscopy of photons slowly leaking out of the condensate, which have a one-to-one mapping to the state of the polaritons from which they came [99, 168, 169].

In this chapter, we adapt previous theory [158, 170] on the damping of nonequilibrium condensates to the case of an exciton-polariton condensate (henceforth simply referred to as polaritons), in which the reservoir of non-condensate particles is a fermionic electron gas instead of just the excited states of the same type of particle as in the condensate. This case is realistic for the polariton condensate experiments, in which the coherent condensate fraction was very high, 90% or more, so that the dominant drag force came from free electrons driven through the system. We will assume that the density of the electrons is low enough, and their temperature high enough, that Pauli statistics do not come into play, and they can be modeled as a classical Boltzmannian gas. Although we will apply this theory to the specific case of a polariton condensate, the theory is quite general, applying to any condensate experiencing a net drag force.

In system-reservoir theory for open quantum systems [171, 172], energy damping in a system arises from its interactions with the reservoir which result in both particle and energy transfer. In far-from-equilibrium or non-steady-state scenarios, processes which do not conserve the number of particles in the condensate, e.g. collisions in which a condensate particle scatters with a non-condensate particle and leaves the condensate, going into the excited-state reservoir, are known to dominate over processes which conserve particle number in the condensate (and in the reservoir), e.g., a collision in which a condensate particle transfers energy to a particle in the reservoir, but remains in the condensate. This second

process will occur even if the reservoir is a distinct species from the condensate, such as a fermionic electron gas. While energy damping is important in thermalization of a condensate out of equilibrium, this latter scenario is also important when a steady state is established between the system and the reservoir. In this chapter we describe the process of energy damping via a two-particles-in, two-particles-out elastic collision between the particles of the system and the reservoir. In particular we emphasize on the connection of this process leading to a drag force acting on the system.

Polaritons inherently have a finite lifetime $\sim 20 - 200$ ps inside a microcavity. It has been shown [47] that in the upper range of these lifetimes, polaritons can reach thermal equilibrium. In general, it is possible to observe the time evolution of a polariton condensate far from equilibrium all the way to equilibrium [68, 173, 174, 175]; spectroscopy and imaging of the leaked photons from the microcavity give direct access to the polariton states inside the microcavity. In this chapter, we consider the case of a steady-state system with continuous generation and decay of the condensate, with constant unidirectional flow of the electron reservoir, which has constant density.

It may at first seem surprising that polaritons, which are electrically neutral and hence do not respond to electric field, will respond at all to an electric current. A polariton spends part of its existence as an exciton, however, which is a bound electron-hole pair, and excitons interact with free electrons in the same way that a hydrogen atom interacts with a free electron, as a charged dipole interacting with a free charge, with a short-range potential [59, 176, 177, 178]. Because of this, the polariton drag effect [154] is effectively a new type of nonlinear process in which an electron transfers its momentum to a photon; in the entire "life cycle", a photon enters the system, is virtually absorbed into becoming an exciton; while it is in that state, it receives a momentum kick from a free electron; and then finally the exciton turns back into a photon which is emitted from the system with an altered momentum. In this chapter, we will not consider in detail the dipole-free charge interaction, and will instead simply model the electron-polariton interaction as a short-range elastic collisional process.

5.2 Theory

Let us consider as an example a classical object moving through a viscous fluid. The drag force on the object is proportional to the relative velocity between the object and the fluid, and there is an equal but opposite force acting on the fluid. When the fluid is not moving, this drag force is responsible for dragging the fluid along with a moving object, and if the object is initially at rest, it can be moved by the drag force of a moving fluid. Our theory aims to capture this effect by showing that the case of a condensate colliding with electrons generates an effective, real-valued potential which depends on the relative motion of the condensate and electrons in the same way as in the case of a classical object moving through the viscous fluid.

The interaction between the polariton condensate $\psi(\vec{r},t)$ and the electrons $\phi(\vec{r},t)$ which comprise the reservoir is modelled using hard core repulsive collisions. The interaction Hamiltonian is given by

$$H_{int} = g\int d^2r\Big(\psi^\dagger(\mathbf{r})\phi^\dagger(\mathbf{r})\phi(\mathbf{r})\psi(\mathbf{r})\Big), \tag{5.1}$$

where the scalar fields $\psi(\vec{r},t)$ and $\phi(\vec{r},t)$ obey the equal time bosonic commutation and fermionic anti-commutation relations, respectively. The fields evolve under the Hamiltonian $H = H_\psi + H_\phi + H_{int}$, where H_ψ and H_ϕ are given by

$$\begin{aligned} H_\psi &= \int d^2r\psi^\dagger(\mathbf{r})\left[\frac{1}{2m_\psi}(-i\hbar\vec{\nabla}-\vec{p}_{rel})^2 + V_\psi(\mathbf{r})\right. \\ &\quad \left. + gn_\phi(\mathbf{r}) + \frac{U}{2}\psi^\dagger(\mathbf{r})\psi(\mathbf{r})\right]\psi(\mathbf{r}), \\ H_\phi &= \int d^2r\phi^\dagger(\mathbf{r})\left[\frac{1}{2m_\phi}(-i\hbar\vec{\nabla})^2\right]\phi(\mathbf{r}). \end{aligned} \tag{5.2}$$

Here $gn_\phi(\boldsymbol{r})$ is the Hartree energy shift due to the interactions between the electron reservoir and the condensate, and U is the strength of the polariton-polariton repulsive interactions. The momentum $\mathbf{p_{rel}} = m_\psi\mathbf{v_{rel}} = m_\psi(\mathbf{v}_\psi - \mathbf{p}_\phi/m_\phi)$, is the steady-state drift momentum of the condensate measured in the rest frame of the electron reservoir. The electron momentum $\mathbf{p}_\phi$ is the steady-state average linear momentum of the reservoir measured in the lab frame due

to the application of an electric field on the electron reservoir. The electrons in the quantum well are assumed to be freely moving and the effect of applying a constant potential in the plane of the well is taken as setting up a steady-state flow with a drift momentum $\mathbf{p}_\phi$. $V_\psi(\mathbf{r})$ is the effective potential experienced by the polaritons due to the photonic energy gradient in the microcavity and repulsive potential due to the interaction with the excitons created by the non-resonant pump.

Our goal in this section is to derive an effective equation of motion for the polariton condensate, ignoring both the thermal and quantum fluctuations of the condensate order parameter. We adopt the formalism of the Master equation approach which has been applied previously to the theory of finite temperature Bose-Einstein condensates to describe number and energy dissipation in such systems [158, 171]. An important consideration in this approach is that the states comprising the system and the reservoir have different energy scales; low-lying energy states make up the "system" while high-energy excited states make up the "reservoir." Such a distinction introduces a cut-off energy parameter separating the two regions, which finds its way into the scattering rate and at first glance seems ad-hoc. In the theory of stochastic Gross-Pitaevskii equations, this cut-off parameter is chosen self consistently using Hartree-Fock theory, conserving the total number of particles, and is found to predict quantitative estimates for observables measured in the experiments [163, 162, 167]. In the case considered here, of a fermionic electron reservoir, there is no need for such an energy cutoff because the reservoir particles are a different species, completely distinguishable from the condensate particles.

We assume that the reservoir maintains thermal equilibrium while interacting with the system, due to strong interactions with lattice phonons. The polaritons, on the other hand, have weak coupling with the phonons [59], and thus must come to equilibrium via interactions with each other, with excitons, and with the free electrons. We assume that the electrons have a much higher average kinetic energy than the polaritons, because the polariton condensate fraction is so high that it mostly occupies very low energy states.

The starting point of the theory is to describe the time evolution of the system density matrix ρ (including polaritons and the reservoir) under the full Hamiltonian H, as follows:

$$\partial_t \rho(t) = -\frac{i}{\hbar}[H, \rho(t)]. \tag{5.3}$$

In the interaction picture, $H_{int}(t) = e^{i(H_\psi + H_\phi)t/\hbar} H_{int} e^{-i(H_\psi + H_\phi)t/\hbar}$ and the interaction picture density matrix $\rho_I(t) = e^{i(H_\psi + H_\phi)t/\hbar} \rho(t) e^{-i(H_\psi + H_\phi)t/\hbar}$, which implies

$$\partial_t \rho_I(t) = -\frac{i}{\hbar}\Big[H_{int}(t), \rho_I(t)\Big]. \tag{5.4}$$

The above equation can also be written as

$$\begin{aligned} \partial_t \rho_I(t) &= -\frac{i}{\hbar}\Big[H_{int}(t), \rho_I(0)\Big] \\ &- \frac{1}{\hbar^2}\int_0^t dt' \Bigg[H_{int}(t), \Big[H_{int}(t'), \rho_I(t')\Big]\Bigg]. \end{aligned} \tag{5.5}$$

Taking the partial trace $Tr_\phi[...]$ over the electron field leads to

$$\begin{aligned} \partial_t Tr_\phi\Big[\rho_I(t)\Big] &= Tr_\phi\Bigg[-\frac{i}{\hbar}\Big[H_{int}(t), \rho_I(0)\Big] \\ &- \frac{1}{\hbar^2}\int_0^t dt' \Bigg[H_{int}(t), \Big[H_{int}(t'), \rho_I(t')\Big]\Bigg]\Bigg]. \end{aligned} \tag{5.6}$$

We assume that at the initial time the electrons and the polaritons are uncorrelated, allowing us to represent the density matrix at $t = 0$ as a direct product of the two subsystems $\rho_I(0) = \rho_\psi \otimes \rho_\phi$. The first term on the right hand side of the above equation gives a Hartree energy contribution $= g n_\phi(\mathbf{r})$ which has already been absorbed in the definition of H_ψ. Therefore this term is dropped. Further, we assume that the electron-polariton interactions are weak, so that correlations between the reservoir and the polaritons are small even on long time scales, such that $\rho_I(t') \approx \rho^I_\psi(t') \otimes \rho_\phi$. As discussed above, we assume that the energy separation between the electrons and the polaritons is large, which implies a much slower evolution of $\rho^I_\psi(t')$, allowing us to replace $\rho^I_\psi(t') \to \rho^I_\psi(t)$ in the time integral. This approximation is known as the Markov approximation and amounts to assuming that the evolution of the density matrix depends on the instantaneous state of the system and makes no reference to the past. In addition to the electron reservoir considered here, there exists

an exciton reservoir whose effect on the polaritons will be considered later. After evaluating the bath correlation functions we arrive at

$$\begin{aligned}\partial_t\rho_\psi(t) = &-\frac{i}{\hbar}\Big[H_\psi, \rho_\psi(t)\Big] - \frac{\pi\hbar g^2}{4\pi^2\left(2\pi\hbar\right)^2}\int d^2r d^2r' d^2k_1 d^2k_2 F(\boldsymbol{k_1})\Big(1-F(\boldsymbol{k_2})\Big)\\ &\Bigg\{\Big[\hat{n}_\psi(\boldsymbol{r}), \delta\left(\hat{L}_\psi + E_\phi(\boldsymbol{k_1}) - E_\phi(\boldsymbol{k_2})\right)\hat{n}_\psi(\boldsymbol{r'})\rho_\psi(t)\Big]e^{-i(\boldsymbol{k_1}-\boldsymbol{k_2}).(\boldsymbol{r}-\boldsymbol{r'})}\\ &+\Big[\rho_\psi(t)\delta\left(\hat{L}_\psi - E_\phi(\boldsymbol{k_1}) + E_\phi(\boldsymbol{k_2})\right)\hat{n}_\psi(\boldsymbol{r'}), \hat{n}_\psi(\boldsymbol{r})\Big]e^{i(\boldsymbol{k_1}-\boldsymbol{k_2}).(\boldsymbol{r}-\boldsymbol{r'})}\Bigg\},\end{aligned} \tag{5.7}$$

with the definitions $\rho_\psi(t) = Tr_\phi\Big[\rho(t)\Big]$, $\hat{n}_\psi(\boldsymbol{r}) = \psi^\dagger(\boldsymbol{r})\psi(\boldsymbol{r})$, $\hat{L}_\psi\hat{n}_\psi(\boldsymbol{r}) = [\hat{n}_\psi(\boldsymbol{r}), H_\psi]$, $E_\phi(\boldsymbol{k}) = \hbar^2\boldsymbol{k}^2/2m_\phi$ and $F(\boldsymbol{k}) = 1/(e^{(E_\phi(\boldsymbol{k})-\mu)/k_BT}+1)$, assuming the electronic reservoir is in thermal equilibrium with chemical potential μ and temperature T. Details of the calculation in going from (5.6) to (5.7) are given in Supplementary information 5.5.1. For book-keeping purposes, we define the eigenenergies of the super-operator $\hat{L}_\psi$, which are given by $\{\epsilon\}$. With this we define

$$\begin{aligned}M_1(\boldsymbol{r}-\boldsymbol{r'},\epsilon) &= \int d^2k_1 d^2k_2 F(\boldsymbol{k_1})\Big(1-F(\boldsymbol{k_2})\Big)\delta\left(\epsilon + E_\phi(\boldsymbol{k_1}) - E_\phi(\boldsymbol{k_2})\right)e^{-i(\boldsymbol{k_1}-\boldsymbol{k_2}).(\boldsymbol{r}-\boldsymbol{r'})},\\ M_2(\boldsymbol{r}-\boldsymbol{r'},\epsilon) &= \int d^2k_1 d^2k_2 F(\boldsymbol{k_1})\Big(1-F(\boldsymbol{k_2})\Big)\delta\left(-\epsilon + E_\phi(\boldsymbol{k_1}) - E_\phi(\boldsymbol{k_2})\right)e^{i(\boldsymbol{k_1}-\boldsymbol{k_2}).(\boldsymbol{r}-\boldsymbol{r'})}.\end{aligned} \tag{5.8}$$

Interchanging $\boldsymbol{k_1}$ and $\boldsymbol{k_2}$ in $M_1(\boldsymbol{r}-\boldsymbol{r'},\epsilon)$ and using the property $F(\boldsymbol{k_2})\Big(1-F(\boldsymbol{k_1})\Big) = e^{\beta\epsilon}F(\boldsymbol{k_1})\Big(1-F(\boldsymbol{k_2})\Big)$ we arrive at,

$$\frac{M_1(\boldsymbol{r}-\boldsymbol{r'},\epsilon)}{e^{\beta\epsilon/2}} = \frac{M_2(\boldsymbol{r}-\boldsymbol{r'},\epsilon)}{e^{-\beta\epsilon/2}}. \tag{5.9}$$

For $\beta\epsilon \ll 1$, we can linearize (5.8) using (5.9) to obtain

$$\begin{aligned}M_1(\boldsymbol{r}-\boldsymbol{r'},\epsilon) &\approx \Big(1+\frac{\beta\epsilon}{2}\Big)M(\boldsymbol{r}-\boldsymbol{r'},0),\\ M_2(\boldsymbol{r}-\boldsymbol{r'},\epsilon) &\approx \Big(1-\frac{\beta\epsilon}{2}\Big)M(\boldsymbol{r}-\boldsymbol{r'},0).\end{aligned} \tag{5.10}$$

Using (5.8), (5.9) and (5.10), we can approximate (5.7) as

$$\partial_t \rho_\psi(t) \approx -\frac{i}{\hbar}\Big[H_\psi, \rho_\psi(t)\Big] - \frac{\pi\hbar g^2}{4\pi^2\,(2\pi\hbar)^2}\int d^2r d^2r' M(\boldsymbol{r}-\boldsymbol{r}')\Bigg\{\Big[\hat{n}_\psi(\boldsymbol{r}), \hat{n}_\psi(\boldsymbol{r}')\rho_\psi(t)\Big] + \Big[\rho_\psi(t)\hat{n}_\psi(\boldsymbol{r}'), \hat{n}_\psi(\boldsymbol{r})\Big] + \frac{\beta}{2}\Big[\hat{n}_\psi(\boldsymbol{r}), \hat{L}_\psi\hat{n}_\psi(\boldsymbol{r}')\rho_\psi(t)\Big] - \frac{\beta}{2}\Big[\rho_\psi(t)\hat{L}_\psi\hat{n}_\psi(\boldsymbol{r}'), \hat{n}_\psi(\boldsymbol{r})\Big]\Bigg\}. \tag{5.11}$$

Next, we map this equation to the Fokker-Planck equation in the semi-classical limit, which is found by introducing a Wigner-Weyl transform [171, 179] of the density and field operators. The terms $\Big[\hat{n}_\psi(\boldsymbol{r}), \hat{n}_\psi(\boldsymbol{r}')\rho_\psi(t)\Big]$ and $\Big[\rho_\psi(t)\hat{n}_\psi(\boldsymbol{r}'), \hat{n}_\psi(\boldsymbol{r})\Big]$ inside the integral map to second-order field derivatives, which give rise to a multiplicative noise in the time evolution of the c-field $\psi(\mathbf{r}, t)$ [180]. As we are only interested in the coherent field dynamics, we drop this term. The terms proportional to β transform to

$$\begin{aligned}&\frac{i\hbar\beta}{2}\vec{\nabla}'\cdot\left(\frac{\boldsymbol{p}_{rel}}{m_\psi}|\psi(\boldsymbol{r}')|^2 + \frac{i\hbar}{2m_\psi}\psi^*(\boldsymbol{r}')\vec{\nabla}'\psi(\boldsymbol{r}') - \frac{i\hbar}{2m_\psi}\psi(\boldsymbol{r}')\vec{\nabla}'\psi^*(\boldsymbol{r}')\right)\\ &\left(\psi^*(\boldsymbol{r})\frac{\partial W}{\partial\psi^*(\boldsymbol{r})} - \psi(\boldsymbol{r})\frac{\partial W}{\partial\psi(\boldsymbol{r})}\right)\\ &= -\frac{i\hbar\beta}{2}\vec{\nabla}'\cdot\left(\frac{\boldsymbol{p}_{rel}}{m_\psi}|\psi(\boldsymbol{r}')|^2 + \mathbf{j}(\mathbf{r}')\right)\left(\psi(\boldsymbol{r})\frac{\partial W}{\partial\psi(\boldsymbol{r})} - \psi^*(\boldsymbol{r})\frac{\partial W}{\partial\psi^*(\boldsymbol{r})}\right).\end{aligned} \tag{5.12}$$

Here $W(\psi, \psi^*)$ is the Wigner function which is defined as the Weyl transform of the density matrix, ∇' denotes spatial derivatives with respect to $\mathbf{r}'$ co-ordinates, and $\mathbf{j}(\mathbf{r}')$ is the condensate current. Details of this mapping are discussed in Supplementary information 5.5.2. Similarly, applying the Wigner-Weyl transform to the other terms in (5.11), we arrive at a semi-classical equation for the evolution of the Wigner function after ignoring the second and higher order field derivatives:

$$\begin{aligned}\partial_t W &= -\frac{i}{\hbar}\int d^2r\Big(L_{op} + V_\epsilon(\mathbf{r})\Big)\left(\psi(\boldsymbol{r})\frac{\partial W}{\partial\psi(\boldsymbol{r})} - \psi^*(\boldsymbol{r})\frac{\partial W}{\partial\psi^*(\boldsymbol{r})}\right),\\ L_{op} &= \frac{1}{2m_\psi}(-i\hbar\vec{\nabla} - \vec{p}_{rel})^2 + V_\psi(\mathbf{r}) + gn_\phi(\mathbf{r}) + U|\psi(\mathbf{r})|^2,\\ V_\epsilon(\mathbf{r}) &= -\frac{\hbar\beta g^2}{32\pi^3}\int d^2r' M(\mathbf{r}-\mathbf{r}')\vec{\nabla}'\cdot\underbrace{\left(\frac{\boldsymbol{p}_{rel}}{m_\psi}|\psi(\boldsymbol{r}')|^2 + \mathbf{j}(\mathbf{r}')\right)}_{\mathbf{J}(\mathbf{r}')}.\end{aligned} \tag{5.13}$$

$V_\epsilon(\mathbf{r})$ is the field-dependent drag potential which is nonlinear. It is straightforward to show [170] that the drag potential causes energy dissipation of the condensate, since it is proportional to the negative of the divergence of the condensate current. To apply this theory to the interpretation of the experimental observations under consideration here, we first impose the geometrical constraints of the experiments. We assume that the condensate can flow only along one-dimension (x-direction) while its motion is frozen in the transverse direction (y-direction). The condensate is assumed to be in the ground state of the particle in a box potential of width w along the y-direction. The condensate c-field can now be written as $\psi(x,y,t) = \sqrt{(2/w)}\cos(\pi y/w)\psi(x,t)$. The equation of motion for the condensate field $\psi(\mathbf{r},t)$ in one-dimension is given by

$$\begin{aligned} i\hbar\partial_t\psi(x,t) &= \frac{2}{w}\int_{-w/2}^{w/2} dy \cos(\pi y/w)\big(L_{op} + V_\epsilon(x,y,t)\big)\cos(\pi y/w)\psi(x,t) \\ &= \left(E_c + \frac{1}{2m_\psi}(-i\hbar\partial_x - p_{rel})^2 + V_\psi(x) + gn_\phi(x) + \frac{3}{2w}U|\psi(x)|^2 + V_\epsilon(x,t)\right)\psi(x,t). \end{aligned} \tag{5.14}$$

Here E_c is the confinement energy due to the confinement along the y-direction and can be dropped. An expression for $V_\epsilon(x,t)$ is derived in Supplementary information 5.5.4. In a typical experiment, the electron density concentration n_ϕ can only be estimated and cannot be determined precisely, nor the chemical potential μ and the effective temperature $1/\beta$ of the electron reservoir. These parameters are free parameters in our theory, which we can adjust to obtain qualitative agreement with the overall behavior in the experiments, to show that the drag effect exists.

We will now refer to the general mathematical form of the Fokker-Planck equation for understanding the equivalence between the above two equations 5.13 and 5.14. In one dimension Fokker-Planck equation takes the form,

$$\partial_t\rho - \partial_x\Big(f(x)\rho\Big) = \beta\partial_x\Big(A(x)A^T(x)\partial_x\rho\Big). \tag{5.15}$$

This gets mapped to a stochastic differential equation for the stochastic variable x_t [180],

$$dx_t = f(x_t)dt + \sqrt{2\beta}A(x_t)dW_t, \tag{5.16}$$

where W_t describes a Wiener process (Brownian motion). In Equation 5.15, ρ is the probability distribution for drawing the stochastic variable x_t, $\partial_x\Big(f(x)\rho\Big)$ is the drift term and $\beta\partial_x\Big(A(x)A^T(x)\partial_x\rho\Big)$ is the diffusion term. The Wigner function is a quasi-probability distribution mapping the wavefunction to a probability distribution in phase space. It could be easily shown that the one-dimensional form of the Equation 5.13 and 5.15 are of the same form,

$$\begin{aligned}\partial_t W &= \frac{i}{\hbar}\int dx\Big(L_{op}+V_\epsilon(x)\Big)\Big(\psi(x)\frac{\partial W}{\partial\psi(x)}-\psi^*(x)\frac{\partial W}{\partial\psi^*(x)}\Big),\\ &= \frac{i}{\hbar}\int dx\Big(L_{op}+V_\epsilon(x)\Big)\Big(\psi(x)\frac{\partial W}{\partial\psi(x)}+W-W-\psi^*(x)\frac{\partial W}{\partial\psi^*(x)}\Big),\\ &= \int dx\Big(\frac{\partial}{\partial\psi(x)}\Big(\frac{i}{\hbar}\Big(L_{op}+V_\epsilon(x)\Big)\psi(x)W\Big)+c.c.\Big).\end{aligned} \tag{5.17}$$

This leads to two stochastic differential equations for the fields ψ and ψ^* with no noise (quantum jumps), since $\beta = 0$

$$\begin{aligned}\psi_t &= -\frac{i}{\hbar}\Big(L_{op}+V_\epsilon(x)\Big)\psi_t dt,\\ \psi_t^* &= \frac{i}{\hbar}\Big(L_{op}+V_\epsilon(x)\Big)\psi_t^* dt.\end{aligned} \tag{5.18}$$

The Gross-Pitaevsksii equation for the polariton condensate is further adjusted by introducing a finite lifetime and decay out as photons from the microcavity, and generation of the polaritons by a source term proportional to an external pump laser intensity. The system can reach steady state when a continuous wave (CW) laser is tuned in wavelength to create excitons and exciton-polaritons at high energy, which then cool down into the condensate by stimulated scattering [57, 181, 40]. We also consider an exciton reservoir which is known to be present beyond the non-resonant pumping region [68] and provides an additional source of energy dissipation. Treating the exciton reservoir classically with free particle dispersion, the interactions between the polaritons and the excitons lead to a dissipative potential $V_\chi(x,t)$ of the same form as $V_\epsilon(x,t)$

$$V_\chi(\mathbf{r}) = -\frac{\hbar\beta_\chi g_\chi^2}{32\pi^3}\int d^2r' M_\chi(\mathbf{r}-\mathbf{r}')\vec{\nabla}'\cdot\mathbf{j}(\mathbf{r}'), \tag{5.19}$$

where $1/\beta_\chi$ is the temperature of the exciton reservoir, g_χ is the interaction strength between the excitons and the polaritons and $M_\chi(\mathbf{r}-\mathbf{r}')$ is the exciton-polariton scattering amplitude given by the Fourier transform $\tilde{M}_\chi(\mathbf{q})$

$$\tilde{M}_\chi(\mathbf{q}) = \frac{m_\chi^{3/2}}{\hbar^3}\sqrt{\frac{2\pi}{\beta_\chi}}e^{\beta_\chi\mu_\chi}\frac{e^{-\beta_\chi\hbar^2\mathbf{q}^2/8m_\chi}}{|\mathbf{q}|}, \tag{5.20}$$

where m_χ is the exciton mass and μ_χ is the exciton chemical potential. The exciton reservoir is unaffected by the application of the electric field in the quantum well.

The decay rate of the polaritons is included in Equation 5.14 by the imaginary term $-i\hbar\gamma\psi(x,t)/2$. The rate of generation of the polaritons by the pump $P(x,t)$ is included in the continuity relation for the condensate density $n(x,t) = |\psi(x,t)|^2$ as

$$\frac{dn(x,t)}{dt} = P(x,t) - \gamma n(x,t) - \frac{dj(x,t)}{dx}, \tag{5.21}$$

where $j(x,t)$ is the condensate current. Equations 5.14 and 5.21 describe an energy dissipative system with the particle number given by the balance between the generation and loss of polaritons. These equations are evolved for a long time until a steady state is reached under a CW pump.

A simple model is considered first to illustrate the effect of the drag potential on the condensate. By assuming very short polariton lifetime (2 ps) in a flat one dimensional wire we restrict the polaritons closer to the region of their generation because their population decays rapidly. They are produced on top of a hill due to the repulsion of the polaritons with the excitons at the pump location. When there is no drag potential, the expansion of the condensate is given by the kinetic and the repulsive polariton-polariton interactions as well as the generation and decay rate of the polaritons. This creates a population of the condensate extending outside the pump region. When the drag potential is introduced, the condensate density looks squeezed with more particles in the center than in the tails of the spatial profile, as shown in Figure 50. In Figure 50 we also see that the momentum distribution is altered when the drag potential is turned on. The drag potential slows down the velocity of the particles moving outwards as a result the maximum velocity reached by the particles is smaller when drag is present. A smaller velocity distribution of the particles implies that the particles cannot travel as much farther in their lifetime as when the drag

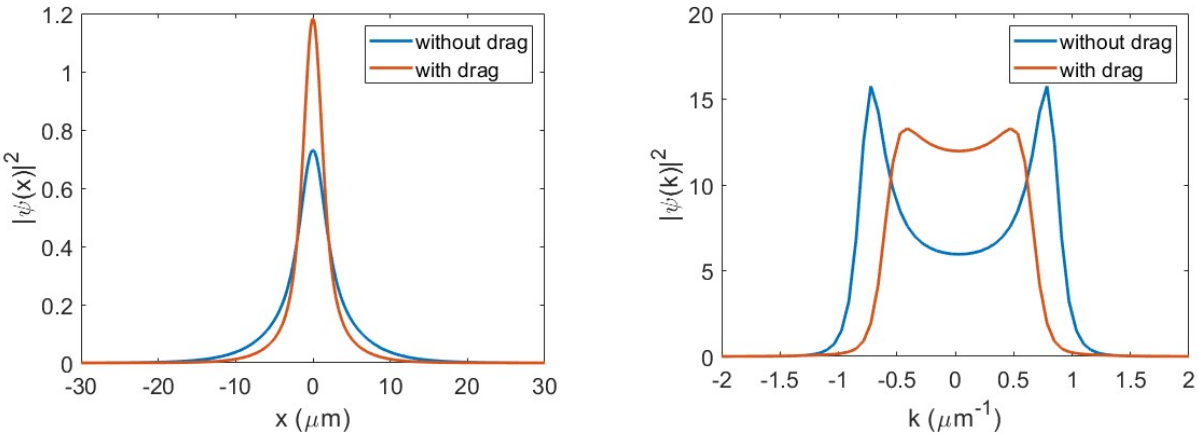

Figure 50: Example of the effect of the drag potential on a freely expanding polariton wavepacket in presence of a continuous generation and decay rates. The left figure compares the spatial profile of the wavepacket in presence and absence of the drag potential when a steady state has been reached. The right figure shows the momentum distribution of the steady state corresponding to the spatial profiles shown left.

is absent. This results in a shrunken tail of the condensate spatial distribution as seen in Figure 50. Another aspect of the drag potential is discussed in the next section, which gives an energy shift to the chemical potential of the condensate.

5.3 Polariton drag effect

The experiments reported in this section were performed in a straight wire microcavity which was fabricated by etching the top DBR layers and exposing the quantum wells. Two NiAuGe contacts were then placed upon the quantum wells at the ends of the wire, allowing electrical current to flow through the quantum wells. A simple schematic of the experimental setup is shown in Figure 51. More details of the experiment are given in reference [154]. For our purposes here, the system can be modeled as follows. First, a tightly-focused pump spot

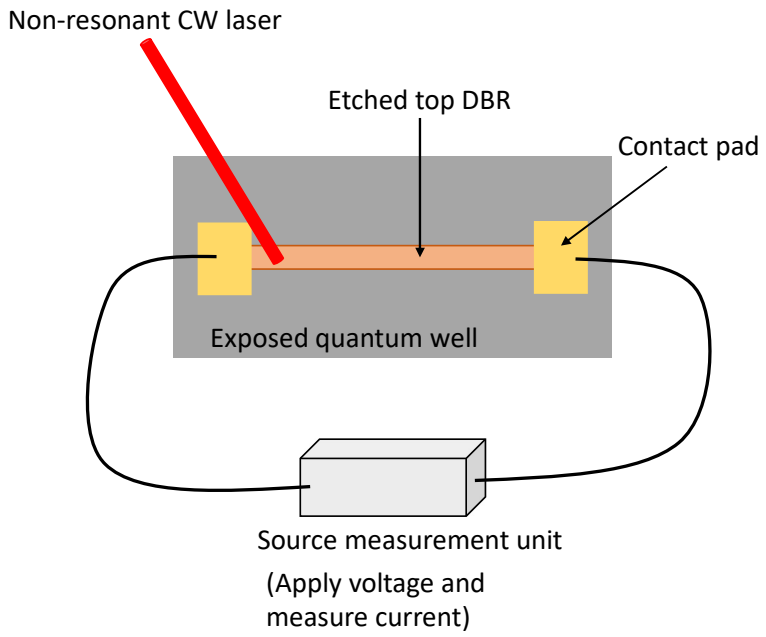

Figure 51: Top view sketch of the polariton wire fabricated by etching the top DBR layers. Polariton condensate is created in the wire by pumping non-resonantly with a CW laser near one of the edges of the wire. A current is driven through the wire by applying voltages at the two ends of the wire as shown above.

generated polaritons near one end, but not exactly at the end, of a one-dimensional (1D) wire. Free excitons generated by the laser (in addition to the condensate polaritons) created a potential energy maximum felt by the polaritons at that point, since the excitons have a strong repulsion on the polaritons. Some of these excitons diffuse away from the pump spot [67], giving a smeared-out spatial peak that repels the polariton condensate. An example of an effective potential experienced by the polaritons in the wire, used in the numerical model, is shown in Figure 52.

The polariton condensate flows away from this generation spot in both directions along the 1D wire. At the end of the wire nearest to the pump spot, a local trap is formed for the condensate, in which the condensate velocity is nearly zero; on the other side, which has much longer distance for the condensate to travel, a steady-state flow is set up in which the polaritons have net velocity away from the pump spot, as they are continuously gen-

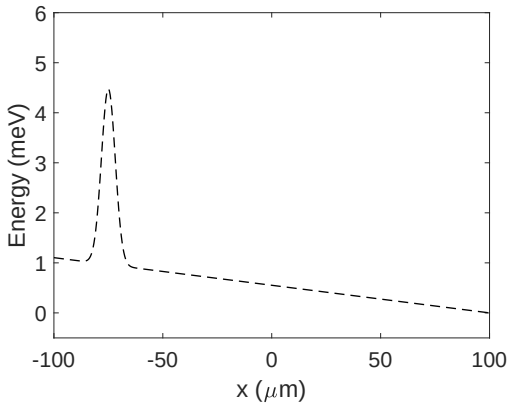

Figure 52: Static potential felt by the polaritons in the wire due to the overall cavity gradient and the exciton hill created by the non-resonant pump. The ends of the wire are modeled as a hard wall.

erated at the pump spot and then decay away as they travel. Angle-resolved spectroscopy experimentally determined the average momentum of this moving condensate [154]. Electric current was introduced into the same structure in which the optically-generated condensate flowed, using electrical contacts. The energy of both the extended as well as the localized condensate were found to shift in response to the magnitude and direction of the electric current. Examples of typical average momentum shifts observed in the PL on applying voltage in the wire are shown in Figure 53. In the experiments no energy shift was observed at the location of the pump spot, which is primarily composed of excitons, any excitonic mechanism contributing to the energy shifts of the condensate due to the variation of the exciton density could be ruled out.

Real-space, time-integrated spectra of the condensate moving to the right (positive x-direction) in the wire is shown in the top row of Figure 54. These data were taken by energy resolving the PL using a grating. The PL was collected from the region in the wire away from the pump spot. Results from the model developed here is shown in the bottom row. From the experimental spectra it is evident that the energy of the steady state condensate is continuously dropping as it travels along the wire. Similar feature is seen in our model

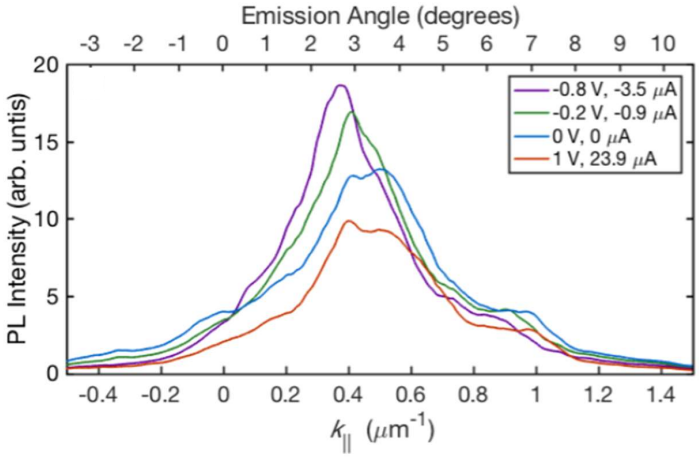

Figure 53: PL intensity vs. $k_{||}$ at various applied voltages, taken by integrating along the energy axis in spectral images recorded in the CCD. Figure taken from Ref. [154].

where the energy dissipation is caused by the drag potential. Since in the model we assumed a longer polariton lifetime (200 ps), the condensate reaches the end of the wire, which is also the minimum energy in the wire and accumulates there. In the actual wires due to the strain at the end of the wire there is a small trap as shown in Figure 55 where polaritons could be seen accumulating. Since the condensate is moving to the right, the net momentum is non-zero and positive as shown in the Figure 53 with no applied voltage. When a negative voltage is applied, the moving electrons apply a force on the condensate to the left, which slows down the condensate. Conversely, when a positive voltage is applied the condensate receives a kick from the moving electron reservoir and the net momentum is increased. These features are shown in Figure 53. We now compare the energy shifts of the condensate observed in the real space spectra when the reservoir is moving. The electron concentration can be considered homogeneous, therefore it will result only in a uniform blue shift of the energy of the condensate. As the photoluminiscence intensity, which directly indicates the density of the condensate, was not found to be significantly different for different applied voltages, we can rule out the shifts in the condensate energy due to the polariton-polariton and polariton-exciton interactions. What remains is the effect of the real-valued effective

potential derived for the electron drag in the previous section of this chapter.

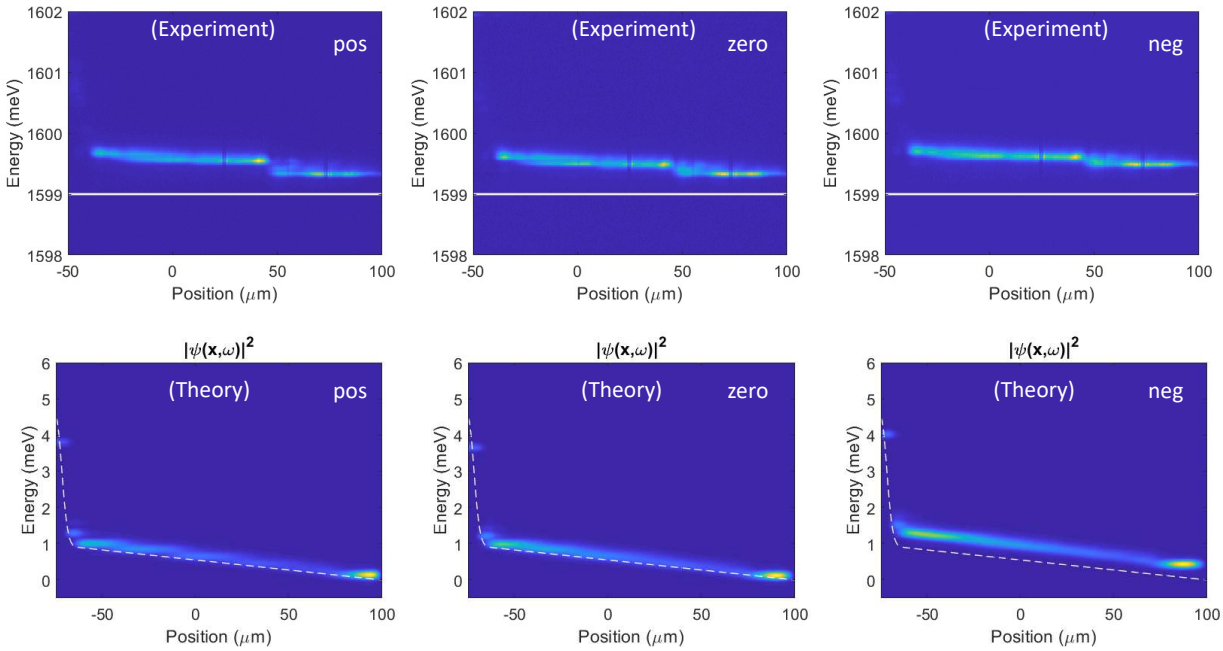

Figure 54: Top row: Experimental time-integrated spectra of the condensate along the wire for different relative velocities of the electron reservoir. The solid white line serves as a guide to the eye for observing the changes in the condensate energy. Bottom row: Real space spectra obtained by the Fourier transform of the late time wavefunction in a temporal window and averaged over many such windows. In the simulation, the parameters used were $m_\psi = 1 \times 10^{-4} m_e$, $U = 10\ \mu eV \mu m^2$, $v_{rel} = 1 \times 10^5$ m/s. Exciton drag potential was included which did not responded to the applied electric field in the quantum well in addition to the electron drag potential to observe the energy shifts in the model. The strength of the exciton drag potential was chosen to be a quarter of the electron drag potential in this simulation. Each image is plotted on a normalized color scale from 0 - 1.

In a closed system with no particle generation or loss, the drag potential will cause any excited state of a trapping potential to evolve towards the stationary ground state of the trap. Once this state is reached, the drag potential becomes zero since there is no net current in this state. The scenario discussed in this section is different since the condensate in the trap

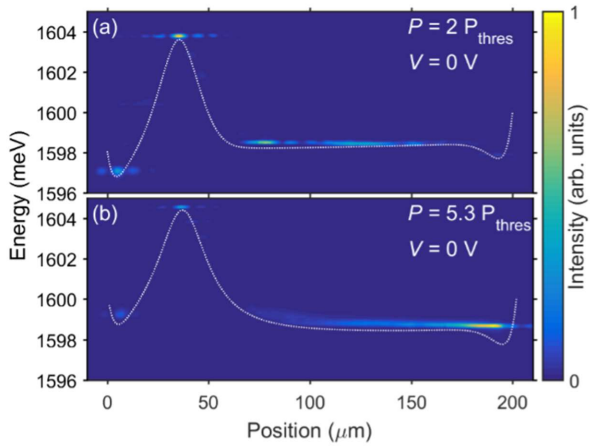

Figure 55: PL intensity vs. energy and position along the length of the wire at zero applied voltage for two different pumping rates. The white dotted lines give the outline of the potential felt by the polaritons. The PL intensity was normalized separately for each image. Figure taken from Ref. [154].

does not reach the stationary ground state of the trap, instead it reaches a non-equilibrium steady state. In this state, the drag potential is non-zero since there is a finite inhomogeneous particle current in the condensate. By creating a moving reservoir we probe the change in the drag potential which gives an energy shift to the condensate. This is clearly seen in Figures 54 and 56. There is relative shift of the energy of the condensate with respect to the stationary reservoir scenario when the reservoir is either co-moving with the condensate or moving in the opposite direction. Moreover, the shift in the energy is not symmetric for the motion of the electron reservoir in the same and the opposite directions to the motion of the condensate. This asymmetric shift could be understood as due to the different velocities seen by the condensate in the rest frame of the reservoir, when the reservoir moves with or against the condensate.

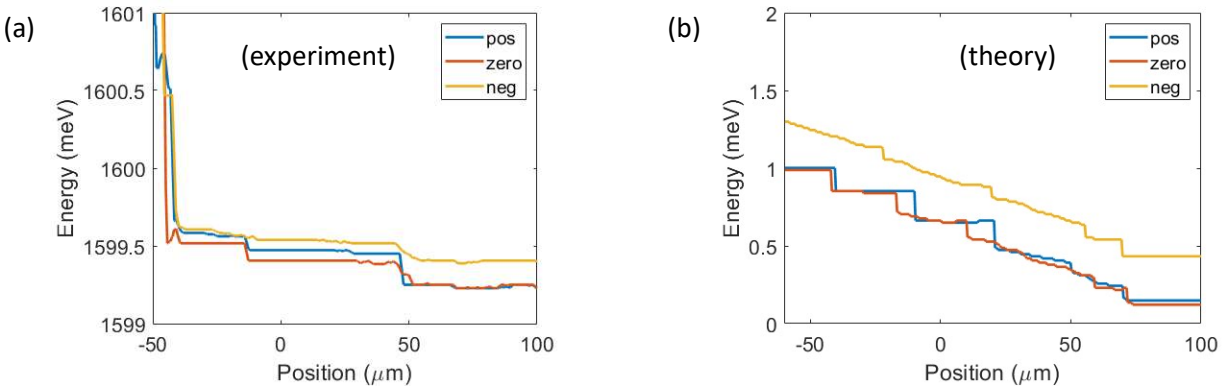

Figure 56: Trace of the spectral energy of the condensate in the wire shown in Figure 54 for the three different cases considered, highlighting the energy shifts.

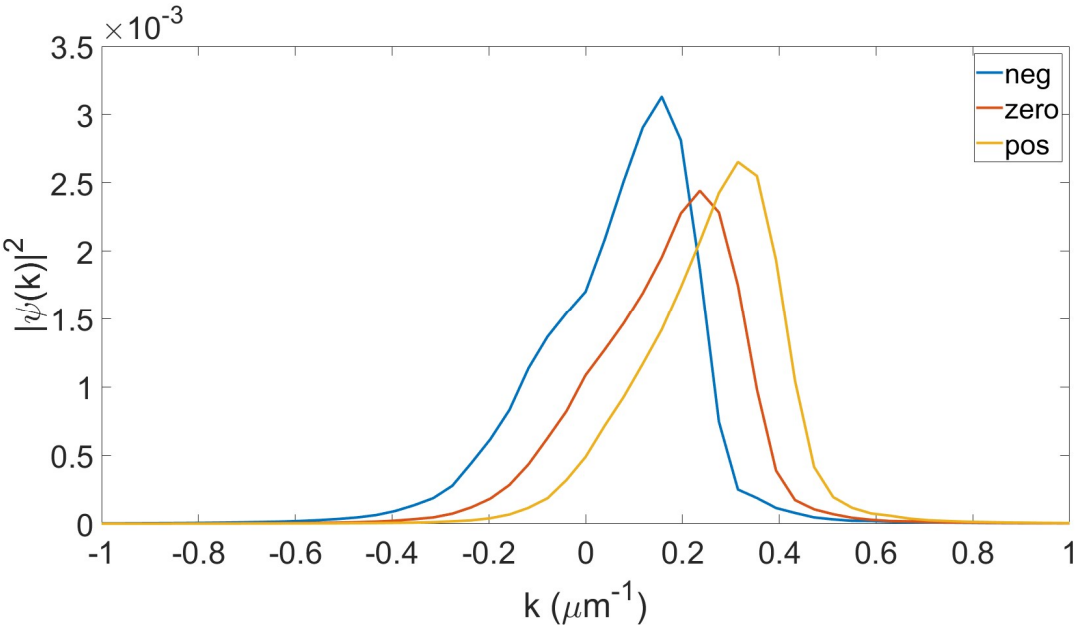

Figure 57: Time-integrated average momentum of the condensate corresponding to the theory plots in Figure 54. For comparison with the experiments see Figure 53.

5.4 Conclusion

We have shown that the general theory for dissipation of a nonequilibrium condensate can be directly adapted to describe the case of a steady-state condensate with net current of a different species passing through it. This theory directly reproduces the experimental results for polariton drag, that is, the direct effect of DC electric current on the velocity and energy of neutral polaritons. The same theory underlies the cooling of a nonequilibrium condensate, which has been observed experimentally in a ring geometry [68].

The general picture that emerges from this theoretical model is one in which the condensate keeps its overall coherence, and is well described by a modified Gross-Pitaevskii equation for a single-valued wave function, but still undergoes energy damping and drift force, which are modeled in the Gross-Pitaevskii equation by introducing a real term for an effective potential due to the drift force, which has been the subject of this chapter. More common way of introducing energy damping is through an imaginary term [146] which also arise from the same underlying theory of interaction of the condensate with an incoherent reservoir and adapted in the previous chapters for modelling energy loss in the system.

5.5 Supplementary information

5.5.1 Quantum master equation

In this Supplementary information we will fill the steps between (5.6) and (5.7). As mentioned earlier, we'll assume that at the initial time the electrons and the polaritons are uncorrelated implying that we could represent the density matrix at $t = 0$ as a direct product of the two subsystems $\rho_I(0) = \rho_\psi \otimes \rho_\phi$. With this let us now unpack the first term of (5.6),

$$Tr_\phi\left[-\frac{i}{\hbar}\Big[H_{int}(t), \rho_I(0)\Big]\right] = -\frac{ig}{\hbar}\int d^2r Tr_\phi\left[\Big[\psi^\dagger(\mathbf{r},t)\phi^\dagger(\mathbf{r},t)\phi(\mathbf{r},t)\psi(\mathbf{r},t), \rho_\psi \otimes \rho_\phi\Big]\right]. \quad (5.22)$$

Using the cyclic property of the trace we can simplify the above expression to

$$Tr_\phi\left[-\frac{i}{\hbar}\Big[H_{int}(t), \rho_I(0)\Big]\right] = -\frac{ig}{\hbar}\int d^2r Tr_\phi\Big[\phi^\dagger(\mathbf{r},t)\phi(\mathbf{r},t)\rho_\phi\Big] \otimes \Big[\psi^\dagger(\mathbf{r},t)\psi(\mathbf{r},t), \rho_\psi\Big]. \quad (5.23)$$

We recall from the definition of $H_{int}(t)$ above that $\phi^\dagger(\mathbf{r},t)\phi(\mathbf{r},t) = e^{iH_\phi t/\hbar}\phi^\dagger(\mathbf{r})\phi(\mathbf{r})e^{-iH_\phi t/\hbar}$ and again using the cyclic property of the trace we can write the trace term as,

$$Tr_\phi\Big[\phi^\dagger(\mathbf{r},t)\phi(\mathbf{r},t)\rho_\phi\Big] = Tr_\phi\Big[\phi^\dagger(\mathbf{r})\phi(\mathbf{r})e^{-iH_\phi t/\hbar}\rho_\phi e^{iH_\phi t/\hbar}\Big]. \tag{5.24}$$

The time dependence in the above trace drops out because $\Big[H_\phi, \rho_\phi\Big] = 0$. Now let us make an assumption that the electron reservoir remains in the thermal equilibrium at all times, which would imply that

$$Tr_\phi\Big[\phi^\dagger(\mathbf{r})\phi(\mathbf{r})\rho_\phi\Big] = n_\phi(\mathbf{r}), \tag{5.25}$$

where $n_\phi(\mathbf{r})$ is the local density of the reservoir. Putting this back in Equation (12),

$$Tr_\phi\Bigg[-\frac{i}{\hbar}\Big[H_{int}(t), \rho_I(0)\Big]\Bigg] = -\frac{ig}{\hbar}\int d^2r n_\phi(\mathbf{r})\Big[\psi^\dagger(\mathbf{r},t)\psi(\mathbf{r},t), \rho_\psi\Big]. \tag{5.26}$$

We have already absorbed this term in the definition of H_ψ as given in (5.2). Let us now simplify the commutator in the second term in (5.6)

$$\begin{aligned}\Bigg[H_{int}(t), \Big[H_{int}(t'), \rho_I(t')\Big]\Bigg] &= H_{int}(t)H_{int}(t')\rho_I(t') - H_{int}(t)\rho_I(t')H_{int}(t') \\ &\quad - H_{int}(t')\rho_I(t')H_{int}(t) + \rho_I(t')H_{int}(t')H_{int}(t).\end{aligned} \tag{5.27}$$

$$H_{int}(t)H_{int}(t')\rho_I(t') = g^2\int d^2r\int d^2r'\psi^\dagger(1)\phi^\dagger(1)\phi(1)\psi(1)\psi^\dagger(2)\phi^\dagger(2)\phi(2)\psi(2)\rho_I(t') \tag{5.28}$$

where we have used a short hand notation, $1 = (\mathbf{r}, t)$ and $2 = (\mathbf{r}', t')$. Taking partial trace on this term gives,

$$g^2\int d^2r\int d^2r'\psi^\dagger(1)\psi(1)\psi^\dagger(2)\psi(2)Tr_\phi\Big[\phi^\dagger(1)\phi(1)\phi^\dagger(2)\phi(2)\rho_I(t')\Big]. \tag{5.29}$$

Similarly the other terms in (5.27) could be simplified as,

$$-H_{int}(t)\rho_I(t')H_{int}(t') = -g^2\int d^2r\int d^2r'\psi^\dagger(1)\phi^\dagger(1)\phi(1)\psi(1)\rho_I(t')\psi^\dagger(2)\phi^\dagger(2)\phi(2)\psi(2) \tag{5.30}$$

Taking partial trace on this term gives,

$$-g^2\int d^2r\int d^2r'\psi^\dagger(1)\psi(1)Tr_\phi\Big[\phi^\dagger(1)\phi(1)\rho_I(t')\phi^\dagger(2)\phi(2)\Big]\psi^\dagger(2)\psi(2). \tag{5.31}$$

The third term $-H_{int}(t')\rho_I(t')H_{int}(t)$ simplifies to

$$-H_{int}(t')\rho_I(t')H_{int}(t) = -g^2 \int d^2r \int d^2r' \psi^\dagger(2)\phi^\dagger(2)\phi(2)\psi(2)\rho_I(t')\psi^\dagger(1)\phi^\dagger(1)\phi(1)\psi(1). \tag{5.32}$$

Taking partial trace we find,

$$-g^2 \int d^2r \int d^2r' \psi^\dagger(2)\psi(2) Tr_\phi\Big[\phi^\dagger(2)\phi(2)\rho_I(t')\phi^\dagger(1)\phi(1)\Big]\psi^\dagger(1)\psi(1). \tag{5.33}$$

Finally, the fourth term is

$$\rho_I(t')H_{int}(t')H_{int}(t) = g^2 \int d^2r \int d^2r' \rho_I(t')\psi^\dagger(2)\phi^\dagger(2)\phi(2)\psi(2)\psi^\dagger(1)\phi^\dagger(1)\phi(1)\psi(1) \tag{5.34}$$

which after taking trace gives

$$g^2 \int d^2r \int d^2r' Tr_\phi\Big[\rho_I(t')\phi^\dagger(2)\phi(2)\phi^\dagger(1)\phi(1)\Big]\psi^\dagger(2)\psi(2)\psi^\dagger(1)\psi(1). \tag{5.35}$$

Let us introduce another short hand notation for the trace

$$Tr_\phi(12) = Tr_\phi\Big[\phi^\dagger(1)\phi(1)\phi^\dagger(2)\phi(2)\rho_I(t')\Big], \tag{5.36}$$

$$Tr_\phi(21) = Tr_\phi\Big[\phi^\dagger(2)\phi(2)\phi^\dagger(1)\phi(1)\rho_I(t')\Big]. \tag{5.37}$$

Using the cyclic property of the trace we can combine terms (5.29) and (5.33) into

$$g^2 \int d^2r \int d^2r' \Big[\psi^\dagger(1)\psi(1), \psi^\dagger(2)\psi(2) Tr_\phi(12)\Big]. \tag{5.38}$$

Similarly combining terms (5.31) and (5.35) gives

$$g^2 \int d^2r \int d^2r' \Big[Tr_\phi(21)\psi^\dagger(2)\psi(2), \psi^\dagger(1)\psi(1)\Big]. \tag{5.39}$$

To make further progress we'll make assumptions about $\rho_I(t')$. First we assume that the interactions are weak so that correlations between the reservoir and the polaritons are small even at long time scales. This motivates us to approximate $\rho_I(t') \approx \rho^I_\psi(t') \otimes \rho_\phi$. Secondly we'll assume that the energy separation scale between the electrons and the polaritons is large. This will result in a much slower evolution of $\rho^I_\psi(t')$ allowing us to replace $\rho^I_\psi(t') \to \rho^I_\psi(t)$ in the time integral. This approximation is also known as the Markov approximation because

it says that the evolution of the density matrix depends on the instantaneous state of the system and makes no reference to the past. We'll introduce another notation for the trace in terms of calculating thermal reservoir average, $Tr_\phi[\rho_\phi \ . \ ] = \langle \ . \ \rangle$. Therefore the above expressions will approximate to,

$$g^2 \int d^2r \int d^2r' \Big[\psi^\dagger(1)\psi(1), \psi^\dagger(2)\psi(2)\rho^I_\psi(t)\Big] \otimes \langle \phi^\dagger(1)\phi(1)\phi^\dagger(2)\phi(2)\rangle \tag{5.40}$$

$$g^2 \int d^2r \int d^2r' \Big[\rho^I_\psi(t)\psi^\dagger(2)\psi(2), \psi^\dagger(1)\psi(1)\Big] \otimes \langle \phi^\dagger(2)\phi(2)\phi^\dagger(1)\phi(1)\rangle \tag{5.41}$$

Let us now simplify the temporal part of the reservoir correlation function

$$\begin{aligned}
\langle \phi^\dagger(2)\phi(2)\phi^\dagger(1)\phi(1)\rangle =& \langle e^{iH_\phi t'/\hbar}\phi^\dagger(\mathbf{r}')\phi(\mathbf{r}')e^{-iH_\phi t'/\hbar}e^{iH_\phi t/\hbar}\phi^\dagger(\mathbf{r})\phi(\mathbf{r})e^{-iH_\phi t/\hbar}\rangle \\
&= \langle \phi^\dagger(\mathbf{r}')\phi(\mathbf{r}')e^{-iH_\phi t'/\hbar}e^{iH_\phi t/\hbar}\phi^\dagger(\mathbf{r})\phi(\mathbf{r})e^{-iH_\phi t/\hbar}e^{iH_\phi t'/\hbar}\rangle \\
&= \langle \phi^\dagger(\mathbf{r}')\phi(\mathbf{r}')e^{iH_\phi (t-t')/\hbar}\phi^\dagger(\mathbf{r})\phi(\mathbf{r})e^{-iH_\phi (t-t')/\hbar}\rangle \\
&= \langle \phi^\dagger(\mathbf{r}',0)\phi(\mathbf{r}',0)\phi^\dagger(\mathbf{r},\tau)\phi(\mathbf{r},\tau)\rangle,
\end{aligned} \tag{5.42}$$

where we have defined $\tau = t - t'$. Repeating the same steps we have

$$\langle \phi^\dagger(1)\phi(1)\phi^\dagger(2)\phi(2)\rangle = \langle \phi^\dagger(\mathbf{r},\tau)\phi(\mathbf{r},\tau)\phi^\dagger(\mathbf{r}',0)\phi(\mathbf{r}',0)\rangle. \tag{5.43}$$

Also the commutators in the expressions (5.40) and (5.41) would be,

$$\begin{aligned}
\Big[\psi^\dagger(1)\psi(1), \psi^\dagger(2)\psi(2)\rho^I_\psi(t)\Big] &= \Big[\psi^\dagger(\mathbf{r},t)\psi(\mathbf{r},t), \psi^\dagger(\mathbf{r}',t-\tau)\psi(\mathbf{r}',t-\tau)\rho^I_\psi(t)\Big] \\
&= \Big[\hat{n}_\psi(\mathbf{r},t), \hat{n}_\psi(\mathbf{r}',t-\tau)\rho^I_\psi(t)\Big]
\end{aligned} \tag{5.44}$$

$$\begin{aligned}
\Big[\rho^I_\psi(t)\psi^\dagger(2)\psi(2), \psi^\dagger(1)\psi(1)\Big] &= \Big[\rho^I_\psi(t)\psi^\dagger(\mathbf{r}',t-\tau)\psi(\mathbf{r}',t-\tau), \psi^\dagger(\mathbf{r},t)\psi(\mathbf{r},t)\Big] \\
&= \Big[\rho^I_\psi(t)\hat{n}_\psi(\mathbf{r}',t-\tau), \hat{n}_\psi(\mathbf{r},t)\Big]
\end{aligned} \tag{5.45}$$

Going back to the reservoir correlation functions we'll apply Hartree Fock factorization to express the four field correlation function as a product of two field correlators. Keeping in mind that the anti-commutation relation results in a negative sign for odd number of field exchanges, we see that the only relevant factorization involves even exchanges. We'll drop anomalous paired correlators like $\langle \phi^\dagger\phi^\dagger\rangle$ and $\langle \phi\phi\rangle$ because they don't conserve particle

number. Also equal time correlators like $\langle\phi^\dagger\phi\rangle$ will be dropped because they are time independent, which will lead to incorrect energy conservation relation as seen after doing the integral w.r.t. τ. Therefore correlators (5.42) and (5.43) simplify to

$$\langle\phi^\dagger(\mathbf{r}',0)\phi(\mathbf{r}',0)\phi^\dagger(\mathbf{r},\tau)\phi(\mathbf{r},\tau)\rangle = \langle\phi^\dagger(\mathbf{r}',0)\phi(\mathbf{r},\tau)\rangle\langle\phi(\mathbf{r}',0)\phi^\dagger(\mathbf{r},\tau)\rangle \tag{5.46}$$

$$\langle\phi^\dagger(\mathbf{r},\tau)\phi(\mathbf{r},\tau)\phi^\dagger(\mathbf{r}',0)\phi(\mathbf{r}',0)\rangle = \langle\phi^\dagger(\mathbf{r},\tau)\phi(\mathbf{r}',0)\rangle\langle\phi(\mathbf{r},\tau)\phi^\dagger(\mathbf{r}',0)\rangle \tag{5.47}$$

We can evaluate the above correlation functions by introducing the field operator for the electrons,

$$\phi(\vec{r},t) = \frac{1}{L}\sum_k e^{i(\vec{k}.\vec{r}-\omega_k t)}b_{\vec{k}}. \tag{5.48}$$

The plane wave basis is chosen since the electrons are assumed to be propagating freely in the quantum well. The density of the free electrons are assumed to be low such that we can ignore the repulsive interactions between them. Thermal expectation value for the operator $b^\dagger_{\vec{k}}b_{\vec{k}}$ is given by,

$$\langle b^\dagger_{\vec{k}}b_{\vec{k}}\rangle = \sum_{\vec{k}} n_{\vec{k}} = \frac{L^2}{4\pi^2}\int d^2k \frac{1}{e^{(E_\phi(\vec{k})-\mu)/k_BT}+1} \tag{5.49}$$

where $E_\phi(\vec{k})/\hbar = \omega_{\vec{k}} = \hbar\vec{k}^2/2m_\phi$. Calculating products of the field operators at different space and time coordinates is straightforward,

$$\phi^\dagger(\mathbf{r}',t')\phi(\mathbf{r},t) = \frac{1}{L^2}\sum_{\vec{k},\vec{k}'} b^\dagger_{\vec{k}'}b_{\vec{k}}e^{-i\vec{k}'\cdot\vec{r}'+i\vec{k}\cdot\vec{r}-i\omega_{\vec{k}}t+i\omega_{\vec{k}'}t'}. \tag{5.50}$$

Using these we can now look at the correlators,

$$\begin{aligned}\langle\phi^\dagger(\mathbf{r}',0)\phi(\mathbf{r},\tau)\rangle &= \frac{1}{L^2}\sum_{\vec{k},\vec{k}'}\langle b^\dagger_{\vec{k}'}b_{\vec{k}}\rangle e^{-i\vec{k}'.\vec{r}'+i\vec{k}.\vec{r}-i\omega_{\vec{k}}\tau} \\ &= \frac{1}{L^2}\sum_{\vec{k},\vec{k}'} n_{\vec{k}}\delta_{\vec{k},\vec{k}'}e^{-i\vec{k}'.\vec{r}'+i\vec{k}.\vec{r}-i\omega_{\vec{k}}\tau} \\ &= \frac{1}{4\pi^2}\int d^2k n_{\vec{k}}e^{i\vec{k}.(\vec{r}-\vec{r}')-iE_\phi\tau/\hbar}.\end{aligned} \tag{5.51}$$

$$\begin{aligned}
\langle\phi(\mathbf{r}',0)\phi^\dagger(\mathbf{r},\tau)\rangle &= \frac{1}{L^2}\sum_{\vec{k},\vec{k}'}\langle b_{\vec{k}'}b^\dagger_{\vec{k}}\rangle e^{i\vec{k}'.\vec{r}'-i\vec{k}.\vec{r}+i\omega_{\vec{k}}\tau} \\
&= \frac{1}{L^2}\sum_{\vec{k},\vec{k}'}\Big(1-n_{\vec{k}}\Big)\delta_{k,k'}e^{i\vec{k}'.\vec{r}'-i\vec{k}.\vec{r}+i\omega_{\vec{k}}\tau} \qquad (5.52)\\
&= \frac{1}{4\pi^2}\int d^2k\Big(1-n_{\vec{k}}\Big)e^{-i\vec{k}.(\vec{r}-\vec{r}')+iE_\phi\tau/\hbar}.\\
\langle\phi^\dagger(\mathbf{r},\tau)\phi(\mathbf{r}',0)\rangle &= \frac{1}{L^2}\sum_{\vec{k},\vec{k}'}\langle b^\dagger_{\vec{k}}b_{k'}\rangle e^{i\vec{k}'.\vec{r}'-i\vec{k}.\vec{r}+i\omega_{\vec{k}}\tau} \\
&= \frac{1}{L^2}\sum_{\vec{k},\vec{k}'}n_{\vec{k}}\delta_{\vec{k},\vec{k}'}e^{i\vec{k}'.\vec{r}'-i\vec{k}.\vec{r}+i\omega_{\vec{k}}\tau} \qquad (5.53)\\
&= \frac{1}{4\pi^2}\int d^2k n_{\vec{k}}e^{-i\vec{k}.(\vec{r}-\vec{r}')+iE_\phi\tau/\hbar}.\\
\langle\phi(\mathbf{r},\tau)\phi^\dagger(\mathbf{r}',0)\rangle &= \frac{1}{L^2}\sum_{\vec{k},\vec{k}'}\langle b_{\vec{k}}b^\dagger_{\vec{k}'}\rangle e^{-i\vec{k}'.\vec{r}'+i\vec{k}.\vec{r}-i\omega_{\vec{k}}\tau} \\
&= \frac{1}{L^2}\sum_{\vec{k},\vec{k}'}\Big(1-n_{\vec{k}}\Big)\delta_{\vec{k},\vec{k}'}e^{-i\vec{k}'.\vec{r}'+i\vec{k}.\vec{r}-i\omega_k\tau} \qquad (5.54)\\
&= \frac{1}{4\pi^2}\int d^2k\Big(1-n_{\vec{k}}\Big)e^{i\vec{k}.(\vec{r}-\vec{r}')-iE_\phi\tau/\hbar}.
\end{aligned}$$

With the definition $n_{\vec{k}} = F(\mathbf{k}) = 1/(e^{(E_\phi(\vec{k})-\mu)/k_BT}+1)$ and using the above results we can write (5.46) as

$$\frac{1}{(2\pi)^4}\int d^2k_1\int d^2k_2F(\mathbf{k_1})\Big(1-F(\mathbf{k_2})\Big)e^{i(\mathbf{k_1}-\mathbf{k_2}).(\mathbf{r}-\mathbf{r}')-i(E_\phi(\mathbf{k_1})-E_\phi(\mathbf{k_2}))\tau/\hbar}, \qquad (5.55)$$

and (5.47) as

$$\frac{1}{(2\pi)^4}\int d^2k_1\int d^2k_2F(\mathbf{k_1})\Big(1-F(\mathbf{k_2})\Big)e^{-i(\mathbf{k_1}-\mathbf{k_2}).(\mathbf{r}-\mathbf{r}')+i(E_\phi(\mathbf{k_1})-E_\phi(\mathbf{k_2}))\tau/\hbar}. \qquad (5.56)$$

In expressions (5.44) and (5.45) we could define an operator $\hat{L}_\psi$ whose action is defined through $\hat{L}_\psi\hat{n}_\psi(\mathbf{r}') = [\hat{n}_\psi(\mathbf{r}'), H_\psi]$, which leads to $\hat{n}_\psi(\mathbf{r}',t) = e^{-i\hat{L}_\psi t/\hbar}\hat{n}_\psi(\mathbf{r}')$. We will make a change of variable for the integral over t' in equation (5.6),

$$\int_0^t t' \to \int_0^t d\tau \qquad (5.57)$$

and also set the upper limit of the integral to ∞. This is done with a presumption that if we wait long enough we can recover energy and momentum conserving scattering between

the coherent polaritons and the reservoir. This is usually true if $t \gg$ correlation time of the reservoir. Doing the τ integral one obtains for product of the expressions (5.44) and (5.56),

$$\hbar\pi\delta\left(\hat{L}_\psi + E_\phi(\mathbf{k_1}) - E_\phi(\mathbf{k_2})\right) \tag{5.58}$$

and for (5.45) and (5.55)

$$\hbar\pi\delta\left(\hat{L}_\psi - E_\phi(\mathbf{k_1}) + E_\phi(\mathbf{k_2})\right). \tag{5.59}$$

We have now calculated everything we need to put back in equation (5.6) to obtain (5.7).

5.5.2 Weyl-Wigner transformations

Strings of quantum operators appearing in Equation (5.11) are mapped to classical variables using Wigner-Weyl transformations. Readers are directed to references [172, 179] for an introduction to semi-classical transformations which are used in studying quantum dynamics using phase space methods. In this section we simply provide the transformation rules for the three types of terms which are encountered while expanding the commutator in Equation (5.11).

$$\begin{aligned}
\psi^\dagger\psi\psi^\dagger\psi\rho &\longrightarrow \left(\psi^* - \frac{1}{2}\partial_\psi\right)\left(\psi + \frac{1}{2}\partial_{\psi^*}\right)\left(\psi^* - \frac{1}{2}\partial_\psi\right)\left(\psi + \frac{1}{2}\partial_{\psi^*}\right)W(\psi,\psi^*) \\
\psi^\dagger\psi\rho\psi^\dagger\psi &\longrightarrow \left(\psi^* - \frac{1}{2}\partial_\psi\right)\left(\psi + \frac{1}{2}\partial_{\psi^*}\right)\left(\psi - \frac{1}{2}\partial_{\psi^*}\right)\left(\psi^* + \frac{1}{2}\partial_\psi\right)W(\psi,\psi^*) \\
\rho\psi^\dagger\psi\psi^\dagger\psi &\longrightarrow \left(\psi - \frac{1}{2}\partial_{\psi^*}\right)\left(\psi^* + \frac{1}{2}\partial_\psi\right)\left(\psi - \frac{1}{2}\partial_{\psi^*}\right)\left(\psi^* + \frac{1}{2}\partial_\psi\right)W(\psi,\psi^*).
\end{aligned} \tag{5.60}$$

5.5.3 Calculation of the scattering amplitude $M(\mathbf{r} - \mathbf{r}')$

In this section we consider a general case of the electron reservoir drifting with a momentum $\hbar\mathbf{k_0}$, such that the energy of the electrons are now given by $E(\mathbf{k}) = \hbar^2(\mathbf{k} - \mathbf{k_0})^2/2m_\phi$.

We evaluate the scattering amplitude $M(\mathbf{r}-\mathbf{r}') = M(\mathbf{v})$ by defining the Fourier transform $\tilde{M}(\mathbf{q})$ which is given by,

$$\begin{aligned}
\tilde{M}(\mathbf{q}) &= \frac{1}{(2\pi)^2}\int d^2v M(\mathbf{v}) e^{-i\mathbf{q}\cdot\mathbf{v}} \\
&= \frac{1}{(2\pi)^2}\int d^2v d^2k_1 d^2k_2 F(\boldsymbol{k_1})\Big(1-F(\boldsymbol{k_2})\Big)\delta\left(E_\phi(\boldsymbol{k_1})-E_\phi(\boldsymbol{k_2})\right) e^{i(\boldsymbol{k_1}-\boldsymbol{k_2}-\mathbf{q})\cdot\mathbf{v}} \\
&= \int d^2k_1 d^2k_2 F(\boldsymbol{k_1})\Big(1-F(\boldsymbol{k_2})\Big)\delta\left(E_\phi(\boldsymbol{k_1})-E_\phi(\boldsymbol{k_2})\right)\delta\big(\boldsymbol{k_1}-\boldsymbol{k_2}-\mathbf{q}\big) \\
&= \int d^2k_1 F(\boldsymbol{k_1})\Big(1-F(\boldsymbol{k_1}-\mathbf{q})\Big)\delta\left(E_\phi(\boldsymbol{k_1})-E_\phi(\boldsymbol{k_1}-\mathbf{q})\right) \\
&= \frac{m_\phi}{\hbar^2}\int d^2k_1 F(\boldsymbol{k_1})\Big(1-F(\boldsymbol{k_1}-\mathbf{q})\Big)\delta\left(\mathbf{k_1}\cdot\mathbf{q}-\frac{\mathbf{q}^2}{2}-\mathbf{k_0}\cdot\mathbf{q}\right) \\
&= \frac{m_\phi}{\hbar^2}\int d^2k_1 F(\boldsymbol{k_1})\Big(1-F(\boldsymbol{k_1})\Big)\delta\left(\mathbf{k_1}\cdot\mathbf{q}-\frac{\mathbf{q}^2}{2}-\mathbf{k_0}\cdot\mathbf{q}\right) \\
&= \frac{m_\phi}{\hbar^2}\int d^2k_1 F(\boldsymbol{k_1})\Big(1-F(\boldsymbol{k_1})\Big)\frac{1}{|\mathbf{q}|}\delta\left(\mathbf{k_1}\cdot\hat{\mathbf{q}}-\frac{|\mathbf{q}|}{2}-\mathbf{k_0}\cdot\hat{\mathbf{q}}\right) \\
&= \frac{m_\phi}{\hbar^2}\int dk_1^{||} dk_1^{\perp} F(\boldsymbol{k_1}^{\parallel}+\mathbf{k_1}^{\perp})\Big(1-F(\boldsymbol{k_1}^{\parallel}+\mathbf{k_1}^{\perp})\Big)\frac{1}{|\mathbf{q}|}\delta\left(k_1^{||}-\frac{|\mathbf{q}|}{2}-k_0^{||}\right) \\
&= \frac{m_\phi}{\hbar^2}\int dk_1^{\perp} F\Big(\frac{\mathbf{q}}{2}+\mathbf{k_0}^{||}+\mathbf{k_1}^{\perp}\Big)\Big(1-F\Big(\frac{\mathbf{q}}{2}+\mathbf{k_0}^{||}+\mathbf{k_1}^{\perp}\Big)\Big)\frac{1}{|\mathbf{q}|}
\end{aligned} \tag{5.61}$$

We consider the high temperature and low electron density limit in which $F_{FD}(1-F_{FD}) \to F_{MB}$, where subscripts stand for Fermi-Dirac and Maxwell-Boltzmann distributions respectively. F_{MB} is given by $e^{\beta\mu}e^{-\beta\hbar^2q^2/8m_\phi}e^{-\beta\hbar^2(k_1^\perp-k_0^\perp)^2/2m_\phi}$. Integrating w.r.t. $k_1^\perp$ we get

$$\tilde{M}(\mathbf{q}) = \frac{m_\phi^{3/2}}{\hbar^3}\sqrt{\frac{2\pi}{\beta}}e^{\beta\mu}\frac{e^{-\beta\hbar^2\mathbf{q}^2/8m_\phi}}{|\mathbf{q}|}. \tag{5.62}$$

5.5.4 Drag potential in one-dimension

Using $\psi(x,y) = \sqrt{(2/w)}\cos(\pi y/w)\psi(x)$ we can write $\mathbf{J}(\mathbf{r}')$ as

$$\mathbf{J}(\mathbf{r}') = \frac{2}{w}\cos^2\left(\pi y'/w\right)\Big(\mathbf{v}_{rel}|\psi(x')|^2+\mathbf{j}(x')\Big). \tag{5.63}$$

$\mathbf{j}(x')$ and $\mathbf{v}_{rel}$ has non- zero components only along $\pm$ x-direction. Therefore, $\mathbf{J}(\mathbf{r}')$ is a vector pointing along $\pm$ x-direction. Divergence of this current gives

$$\begin{aligned}
\nabla'\cdot\mathbf{J}(\mathbf{r}') =& \frac{2}{w}\cos^2\left(\pi y'/w\right)\Big(|\mathbf{v}_{rel}|(\hat{\mathbf{v}}_{rel}\cdot\hat{\mathbf{x}}')\partial_{x'}|\psi(x')|^2 \\
&+\partial_{x'}j(x')\Big).
\end{aligned} \tag{5.64}$$

Substituting for the divergence of current and the inverse Fourier transform of $M(\mathbf{r}-\mathbf{r}')$ in the expression for $V_\epsilon(\mathbf{r})$ in (5.13)

$$\begin{aligned}
V_\epsilon(\mathbf{r}) &= -\frac{\hbar\beta g^2}{32\pi^3 w}\int d^2r'd^2q e^{i\mathbf{q}\cdot\mathbf{r}}\tilde{M}(\mathbf{q})e^{-i\mathbf{q}\cdot\mathbf{r}'}\Big(1+\cos\big(2\pi y'/w\big)\Big)\Big(|\mathbf{v}_{rel}|(\hat{\mathbf{v}}_{rel}\cdot\hat{\mathbf{x}}')\partial_{x'}|\psi(x')|^2 \\
&\qquad + \partial_{x'}j(x')\Big), \\
&= -\frac{2\pi\hbar\beta g^2}{32\pi^3 w}\int dx'dq_x e^{iq_x x}\Big(\tilde{M}(q_x,0)+\frac{e^{i2\pi y/w}}{2}\tilde{M}\big(q_x,2\pi/w\big)+\frac{e^{-i2\pi y/w}}{2}\tilde{M}\big(q_x,-2\pi/w\big)\Big) \\
&\qquad \Big(|\mathbf{v}_{rel}|(\hat{\mathbf{v}}_{rel}\cdot\hat{\mathbf{x}}')\partial_{x'}|\psi(x')|^2+\partial_{x'}j(x')\Big)e^{-iq_x x'}, \\
&= -\frac{2\pi\hbar\beta g^2}{16\pi^2 w}\int dq_x e^{iq_x x}\Big(\tilde{M}(q_x,0)+\frac{e^{i2\pi y/w}}{2}\tilde{M}\big(q_x,2\pi/w\big)+ \\
&\qquad \frac{e^{-i2\pi y/w}}{2}\tilde{M}\big(q_x,-2\pi/w\big)\Big)\mathcal{J}(q_x).
\end{aligned} \tag{5.65}$$

$\mathcal{J}(q_x)$ is defined as the Fourier transform of $\big(|\mathbf{v}_{rel}|(\hat{\mathbf{v}}_{rel}\cdot\hat{\mathbf{x}}')\partial_{x'}|\psi(x')|^2+\partial_{x'}j(x')\big)$. Finally, to obtain $V_\epsilon(x)$ we simply multiply $V_\epsilon(\mathbf{r})$ with the transverse probability of finding the particles and integrate over the transverse direction and is given by,

$$\begin{aligned}
V_\epsilon(x) &= \frac{2}{w}\int_{-w/2}^{w/2} dy\cos^2\big(\pi y/w\big)V_\epsilon(\mathbf{r}), \\
&= -\frac{2\pi\hbar\beta g^2}{16\pi^2 w}\int dq_x e^{iq_x x}\Big(\tilde{M}(q_x,0)+\frac{1}{4}\tilde{M}\big(q_x,2\pi/w\big)+\frac{1}{4}\tilde{M}\big(q_x,-2\pi/w\big)\Big)\mathcal{J}(q_x).
\end{aligned} \tag{5.66}$$

6.0 Final remarks

The primary focus of this thesis was to study the dynamics of the polariton condensate flowing in a quasi-one dimensional ring microcavity. Using ultraviolet lithography, the narrow ring channels were etched to confine polaritons in the radial direction and allow continuous motion in the azimuthal direction. The polaritons were produced by a tightly focused, pulsed and non-resonant pump laser which acted as a quench. By imaging the PL we studied the nonequilibrium dynamics of the polariton condensate in the rings. Much to our surprise, the coherent polaritons showed energy dissipative dynamics away from the pumping region. This behaviour is in stark contrast to the dissipationless flow observed in these planar microcavity structures when polaritons were created by a resonant pump [122]. In those experiments, polaritons even after traveling distances over 100 μm away from the pump region did not show any drop in energy. The difference between these two experiments lies in the generation of the reservoir due to the pumping scheme. This thesis puts forward the direct evidence of the presence of a reservoir away from the region where they were first created. The time-resolved measurements in this thesis as well as steady-state measurements in long wires reported in Ref. [154] corroborate this evidence.

Apart from dissipation, we showed the importance of polariton-polariton interactions for reaching a single-mode extended condensate in a macroscopic rigid pendulum potential. Due to collisions between the polaritons flowing in the opposite direction, the first temporal signal of condensation in the trap was observed when they met near the bottom of the trap. The time scale of the dynamical motion of these non-equilibrium polaritons in the low density limit agreed well with the energy scale set by the rigid pendulum potential. By creating a spatio-temporal map of the energy of the single mode condensate in the rigid pendulum trap we found the spatial coherence extended up to 100 μm while the temporal coherence lasted up to 1 ns until the polaritons leaked from the trap. These length and time scales of coherence indicate promising applications to ultrafast polariton circuits.

We performed a direct measurement of the mean field interaction strength of the polaritons in a polariton condensate. We found the upper and lower bounds on the value of

the interaction strength by developing a detailed polariton density counting method which accounts for the blueshift and the redshift of the polariton dispersion due to interactions and strain effects in the etched channel respectively. Through these measurements we also deduced an estimate of the reservoir population at the bottom of the trapping potential. Since the mass of the polaritons and the reservoir particles differ by at least three orders of magnitude, the dynamical nature of the experiments helped to separate their effects in real time. Future work with these rings may be to study the energy and momentum distribution of the early non-equilibrium condensate to find out the energy relaxation rate and then to compare it against the damping rate of the oscillations of the trap. Obtaining a quantitative agreement with a microscopic theory will cement our understanding of the energy dissipation in this system.

We studied the pseudospin-1/2 character of the polariton condensate in the rings. By performing polarization-resolved PL measurements, we observed the intrinsic optical spin Hall effect of the precession of the polariton spins as they flowed in the ring. The polarization dynamics resulted in the formation of a nearly stationary linear polarization pattern in the ring which was stable. The polarization of the condensate appeared to be close to the ground state polarization of a ring without any energy gradient. This polarization was unaffected by the changing density of the inhomogeneous condensate as the polaritons leaked from the trap. This is an indication that the late-time condensate polarization is not random and is connected to the polarization states of the trap. This fact could be utilized to create complex polarization patterns for optical spintronic applications by engineering the trapping potential.

I presented a general theory of drag on a condensate due to interactions with a moving thermal bath of non-condensate particles, adapted from previous theory of equilibration of a condensate in a trap [163, 164, 180, 165]. This theory can be used to model the polariton drag effect observed previously [154], in which an electric current passing through a polariton condensate gives a measurable momentum transfer to the condensate, and an effective potential energy shift.

The present thesis opens several directions for future work. The process by which the reservoir particles travel from their point of generation is not clearly understood. Theoretical

as well as experimental efforts are required to understand this effect. A part of the reservoir, the "bottleneck polaritons", may come from the interplay of the repulsive interactions and the negative curvature of the polariton dispersion creating bright solitons which can travel at high group velocities. Solitons are non-dissipative wavepackets which maintain their shape as they propagate and are robust against perturbations. Just as in stable modelocked lasers which create soliton pulse trains [182], the polaritonic solitons could be formed when they are excited on the non-parabolic part of the dispersion which has a negative curvature. Due to the relative sign change between the kinetic energy term and the nonlinear interactions, effectively the polaritons in this region of the dispersion interact with attractive interactions. When the attractive interactions compensate the dispersion (kinetic energy) of the polaritons, solitons are formed. The region of the dispersion where the "bottleneck polaritons" were observed have the right energy and momentum for soliton formation. The polaritons, having high in-plane momenta and a high excitonic fraction, may travel as waveguide modes in these channels. The "bottleneck polaritons" may collide with each other in a process by which one of them can scatter to higher momentum and energy states which make up the excitons while the other enters the low energy and momentum polariton states. The excitons may also collide in a Auger-like process where one of the exciton is ionized, forming free electron and hole, while the other loses energy and enters the condensate. Investigation into these effects will provide great insight into the propagation of the polariton condensate in narrow channels. Another aspect of this study is that it will help to gain better control over optical traps created by a non-resonant pump.

Future experiments with tilted rings may look for collective excitations of the rigid pendulum potential. Circulation in the ring was not observed due to the presence of cavity gradient. It would be interesting to look at systems with rotational symmetry, that is, with no gradient, to see quantized circulation effects. Fabricating energy degenerate rings with smaller radii as well as thinner widths at nearly resonant detunings would help to study the circulation due to the different orbital modes in the ring. One such experiment would be to study the spontaneous generation of condensate with non-zero orbital angular momentum using a CW non-resonant laser pumping the whole ring. Performing the same experiment with temporal pulses would let us see the dynamics of these orbital modes. Having demonstrated

that the polariton condensate in these long lifetime microcavities can find the ground state of the rigid pendulum trap, we can utilize the dissipation as a resource to find the ground state of an optically pumped complex potential [183, 184, 185, 186, 187]. The problem of finding the ground state in a physical system is analogous to finding the optimal solution which minimizes the cost function in an optimization problem [188]. The Hamiltonian of our physical system plays the role of the cost function and the ground state is equivalent to the solution which minimizes the cost function. The dissipation drives the system towards the ground state by selectively eliminating the excited states. Thus, mapping cost functions which are difficult to optimize to the physical Hamiltonian of the polaritons, one could speed up the search for the optimal solutions.

Appendix A

A.1 Radial modes in the ring

In this section I will consider a zero temperature model for the polariton condensate in a quasi 1D ring where the condensate is confined in the radial direction by the harmonic potential. I derive the effective equation of motion for the different radial modes. I start by writing the Gross-Pitaevskii equation (GPE) for a non-interacting planar 2D geometry with radial symmetry.

$$i\hbar\partial_t\Psi(r,\theta,t) = \left[-\frac{\hbar^2}{2m}(\partial_r^2 + \frac{1}{r}\partial_r + \frac{1}{r^2}\partial_\theta^2) + \frac{m\omega_r^2}{2}(r-a)^2 + \frac{V_0}{2}(1-\cos\theta)\right]\Psi(r,\theta,t) \quad (.1)$$

I expand the solution $\Psi(r,\theta,t)$ in the basis of 1D harmonic oscillator $\{\phi_m(r)\}$. In cylindrical co-ordinates, this basis is non-orthogonal. It could be shown that as the ratio of the radial confinement width ($a_r = \sqrt{\hbar/m\omega_r}$) to the radius of the ring (a) is made smaller, this basis becomes orthogonal because the approximation of neglecting ∂_r with respect to ∂_r^2 becomes exact.

$$\Psi(r,\theta,t) = \sum_m \phi_m(r-a)\psi_m(\theta,t) \quad (.2)$$

Basis functions ϕ_n are given below where $\mathcal{H}_n$ is the n^{th} order Hermite polynomial

$$\phi_n(r-a) = \frac{1}{\sqrt{\left(\pi^{1/2}2^n n!\left(a/a_r\right)\right)}}\mathcal{H}_n\left(r-\left(a/a_r\right)\right)\exp\left[-\left(r-\left(a/a_r\right)\right)^2/2\right]. \quad (.3)$$

Substituting (.2) in (.1) and multiplying (.1) by $\phi_n^*(r)$ and integrating out the radial co-ordinates, we have in the left hand side (L.H.S.) of Equation (.1)

$$LHS = i\hbar\sum_m Q_{nm}\partial_t\psi_m(\theta,t) \quad (.4)$$

where we have defined Q_{nm} as

$$Q_{nm} = \int_0^\infty dr\left(r\phi_n^*(r-a)\phi_m(r-a)\right) \approx \delta_{nm} + \mathcal{O}\left(\frac{a_r}{a}\right)\left(\delta_{n,m+1}+\delta_{n,m-1}\right). \quad (.5)$$

For a quasi-1D ring we ignore the off-diagonal terms and obtain,

$$LHS = i\hbar\partial_t\psi_n(\theta,t). \tag{.6}$$

The right hand side (R.H.S.) of Equation (.1) becomes

$$RHS = \sum_m \Big(V_{nm} - K_{nm}\partial_\theta^2 + Q_{nm}V(\theta)\Big)\psi_m(\theta,t). \tag{.7}$$

V_{nm} and K_{nm} are given by

$$V_{nm} = \int_0^\infty dr\phi_n^*(r-a)\Big(-\frac{\hbar^2}{2m}r\Big[\partial_r^2 + \frac{1}{r}\partial_r\Big] + \frac{m\omega_r^2}{2}r(r-a)^2\Big)\phi_m(r-a) \tag{.8}$$

$$K_{nm} = \frac{\hbar^2}{2m}\int_0^\infty dr\phi_n^*(r-a)\frac{1}{r}\phi_m(r-a) \tag{.9}$$

The interactions between the polaritons occupying different radial modes (g_{nijm}) are identified from the expansion of the cubic nonlinear term which results in an additional term in Equation 1.

$$g_{nijm} = g_{2D}|X|^4\int_0^\infty dr\Big(r\phi_n^*(r-a)\phi_i^*(r-a)\phi_j(r-a)\phi_m(r-a)\Big) \tag{.10}$$

$|X|^2$ is the exciton fraction of the polaritons which is taken to be constant over the dimensions of a ring. The interaction leads to the addition of the following term to .1.

$$\tilde{V}_n = \sum_{ijm} g_{nijm}\psi_i^*(\theta,t)\psi_j(\theta,t)\psi_m(\theta,t) \tag{.11}$$

We also consider an additional contribution to the potential which arises due to the interaction of the polaritons with the reservoir

$$g_{2D}|X|^2\sum_m Q_{nm}\psi_m(\theta,t)n_{res} \approx g_{2D}|X|^2\sum_m \delta_{nm}n_{res}\psi_m(\theta,t). \tag{.12}$$

We introduce energy relaxation phenomenologically through the parameter α as shown below

$$i\hbar\partial_t\psi_n = \Big(1 - \frac{i\hbar\alpha}{2}\Big)\sum_m H_{nm}\psi_m. \tag{.13}$$

The Hamiltonian H_{nm} is given by

$$H_{nm} = V_{nm} - K_{nm}\partial_\theta^2 + \delta_{nm}\Big[V(\theta) + g_{2D}|X|^2 n_{res}\Big] + \sum_{ij} g_{nijm}\psi_i^*\psi_j. \tag{.14}$$

The process of stimulated gain of condensate from reservoir and the lifetime of the polaritons are accounted by adding imaginary term to the above equation which now becomes,

$$i\hbar\partial_t\psi_n = \Big(1 - \frac{i\hbar\alpha}{2}\Big)\sum_m H_{nm}\psi_m + \frac{i\hbar}{2}\Big(\beta n_{res} - \frac{1}{\tau_{pol}}\Big)\psi_n \tag{.15}$$

The dynamics of the reservoir is given by the following equation which accounts for the loss of reservoir due to the stimulated scattering into the condensate and finite lifetime of the reservoir. A back-action term proportional to the particle loss of the condensate due to the energy relaxation process is added to the reservoir to support the indirect observation of the reservoir away from the pump spot.

$$\partial_t n_{res} = -\beta\sum_m |\psi_m|^2 n_{res} - \gamma\sum_m \partial_t|\psi_m|^2\Big|_\alpha - \frac{n_{res}}{\tau_{res}} \tag{.16}$$

The equations .15 and .16 are solved numerically using a combination of Split-step Fourier method and fourth-order Runge Kutta (RK-4) method [189] as outlined below. For a given time interval $t_i < t < t_{i+1}$, we re-arrange the above equations into two sets

$$i\hbar\partial_t\psi_n = \Big(1 - \frac{i\hbar\alpha}{2}\Big)\sum_m H_{nm}\psi_m \tag{.17}$$

$$\begin{aligned}
\partial_t\psi_n &= \frac{1}{2}\Big(\beta n_{res} - \frac{1}{\tau_{pol}}\Big)\psi_n + \frac{\gamma}{2}\partial_t\psi_n\Big|_\alpha \\
\partial_t n_{res} &= -\beta\sum_m |\psi_m|^2 n_{res} - \gamma\sum_m \partial_t|\psi_m|^2\Big|_\alpha - \frac{n_{res}}{\tau_{res}}
\end{aligned} \tag{.18}$$

Starting with $\psi_n(t_i)$, equation .17 is integrated using a symmetric splitting scheme to obtain $\psi_n(t_{i+1})$. The solution $\psi_n(t_{i+1})$ is normalized w.r.t. $\sum_n |\psi_n(t_i)|^2$ to keep the total condensate particle number constant. The set of equations in .18 are integrated with RK-4 method starting with the initial conditions $n_{res}(t_i)$ and $\psi_n(t_{i+1})$.

Bibliography

[1] Satyendra Nath Bose. Plancks gesetz und lichtquantenhypothese. 1924.

[2] A Einstein. Quantentheorie des idealen einatomigen gases, zweite abhandlung. *Sitzungsberichte der Preußischen Akademie der Wissenschaften, Physikalisch-Mathematische Klasse, Berlin*, pages 3–14, 1925.

[3] Lev Pitaevskii and Sandro Stringari. *Bose-Einstein condensation and superfluidity*, volume 164. Oxford University Press, 2016.

[4] H Kamerlingh Onnes. The resistance of pure mercury at helium temperatures. *Commun. Phys. Lab. Univ. Leiden, b*, 120, 1911.

[5] Pyotr Kapitza. Viscosity of liquid helium below the λ-point. *Nature*, 141(3558):74–74, 1938.

[6] John F Allen and AD Misener. Flow of liquid helium ii. *Nature*, 141(3558):75–75, 1938.

[7] Kendall B Davis, M-O Mewes, Michael R Andrews, Nicolaas J van Druten, Dallin S Durfee, DM Kurn, and Wolfgang Ketterle. Bose-einstein condensation in a gas of sodium atoms. *Physical review letters*, 75(22):3969, 1995.

[8] Mike H Anderson, Jason R Ensher, Michael R Matthews, Carl E Wieman, and Eric A Cornell. Observation of bose-einstein condensation in a dilute atomic vapor. *science*, 269(5221):198–201, 1995.

[9] Selim Jochim, Markus Bartenstein, Alexander Altmeyer, Gerhard Hendl, Stefan Riedl, Cheng Chin, J Hecker Denschlag, and Rudolf Grimm. Bose-einstein condensation of molecules. *Science*, 302(5653):2101–2103, 2003.

[10] Martin W Zwierlein, Claudiu A Stan, Christian H Schunck, Sebastian MF Raupach, Subhadeep Gupta, Zoran Hadzibabic, and Wolfgang Ketterle. Observation of bose-einstein condensation of molecules. *Physical review letters*, 91(25):250401, 2003.

[11] Markus Greiner, Cindy A Regal, and Deborah S Jin. A molecular bose-einstein condensate emerges from a fermi sea. *arXiv preprint cond-mat/0311172*, 2003.

[12] Jan Klaers, Julian Schmitt, Frank Vewinger, and Martin Weitz. Bose–einstein condensation of photons in an optical microcavity. *Nature*, 468(7323):545–548, 2010.

[13] T Nikuni, M Oshikawa, A Oosawa, and H Tanaka. Bose-einstein condensation of dilute magnons in tlcucl 3. *Physical review letters*, 84(25):5868, 2000.

[14] Ch Rüegg, N Cavadini, A Furrer, H-U Güdel, Karl Krämer, H Mutka, A Wildes, K Habicht, and P Vorderwisch. Bose–einstein condensation of the triplet states in the magnetic insulator tlcucl 3. *Nature*, 423(6935):62–65, 2003.

[15] Sergej O Demokritov, Vladislav E Demidov, Oleksandr Dzyapko, Gennadii A Melkov, Alexandar A Serga, Burkard Hillebrands, and Andrei N Slavin. Bose–einstein condensation of quasi-equilibrium magnons at room temperature under pumping. *Nature*, 443(7110):430–433, 2006.

[16] Tommi K Hakala, Antti J Moilanen, Aaro I Väkeväinen, Rui Guo, Jani-Petri Martikainen, Konstantinos S Daskalakis, Heikki T Rekola, Aleksi Julku, and Päivi Törmä. Bose–einstein condensation in a plasmonic lattice. *Nature Physics*, 14(7):739–744, 2018.

[17] Jacek Kasprzak, M Richard, S Kundermann, A Baas, P Jeambrun, JMJ Keeling, FM Marchetti, MH Szymańska, R André, JL Staehli, et al. Bose–einstein condensation of exciton polaritons. *Nature*, 443(7110):409–414, 2006.

[18] R Balili, V Hartwell, D Snoke, L Pfeiffer, and K West. Bose-einstein condensation of microcavity polaritons in a trap. *Science*, 316(5827):1007–1010, 2007.

[19] Wolfgang Ketterle and Hans-Joachim Miesner. Coherence properties of bose-einstein condensates and atom lasers. *Physical Review A*, 56(4):3291, 1997.

[20] MR Andrews, CG Townsend, H-J Miesner, DS Durfee, DM Kurn, and W Ketterle. Observation of interference between two bose condensates. *Science*, 275(5300):637–641, 1997.

[21] H-J Miesner, DM Stamper-Kurn, MR Andrews, DS Durfee, S Inouye, and W Ketterle. Bosonic stimulation in the formation of a bose-einstein condensate. *Science*, 279(5353):1005–1007, 1998.

[22] DM Stamper-Kurn, AP Chikkatur, A Görlitz, S Inouye, S Gupta, DE Pritchard, and W Ketterle. Excitation of phonons in a bose-einstein condensate by light scattering. *Physical review letters*, 83(15):2876, 1999.

[23] JM Vogels, K Xu, C Raman, JR Abo-Shaeer, and W Ketterle. Experimental observation of the bogoliubov transformation for a bose-einstein condensed gas. *Physical review letters*, 88(6):060402, 2002.

[24] Michael R Andrews, Dan M Kurn, H-J Miesner, Dallin S Durfee, Christopher G Townsend, Shin Inouye, and Wolfgang Ketterle. Propagation of sound in a bose-einstein condensate. *Physical review letters*, 79(4):553, 1997.

[25] DM Stamper-Kurn, H-J Miesner, S Inouye, MR Andrews, and W Ketterle. Collisionless and hydrodynamic excitations of a bose-einstein condensate. *Physical Review Letters*, 81(3):500, 1998.

[26] M-O Mewes, MR Andrews, NJ Van Druten, DM Kurn, DS Durfee, CG Townsend, and W Ketterle. Collective excitations of a bose-einstein condensate in a magnetic trap. *Physical review letters*, 77(6):988, 1996.

[27] DS Jin, JR Ensher, MR Matthews, CE Wieman, and Eric A Cornell. Collective excitations of a bose-einstein condensate in a dilute gas. *Physical review letters*, 77(3):420, 1996.

[28] R Onofrio, C Raman, JM Vogels, JR Abo-Shaeer, AP Chikkatur, and W Ketterle. Observation of superfluid flow in a bose-einstein condensed gas. *Physical review letters*, 85(11):2228, 2000.

[29] C Raman, R Onofrio, JM Vogels, JR Abo-Shaeer, and W Ketterle. Dissipationless flow and superfluidity in gaseous bose-einstein condensates. *Journal of low temperature physics*, 122(1):99–116, 2001.

[30] C Raman, M Köhl, R Onofrio, DS Durfee, CE Kuklewicz, Z Hadzibabic, and W Ketterle. Evidence for a critical velocity in a bose-einstein condensed gas. *Physical Review Letters*, 83(13):2502, 1999.

[31] AE Leanhardt, A Görlitz, AP Chikkatur, D Kielpinski, Y-i Shin, DE Pritchard, and W Ketterle. Imprinting vortices in a bose-einstein condensate using topological phases. *Physical review letters*, 89(19):190403, 2002.

[32] C Raman, JR Abo-Shaeer, JM Vogels, K Xu, and W Ketterle. Vortex nucleation in a stirred bose-einstein condensate. *Physical review letters*, 87(21):210402, 2001.

[33] S Inouye, S Gupta, T Rosenband, AP Chikkatur, A Görlitz, TL Gustavson, AE Leanhardt, DE Pritchard, and W Ketterle. Observation of vortex phase singularities in bose-einstein condensates. *Physical Review Letters*, 87(8):080402, 2001.

[34] JR Abo-Shaeer, Chandra Raman, JM Vogels, and Wolfgang Ketterle. Observation of vortex lattices in bose-einstein condensates. *Science*, 292(5516):476–479, 2001.

[35] JR Abo-Shaeer, C Raman, and W Ketterle. Formation and decay of vortex lattices in bose-einstein condensates at finite temperatures. *Physical review letters*, 88(7):070409, 2002.

[36] S Inouye, RF Löw, S Gupta, T Pfau, A Görlitz, TL Gustavson, DE Pritchard, and W Ketterle. Amplification of light and atoms in a bose-einstein condensate. *Physical review letters*, 85(20):4225, 2000.

[37] William D Phillips. Nobel lecture: Laser cooling and trapping of neutral atoms. *Reviews of Modern Physics*, 70(3):721, 1998.

[38] Wolfgang Ketterle. Nobel lecture: When atoms behave as waves: Bose-einstein condensation and the atom laser. *Reviews of Modern Physics*, 74(4):1131, 2002.

[39] Stephen Eckel, Daniel S Barker, James A Fedchak, Nikolai N Klimov, Eric Norrgard, Julia Scherschligt, Constantinos Makrides, and Eite Tiesinga. Challenges to miniaturizing cold atom technology for deployable vacuum metrology. *Metrologia*, 55(5):S182, 2018.

[40] David Snoke. *Solid state physics: Essential concepts*. Cambridge University Press, 2020.

[41] Gerald Bastard et al. Wave mechanics applied to semiconductor heterostructures. 1988.

[42] Svâtoslav Anatol'evič Moskalenko, SA Moskalenko, and DW Snoke. *Bose-Einstein condensation of excitons and biexcitons: and coherent nonlinear optics with excitons*. Cambridge University Press, 2000.

[43] JJ Hopfield. Theory of the contribution of excitons to the complex dielectric constant of crystals. *Physical Review*, 112(5):1555, 1958.

[44] Xinglin Wen and Qihua Xiong. Bose-einstein condensation of exciton polariton in perovskites semiconductors. *Frontiers of Optoelectronics*, 13(3):193–195, 2020.

[45] JJ Baumberg, AV Kavokin, S Christopoulos, AJD Grundy, R Butté, G Christmann, DD Solnyshkov, G Malpuech, G Baldassarri Höger von Högersthal, El Feltin, et al. Spontaneous polarization buildup in a room-temperature polariton laser. *Physical Review Letters*, 101(13):136409, 2008.

[46] Thierry Guillet, Meletios Mexis, J Levrat, G Rossbach, Christelle Brimont, Thierry Bretagnon, Bernard Gil, R Butté, N Grandjean, Laurent Orosz, et al. Polariton lasing in a hybrid bulk zno microcavity. *Applied Physics Letters*, 99(16):161104, 2011.

[47] Yongbao Sun, Patrick Wen, Yoseob Yoon, Gangqiang Liu, Mark Steger, Loren N. Pfeiffer, Ken West, David W. Snoke, and Keith A. Nelson. Bose-einstein condensation of long-lifetime polaritons in thermal equilibrium. *Phys. Rev. Lett.*, 118:016602, Jan 2017.

[48] Davide Caputo, Dario Ballarini, Galbadrakh Dagvadorj, Carlos Sánchez Muñoz, Milena De Giorgi, Lorenzo Dominici, Kenneth West, Loren N Pfeiffer, Giuseppe Gigli, Fabrice P Laussy, Marzena H. Szymańska, and Daniele Sanvitto. Topological order and thermal equilibrium in polariton condensates. *Nature Materials*, 17:145, dec 2017.

[49] Carl M Bender. Making sense of non-hermitian hamiltonians. *Reports on Progress in Physics*, 70(6):947, 2007.

[50] Nimrod Moiseyev. *Non-Hermitian quantum mechanics*. Cambridge University Press, 2011.

[51] Tiejun Gao, E Estrecho, KY Bliokh, TCH Liew, MD Fraser, Sebastian Brodbeck, Martin Kamp, Christian Schneider, Sven Höfling, Y Yamamoto, et al. Observation of non-hermitian degeneracies in a chaotic exciton-polariton billiard. *Nature*, 526(7574):554–558, 2015.

[52] T. Gao, G. Li, E. Estrecho, T. C. H. Liew, D. Comber-Todd, A. Nalitov, M. Steger, K. West, L. Pfeiffer, D. W. Snoke, A. V. Kavokin, A. G. Truscott, and E. A. Ostrovskaya. Chiral modes at exceptional points in exciton-polariton quantum fluids. *Phys. Rev. Lett.*, 120:065301, Feb 2018.

[53] Maciej Pieczarka, Dario Poletti, Christian Schneider, Sven Höfling, Elena A Ostrovskaya, Grzegorz Sęk, and Marcin Syperek. Observation of gain-pinned dissipative solitons in a microcavity laser. *APL Photonics*, 5(8):086103, 2020.

[54] Mark Steger, Chitra Gautham, David W. Snoke, Loren Pfeiffer, and Ken West. Slow reflection and two-photon generation of microcavity exciton–polaritons. *Optica*, 2(1):1–5, Jan 2015.

[55] Mark Steger, Gangqiang Liu, Bryan Nelsen, Chitra Gautham, David W Snoke, Ryan Balili, Loren Pfeiffer, and Ken West. Long-range ballistic motion and coherent flow of long-lifetime polaritons. *Physical Review B*, 88(23):235314, 2013.

[56] M. D. Barrett, J. A. Sauer, and M. S. Chapman. All-optical formation of an atomic bose-einstein condensate. *Phys. Rev. Lett.*, 87:010404, Jun 2001.

[57] D. W. Snoke and J. P. Wolfe. Population dynamics of a bose gas near saturation. *Phys. Rev. B*, 39:4030–4037, Mar 1989.

[58] F. Tassone and Y. Yamamoto. Exciton-exciton scattering dynamics in a semiconductor microcavity and stimulated scattering into polaritons. *Phys. Rev. B*, 59:10830–10842, Apr 1999.

[59] V. E. Hartwell and D. W. Snoke. Numerical simulations of the polariton kinetic energy distribution in gaas quantum-well microcavity structures. *Phys. Rev. B*, 82:075307, Aug 2010.

[60] Hui Deng, David Press, Stephan Götzinger, Glenn S. Solomon, Rudolf Hey, Klaus H. Ploog, and Yoshihisa Yamamoto. Quantum degenerate exciton-polaritons in thermal equilibrium. *Phys. Rev. Lett.*, 97:146402, Oct 2006.

[61] DW Snoke, V Hartwell, J Beaumariage, S Mukherjee, Y Yoon, DM Myers, M Steger, Z Sun, KA Nelson, and LN Pfeiffer. Experimental determinations of polariton-polariton interactions in microcavities. *arXiv preprint arXiv:2106.12509*, 2021.

[62] F. Tassone, C. Piermarocchi, V. Savona, A. Quattropani, and P. Schwendimann. Bottleneck effects in the relaxation and photoluminescence of microcavity polaritons. *Phys. Rev. B*, 56:7554–7563, Sep 1997.

[63] Robert W Boyd. *Nonlinear optics*. Academic press, 2020.

[64] Ch Schneider, K Winkler, MD Fraser, M Kamp, Y Yamamoto, EA Ostrovskaya, and Sven Höfling. Exciton-polariton trapping and potential landscape engineering. *Reports on Progress in Physics*, 80(1):016503, 2016.

[65] TCH Liew, AV Kavokin, and IA Shelykh. Optical circuits based on polariton neurons in semiconductor microcavities. *Physical Review Letters*, 101(1):016402, 2008.

[66] Yongbao Sun, Yoseob Yoon, Mark Steger, Gangqiang Liu, Loren N. Pfeiffer, Ken West, David W. Snoke, and Keith A. Nelson. Direct measurement of polariton-polariton interaction strength. *Nature Physics*, 13:870 EP –, Jun 2017.

[67] D. M. Myers, S. Mukherjee, J. Beaumariage, D. W. Snoke, M. Steger, L. N. Pfeiffer, and K. West. Polariton-enhanced exciton transport. *Phys. Rev. B*, 98:235302, Dec 2018.

[68] S Mukherjee, David M. Myers, Rosaria G Lena, B Ozden, J Beaumariage, Z Sun, M Steger, Loren N Pfeiffer, K West, Andrew J Daley, and David W. Snoke. Observation of nonequilibrium motion and equilibration in polariton rings. *Physical Review B*, 100(24):245304, 2019.

[69] Alexey Kavokin, Jeremy J Baumberg, Guillaume Malpuech, and Fabrice P Laussy. *Microcavities*. Oxford university press, 2017.

[70] Maria Maragkou, Caryl E Richards, Tomas Ostatnickỳ, Alastair JD Grundy, Joanna Zajac, Maxime Hugues, Wolfgang Langbein, and Pavlos G Lagoudakis. Optical analogue of the spin hall effect in a photonic cavity. *Optics letters*, 36(7):1095–1097, 2011.

[71] Charles Leyder, Marco Romanelli, J Ph Karr, Elisabeth Giacobino, Tim CH Liew, Mikhail M Glazov, Alexey V Kavokin, Guillaume Malpuech, and Alberto Bramati. Observation of the optical spin hall effect. *Nature Physics*, 3(9):628–631, 2007.

[72] C. Antón, S. Morina, T. Gao, P. S. Eldridge, T. C. H. Liew, M. D. Martín, Z. Hatzopoulos, P. G. Savvidis, I. A. Shelykh, and L. Viña. Optical control of spin textures in quasi-one-dimensional polariton condensates. *Phys. Rev. B*, 91:075305, Feb 2015.

[73] Kerry J Vahala. Optical microcavities. *nature*, 424(6950):839–846, 2003.

[74] JMea Gerard, D Barrier, JY Marzin, R Kuszelewicz, L Manin, E Costard, V Thierry-Mieg, and T Rivera. Quantum boxes as active probes for photonic microstructures: The pillar microcavity case. *Applied Physics Letters*, 69(4):449–451, 1996.

[75] B Gayral, JM Gérard, A Lemaıtre, C Dupuis, L Manin, and JL Pelouard. High-q wet-etched gaas microdisks containing inas quantum boxes. *Applied physics letters*, 75(13):1908–1910, 1999.

[76] DK Armani, TJ Kippenberg, SM Spillane, and KJ Vahala. Ultra-high-q toroid microcavity on a chip. *Nature*, 421(6926):925–928, 2003.

[77] David Snoke. The connection of polaritons and vacuum rabi splitting, 2015.

[78] RB Balili, DW Snoke, Loren Pfeiffer, and Kenneth West. Actively tuned and spatially trapped polaritons. *Applied Physics Letters*, 88(3):031110, 2006.

[79] D. M. Myers, J. K. Wuenschell, B. Ozden, J. Beaumariage, D. W. Snoke, L. Pfeiffer, and K. West. Edge trapping of exciton-polariton condensates in etched pillars. *Applied Physics Letters*, May 2017.

[80] C. Ciuti, V. Savona, C. Piermarocchi, A. Quattropani, and P. Schwendimann. Role of the exchange of carriers in elastic exciton-exciton scattering in quantum wells. *Phys. Rev. B*, 58:7926–7933, Sep 1998.

[81] E. Estrecho, T. Gao, N. Bobrovska, D. Comber-Todd, M. D. Fraser, M. Steger, K. West, L. N. Pfeiffer, J. Levinsen, M. M. Parish, T. C. H. Liew, M. Matuszewski, D. W. Snoke, A. G. Truscott, and E. A. Ostrovskaya. Direct measurement of polariton-polariton interaction strength in the thomas-fermi regime of exciton-polariton condensation. *Phys. Rev. B*, 100:035306, Jul 2019.

[82] Valentin Walther, Robert Johne, and Thomas Pohl. Giant optical nonlinearities from rydberg excitons in semiconductor microcavities. *Nature communications*, 9(1):1–6, 2018.

[83] Petr Stepanov, Amit Vashisht, Martin Klaas, Nils Lundt, Sefaattin Tongay, Mark Blei, Sven Höfling, Thomas Volz, Anna Minguzzi, Julien Renard, et al. Exciton-exciton interaction beyond the hydrogenic picture in a mose _2 monolayer in the strong light-matter coupling regime. *arXiv preprint arXiv:2007.00431*, 2020.

[84] Daniel Erkensten, Samuel Brem, and Ermin Malic. Exciton-exciton interaction in transition metal dichalcogenide monolayers and van der waals heterostructures. *Physical Review B*, 103(4):045426, 2021.

[85] Vanik Shahnazaryan, Ivan Iorsh, IA Shelykh, and O Kyriienko. Exciton-exciton interaction in transition-metal dichalcogenide monolayers. *Physical Review B*, 96(11):115409, 2017.

[86] Gangqiang Liu, David W. Snoke, Andrew Daley, Loren N. Pfeiffer, and Ken West. A new type of half-quantum circulation in a macroscopic polariton spinor ring condensate. *Proceedings of the National Academy of Sciences*, 112(9):2676–2681, 2015.

[87] Evelyn Tang and Liang Fu. Strain-induced partially flat band, helical snake states and interface superconductivity in topological crystalline insulators. *Nature Physics*, 10:964 EP –, Nov 2014. Article.

[88] Dario Ballarini, Milena De Giorgi, Emiliano Cancellieri, Romuald Houdré, Elisabeth Giacobino, Roberto Cingolani, Alberto Bramati, Giuseppe Gigli, and Daniele Sanvitto. All-optical polariton transistor. *Nature communications*, 4(1):1–8, 2013.

[89] Tingge Gao, PS Eldridge, Timothy Chi Hin Liew, SI Tsintzos, George Stavrinidis, G Deligeorgis, Z Hatzopoulos, and PG Savvidis. Polariton condensate transistor switch. *Physical Review B*, 85(23):235102, 2012.

[90] Anton V Zasedatelev, Anton V Baranikov, Darius Urbonas, Fabio Scafirimuto, Ullrich Scherf, Thilo Stöferle, Rainer F Mahrt, and Pavlos G Lagoudakis. A room-temperature organic polariton transistor. *Nature Photonics*, 13(6):378–383, 2019.

[91] C Antón, TCH Liew, Guilherme Tosi, Marta D Martín, Tingge Gao, Zacharias Hatzopoulos, Peter S Eldridge, Pavlos G Savvidis, and Luis Viña. Dynamics of a polariton condensate transistor switch. *Applied Physics Letters*, 101(26):261116, 2012.

[92] N. P. Proukakis, D. W. Snoke, and P. B. Littlewood. *Universal Themes of Bose-Einstein Condensation*. Cambridge University Press, April 2017.

[93] Sergey Alyatkin, JD Töpfer, Alexis Askitopoulos, Helgi Sigurdsson, and PG Lagoudakis. Optical control of couplings in polariton condensate lattices. *Physical Review Letters*, 124(20):207402, 2020.

[94] Julian D Töpfer, Ioannis Chatzopoulos, Helgi Sigurdsson, Tamsin Cookson, Yuri G Rubo, and Pavlos G Lagoudakis. Engineering spatial coherence in lattices of polariton condensates. *Optica*, 8(1):106–113, 2021.

[95] M Klaas, S Mandal, TCH Liew, M Amthor, S Klembt, L Worschech, C Schneider, and Sven Höfling. Optical probing of the coulomb interactions of an electrically pumped polariton condensate. *Applied Physics Letters*, 110(15):151103, 2017.

[96] Christian Schneider, Arash Rahimi-Iman, Na Young Kim, Julian Fischer, Ivan G Savenko, Matthias Amthor, Matthias Lermer, Adriana Wolf, Lukas Worschech, Vladimir D Kulakovskii, et al. An electrically pumped polariton laser. *Nature*, 497(7449):348, 2013.

[97] Pallab Bhattacharya, Thomas Frost, Saniya Deshpande, Md Zunaid Baten, Arnab Hazari, and Ayan Das. Room temperature electrically injected polariton laser. *Physical review letters*, 112(23):236802, 2014.

[98] Eugene Hecht. Optics 2nd edition. *Optics 2nd edition by Eugene Hecht Reading*, 1987.

[99] Alexey V. Kavokin, Jeremy J. Baumberg, Guillaume Malpuech, and Fabrice P. Laussy. *Microcavities*. Oxford University Press, 2nd editio edition, 2017.

[100] C Antón, Timothy Chi Hin Liew, Guilherme Tosi, MD Martín, Tingge Gao, Z Hatzopoulos, PS Eldridge, PG Savvidis, and Luis Viña. Energy relaxation of exciton-polariton condensates in quasi-one-dimensional microcavities. *Physical Review B*, 88(3):035313, 2013.

[101] Alberto Amo, Jérôme Lefrère, Simon Pigeon, Claire Adrados, Cristiano Ciuti, Iacopo Carusotto, Romuald Houdré, Elisabeth Giacobino, and Alberto Bramati. Superfluidity of polaritons in semiconductor microcavities. *Nature Physics*, 5(11):805, 2009.

[102] Giovanni Lerario, Antonio Fieramosca, Fábio Barachati, Dario Ballarini, Konstantinos S Daskalakis, Lorenzo Dominici, Milena De Giorgi, Stefan A Maier, Giuseppe Gigli, Stéphane Kéna-Cohen, et al. Room-temperature superfluidity in a polariton condensate. *Nature Physics*, 13(9):837, 2017.

[103] RT Juggins, J Keeling, and MH Szymańska. Coherently driven microcavity-polaritons and the question of superfluidity. *Nature communications*, 9(1):1–8, 2018.

[104] M Sich, F Fras, JK Chana, MS Skolnick, DN Krizhanovskii, AV Gorbach, R Hartley, DV Skryabin, SS Gavrilov, EA Cerda-Méndez, et al. Effects of spin-dependent interactions on polarization of bright polariton solitons. *Physical Review Letters*, 112(4):046403, 2014.

[105] Maksym Sich, Lucy E Tapia-Rodriguez, Helgi Sigurdsson, Paul M Walker, Edmund Clarke, Ivan A Shelykh, Benjamin Royall, Evgeny S Sedov, Alexey V Kavokin, Dmitry V Skryabin, et al. Spin domains in one-dimensional conservative polariton solitons. *ACS Photonics*, 5(12):5095–5102, 2018.

[106] M Sich, DN Krizhanovskii, MS Skolnick, Andriy V Gorbach, Robin Hartley, Dmitry V Skryabin, EA Cerda-Méndez, K Biermann, R Hey, and PV Santos. Observation of bright polariton solitons in a semiconductor microcavity. *Nature photonics*, 6(1):50–55, 2012.

[107] DV Skryabin, YV Kartashov, OA Egorov, M Sich, JK Chana, LE Tapia Rodriguez, PM Walker, Edmund Clarke, B Royall, MS Skolnick, et al. Backward cherenkov radiation emitted by polariton solitons in a microcavity wire. *Nature communications*, 8(1):1–9, 2017.

[108] Petr Stepanov, Ivan Amelio, Jean-Guy Rousset, Jacqueline Bloch, Aristide Lemaître, Alberto Amo, Anna Minguzzi, Iacopo Carusotto, and Maxime Richard. Dispersion relation of the collective excitations in a resonantly driven polariton fluid. *Nature communications*, 10(1):1–8, 2019.

[109] Albert G Baca and Carol IH Ashby. *Fabrication of GaAs devices*. Number 6. IET, 2005.

[110] D S Rawal, A Kapoor, H S Sharma, B K Sehgal, and Hitendra K Malik. A highly selective low pressure inductively coupled plasma etching process for gaas using photoresist mask. *The Open Plasma Physics Journal*, 4(1), 2011.

[111] David W. Snoke and Jonathan Keeling. The new era of polariton condensates. *Physics Today*, 70(10):54–60, 2017.

[112] D. S. Jin, M. R. Matthews, J. R. Ensher, C. E. Wieman, and E. A. Cornell. Temperature-dependent damping and frequency shifts in collective excitations of a dilute bose-einstein condensate. *Phys. Rev. Lett.*, 78:764–767, Feb 1997.

[113] D. M. Stamper-Kurn, H.-J. Miesner, S. Inouye, M. R. Andrews, and W. Ketterle. Collisionless and hydrodynamic excitations of a bose-einstein condensate. *Phys. Rev. Lett.*, 81:500–503, Jul 1998.

[114] O. M. Maragò, S. A. Hopkins, J. Arlt, E. Hodby, G. Hechenblaikner, and C. J. Foot. Observation of the scissors mode and evidence for superfluidity of a trapped bose-einstein condensed gas. *Phys. Rev. Lett.*, 84:2056–2059, Mar 2000.

[115] F. Chevy, V. Bretin, P. Rosenbusch, K. W. Madison, and J. Dalibard. Transverse breathing mode of an elongated bose-einstein condensate. *Phys. Rev. Lett.*, 88:250402, Jun 2002.

[116] Henning Moritz, Thilo Stöferle, Michael Köhl, and Tilman Esslinger. Exciting collective oscillations in a trapped 1d gas. *Phys. Rev. Lett.*, 91:250402, Dec 2003.

[117] T. Gao, O. A. Egorov, E. Estrecho, K. Winkler, M. Kamp, C. Schneider, S. Höfling, A. G. Truscott, and E. A. Ostrovskaya. Controlled ordering of topological charges in an exciton-polariton chain. *Phys. Rev. Lett.*, 121:225302, Nov 2018.

[118] Davide Caputo, Nataliya Bobrovska, Dario Ballarini, Michal Matuszewski, Milena De Giorgi, Lorenzo Dominici, Kenneth West, Loren N Pfeiffer, Giuseppe Gigli, and Daniele Sanvitto. Josephson vortices induced by phase twisting a polariton superfluid. *Nature Photonics*, page 1, 2019.

[119] G Tosi, G Christmann, NG Berloff, P Tsotsis, T Gao, Z Hatzopoulos, PG Savvidis, and JJ Baumberg. Sculpting oscillators with light within a nonlinear quantum fluid. *Nature Physics*, 8(3):190, 2012.

[120] A. Askitopoulos, T. C. H. Liew, H. Ohadi, Z. Hatzopoulos, P. G. Savvidis, and P. G. Lagoudakis. Robust platform for engineering pure-quantum-state transitions in polariton condensates. *Phys. Rev. B*, 92:035305, Jul 2015.

[121] Esther Wertz, Lydie Ferrier, DD Solnyshkov, Robert Johne, Daniele Sanvitto, Aristide Lemaître, Isabelle Sagnes, Roger Grousson, Alexey V Kavokin, Pascale Senellart, et al. Spontaneous formation and optical manipulation of extended polariton condensates. *Nature physics*, 6(11):860, 2010.

[122] Bryan Nelsen, Gangqiang Liu, Mark Steger, David W. Snoke, Ryan Balili, Ken West, and Loren Pfeiffer. Dissipationless flow and sharp threshold of a polariton condensate with long lifetime. *Phys. Rev. X*, 3:041015, Nov 2013.

[123] A. V. Sekretenko, S. S. Gavrilov, and V. D. Kulakovskii. Polariton-polariton interactions in microcavities under a resonant 10 to 100 picosecond pulse excitation. *Phys. Rev. B*, 88:195302, Nov 2013.

[124] Xavier Antoine and Romain Duboscq. Gpelab, a matlab toolbox to solve gross–pitaevskii equations ii: Dynamics and stochastic simulations. *Computer Physics Communications*, 193:95 – 117, 2015.

[125] Xavier Antoine and Romain Duboscq. Gpelab, a matlab toolbox to solve gross–pitaevskii equations i: Computation of stationary solutions. *Computer Physics Communications*, 185(11):2969 – 2991, 2014.

[126] P Cristofolini, A Dreismann, G Christmann, G Franchetti, NG Berloff, P Tsotsis, Z Hatzopoulos, PG Savvidis, and JJ Baumberg. Optical superfluid phase transitions and trapping of polariton condensates. *Physical review letters*, 110(18):186403, 2013.

[127] M Wouters, TCH Liew, and V Savona. Energy relaxation in one-dimensional polariton condensates. *Physical Review B*, 82(24):245315, 2010.

[128] Carlo F Barenghi, Ladislav Skrbek, and Katepalli R Sreenivasan. Introduction to quantum turbulence. *Proceedings of the National Academy of Sciences*, 111(Supplement 1):4647–4652, 2014.

[129] Allan Griffin, Tetsuro Nikuni, and Eugene Zaremba. *Bose-condensed gases at finite temperatures*. Cambridge University Press, 2009.

[130] DW Snoke and SM Girvin. Dynamics of phase coherence onset in bose condensates of photons by incoherent phonon emission. *Journal of Low Temperature Physics*, 171(1):1–12, 2013.

[131] Lydie Ferrier, Esther Wertz, Robert Johne, Dmitry D. Solnyshkov, Pascale Senellart, Isabelle Sagnes, Aristide Lemaître, Guillaume Malpuech, and Jacqueline Bloch. Interactions in confined polariton condensates. *Phys. Rev. Lett.*, 106:126401, Mar 2011.

[132] P. M. Walker, L. Tinkler, B. Royall, D. V. Skryabin, I. Farrer, D. A. Ritchie, M. S. Skolnick, and D. N. Krizhanovskii. Dark solitons in high velocity waveguide polariton fluids. *Phys. Rev. Lett.*, 119:097403, Aug 2017.

[133] M. Vladimirova, S. Cronenberger, D. Scalbert, K. V. Kavokin, A. Miard, A. Lemaître, J. Bloch, D. Solnyshkov, G. Malpuech, and A. V. Kavokin. Polariton-polariton interaction constants in microcavities. *Phys. Rev. B*, 82:075301, Aug 2010.

[134] N. Takemura, S. Trebaol, M. Wouters, M. T. Portella-Oberli, and B. Deveaud. Heterodyne spectroscopy of polariton spinor interactions. *Phys. Rev. B*, 90:195307, Nov 2014.

[135] Naotomo Takemura, Stéphane Trebaol, Michiel Wouters, Marcia T Portella-Oberli, and Benoît Deveaud. Polaritonic feshbach resonance. *Nature Physics*, 10(7):500, 2014.

[136] A. S. Brichkin, S. I. Novikov, A. V. Larionov, V. D. Kulakovskii, M. M. Glazov, C. Schneider, S. Höfling, M. Kamp, and A. Forchel. Effect of coulomb interaction on exciton-polariton condensates in gaas pillar microcavities. *Phys. Rev. B*, 84:195301, Nov 2011.

[137] Michiel Wouters and Iacopo Carusotto. Excitations in a nonequilibrium bose-einstein condensate of exciton polaritons. *Phys. Rev. Lett.*, 99:140402, Oct 2007.

[138] Alexey Kavokin, Guillaume Malpuech, and Mikhail Glazov. Optical spin hall effect. *Phys. Rev. Lett.*, 95:136601, Sep 2005.

[139] Elena Kammann, Timothy Chi Hin Liew, Hamid Ohadi, Pasquale Cilibrizzi, Panayiotis Tsotsis, Zacharias Hatzopoulos, Pavlos G Savvidis, Alexey V Kavokin, and Pavlos G Lagoudakis. Nonlinear optical spin hall effect and long-range spin transport in polariton lasers. *Physical Review Letters*, 109(3):036404, 2012.

[140] M. Z. Maialle, E. A. de Andrada e Silva, and L. J. Sham. Exciton spin dynamics in quantum wells. *Phys. Rev. B*, 47:15776–15788, Jun 1993.

[141] Giovanna Panzarini, Lucio Claudio Andreani, A. Armitage, D. Baxter, M. S. Skolnick, V. N. Astratov, J. S. Roberts, Alexey V. Kavokin, Maria R. Vladimirova, and M. A. Kaliteevski. Exciton-light coupling in single and coupled semiconductor microcavities: Polariton dispersion and polarization splitting. *Phys. Rev. B*, 59:5082–5089, Feb 1999.

[142] Mark Steger, Brian Fluegel, Kirstin Alberi, David W Snoke, Loren N Pfeiffer, Ken West, and Angelo Mascarenhas. Ultra-low threshold polariton condensation. *Opt. Lett.*, 42(6):1165–1168, mar 2017.

[143] ES Sedov and AV Kavokin. Artificial gravity effect on spin-polarized exciton-polaritons. *Scientific Reports*, 7(1):1–10, 2017.

[144] S. Mukherjee, V. K. Kozin, A. V. Nalitov, I. A. Shelykh, Z. Sun, D. M. Myers, B. Ozden, J. Beaumariage, M. Steger, L. N. Pfeiffer, K. West, and D. W. Snoke. Dynamics of spin polarization in tilted polariton rings. *Phys. Rev. B*, 103:165306, Apr 2021.

[145] LP Pitaevskii. Phenomenological theory of superfluidity near the l point. *Sov. Phys.—JETP*, 8:282, 1959.

[146] S Choi, SA Morgan, and K Burnett. Phenomenological damping in trapped atomic bose-einstein condensates. *Physical Review A*, 57(5):4057, 1998.

[147] Allan Griffin, Tetsuro Nikuni, and Eugene Zaremba. *Bose-condensed gases at finite temperatures*. Cambridge University Press, 2009.

[148] D. A. Zezyulin, D. R. Gulevich, D. V. Skryabin, and I. A. Shelykh. Chiral solitons in spinor polariton rings. *Phys. Rev. B*, 97:161302, Apr 2018.

[149] VK Kozin, IA Shelykh, AV Nalitov, and IV Iorsh. Topological metamaterials based on polariton rings. *Physical Review B*, 98(12):125115, 2018.

[150] Chuanyi Zhang and Guojun Jin. Rotation of exciton-polariton condensates with te-tm splitting in a microcavity ring. *New Journal of Physics*, 19(9):093002, 2017.

[151] A. V. Yulin, V. K. Kozin, A. V. Nalitov, and I. A. Shelykh. Resonant excitation of acoustic waves in one-dimensional exciton-polariton systems. *Phys. Rev. A*, 100:043610, Oct 2019.

[152] H. Flayac, I. A. Shelykh, D. D. Solnyshkov, and G. Malpuech. Topological stability of the half-vortices in spinor exciton-polariton condensates. *Phys. Rev. B*, 81:045318, Jan 2010.

[153] F. E. Meijer, A. F. Morpurgo, and T. M. Klapwijk. One-dimensional ring in the presence of rashba spin-orbit interaction: Derivation of the correct hamiltonian. *Phys. Rev. B*, 66:033107, Jul 2002.

[154] DM Myers, B Ozden, J Beaumariage, LN Pfeiffer, K West, and DW Snoke. Pushing photons with electrons: Observation of the polariton drag effect. *arXiv preprint arXiv:1808.07866*, 2018.

[155] James F Annett et al. *Superconductivity, superfluids and condensates*, volume 5. Oxford University Press, 2004.

[156] Philippe Nozières. *Theory of quantum liquids*. CRC Press, 2018.

[157] Evgenii Mikhailovich Lifshitz and Lev Petrovich Pitaevskii. *Statistical physics: theory of the condensed state*, volume 9. Elsevier, 2013.

[158] P Blair Blakie, AS Bradley, MJ Davis, RJ Ballagh, and CW Gardiner. Dynamics and statistical mechanics of ultra-cold bose gases using c-field techniques. *Advances in Physics*, 57(5):363–455, 2008.

[159] CW Gardiner, MD Lee, RJ Ballagh, MJ Davis, and P Zoller. Quantum kinetic theory of condensate growth: Comparison of experiment and theory. *Physical review letters*, 81(24):5266, 1998.

[160] Chad N Weiler, Tyler W Neely, David R Scherer, Ashton S Bradley, Matthew J Davis, and Brian P Anderson. Spontaneous vortices in the formation of bose–einstein condensates. *Nature*, 455(7215):948–951, 2008.

[161] TW Neely, AS Bradley, EC Samson, SJ Rooney, Ewan M Wright, KJH Law, R Carretero-González, PG Kevrekidis, MJ Davis, and Brian P Anderson. Characteristics of two-dimensional quantum turbulence in a compressible superfluid. *Physical review letters*, 111(23):235301, 2013.

[162] TW Neely, EC Samson, AS Bradley, MJ Davis, and Brian P Anderson. Observation of vortex dipoles in an oblate bose-einstein condensate. *Physical review letters*, 104(16):160401, 2010.

[163] AS Bradley, CW Gardiner, and MJ Davis. Bose-einstein condensation from a rotating thermal cloud: Vortex nucleation and lattice formation. *Physical Review A*, 77(3):033616, 2008.

[164] AS Bradley, SJ Rooney, and RG McDonald. Low-dimensional stochastic projected gross-pitaevskii equation. *Physical Review A*, 92(3):033631, 2015.

[165] RG McDonald and AS Bradley. Brownian motion of a matter-wave bright soliton moving through a thermal cloud of distinct atoms. *Physical Review A*, 93(6):063604, 2016.

[166] SJ Rooney, AS Bradley, and PB Blakie. Decay of a quantum vortex: Test of nonequilibrium theories for warm bose-einstein condensates. *Physical Review A*, 81(2):023630, 2010.

[167] Guillaume Gauthier, Matthew T Reeves, Xiaoquan Yu, Ashton S Bradley, Mark A Baker, Thomas A Bell, Halina Rubinsztein-Dunlop, Matthew J Davis, and Tyler W Neely. Giant vortex clusters in a two-dimensional quantum fluid. *Science*, 364(6447):1264–1267, 2019.

[168] Hui Deng, Hartmut Haug, and Yoshihisa Yamamoto. Exciton-polariton bose-einstein condensation. *Reviews of modern physics*, 82(2):1489, 2010.

[169] Iacopo Carusotto and Cristiano Ciuti. Quantum fluids of light. *Reviews of Modern Physics*, 85(1):299, 2013.

[170] Rob Glenn McDonald. *Anomalous Dissipation in Bose Gases: Analytic Theory of Energy Damping*. PhD thesis, University of Otago, 2019.

[171] Crispin Gardiner, Peter Zoller, and Peter Zoller. *Quantum noise: a handbook of Markovian and non-Markovian quantum stochastic methods with applications to quantum optics*. Springer Science & Business Media, 2004.

[172] Crispin Gardiner and Peter Zoller. *The quantum world of ultra-cold atoms and light book II: the physics of quantum-optical devices*, volume 4. World Scientific Publishing Company, 2015.

[173] S Mukherjee, VK Kozin, AV Nalitov, IA Shelykh, Z Sun, DM Myers, B Ozden, J Beaumariage, M Steger, LN Pfeiffer, et al. Dynamics of spin polarization in tilted polariton rings. *arXiv preprint arXiv:2011.05462*, 2020.

[174] M Abbarchi, A Amo, VG Sala, DD Solnyshkov, H Flayac, L Ferrier, I Sagnes, E Galopin, A Lemaître, G Malpuech, et al. Macroscopic quantum self-trapping and josephson oscillations of exciton polaritons. *Nature Physics*, 9(5):275–279, 2013.

[175] KG Lagoudakis, B Pietka, M Wouters, Régis André, and Benoit Deveaud-Plédran. Coherent oscillations in an exciton-polariton josephson junction. *Physical review letters*, 105(12):120403, 2010.

[176] Guillaume Malpuech, YG Rubo, FP Laussy, Pierre Bigenwald, and AV Kavokin. Polariton laser: thermodynamics and quantum kinetic theory. *Semiconductor science and technology*, 18(10):S395, 2003.

[177] R Rapaport, R Harel, E Cohen, Arza Ron, E Linder, and LN Pfeiffer. Negatively charged quantum well polaritons in a gaas/alas microcavity: An analog of atoms in a cavity. *Physical review letters*, 84(7):1607, 2000.

[178] I Galbraith and Stephan W Koch. A comparison of lasing mechanisms in znse and gaas. *Journal of crystal growth*, 159(1-4):667–671, 1996.

[179] Anatoli Polkovnikov. Phase space representation of quantum dynamics. *Annals of Physics*, 325(8):1790–1852, 2010.

[180] CW Gardiner and MJ Davis. The stochastic gross–pitaevskii equation: Ii. *Journal of Physics B: Atomic, Molecular and Optical Physics*, 36(23):4731, 2003.

[181] DW Snoke. Density dependence of electron scattering at low density. *Physical Review B*, 50(16):11583, 1994.

[182] Shyamal Mondal, Shouvik Mukherjee, Satya Pratap Singh, Stephen C Rand, Sayantan Bhattacharya, Amit C Das, and Prasanta Kumar Datta. Dynamic gain aperture modelocking in picosecond regime based on cascaded second-order nonlinearity. *Optics express*, 24(14):15274–15288, 2016.

[183] Kirill P Kalinin, Pavlos G Lagoudakis, and Natalia G Berloff. Exotic states of matter with polariton chains. *Physical Review B*, 97(16):161101, 2018.

[184] Kirill P Kalinin and Natalia G Berloff. Gain-dissipative simulators for large-scale hard classical optimisation. *arXiv preprint arXiv:1805.01371*, 2018.

[185] Kirill P Kalinin, Pavlos G Lagoudakis, and Natalia G Berloff. Matter wave coupling of spatially separated and unequally pumped polariton condensates. *Physical Review B*, 97(9):094512, 2018.

[186] Kirill P Kalinin, Sergey Alyatkin, Pavlos G Lagoudakis, Alexis Askitopoulos, and Natalia G Berloff. Simulating the spectral gap with polariton graphs. *Physical Review B*, 102(18):180303, 2020.

[187] Pavlos G Lagoudakis and Natalia G Berloff. A polariton graph simulator. *New Journal of Physics*, 19(12):125008, 2017.

[188] Pankaj Mehta, Marin Bukov, Ching-Hao Wang, Alexandre GR Day, Clint Richardson, Charles K Fisher, and David J Schwab. A high-bias, low-variance introduction to machine learning for physicists. *Physics reports*, 810:1–124, 2019.

[189] William H Press, H William, Saul A Teukolsky, A Saul, William T Vetterling, and Brian P Flannery. *Numerical recipes 3rd edition: The art of scientific computing*. Cambridge university press, 2007.